Academic Press is an imprint of Elsevier
Linacre House, Jordan Hill, Oxford OX2 8DP, UK
32 Jamestown Road, London NW1 7BY, UK
Radarweg 29, PO Box 211, 1000 AE Amsterdam, The Netherlands
30 Corporate Drive, Suite 400, Burlington, MA 01803, USA
525 B Street, Suite 1900, San Diego, CA 92101-4495, USA

First edition 2009

Copyright © 2009, Elsevier Inc. All rights reserved

No part of this publication may be reproduced, stored in a retrieval system
or transmitted in any form or by any means electronic, mechanical, photocopying,
recording or otherwise without the prior written permission of the publisher

Permissions may be sought directly from Elsevier's Science & Technology Rights Department in Oxford, UK: phone (+44) (0) 1865 843830; fax (+44) (0) 1865 853333; email: permissions@elsevier.com. Alternatively you can submit your request online by visiting the Elsevier web site at http://www.elsevier.com/locate/permissions, and selecting: *Obtaining permission to use Elsevier material*

Notice
No responsibility is assumed by the publisher for any injury and/or damage to persons or property as a matter of products liability, negligence or otherwise, or from any use or operation of any methods, products, instructions or ideas contained in the material herein. Because of rapid advances in the medical sciences, in particular, independent verification of diagnoses and drug dosages should be made

ISBN: 978-0-12-375074-7
ISSN: 0065-3276

For information on all Academic Press publications
visit our website at elsevierdirect.com

Printed and bound in USA
09 10 11 12 10 9 8 7 6 5 4 3 2 1

Working together to grow
libraries in developing countries

www.elsevier.com | www.bookaid.org | www.sabre.org

ELSEVIER BOOK AID International Sabre Foundation

PREFACE

The study of confined quantum systems has attracted increasing attention from several research groups in the world due to the unusual physical and chemical properties exhibited by such systems when subject to spatial limitation. Such novel properties, not present in conventional materials, have marked a new era for the synthesis of modern materials – structured at the nanoscale – and leading to what is now called nanotechnology.

As is the case with any scientific development with important technological consequences, basic research plays a fundamental role whereby appropriate models are designed to explore and predict the physical and chemical behavior of a system. A confined quantum system is a clear example where theory constitutes a cornerstone for explanation and prediction of new properties of spatially limited atoms, molecules, electrons, excitons, etc. Theoretical study of possible confined structures might also suggest and stimulate further experimental investigations. In essence, the design of novel materials with exceptional properties requires proper theoretical modeling.

A collection of contributions from leading scientists in the field dealing with different theoretical approaches for tackling a wide variety of quantum systems under different confinement conditions is presented in this and its companion volume: Vol. 57. These volumes also provide an updated view of recent developments and open problems. The type of confined systems studied ranges from the hydrogen, helium and many-electron atoms within geometrical boundaries, atoms and molecules encaged inside fullerene and fullerene-like cages, plasma effects on confined many-electron atoms up to low-dimensional multi-electron quantum dots, to engineering of quantum confined silicon nanostructures.

We hope that these volumes will inspire both new and senior researchers to participate in this exciting and timely field. Although the topics covered in these volumes are by no means exhaustive, and although not all the experts are included, we are certain that the wide span of topics given here constitutes an important reference for the state-of-the-art development in the field of confined quantum systems.

We are grateful to all contributors for devoting their valuable time and dedication in contributing to these volumes.

Salvador A. Cruz
Special Editor

CONTRIBUTORS

Numbers in parentheses indicate the pages where the authors' contributions can be found.

S. Canuto (115)
Instituto de Física, Universidade de São Paulo, CP 66318, São Paulo, SP 05315-970, Brazil
canuto@if.usp.br

D.O. Charkin (69)
Chemical Department, Moscow State University, Vorob'evy gory, Moscow, 119992 Russia
charkin@inorg.chem.msu.ru

O.P. Charkin (69)
Institute of Problems of Chemical Physics, Russian Academy of Sciences, Institutskii pr. 18, Chernogolovka, Moscow oblast, 142432 Russia
charkin@icp.ac.ru

Elena Degoli (203)
CNR-INFM-S^3 and Dipartimento di Scienze e Metodi dell'Ingegneria - Università di Modena e Reggio Emilia - via Amendola 2 Pad. Morselli, I-42100 Reggio Emilia, Italy
degoli.elena@unimore.it

Geerd H.F. Diercksen (177)
Max-Planck-Institut für Astrophysik, Karl-Schwarzschild-Strasse 1, D-85741 Garching, Germany
http://www.mpa-garching.mpg.de/mol_physics/index.shtml
ghd@mpa-garching.mpg.de

V.K. Dolmatov (13)
Department of Physics and Earth Science, University of North Alabama, Florence, Alabama 35632, USA
vkdolmatov@una.edu

Patricio Fuentealba (1)
Departamento de Física, Facultad de Ciencias, Universidad de Chile, Casilla 653, Santiago, Chile
pfuente@abello.dic.uchile.cl

Jorge Garza (1)
Departamento de Química, División de Ciencias Básicas e Ingeniería,
Universidad Autónoma Metropolitana-Iztapalapa, San Rafael Atlixco 186,
Col. Vicentina. Iztapalapa. C. P. 09340, México D. F, México
jgo@xanum.uam.mx

Doris Guerra (1)
Universidad Técnica Federico Santa María, Casilla 110-V Valparaíso, Chile
do.guerra@uandresbello.edu

N.M. Klimenko (69)
Lomonosov State Academy of Fine Chemical Technology, pr. Vernadskogo
86, Moscow, 117571 Russia
klimenko@mitht.ru

P.K. Mukherjee (115)
Department of Spectroscopy, Indian Association for the Cultivation of
Science, Jadavpur, Kolkata-700 032, India
ProfPKMukherjee@gmail.com

Stefano Ossicini (203)
CNR-INFM-S^3 and Dipartimento di Scienze e Metodi dell'Ingegneria -
Università di Modena e Reggio Emilia - via Amendola 2 Pad. Morselli, I-
42100 Reggio Emilia, Italy
stefano.ossicini@unimore.it

Josef Paldus (177)
Department of Applied Mathematics, University of Waterloo, Waterloo,
Ontario N2L 3G1, Canada
paldus@scienide2.uwaterloo.ca

Rubicelia Vargas (1)
Departamento de Química, División de Ciencias Básicas e Ingeniería,
Universidad Autónoma Metropolitana-Iztapalapa, San Rafael Atlixco 186,
Col. Vicentina. Iztapalapa. C. P. 09340, México D. F, México
ruvf@xanum.uam.mx

Tokuei Sako (177)
Laboratory of Physics, College of Science and Technology, Nihon University,
7-24-1 Narashinodai, Funabashi, 274-8501 Chiba, Japan
http://www.phys.ge.cst.nihon-u.ac.jp/~sako/
sako@phys.ge.cst.nihon-u.ac.jp

A.N. Sil (115)
Max Planck Institute for the Physics of Complex Systems, Nöthnitzer Str. 38,
01187 Dresden, Germany
amar@mpipks-dresden.mpg.de

CHAPTER 1

Modeling Pressure Effects on the Electronic Properties of Ca, Sr, and Ba by the Confined Atoms Model

Doris Guerra[a,b], **Rubicelia Vargas**[c],
Patricio Fuentealba[d] and **Jorge Garza**[c]

Contents

1. INTRODUCTION

Matter under extreme conditions of pressure has been an interesting topic for a long time for both experimental and theoretical researchers [1]. The experimental techniques have given insight about the responses of matter under such conditions. From a theoretical point of view, the techniques of

[a] Universidad Técnica Federico Santa María, Casilla 110-V Valparaíso, Chile
[b] Instituto de Química, Universidad de Antioquia, A. A. 1226, Medellín, Colombia
[c] Departamento de Química, División de Ciencias Básicas e Ingeniería, Universidad Autónoma Metropolitana-Iztapalapa, San Rafael Atlixco 186, Col. Vicentina. Iztapalapa. C. P. 09340, México D. F, México
[d] Departamento de Física, Facultad de Ciencias, Universidad de Chile, Casilla 653, Santiago, Chile

E-mail address: ruvf@xanum.uam.mx (R. Vargas).

Advances in Quantum Chemistry, Vol. 58
ISSN: 0065-3276, DOI: 10.1016/S0065-3276(09)00705-9

solid-state physics give a detailed account of the electronic structure when the lattice parameter changes, such that the pressure can be computed and all properties of the system can be studied as function of this pressure [2–5]. Complementary to the solid-state techniques, there is a model that emerged in the early days of quantum mechanics. Michels et al. [6] proposed the hydrogen atom confined within a sphere built with rigid walls, such that the electron density, $\rho(\mathbf{r})$, satisfies

$$\rho(\mathbf{r}) = \begin{cases} 0 & |\mathbf{r}| \geq R_c \\ \text{else} & |\mathbf{r}| < R_c \end{cases} \tag{1}$$

with R_c as the sphere radius. In this way, these authors could give an idea about the pressure effects on the hydrogen atom. Currently, many groups use this model to study many-electron atoms confined under the same boundary conditions imposed in Equation (1). We can find several reports where people use the Hartree-Fock (HF) [7,8] or Kohn-Sham (KS) [9] approaches to find the electron density of confined many-electron atoms. Of course, the Dirichlet boundary conditions imposed in Equation (1) demand new computational codes because the widely used codes are built with different boundary conditions.

One confinement effect observed on the electronic structure in an atom is the crossing between different energy levels, occupied and unoccupied, and consequently the filling of these orbitals is different to that observed on free atoms [8,10]. With this new orbital filling, this model predicts an electronic transition in alkaline metals, such that the d orbitals are more stable than the s orbitals [10]. Thus, the alkaline metals under these circumstances exhibit a similar behavior to that presented by transition metals and consequently these metals can form alloys [11]. This is an important result obtained by this model because such electronic transitions were experimentally detected [12]. The alkaline earth metals present a similar behavior and it has been demonstrated, by theoretical and experimental work, that the structural behavior of heavy alkaline earth metals (Ca, Sr, Ba) is quite complicated. For all these metals, crystal structure transitions are present when high pressures are imposed on these structures [13–23]. The driving force for these crystallographic transitions is the number of d electrons that increase when the metal is compressed [15,16,23], such pressures have been experimentally measured, and they are also estimated by solid-state theoretical methods [13–23]. There are, as in the alkaline metals, alloys between Mg or Ca and Ni used as hydrogen storage devices [24–26].

In this work, we use the confined atoms model, with hard walls, to estimate the pressure on confined Ca, Sr, and Ba atoms. With this approach, we will give an upper limit to the pressure, because it is well known that the Dirichlet boundary conditions give an overestimation to this quantity. By using this approach, we obtain the profiles of some electronic properties as a function of the pressure. The main targets of this study are the possible electronic transitions and their relationship with reactivity concepts developed by the spin-polarized (SP) version of the Density Functional Theory (DFT) [27].

Evidently, an atom confined by rigid walls is a simple model to study electrons restricted to move in small regions, and consequently it bears intrinsic problems. For example, it is clear that within a lattice of atoms under high pressures the electrons between neighboring atoms affect each other, thus the most representative model for this process could be a sphere with soft walls [28,29]. In such a model, the confinement potential is constant from an arbitrary distance to infinity, and people write the wave function in different ways depending on the region. Continuity on the wave function and its derivative are the criteria to assure a correct behavior. Until now, atoms have been systems where this model was used, but the electron-electron interaction was zero within the constant potential region [28–31]. Evidently that is the main failure of this approximation, since in the classical forbidden region there is tunneling and consequently the electron-electron interaction exists in that region.

2. METHODOLOGY

2.1. Energy vs pressure

The first step in our study is the estimation of the pressure. Firstly, we compute the total energy of an atom, Ca for example, as a function of the confinement radius for the ground state electronic configuration of the *free* atom (unconfined atom). Because the total energy, E, is a function of the volume, V, then we estimate numerically the pressure from

$$p = -\frac{\partial E}{\partial V}, \tag{2}$$

in our case, we use five points to compute this derivative. The five points are equally spaced with a distance of 0.1 au. In this way, we obtain profiles of E as a function of p. Additionally, we compute the free energy, G, of each electronic configuration because the pV term is also obtained. We apply this procedure for each electronic configuration, and for the analysis we use the most stable electronic configuration, according to the free energy, depending on the confinement region. The transition pressure is where the minimum of the free energy of each configuration is the same for two electron configurations. We compare this procedure with another where the plot G vs p, for two electron configurations, coincides. For both procedures, the transition pressure is almost the same.

2.2. Spin-potential in density functional theory framework

To describe the chemical reactivity in the context of DFT, there are several global and local quantities useful to understand: the charge transfer in a chemical reaction, the attack sites in a molecule, the chemical stability of a system, etc. In particular, there are processes where the spin number changes with a fixed number of electrons; such processes demand the SP-DFT version [27,32]. In this approach, some natural variables are the number of electrons, N, and the spin number, N_s. The total energy changes, estimated by a Taylor series to the first order, are

$$\Delta E \approx \left(\frac{\partial E}{\partial N_s}\right)_{N,\upsilon} \Delta N_s + \left(\frac{\partial E}{\partial N}\right)_{N_s,\upsilon} \Delta N. \tag{3}$$

Thus, in systems where the multiplicity changes because there are electronic transitions, Equation (3) is suitable.

In this work, we compute the total energy changes in two ways: (a) the difference between the total energy of each electronic configuration, ΔSCF. (b) applying Equation (3). For the case (a), we pick the most stable electronic configuration and report the energy difference between this configuration and the next in energy. For the case (b), we again use the most stable electronic configuration to evaluate the corresponding derivatives in Equation (3). For the considered atoms, there are transitions from singlet to triplet because the electronic configuration for the valence electrons in the free atoms is s^2 and these two electrons are unpaired in the excitation process to produce a triplet. However, in this process the number of electrons is unaltered, thus the Equation (3) is just

$$\Delta E \approx \left(\frac{\partial E}{\partial N_s}\right)_{N,\upsilon} \Delta N_s. \tag{4}$$

By using the definition of the spin potential

$$\mu_s = \left(\frac{\partial E}{\partial N_s}\right)_{N,\upsilon}, \tag{5}$$

with υ as the external potential [32]. For the singlet-triplet transition $\Delta N_S = 2$ then,

$$\Delta E \approx 2\mu_s. \tag{6}$$

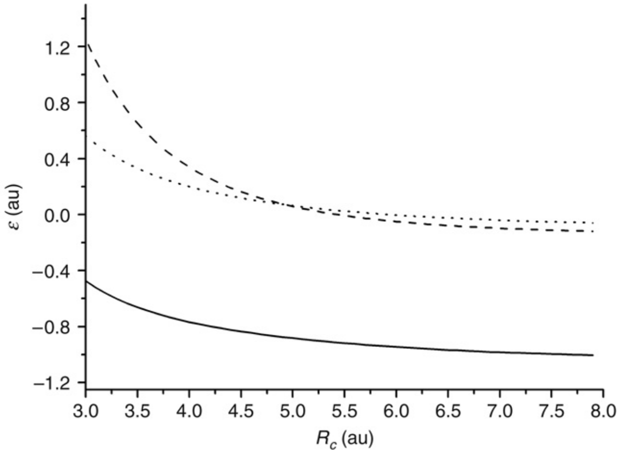

Figure 1 3p (solid line), 3d (dotted line) and 4s (dashed line) orbital energies for the confined Ca atom.

For such a process, Galván et al. [32] wrote the spin potential as

$$\mu_s^+ = \frac{1}{2}\left[\varepsilon_{\text{LUMO}}^{\alpha} - \varepsilon_{\text{HOMO}}^{\beta}\right], \tag{7}$$

where the + indicates an increase in the spin number. Thus, another way to estimate the total energy changes is through the $\text{LUMO}^{\alpha} - \text{HOMO}^{\beta}$ gap

$$\Delta E \approx \left(\varepsilon_{\text{LUMO}}^{\alpha} - \varepsilon_{\text{HOMO}}^{\beta}\right). \tag{8}$$

The computation of the electronic structure for each R_c is by using the KS approach with a code designed to use Dirichlet boundary conditions. In this work, we use the Perdew and Wang exchange-correlation functional [33] within the local density approximation [34]. Details about this code can be found in Ref. [9] and some applications are in Refs. [35–37].

3. RESULTS AND DISCUSSION

3.1. Transition pressures for Ca, Sr and Ba

We use the Ca atom, as an example, to show the main characteristics of all these systems when electronic transitions are present. Such characteristics are almost the same for all atoms considered in this study and consequently we do not discuss them atom by atom. In Figure 1, we show the behavior of some orbital energies for the Ca atom, in its ground state, as a function of the confinement radius. Evidently, for large confinement regions, the 4s

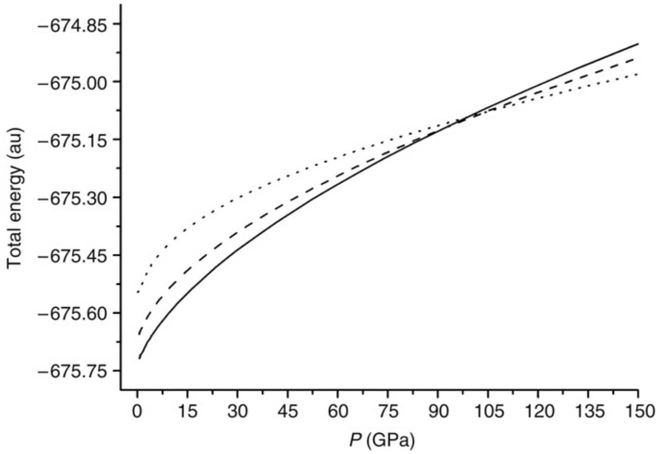

Figure 2 Energy as a function of the pressure for the confined Ca atom in the electronic configurations [Ar]4s^2(solid line), [Ar]4s^{1}3d^1 (dashed line) and [Ar]3d^2 (dotted line).

orbital is the most stable orbital, but it is also evident that there is a crossing between this orbital and the 3d orbital in the range of 4.5 and 5.0 a. u. This result suggests an electronic transition for such confinements, in this way we compute, for the three electronic configurations [Ar]4s^2, [Ar]4s^{1}3d^1 and [Ar]3d^2, the profiles E vs R_c and for each electron configuration we compute p. From these profiles we obtain Figure 2, where it is clear that the energy ordering for the three configurations depends on the pressure regions. As we mentioned in the methodology section, the free energy is obtained by adding the pV term to the total energy, thus we present Figure 3, where G is depicted for the three electronic configurations. Comparing Figure 2 with Figure 3 we notice the importance of working with G instead of E, because with E we may obtain transition pressures quite different to those obtained with G. Following this process, we compute the electronic transitions for Ca, Sr and Ba, and we report the corresponding pressures in Table 1. For the three atoms we consider the transitions $(n-1)\mathrm{p}^6 n\mathrm{s}^2 \rightarrow (n-1)\mathrm{p}^6 n\mathrm{s}^1 (n-1)\mathrm{d}^1 \rightarrow (n-1)\mathrm{p}^6 n\mathrm{s}^0 (n-1)\mathrm{d}^2$ with $n = 4, 5$ and 6 for Ca, Sr and Ba respectively. Also the transition $(n-1)\mathrm{p}^6 n\mathrm{s}^0 (n-1)\mathrm{d}^2 \rightarrow (n-1)\mathrm{p}^5 n\mathrm{s}^0 (n-1)\mathrm{d}^3$ was computed, but the corresponding transition pressures were quite high to be reported.

We see from Table 1 the good agreement found, for Ca and Ba, between our model and the experimental data. The experimental transition pressures reported in Table 1 are those where the semiconducting phase is present. Experimentally, the transition phase involves structural changes, but a correlation was reported [15,16] between these structural changes and population changes between the s and d bands. With the confined atoms model we corroborate such a transition, suggesting that for high pressures the information of one atom may be enough.

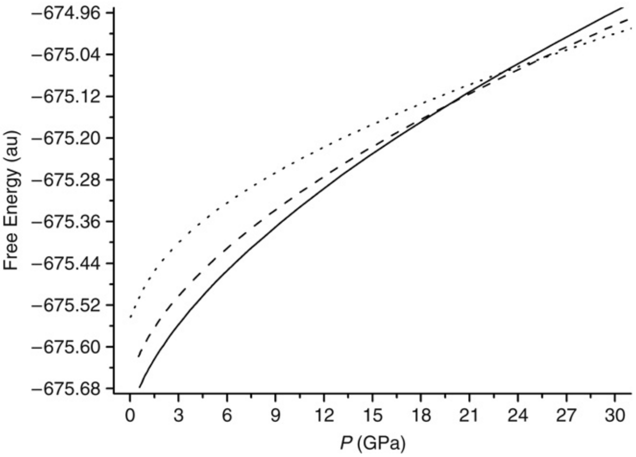

Figure 3 Free energy, G, versus the pressure, p, for the confined Ca atom in the electronic configurations [Ar]4s^2 (solid line), [Ar]4s^{1}3d^1 (dashed line) and [Ar]3d^2 (dotted line).

Table 1 Transition pressures for Ca, Sr and Ba estimated by the confined atom model. Pressure in GPa and confinement radii in atomic units

Most stable electronic configuration	R_c	Multiplicity	Transition pressure	
			This work	Exp.
	Ca			
[Ar]4s^2	∞–5.1	Singlet		
			19.8	19.5[a]
[Ar]3d^{1}4s^1	4.8-4.7	Triplet		
			25.4	
[Ar]3d^2	4.2-1.1	Triplet		
	Sr			
[Kr]5s^2	∞–5.4	Singlet		
			17.8	3.5[a]
[Kr]4d^{1}5s^1	5.1-5.1	Triplet		
			20.1	
[Kr]4d^2	4.7-1.2	Triplet		
	Ba			
[Xe]6s^2	∞–7.6	Singlet		
			1.9	5.5[b]
[Xe]5d^{1}6s^1	7.3-6.6	Triplet		
			3.7	
[Xe]5d^2	6.1-3.4	Triplet		

[a] Ref. [14].
[b] Ref. [18].

In the same Table 1, we report the confinement radii where the transitions are present. Thus, the singlet state for each atom dominates from 5.1, 5.4 and 7.6 to infinity for Ca, Sr and Ba respectively. It is important to note the volume changes associated with the electronic transition. This change may be evaluated from the difference between the R_c found for the different electronic configurations, for Ca there is a R_c change from 5.1 to 4.8 au. In crystalline structures, the changes between different structures, induced by the pressure, involve changes in the volume. Thus, we may say that the pressure induces electronic transitions and these transitions induce changes in the volume, such an observation is valid for confined atoms and for crystalline structures.

We see a large discrepancy between the experimental information and our prediction, obtained with the confined atoms model for the Sr atom. We must mention that this system is a challenge to many theoretical methods. The main reason for such a challenge is the number of phases observed for this element when is under high pressure, and the slight difference between some of the observed structures. Skriver [16] observed a partial filling of the d band when the semiconducting phase is present. In fact, Sr shows structural transition pressures between 3.5 and 50 GPa for occupancies between 0.7 and 1.3 in the d band, respectively. We see from Table 1 that for an occupancy of 1 our model predicts a transition pressure of 17.8 GPa, which is close to the calculated value for that occupancy [16], but does not correspond to the first observed transition pressure. However, we tried to see if the confined atoms model predicts changes on the transition pressures when the d orbital occupancy changes, but the obtained results do not correspond with those observed in previous reports.

3.2. Electronic transitions as a function of the pressure

According to Figure 3 there are three possibilities for excitation energies, $5s^2 \rightarrow 5s^1 4d^1$, $5s^1 4d^1 \rightarrow 4d^2$ and $4d^2 \rightarrow 5s^1 4d^1$. In Figure 4, we present the behavior of the excitation energies as a function of the pressure for the Ca atom. Clearly, we observe a reduction in the excitation energies related to the filling of the d orbital when the pressure is increased. In fact, at the transition point, the first excitation energy is close to zero. This result coincides with that observed in crystalline structures, where the gap between the s and d bands is such that it gives semiconducting phases to this sort of metal. From the same figure we see that, for high pressures, the excitation energy is increased when one electron in the d orbital is transferred to the s orbital. It means that the confined atom prefers the electrons in the d orbital.

3.3. Spin-potential as predictor of the electronic transitions

As a first order approximation, the SP-DFT approach connects the spin-potential directly with the singlet-triplet excitation energy. Thus, the gap defined by the highest beta occupied molecular orbital, HOMO$^{\beta}$, and the

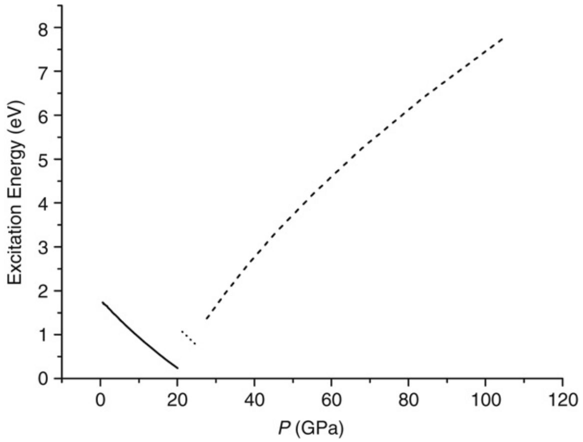

Figure 4 Excitation energies for the confined Ca atom; $5s^2 \rightarrow 5s^1 4d^1$ (solid line), $5s^1 4d^1 \rightarrow 4d^2$ (dotted line), $4d^2 \rightarrow 5s^1 4d^1$ (dashed line).

lowest alpha unoccupied molecular orbital, LUMO$^\alpha$, is a direct measurement of the excitation energy. In Table 2 we report the spin potential, μ_s^+, the HOMO$^\beta$–LUMO$^\alpha$ gap and the corresponding singlet-triplet excitation energy for Ca, Sr and Ba. In this table, we show the R_c values where the configuration $(n-1)p^6 ns^2$ is the most stable and close to the first transition pressure, i.e. the transition $(n-1)p^6 ns^2 \rightarrow (n-1)p^6 ns^1 (n-1)d^1$. It is important to note that only for this transition does the spin-potential make sense, because for the second transition, $(n-1)p^6 ns^1 (n-1)d^1 \rightarrow (n-1)p^6 ns^0 (n-1)d^2$, there are no changes in the number of electrons neither in the spin number. Thus, the spin-potential is an inadequate quantity to estimate singlet-singlet or triplet-triplet transitions. Additionally, we report R_c instead of p, in Table 2, because for two electronic configurations with the same pressure, necessarily such configurations have a different volume to each other. According to the spin-potential definition, we obtain this quantity with an external potential fixed; in our case, the external potential has two contributions, the nucleus, and the sphere walls. Thus, if we have two different values of R_c then the external potential is different for these two cases, and therefore the spin-potential cannot be used to estimate excitation energies as a function of the pressure.

We see from Table 2 a good estimation to ΔE by using the HOMO$^\beta$–LUMO$^\alpha$ gap for Ca, but for Sr and Ba the comparison is not as good. For these two atoms, the HOMO$^\beta$–LUMO$^\alpha$ gap overestimates the corresponding excitation energy with Ba as the worst case. Even when the relationship is not one to one, we see the same trend in both quantities, and for this reason we correlate the spin-potential with the excitation energy. In Figure 5 we plot the excitation energy versus μ_s^+. Clearly, we obtain a linear

Table 2 Spin-potential, $\varepsilon^{\alpha}_{\text{LUMO}} - \varepsilon^{\beta}_{\text{HOMO}}$ gap and singlet-triplet excitation energy, ΔE, for Ca, Sr and Ba. The confinement radius, R_c, is reported in atomic units and the other quantities in eV

R_c	μ_s^+	$\varepsilon^{\alpha}_{\text{LUMO}} - \varepsilon^{\beta}_{\text{HOMO}}$	ΔE
		Ca	
5.5	0.44	0.87	0.83
5.4	0.38	0.76	0.71
5.3	0.31	0.63	0.57
5.2	0.24	0.48	0.41
		Sr	
5.7	0.53	1.05	0.66
5.6	0.47	0.94	0.53
5.5	0.40	0.80	0.39
5.4	0.33	0.65	0.23
		Ba	
7.9	0.18	0.36	0.13
7.8	0.17	0.33	0.10
7.7	0.15	0.31	0.07
7.6	0.14	0.28	0.04

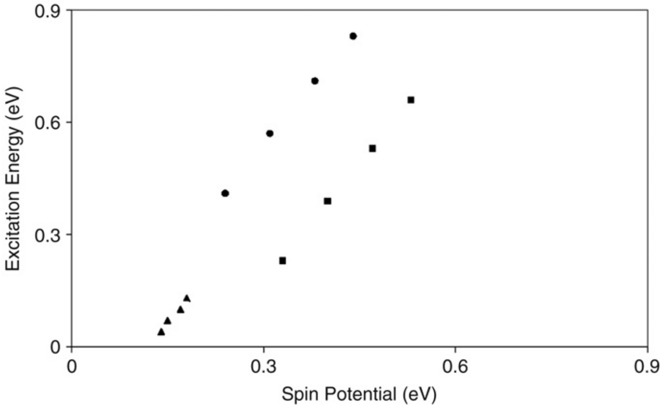

Figure 5 Excitation energy versus spin-potential for Ca (circles), Sr (squares) and Ba (triangles).

relationship. We have found such a behavior for other systems with quite different characteristic than confined atoms [38]. Thus, we again show the strong relationship between the μ_s^+ and the singlet-triplet excitation energies.

4. CONCLUSIONS

In this work, we study the electronic transitions observed for Ca, Sr and Ba atoms. We found, for Ca and Ba, a good correlation between the results obtained by the confined atoms model and those experimentally reported. These results suggest that mainly the filling of the *d* band controls the transitions presented by Ca and Ba alkaline earth metals when they are under high pressures, since the simple confined atoms model predicts just the transitions between the crossings of different orbitals. Furthermore, we interpret such transitions as occurring in situations where the atom's behavior is independent of that of its neighbors and the information obtained from the study of a single atom suffices. However, the results obtained by this model for the Sr atom disagree with the experimental reports. Thus, according with the previous conclusions, the transitions observed for this metal are not reproduced by one confined atom, because the atoms in this metal are not independent each other and consequently the s-d transition involves different spatial configurations between the atoms in the crystalline structure. Additionally, we found a good correlation between the spin-potential and the first excitation energy for the three atoms considered in this work, corroborating that the HOMO–LUMO gap may be used as a first approximation to the singlet-triplet excitation energy, as was found for non-confined systems.

ACKNOWLEDGMENTS

R. V. and J. G. thank CONACYT for the partial support of this work through the projects 60116 and 60614 respectively. P.F. is grateful for partial support by Fondecyt through grant 1080184.

REFERENCES

[1] W. Grochala, R. Hoffmann, J. Feng, N.W. Ashcroft, Angew. Chem.-Int. Edit. 46 (2007) 3620.
[2] O.K. Andersen, Phys. Rev. B 12 (1975) 3060.
[3] L.F. Mattheiss, D.R. Hamann, Phys. Rev. B 33 (1986) 823.
[4] H.L. Skriver, The LMTO Method, Springer, New York, 1984.
[5] J. Kohanoff, Electronic Structure Calculations for Solids and Molecules: Theory and Computational Methods, Cambridge, New York, 2006.
[6] A. Michels, J. de Boer, A. Bijl, Physica 4 (1937) 981.
[7] E. Ludeña, J. Chem. Phys. 69 (1978) 1770.
[8] J.-P. Connerade, V.K. Dolmatov, J. Phys. B 31 (1998) 3557.
[9] J. Garza, R. Vargas, A. Vela, Phys. Rev. E. 58 (1998) 3949.
[10] K.D. Sen, J. Garza, R. Vargas, A. Vela, Proc. Indian Natn. Sci. Acad. 70A (2004) 675.
[11] L.J. Parker, T. Atou, J.V. Badding, Science 273 (1996) 95.
[12] (a) K. Takemura, S. Minomura, O. Shimomura, Phys. Rev. Lett. 49 (1982) 1772;
(b) K. Takemura, K. Syassen, Phys. Rev. B 32 (1985) 2213;
(c) H. Tups, K. Takemura, K. Syassen, Phys. Rev. Lett. 49 (1982) 1776.
[13] A.O.E. Animalu, Phys. Rev. 161 (1967) 445.

[14] H. Olijnyk, W.B. Holzapfel, Phys. Lett. A 100 (1984) 191.
[15] R. Ahuja, O. Eriksson, J.M. Wills, B. Johansson, Phys. Rev. Lett 75 (1995) 3473.
[16] H.L. Skriver, Phys. Rev. Lett. 49 (1982) 1768.
[17] M. Winzenick, W.B. Holzapfel, Phys. Rev. B 53 (1996) 2151.
[18] T. Kenichi, Phys. Rev. B 50 (1994) 16238.
[19] F. Jona, P.M. Marcus, J. Phys.: Condens. Matter 18 (2006) 4623.
[20] R. Ahuja, B. Johansson, O. Eriksson, Phys. Rev. B 58 (1998) 8152.
[21] T. Bovornratanaraks, D.R. Allan, S.A. Belmonte, M.I. McMahon, R.J. Nelmes, Phys. Rev. B 73 (2006) 144112.
[22] A. Phusittrakool, T. Bovornratanaraks, R. Ahuja, U. Pinsook, Phys. Rev. B 77 (2008) 174118.
[23] O.K. Andersen, J. Madsen, U.K. Poulsen, O. Jepsen, J. Kollar, Physica (Utrecht) 86–88B (1977) 249.
[24] A. Kamegawa, Y. Goto, R. Kataoka, H. Takamura, M. Okada, Renew. Energy 33 (2008) 221.
[25] D. Uremovich, F. Islam, M. Medraj, Sci. Technol. Adv. Mater. 7 (2006) 119.
[26] G. Liang, R. Schulz, J. Alloy. Compd. 356 (2003) 612.
[27] R. Vargas, A. Cedillo, J. Garza, M. Galván, in: K.D. Sen (Ed.), Reviews of Modern Quantum Chemistry, vol. II, World Scientific, New Jersey, 2002, p. 936.
[28] J. Gorecki, W.B. Brown, J. Chem. Phys. 89 (1988) 2138.
[29] J. Gorecki, W.B. Brown, J. Phys. B 21 (1988) 403.
[30] J.L. Marín, S.A. Cruz, J. Phys. B 25 (1992) 4365.
[31] C. Díaz-García, S.A. Cruz, Int. J. Quantum Chem. 108 (2008) 1572.
[32] (a) M. Galván, A. Vela, J.L. Gázquez, J. Phys. Chem. 92 (1988) 6470;
(b) M. Galván, R. Vargas, J. Phys. Chem. 96 (1992) 1625.
[33] J.P. Perdew, Y. Wang, Phys. Rev. B 45 (1992) 13244.
[34] (a) W. Kohn, L.J. Sham, Phys. Rev 140 (1965) A1133;
(b) U. von Barth, L. Hedin, J. Phys. C 5 (1972) 1629.
[35] K.D. Sen, J. Garza, R. Vargas, A. Vela, Chem. Phys. Lett. 325 (2000) 29.
[36] J. Garza, R. Vargas, N. Aquino, K.D. Sen, J. Chem. Sci. 117 (2005) 379.
[37] J. Garza, R. Vargas, A. Vela, K.D. Sen, J. Mol. Struc. (Theochem) 501 (2000) 183.
[38] A. Vazquez-Mayagoitia, R. Vargas, J.A. Nichols, P. Fuentealba, J. Garza, Chem. Phys. Lett 419 (2006) 207.

CHAPTER 2

Photoionization of Atoms Encaged in Spherical Fullerenes

V.K. Dolmatov[a]

Contents

[a] Department of Physics and Earth Science, University of North Alabama, Florence, Alabama 35632, USA

E-mail address: vkdolmatov@una.edu.

Advances in Quantum Chemistry, Vol. 58
ISSN: 0065-3276, DOI: 10.1016/S0065-3276(09)00706-0

---

1. INTRODUCTION

Since the discovery of the fullerene molecule C_{60} [1], various synthesized fullerenes C_n (n being the number of carbon atoms in the fullerene; the latter is termed giant fullerene if $n \geq 240$) have become subjects of a significant interest to study. This is because, firstly, they are new fascinating objects to study and, secondly, they are perceived as new building blocks for the production of materials and tools with unique properties having a broad range of applicability [2–5]. Moreover, doped fullerenes with trapped noble gas atoms present a significance for astrophysical phenomena as well [6]. The outstanding feature of a C_n fullerene is that its carbon atoms are positioned on a closed surface, thereby forming a stable carbon cage with a hollow inner space. The volume of the empty space of the carbon cage C_n varies over a large range depending on the number of carbon atoms in the cage. Thus, the mean radius of the smallest known spherical fullerene C_{20} is about 3.86 au [7], whereas it is approximately 36 au in the giant fullerene C_{1500} [8]. Consequently, the hollow interior of C_n may be large enough to accommodate an atom A or even a cluster of atoms A_N inside the cage, thereby forming doped fullerenes $A@C_n$ or $A_N@C_n$, respectively [2–4]. Furthermore, a giant fullerene can encage one or more smaller fullerenes inside its giant cage, $C_n@C_{m>n}$, $C_n@C_{m>n}@C_{l>m}$, etc.; these are termed fullerene onions [4,8]. Chemical properties of doped fullerenes differ from those of empty fullerenes, thereby providing a greater flexibility for the production of a large variety of new materials with unusual properties. To name a few, $La@C_{60}$-based crystal turns out to be an air-stable superconductor [9], whereas in $N@C_{60}$ the encaged nitrogen atom preserves its atomic properties while being effectively screened by C_{60} from outside atoms, so that it is perceived as an ideal candidate for building quantum computers [10]. Doped fullerene onions, $C_n@C_{m>n}$, etc., provide another way for tailoring fullerene systems to synthesize materials with unusual properties, thereby signifying their importance. No wonder that the quantum structure and properties of doped fullerene systems have become frontline topics of research in the chemistry and physics of nanoformations.

The quantum structure and properties of empty fullerenes C_n are extensively studied with the help of the powerful photoelectron (photoabsorption) spectroscopy technique [2,11]. As for the spectroscopy of gas phase doped fullerenes, $A@C_n$, it has been rather difficult to perform due to the difficulty to produce sufficient amounts of purified doped fullerenes for gas phase experiments [12,13]. However, recently, the experimental situation has clearly changed for the better, and the very first experiments on photoionization of encaged atoms from doped fullerenes ($Sc_3@C_{82}^+$ [12] and $Ce@C_{82}$ [13]) have emerged. Thus the spectroscopy of atoms encaged in doped fullerenes is turning into a promising area of new exciting investigations. Consequently, detailed knowledge on the modifications in the structure and photo-spectra of an atom A encaged by the carbon confinement, compared to the free atom, is extremely relevant. First, it is a matter of practical importance to be capable of distinguishing which part of the spectrum of the doped fullerene is due to photoionization of its carbon cage(s) and which is due to photoionization of the encaged atom itself. Second, by confining the atom inside finite cages there is the possibility of controllably modifying atomic properties [3, 14,15] (and references therein) or isolating atomic properties from the effects of an aggressive external medium (as in $N@C_{60}$ [10]). One way to investigate, make use of, or to manipulate such "hidden" atoms is, obviously, through their photoionization.

To date, since the photoelectron spectroscopy of doped fullerenes has been difficult to perform, numerous theoretical studies of photoionization spectra of atoms encaged in doped fullerenes, performed at various levels of approximations, [15–46], have been prevalent. Consequently, to aid emerging experiments and new theories on gas phase doped fullerenes, a review of the theoretical findings and predictions that have been accumulated in this area of research so far is very timely. This is precisely the aim of the present paper.

In this paper, the author focuses the reader's attention on two particularly simple models, from a variety of the existing models cited above, that have been used extensively to probe the structure and spectra of atoms encaged in various doped spherical fullerene systems. Both models are semiempirical models. They assume the encaged atom to be sitting at the center of the carbon cage C_n which, itself, is simulated by a spherical attractive potential well of an adjustable radius R_n, thickness Δ and depth U_n^0 [20,34]. There are important differences between the two models. One of the two models [20], termed Δ-potential model, accounts for the finite thickness Δ of the C_n cage as well as for the interaction between the ground state encaged atom and the carbon cage itself, at a certain level of approximation. The other model [34], termed δ-potential model, simulates the carbon cage with the help of the Dirac δ-function $\delta(r - R_n)$, thereby viewing the cage as an infinitesimally thin sphere ($\Delta = 0$). This model assumes no interaction between the ground state encaged atom and the carbon cage. The limits of validity of the models are considered. Discovered on the basis of these two models, significant modifications and trends in the structure and photoionization spectra of atoms encaged in neutral and charged single-walled fullerenes C_n with

$n = 60$, 240 and 540, as well as in multiwalled fullerene onions $C_{60}@C_{240}$ and $C@_{60}@C_{240}@C_{540}$ are reviewed. A side by a side comparison of results produced by the Δ- and δ-potential models is presented. The discussion encompasses both the individual and combined effects of the confinement, electron correlation and relativistic effects on the photoionization spectra of thus encaged atoms. Many of the results obtained on the basis of the Δ- and δ-potential models prior to 2004 have been summarized earlier [15]. The present paper focuses primarily on newer results. Nevertheless, some of the most important results (from the author's viewpoint) from earlier years are detailed in the paper as well.

Atomic units (au) where $e = \hbar = m_e$ (e and m_e being the electron's charge and mass, respectively) are used throughout the paper.

2. MODELING DOPED FULLERENES

2.1. Preliminaries

The description of the interaction of electromagnetic radiation with a doped fullerene is a complicated theoretical problem. Therefore, to get an insight into the rich variety of effects that might occur in photoionization spectra of doped fullerenes, rather than to make detailed predictions for one particular spectrum, some, even considerable, simplifications of the problem are useful. In fact, differences between predictions using various approximations could be a first step in identifying the most useful measurements to perform. One of the simplifications comes from the assumption that the radius of the fullerene cage is significantly bigger than the radius of any *nl* subshell of the ground state encaged atom. Thus, to a good approximation, with some exceptions, the ground state encaged atom is only perturbed insignificantly by the cage. Therefore, the atom preserves its atomic structure whereas the cage preserves its own structure. Furthermore, when the wavelength of the *nl* photoelectron significantly exceeds the bond length between the carbon atoms of the C_n cage, the C_n cage can be replaced by an effective spherical, attractive, continuous, homogeneous medium acting on the photoelectron. For this, the *nl* photoelectron must be slow; this corresponds to near-threshold *nl* photoionization of the encaged atom. Thus, the slow photoelectron will perceive the fullerene cage as an unstructured semi-transparent spherical shell that generates a reflected electronic wave inside the sphere and a transmitted wave outside.

In this section, the two simple models mentioned in the Introduction, the Δ-potential model and the δ-potential model, both of which are based on the listed simplifications, are reviewed.

2.2. The Δ-potential model: Neutral doped fullerenes $A@\mathrm{C}_n$

In the Δ-potential model, the C_n cage is modeled by a spherical, short-range, attractive potential $V_n(r)$ of inner radius R_n, thickness Δ, and depth U_n^0:

$$V_n(r) = \begin{cases} -U_n < 0, & \text{if } R_n \le r \le R_n + \Delta \\ 0 & \text{otherwise.} \end{cases} \tag{1}$$

This model was, perhaps, first suggested by Pushka and Nieminen [16] in conjunction with the jellium model of C_{60}. Later on, it was used, independently, in another work [47]. At a later stage, the idea was greatly extended to numerous studies of various aspects of structure and photoionization of atoms A encaged in various spherical fullerenes [15,20–22,27–33,42–44].

For a spherical fullerene C_n, in accordance with the model, the atom A is placed at the geometrical center of C_n, which, in turn, is simulated by the potential (1). Positioning the encaged atom at the center of C_n is reasonable, since experimental studies of $A@\mathrm{C}_{60}$ show that noble gas atoms [48] and group-V atoms [49] are, as a rule, located at the center of the carbon cage without any charge transfer to the cage. It is the very small van der Waals forces that cause the atom to be located at the center of the cage. These van der Waals forces are quite weak, compared to atomic (Coulomb) forces, so they do not alter the ground state wave function of the encaged atom A appreciably. Electronic wave functions $\psi_{nlm}(\boldsymbol{r}) = r^{-1}P_{nl}(r)Y_{lm}(\theta, \phi)$ and electron binding energies ϵ_{nl} of the N-electron encapsulated atom are obtained by substituting the potential V_n into HF equations for the free atom, thereby turning them into HF equations for a neutral single-walled doped fullerene $A@\mathrm{C}_{60}$ [20]:

$$\left[-\frac{\Delta}{2} - \frac{Z}{r} + V_n(r)\right]\psi_i(\boldsymbol{r}) + \sum_{j=1}^{N}\int \frac{\psi_j^*(\boldsymbol{r}')}{|\boldsymbol{r} - \boldsymbol{r}'|} \times [\psi_j(\boldsymbol{r}')\psi_i(\boldsymbol{r}) - \psi_i(\boldsymbol{r}')\psi_j(\boldsymbol{r})]\mathrm{d}\boldsymbol{r}' = \epsilon_i\psi_i(\boldsymbol{r}). \tag{2}$$

The thus obtained HF equations are solved with the additional (compared to the free atom) boundary conditions imposed on radial wavefunctions $P_{nl}(r)$:

$$\frac{P_{nl}'^{(A)}(R_n)}{P_{nl}^{(A)}(R_n)} = \frac{P_{nl}'^{(B)}(R_n)}{P_{nl}^{(B)}(R_n)}, \qquad \frac{P_{nl}'^{(B)}(R_n + \Delta)}{P_{nl}^{(B)}(R_n + \Delta)} = \frac{P_{nl}'^{\,(C)}(R_n + \Delta)}{P_{nl}^{(C)}(R_n + \Delta)}. \tag{3}$$

Here, a prime denotes differentiation which respect to r, while A, B and C specify P_{nl} in spatial regions of $0 < r \le R_n$, $R_n \le r \le R_n + \Delta_n$ and $R_n + \Delta_n \le r < \infty$, respectively.

For C_{60}, parameters Δ_{60} and R_{60} readily come from [47], where Δ_{60} was determined by fitting the calculated photoabsorption cross section of C_{60} to the experimentally measured cross section. Correspondingly [47], $\Delta_{60} \approx 1.9$ au and $R_{60} \approx 5.8$ au The potential depth U^0_{60} was determined in [20] by fitting the calculated, within the model, electron affinity of C_{60} to the experimentally known value of 2.65 eV [50]. Correspondingly, $U^0_{60} = 8.2$ eV [20].

For C_{240} (as well as for other fullerenes C_n), the thickness Δ of the cage is assumed to be the same as that of C_{60}, $\Delta \approx 1.9$ au, since the thickness is determined largely by the extent of the carbon atom. With the distance $R^{\rm mid}_{240}$ from the center of the C_{240} cage to the middle of the C_{240} wall being $R^{\rm mid}_{240} \approx 13.50$ au [8], and the C_{240} electron affinity being 3.81 eV [51], one readily finds $R_{240} = 12.6$ au and $U^0_{240} = 10.0$ eV [32].

For C_{540}, from [8], $R^{\rm mid}_{540} = 19.80$ au and, correspondingly, $R_{540} = 18.85$ au [32]. The problem remains of determining the potential depth U^0_{540}, since a measured or *ab initio* calculated value of the electron affinity of C_{540} could not be found. However, it is reasonable to assume that U^0_{540} may not be much different from that of C_{60} or C_{240}, since it is determined by the electron affinity which, in turn, may not be much different from the electron affinity of C_{60} and C_{240}. A trial calculation showed [31] that varying the potential depth U^0_{540} of C_{540} within a range of a few eV by setting it to 10, 11, 12, or 13 eV did not appreciably change any calculated photoionization parameters of the atom encaged in C_{540} in the most interesting domain of the photon energy spectrum. For the sake of completeness, it was assumed in [31,32] that $U^0_{540} \approx 12$ eV.

2.3. The Δ-potential model: Charged doped fullerenes $A@C_n^{\pm z}$

The extension of the above described model from neutral doped single-walled fullerenes $A@C_n$ to charged doped fullerenes $A@C_n^{\pm z}$ is pretty straightforward [28]. To account for the effects of a charged shell $C_n^{\pm z}$, one reasonably assumes that the extra charge z is evenly distributed over the entire *outer* surface of C_n. Correspondingly, the entire model potential $\tilde{V}_n(r)$ in the case of charged $C_n^{\pm z}$ is

$$\tilde{V}_n(r) = V_n(r) + V^z(r), \tag{4}$$

where $V^z(r)$ is the potential due to the charge on the fullerene cage,

$$V^z(r) = \begin{cases} \dfrac{z}{R_n + \Delta}, & \text{if } 0 \le r \le R_n + \Delta \\ \dfrac{z}{r} & \text{otherwise.} \end{cases} \tag{5}$$

This potential $\tilde{V}_n(r)$ replaces the potential V_n, Equation (1), in HF equations (2), thereby turning them into HF equations for a charged doped $A@C_n^{\pm z}$ fullerene. Parameters, Δ, R_n, and U_n^0 remain the same as for the neutral fullerene cage C_n [28].

2.4. The Δ-potential model: multiwalled doped fullerene onions

For neutral doped fullerene onions $A@C_{60}@C_{240}$, $A@C_{60}@C_{240}@C_{540}$, etc., the confining potential V_n of a multiwalled cage is replaced by a linear combination of corresponding single-walled potentials V_n [32]

$$V_n \to aV_{60} + bV_{240} + cV_{540} + \cdots, \tag{6}$$

where a, b, and c are either 0 or 1 depending on a chosen fullerene onion. The parameters R_n, U_n^0 and Δ of C_{60}, C_{240} and C_{540} in fullerene onions are assumed to be the same as for the corresponding isolated single-walled fullerenes. The potential (6) replaces V_n in HF equations (2), thereby turning them into HF equations for doped fullerene onions.

2.5. The δ-potential model of single-walled doped fullerenes

An alternative simple modeling of doped fullerenes, specifically, $A@C_{60}$, was developed initially in [34]. It was then used extensively in a number of photoionization studies of thus encaged atoms [34–41]. The method is based on approximating the C_{60} cage by a spherical potential $V(r)$ which differs from zero only within an infinitesimally thin wall of a sphere of radius R_c, the latter being considered the C_{60} radius, $R_c = 6.639$ au [47]:

$$V(r) = -V_0\delta(R_c - r). \tag{7}$$

Here, $\delta(R_c - r)$ is the Dirac δ-function, V_0 is the strength of the potential $V(r)$ that can be determined as [34]

$$V_0 = \frac{1}{2}\beta(1 + coth\beta R_c), \quad \beta = (2I_0)^{1/2}. \tag{8}$$

Here, I_0 is the electron affinity of C_{60} ($I_0 = 2.65$ eV [50]). Thus, the δ-potential model ignores the finite thickness nature of the carbon cage; within the model, $\Delta = 0$. Furthermore, in the framework of this model, the size of the embedded atom r_a is considered to be so small, compared to the size of C_{60}, that the ground state electronic wavefunctions of the embedded atom coincide exactly with those for a free atom. In other words, the model assumes no interaction between the ground state encaged atom and the carbon cage at all. Therefore, the model is applicable only to the deep inner subshells of the encaged atom. As for the carbon atoms from the C_{60} cage, their role is only to modify the radial part $P_{kl}(r)/r$ of the electronic wavefunction in the continuous state with the orbital quantum number l and electron momentum k. Function $P_{kl}(r)$ is the solution of the radial Schrödinger equation

$$\frac{1}{2}\left[P''_{kl}(r) - \frac{l(l+1)}{r^2}P_{kl}(r)\right] + \left[V_0\delta(r-R_c) - U(r) + \frac{1}{2}k^2\right]P_{kl}(r) = 0. \quad (9)$$

Here, $U(r)$ is the self-consistent field of the encaged atomic core "felt" by an electron in the continuous spectrum. To determine $P_{kl}(r)$, one must solve (9) separately for $r < R_c$ and $r > R_c$ and match both solutions at $r = R_c$ with the help of boundary conditions.

Both for $r < R_c$ and $r > R_c$, Equation (9) coincides with the equation for a free atom:

$$u''_{kl}(r) + \left[k^2 - \frac{l(l+1)}{r^2} - 2U(r)\right]u_{kl}(r) = 0. \quad (10)$$

Therefore, for $r < R_c$, function $P_{kl}(r)$ coincides, up to a constant $G_l(k)$ (with regard to r), with the wavefunction $u_{kl}(r)$ for the free atom:

$$P_{kl}(r)|_{r<R_c} = G_l(k)u_{kl}(r), \quad (11)$$

where the coefficient $G_l(k)$ is to be found from boundary conditions at $r = R_c$. For $r \geq R_c$, $P_{kl}(r)$ is a linear combination of the regular $u_{kl}(r)$ and irregular $v_{kl}(r)$ (at $r = 0$) solutions of Equation (10):

$$R_{kl}(r) = u_{kl}(r)\cos\xi_l(k) + v_{kl}(r)\sin\xi_l(k), \quad (12)$$

where $\xi_l(k)$ is the electron wavefunction phase shift on the potential $V(r)$ (7). The equations for regular $u_{kl}(r)$ and irregular $v_{kl}(r)$ functions coincide with Equation (10), where $r \geq R_c$. The asymptotic forms of $v_{kl}(r)$ and $u_{kl}(r)$ are

$$u_{kl}(r)|_{r\gg 1} \propto \sin\left[kr + \frac{1}{k}\ln(2kr) - \frac{\pi l}{2} + \Delta_l(k)\right], \quad (13)$$

$$v_{kl}(r)|_{r\gg 1} \propto -\cos\left[kr + \frac{1}{k}\ln(2kr) - \frac{\pi l}{2} + \Delta_l(k)\right]. \quad (14)$$

Here, $\Delta_l(k)$ are phase shifts of the continuous electron radial wavefunctions $P_{kl}(r)$ in the field of the ionic core.

For each given k, $\Delta_l(k)$ is obtained from the equation for nodes in the asymptotic behavior of $u_{kl}(r)$ versus r:

$$\sin\left[kr + \frac{1}{k}\ln(2kr) - \frac{\pi l}{2} + \Delta_l(k)\right] = 0. \tag{15}$$

Parameter $G_l(k)$ and electron phase shifts $\xi_l(k)$ on the potential $V(r)$ can be found by matching the logarithmic derivatives of $P_{kl}(r)$ at $r = R_c$. The corresponding solutions are [34]:

$$G_l(k) = \cos\xi_l(k)\left[1 - \frac{v_{kl}(R_c)}{u_{kl}(R_c)}\tan\xi_l(k)\right], \tag{16}$$

$$\tan\xi_l(k) = \frac{u_{kl}^2(R_c)}{u_{kl}(R_c)v_{kl}(R_c) + \frac{k}{2V_0}}. \tag{17}$$

The thus determined wavefunctions of the continuous spectrum of the atom A encage in C_{60}, combined with the wavefunctions of the ground state of the *free* atom A, are used in determining the total and differential photoionization cross sections of the encaged form.

3. PHOTOIONIZATION THEORY OF ENCAGED ATOMS

3.1. Basic formulae of the atomic photoeffect

Here, a summary of general formulae for determining angle-integrated, $\sigma_{nl}(\omega)$, and differential, $d\sigma_{nl}(\omega)/d\Omega$, photoionization cross sections of an nl-subshell in the free atom is presented. The consideration extends beyond the dipole approximation by accounting for the first-order correction term to the dipole approximation for a photoionization matrix element M_{ba} between the initial $|a)$ and final $(b|$ states: $M_{ab} \propto (b|\mathbf{A}\hat{\mathbf{p}}|a) \propto (b|\mathbf{e}[\exp(\mathrm{i}\mathbf{kr})]\hat{\mathbf{p}}|b) \approx (b|(1 + \mathrm{i}\mathbf{kr})\mathbf{e}\hat{\mathbf{p}}|a)$, where $\mathbf{A}$ and $\mathbf{e}$ are the vector-potential and polarization vector of the incoming radiation, respectively, $\mathbf{k}$ is the photon momentum and $\mathbf{r}$ and $\hat{\mathbf{p}}$ are the electron position and electron momentum operator, respectively. The reason to go beyond the dipole approximation is due to a relatively recent striking discovery ([52] and references therein) that nondipole effects in photoelectron angular distributions (represented by the interference term between the electric dipole and quadrupole photoionization amplitudes) are often significant at as low photon energies as only hundreds eV [52], or even tens eV [53]. Consequently, as a result of that discovery, both dipole and nondipole channels should be taken into account in studies of photoelectron angular distributions for a reliable interpretation of differential photoionization cross sections. Corresponding nonrelativistic

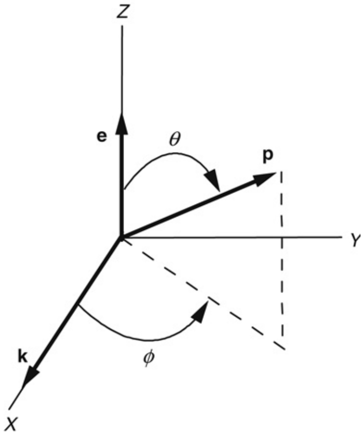

Figure 1 Angles θ and ϕ in Equations (19) and (20) as relative to the photoelectron momentum **p**, photon momentum **k**, and photon polarization vector **e**.

equations for $\sigma_{nl}(\omega)$ and $\mathrm{d}\sigma_{nl}(\omega)/\mathrm{d}\Omega$ for photoionization of a closed nl subshell of the atom are [54]:

$$\sigma_{nl}(\omega) = \frac{4\pi^2\alpha N_{nl}}{3(2l+1)}\omega[lD^2_{nl\to\epsilon l-1}(\omega) + (l+1)D^2_{nl\to\epsilon l+1}(\omega)], \tag{18}$$

$$\frac{\mathrm{d}\sigma_{nl}(\omega)}{\mathrm{d}\Omega} = \frac{\sigma_{nl}(\omega)}{4\pi}\left[1 + \frac{\beta_{nl}(\omega)}{2}(3\cos^2\theta - 1)\right] + \Delta E_{12}(\omega). \tag{19}$$

The latter equation assumes a 100% linearly polarized ionizing radiation, α is the fine structure constant, N_{nl} is the number of electrons in a nl subshell, $D_{nl\to\epsilon l\pm1}$ is a radial dipole photoionization amplitude, β_{nl} is the dipole photoelectron angular asymmetry parameter, and ΔE_{12} is the electric dipole-quadrupole interference term arising due to the correction term $\mathrm{i}\mathbf{kr}$ in the above expression for M_{ab},

$$\Delta E_{12}(\omega) = \frac{\sigma_{nl}(\omega)}{4\pi}[\delta_{nl}(\omega) + \gamma_{nl}(\omega)\cos^2\theta]\sin\theta\cos\phi. \tag{20}$$

In this equation, the spherical angles θ and ϕ are defined relative to the photon momentum **k**, photoelectron momentum **p**, and photon polarization vector **e**, as indicated in Figure 1, β_{nl} is a dipole photoelectron angular distribution parameter, γ_{nl} and δ_{nl} are nondipole photoelectron angular distribution parameters.

The dipole, β_{nl}, and nondipole, γ_{nl} and δ_{nl}, photoelectron angular distribution parameters are defined by [54]

$$\begin{aligned}\beta_{nl} &= \frac{l(l-1)|D_{l-1}|^2 + (l+1)(l+2)|D_{l+1}|^2}{(2l+1)[l|D_{l-1}|^2 + (l+1)|D_{l+1}|^2]} \\ &\quad - \frac{6l(l+1)|D_{l-1}||D_{l+1}|\cos(\xi_{l+1} - \xi_{l-1})}{(2l+1)[l|D_{l-1}|^2 + (l+1)|D_{l+1}|^2]}, \qquad (21)\\ \gamma_{nl} &= \frac{3k}{2[l|D_{l-1}|^2 + (l+1)|d_{l+1}|^2]} \\ &\quad \times \sum_{l',l''} A_{l',l''}|D_{l'}||Q_{l''}|\cos(\xi_{l''} - \xi_{l'}), \qquad (22)\\ \delta_{nl} &= \frac{3k}{2[l|D_{l-1}|^2 + (l+1)|D_{l+1}|^2]} \\ &\quad \times \sum_{l',l''} B_{l',l''}|D_{l'}||Q_{l''}|\cos(\xi_{l''} - \xi_{l'}). \qquad (23)\end{aligned}$$

Here, $l' = l \pm 1$ for dipole and $l'' = l, l \pm 2$ for quadrupole transitions, the coefficients $A_{l',l''}$ and $B_{l',l''}$ are given in Ref. [54], ξ_λ are the phase shifts of corresponding radial dipole $D_{l'}$ and quadrupole $Q_{l''}$ photoionization amplitudes of an *nl* subshell in the atom.

In a single-electron approximation, to be chosen at a Hartree-Fock approximation level, $D_{l'}$ and $Q_{l''}$ are defined as

$$D_{l'} = \int_0^\infty P_{\epsilon l'}(r) r P_{nl}(r)\mathrm{d}r, \quad l' = l \pm 1, \qquad (24)$$

$$Q_{l''} = \int_0^\infty P_{\epsilon l''}(r) r^2 P_{nl}(r)\mathrm{d}r, \quad l'' = l, l \pm 2, \qquad (25)$$

where $P_{nl}(r)/r$ and $P_{\epsilon L}(r)/r$ ($L = l', l''$) are the radial parts of the electron wave functions in the bound *nl* state and in the continuous ϵL spectrum, respectively, with ϵ being the photoelectron energy, $\epsilon = k^2/2$.

To account for the interchannel coupling, or, which is the same, electron correlation in calculations of photoionization parameters, various many-body theories exist. In this paper, following Refs. [20,29,30,33], the focus is on results obtained in the framework of both the nonrelativistic random phase approximation with exchange (RPAE) [55] and its relativistic analogy the relativistic random phase approximation (RRPA) [56]. RPAE makes use of a nonrelativistic HF approximation as the zero-order approximation. RRPA is based upon the relativistic Dirac HF approximation as the zero-order basis, so that relativistic effects are included not as perturbations but explicitly. Both RPAE and RRPA implicitly sum up certain electron–electron perturbations, including the interelectron interaction between electrons from various subshells of the atom, to infinite order, i.e., interchannel coupling is taken care of.

The resulting RPAE equation for the photoionization amplitude $D_{\nu_2\nu_1}$ from an initial state ν_1 into a final state ν_2, (ν is the total set of quantum numbers that characterize a single-electron state; the principal quantum number n, orbital quantum number l, magnetic quantum number m_l, and the z projection of the electron spin s_z) is given by [55]

$$D_{\nu_2\nu_1}(\omega) = d_{\nu_2\nu_1} + \sum_{\nu_3,\nu_4} \frac{d_{\nu_3\nu_4}(\eta_{\nu_4} - \eta_{\nu_3})\Gamma^{\nu_3\nu_1}_{\nu_4\nu_2}(\omega)}{\epsilon_{\nu_4} - \epsilon_{\nu_3} + \omega + \mathrm{i}\xi(1 - 2\eta_{\nu_3})}. \tag{26}$$

Here, $d_{\nu_j\nu_i}$ is the HF photoionization amplitude, $\Gamma^{\nu_3\nu_1}_{\nu_4\nu_2}(\omega)$ is the effective interelectron interaction accounting for electron–electron correlation in the atom [55], i.e., the interchannel coupling matrix element, ϵ_{ν_i} is the energy of a state ν_i, $\eta_\nu = 1$ for occupied states ν in the atom, whereas $\eta_\nu = 0$ for vacant states ν, the sum, when taken over continuum vacant states ν, transforms into the integral over the energy ϵ_ν of the vacant states, and $\xi \to +0$.

The reader is referred to [55] for further details of RPAE and to [56] for details of RRPA.

3.2. Frozen-cage approximation

The ionizing radiation acting on the atom A in $A@C_n$ may be quite different from the actual incoming radiation. This is due to dynamical polarization of the subsystem of delocalized electrons in the carbon cage (the former $2s^2$ and $2p^2$ electrons in the originally free carbon atoms) by the radiation. This results in the emergence of an indirect electromagnetic field inside the cage in addition to the incoming radiation, because the subsystem of the delocalized electrons in C_n oscillates as a whole relative to the ionic cage. Obviously, the actual resultant field "felt" by the encaged atom can get either enhanced or suppressed compared to the original incoming field depending on the frequency of the latter, thereby inducing new features in the photoionization process of doped fullerenes. The effect of the dynamical polarization of C_n by the incoming radiation, or, which is the same, the effect of the dynamical screening of the incoming radiation by the C_n cage on the photoionization of thus encaged atoms was studied and detailed in [38–40,43,44]. The effect was found to be very sizable in a photon energy region around the giant dipole plasmon resonance in C_n; for C_{60}, the resonance energy is approximately 20 eV [57]. However, the effect falls off rapidly with increasing photon energy beyond 20 eV [38–40,43,44]. It practically ceases to exist beyond approximately 60 eV of the photon energy where, consequently, it can be discarded from consideration. In this paper, the approximation that discards the dynamical polarization effect of the carbon cage is being termed the frozen-cage approximation in contrast to the dynamical-cage approximation which accounts for the polarization effect in question. Obviously, the frozen-cage approximation is applicable to photoionization of deep inner shells of the encaged atom for which photon energies of hundreds to thousands eV are needed. The frozen-cage approximation is subject to discussion in this subsection both at the Δ-potential and δ-potential model levels.

In the framework of the Δ-potential model, combined with the frozen-cage approximation, the problem is solved simply. Namely, HF wavefunctions and energies of the *encaged* atom, solutions of the extended to encaged atoms Hartree-Fock equations (2), must be substituted into corresponding formulae for the photoionization of an nl subshell of the free atom, Equations (18)–(26), thereby turning them into formulae for the encaged atom (to be marked with superscript "$@\Delta$"): $\sigma_{nl}(\omega) \to \sigma_{nl}^{@\Delta}(\omega)$, $\beta_{nl}(\omega) \to \beta_{nl}^{@\Delta}(\omega)$, $\gamma_{nl}(\omega) \to \gamma_{nl}^{@\Delta}(\omega)$ and $\delta_{nl}(\omega) \to \delta_{nl}^{@\Delta}(\omega)$. This accounts for emerging confinement effects, brought about by the carbon cage(s), in the photoionization of the encaged atom. In the framework of this approach, interesting new phenomena, specifically various kinds of so-called confinement resonances in the photoionization spectra of atoms encaged in a variety of doped fullerenes, have been unraveled and detailed in depth [15, 20–22,27–32]. Note, at this point, that the confinement resonances in question are due to the interference of the photoelectron waves going directly out of the encaged atom and those scattered off the inner and outer walls of the fullerene cage or fullerene onion cages, respectively. This will be detailed later in the paper.

In the δ-potential model [34], combined with the frozen-cage approximation model, once again, the corresponding photoionization formulae for an nl subshell of a free atom, Equations (18)–(26), are used in order to determine the photoionization parameters of the encaged atom. Furthermore, in accordance with the δ-potential model concept, the ground state electronic energies ϵ_{nl} and wavefunctions $u_{nl}(r)$ of the free atom are substituted into Equations (18)–(26) instead of those actually corresponding to the encaged atom. As for photoelectron wavefunctions $P_{kl'}(r)$ in the continuous spectrum, these are determined by Equations (11) and (12) for $r < R_c$ and $r > R_c$, respectively. Corresponding photoionization parameters of encaged atoms in the δ-potential model at the frozen-cage approximation level will be marked with superscript "$@\delta$". The dipole photoionization amplitude $D_{l'}^{@\delta}(k) \equiv M_{nl\to kl'}^{(q=1)@\delta}(k)$ ($l' = l \pm 1$) and quadrupole photoionization amplitude $Q_{l''}^{@\delta}(k) \equiv M_{nl\to kl'}^{(q=2)@\delta}(k)$ ($l'' = l, l \pm 2$) are standardly determined by

$$M_{nl\to kl'}^{(q)@\delta}(k) = \int_0^\infty P_{kl'}(r) r^q u_{nl}(r) \mathrm{d}r. \tag{27}$$

Since the δ-potential model assumes that the size r_a of the confined atom is much smaller than the size R_c of the fullerene cage, $r_a \ll R_c$, only small distances $r \sim r_a \ll R_c$ are important in the integration in (27). Correspondingly, the continuous state wavefunction $P_{kl'}(r)$ in (27) can be approximated as $P_{kl'}(r) \approx G_{l'}(k)u_{kl'}(r)$, Equation (11). Consequently,

$$M^{(q)@\delta}_{nl\to kl'} \approx G_{l'}(k)\int_0^\infty u_{kl'}r^q u_{nl}(r)\mathrm{d}r = G_{l'}(k)M^{(q)a}_{nl\to l'}, \tag{28}$$

with $M^{(q)a}_{nl\to l'}$ being the dipole ($q = 1$) or quadrupole ($q = 2$) photoionization amplitude of the free atom. Therefore, the angle-integrated dipole photoionization cross section $\sigma^{@\delta}_{nl\to l'}(\omega)$ of the encaged atom is given by

$$\sigma^{@\delta}_{nl\to l'}(k) = G^2_{l'}(k)\sigma^a_{nl\to l'}(k), \tag{29}$$

where $\sigma^a_{nl\to l'}(k)$ is the photoionization cross section of the *free* atom. The photoionization cross section $\sigma^{@\delta}_{nl\to l'}(k)$ differs from that of the free atom by a factor $G^2_{l'}(k)$. Similarly, the differential photoionization cross section (19) and photoelectron angular distribution parameters β_{nl}, γ_{nl} and δ_{nl}, determined by (21)–(23), become functions of the factor $G_{l'}(k)$ as well. Since $G_{l'}(k)$, Equation (16), is an oscillating (resonance) function of the photon momentum k (or of the photon energy $\omega = I_{nl} - k^2/2$, in au, I_{nl} being the ionization potential of an nl subshell in the free atom), there emerge resonances in the photoionization cross sections $\sigma^{@\delta}_{nl\to l'}(\omega)$ and $\mathrm{d}\sigma^{@\delta}_{nl\to l'}(\omega)/\mathrm{d}\Omega$ and photoelectron angular asymmetry parameters $\beta^{@\delta}_{nl}(\omega)$, $\gamma^{@\delta}_{nl}(\omega)$ and $\delta^{@\delta}_{nl}(\omega)$ from the confined atom at certain ω's. These resonances are, in essence, the same confinement resonances that are predicted by the Δ-potential model; they were discussed above. However, in the δ-potential model, where the carbon cage thickness $\Delta = 0$, the confinement resonances are due to the interference between only two photoelectron waves, the outgoing photoelectron wave and the photoelectron wave scattered off the infinitesimally thin cage. Hence, confinement resonance patterns in photoionization parameters of the encaged atom are expected to be, and, actually, *are* simpler in the δ-potential model than in the Δ-potential model, where confinement resonances are brought about by interference between three photoelectron waves. For example, beating points in the confinement resonance pattern [21,32], brought about by the three wave interference, cannot appear in the δ-potential model.

3.3. Dynamical-cage approximation

In the frozen-cage approximation, the carbon cage is considered totally invisible to the incoming electromagnetic radiation. However, as was explained earlier, following [38–40,43,44], when A@C$_{60}$ is exposed to the external electromagnetic field, the latter polarizes the carbon cage, thereby creating an indirect field inside the cage. When this happens, the photoionization probability of the encaged atom is altered compared to the frozen-cage model. The quintessence of the dynamical-cage approximation for the photoionization of doped fullerenes is to account for the effect of the polarization of the carbon cage by the incoming radiation [38–40,43,44].

Three versions of the dynamical-cage approximation have been developed to date. They are based on: (a) approximating the C_n cage by a classical infinitesimally thin conducting sphere [43], (b) approximating the C_n cage by a classical dielectric sphere of finite thickness Δ [44] and (c) using the quantum mechanical approach to treat the dynamical polarizability of the cage, assuming the cage is infinitesimally thin [38,39]. Despite all being different, these three versions of the dynamical-cage approximation are united by a key common assumption that the size of the encaged atom is much smaller compared to the size of the hollow space inside C_n, so that the ground state encaged atom and the cage itself can be considered independently. In this case, the photoionization cross section of the encaged atom in the dynamical-cage approximation [to be referred to as $\tilde{\sigma}_{nl}^{@}(\omega)$], on the one hand, and the photoionization cross section of the encaged atom in the frozen-cage approximation [to be referred to as $\sigma_{nl}^{@}(\omega)$], on the other hand, are related to each other as

$$\tilde{\sigma}_{nl}^{@}(\omega) = F(\omega)\sigma_{nl}^{@}(\omega). \tag{30}$$

Here, $F(\omega)$, termed the dynamical screening factor, is uniquely defined by the dynamical polarizability $\alpha_d(\omega)$ of the carbon cage [38,39,43]:

$$F(\omega) = \left|1 - \frac{\alpha_d(\omega)}{R_c^3}\right|^2, \tag{31}$$

with R_c being the cage radius. The differences between the three versions of the dynamical-cage approximation emerge with regard to determining $\alpha_d(\omega)$. We will consider all three versions individually.

3.3.1. Approximation of a classical infinitesimally thin metallic sphere

In [43], the carbon cage was represented as a classical infinitesimally thin spherical conducting sphere. Methods of classical physics were used to determine the dipole polarizability $\alpha_d(\omega)$ of the sphere. Accordingly,

$$\alpha_d(\omega) = \frac{\varepsilon(\omega) - 1}{\varepsilon(\omega) + 2} R_0^3. \tag{32}$$

Here, $\varepsilon(\omega)$ is the dielectric function of the metallic sphere. Near a surface dipole plasmon resonance in C_n, $\varepsilon(\omega)$ acquires the following form [43]

$$\varepsilon(\omega) = 1 - \frac{3\omega_1^2}{\omega^2 + \mathrm{i}\omega\Gamma_1}. \tag{33}$$

Here, ω_1 and Γ_1 are the dipole surface plasmon resonance frequency/energy and its width, respectively. The resonance emerges when a condition $\varepsilon = -2$ is met, see Equation (32) (for C_{60}, $\omega_1 \approx 20$ eV [57]). Correspondingly, within the resonance,

$$F(\omega) = \frac{\omega^4 + \omega^2\Gamma_1^2}{(\omega_1^2 - \omega^2)^2 + \omega^2\Gamma_1^2}. \tag{34}$$

Obviously, in the high frequency limit, when $\omega \gg \omega_1 = 20$ eV, $F(\omega) \approx 1$, i.e., the C_{60} cage is invisible to the incoming radiation. This is when the frozen-cage approximation is applicable. In the opposite limiting case, $\omega \to 0$, $\alpha_d(0) = R_0^3 \equiv \alpha_s$ (α_s being the static polarizability of the conducting sphere). Correspondingly, $F(0) = 0$. The implication is that static field does not penetrate inside a classical conducting sphere, exactly as it should be. When the frequency ω of the incoming radiation matches the C_n dipole plasmon resonance frequency, say $\omega \sim \omega_1 = 20$ eV for C_{60}, one gets $F(\omega) \approx \frac{\omega_1^2}{\Gamma_1^2} \gg 1$ assuming $\Gamma_1 \ll \omega_1$. This should result in a potentially large enhancement of the photoionization cross section of the encaged atom. Hence, the dynamical-cage approximation is of an indisputable importance when $0 < \omega \sim \omega_1 \approx 20$ eV (for C_{60}).

3.3.2. Approximation of a classical dielectric sphere of finite thickness

In [44], the above theory was generalized in that the infinitesimally thin metallic spherical cage was replaced by the metallic cage of a finite thickness Δ. Once again, methods of classical physics were employed to determine the screening factor $F(\omega)$ with the following assumptions. (a) The radius r_a of the encaged atom is much smaller than the R_c of the empty space inside the cage. (b) The static polarizability α_s^a of any atom is of the order of its radius, $\alpha_s^a \approx r_a^3$. (c) The dielectric function $\epsilon(\omega)$ follows the Drude model [58]

$$\epsilon(\omega) = 1 - \frac{\omega_p^2}{\omega^2}. \tag{35}$$

Here, ω_p is the volume plasmon resonance frequency determined by the total number N of delocalized electrons and the finite-thickness volume V of the cage,

$$\omega^2 = \frac{4\pi N}{V}, \quad V = \frac{4}{3}\pi(R_2^3 - R_1^3), \tag{36}$$

with R_1 and R_2 being the inner and outer radius of the C$_n$ cage, respectively. With these assumptions, the screening factor $F(\omega)$ of the finite-thickness C$_n$ carbon cage was found [44] to be

$$F(\omega) = \left|1 + \frac{2N}{pR_2^3}\left(\frac{1}{\omega^2 - \omega_1^2 + \mathrm{i}\Gamma_1\omega} - \frac{1}{\omega^2 - \omega_2^2 + \mathrm{i}\Gamma_2\omega}\right)\right|^2. \tag{37}$$

Here, Γ_1, Γ_2 and ω_1, ω_2 are the widths and resonance frequencies of the surface plasmon modes of the carbon cage, respectively [44] (the plasmons at the inner and outer surfaces are coupled oscillators and have two normal modes [59])

$$\omega_{2,1}^2 = \frac{\omega_p^2}{6}(3 \pm p), \quad p = \sqrt{1 + 8(R_1/R_2)^3}. \tag{38}$$

Thus, $F(\omega)$ has a complicated ω-dependence. The latter will be mirrored in the photoionization cross section of the encaged atom. Correspondingly, the photoionization cross section of the encaged atom in the dynamical-cage approximation might differ greatly from that in the frozen-core approximation, both quantitatively and qualitatively.

As a calculational insight into the problem, with the C$_{60}$ fullerene cage as a case study, the authors of work [44] calculated $\omega_1 \approx 16.9$ eV and $\omega_2 \approx 33.5$ eV with the help of Equation (38), but expressed Γ_1 and Γ_2 in terms of fractions γ of the plasmon resonance frequencies ω_1 and ω_2, $\Gamma_{1,2} = \gamma\omega_{1,2}$, with $\gamma = 0.25$. The thus determined screening factor $F(\omega)$ [marked as $F(\omega)^{\Delta}$] of C$_{60}$ is plotted in Figure 2 along with that $F^{\Delta=0}(\omega)$ calculated in the approximation of the infinitesimally thin metallic sphere.

One can see, that (a) $F^{\Delta=0}(\omega)$ differs strongly from $F^{\Delta}(\omega)$, i.e., the finite thickness cage effect is important, (b) both screening factors achieve appreciable values at the maximum around corresponding plasmon resonance frequencies and (c) at $\omega \to 0$, both $F^{\Delta=0}(\omega \to 0) = 0$ and $F^{\Delta}(\omega \to 0) = 0$, whereas at $\omega \gg \omega_{1,2}$, both screening factors approach unity, $F^{\Delta=0}(\omega \gg \omega_{1,2}) \to 1$ and $F^{\Delta}(\omega \gg \omega_{1,2}) \to 1$; this is exactly as a classical conducting sphere must behave at these limiting frequencies. Thus, in the photon energy domain on the extent of about 20 eV below and above the first plasmon resonance energy $\omega_1 \approx 17$ eV of the C$_{60}$ fullerene cage, the dynamical screening effect is of such great importance that it makes

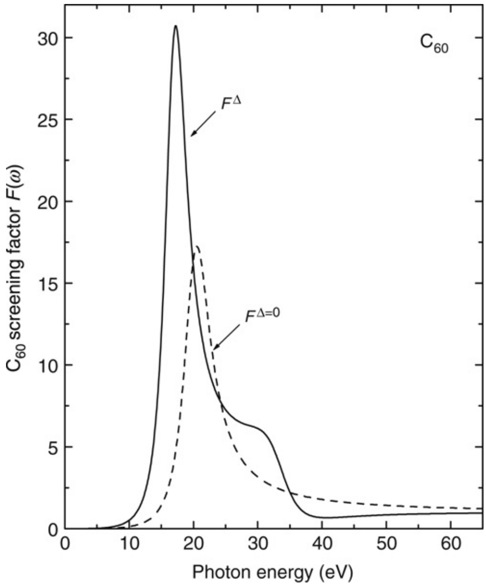

Figure 2 The screening factors $F(\omega)$ of C_{60} calculated [44] on the basis of classical physics for the infinitesimally thin fullerene cage, $F^{\Delta=0}(\omega)$, and that $F^{\Delta}(\omega)$ calculated for the finite-thickness cage ($\Delta = 1.5$ Å, $\Gamma_{1,2}/\omega_{1,2} \equiv \gamma = 0.25$); refer to [44] for more details.

the frozen-cage approximation quantitatively inadequate at these photon energies.

The calculated plasmon resonance energies, ω_1 and ω_2, and screening factors $F^{\Delta}(\omega)$ for other spherical fullerenes, C_{20}, C_{240} and C_{960} are given in [44] as well.

3.3.3. Quantum mechanical approximation of an infinitesimally thin fullerene sphere

In contrast to the just discussed classical models [43,44], authors of works [38, 39] treated the problem of the dynamical polarizability $\alpha_d(\omega)$ of the C_{60} carbon cage quantum-mechanically, utilizing the δ-potential model concept, where the C_{60} cage is simulated by the Dirac δ-potential, $V(r) = -V_0\delta(R_c - r)$. However, instead of calculating $\alpha_d(\omega)$ directly, the latter was determined from experimental data on the C_{60} photoabsorption cross section $\sigma(\omega)$ [60, 61] with the help of the dispersion relations for the real $\mathrm{Re}\,\alpha_d$ and imaginary $\mathrm{Im}\,\alpha_d$ parts of the dipole polarizability $\alpha_d(\omega)$:

$$\mathrm{Re}\,\alpha_d(\omega) = \frac{c}{2\pi^2}\int_I^{\infty}\frac{\sigma(\omega')\mathrm{d}\omega'}{\omega'^2 - \omega^2}, \qquad \mathrm{Im}\,\alpha_d(\omega) = \frac{c}{4\pi}\sigma(\omega), \tag{39}$$

where c is the speed of light.

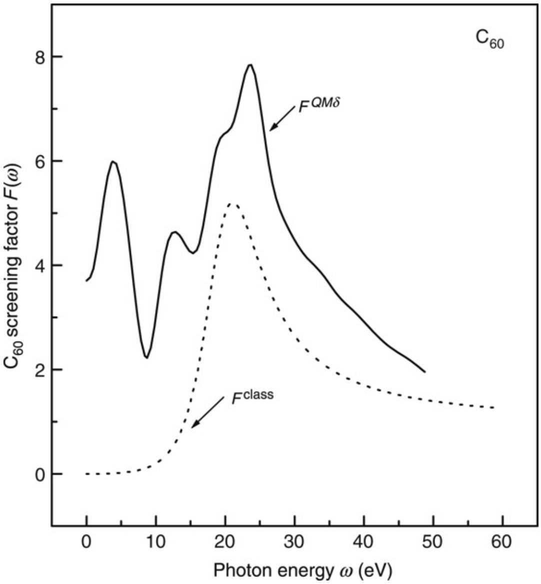

Figure 3 The screening factor $F(\omega)$ of C_{60} calculated on the basis of (a) the classical dielectric model of infinitesimally thin C_{60}, $F^{\text{class}}(\omega)$ [43] and (b) the quantum mechanical δ-potential model of infinitesimally thin C_{60}, $F^{QM\delta}(\omega)$ [38,39]. The calculated data for $F^{\text{class}}(\omega)$ were obtained assuming $\Gamma = 10$ eV (Γ being the dipole giant plasmon resonance width), as in [43].

A finding of significant importance in work [39] is that the C_{60} cage behaves as a set of isolated carbon atoms rather than as a conducting sphere. Therefore, the polarizability $\alpha_d(\omega)$ of the C_{60} cage in the limiting case of $\omega \to 0$ is $\alpha_d(0) \approx N\alpha_s^a = 840$ rather than $\alpha_s = R_c^3$, as in the model of a classical conducting sphere [43,44]. Here, $\alpha_s^a = 14$ is the static polarizability of the carbon atom, N is the number of the collectivized electrons in C_{60}, $N = 240$, and R_c is the mean radius of C_{60}. Correspondingly, in the static limit, when $\omega \to 0$, the screening factor $F(\omega)$ is no longer a zero [38, 39], in contrast to the classical models developed in [43,44]. Overall, there turn out to be considerable differences, both quantitative and qualitative, in calculated $F(\omega)$ between the classical and quantum mechanical models. This is illustrated in Figure 3, where calculated data for $F(\omega)$ in the framework of the classical [43] and quantum mechanical [38,39] models are compared.

In summary, despite the assumption of a zero thickness Δ of the fullerene cage [38,39] being an obvious drawback of the quantum mechanical model, this model seems to be more realistic than the discussed classical models of the C_n cage [43,44]. Correspondingly, in the present paper, the screening factor $F(\omega)$ from [38,39] is used whenever the dynamical-cage approximation is deemed to be appropriate for the calculation of the photoionization of the atom encaged in C_{60}.

4. RESULTS: THE FROZEN-CAGE MODEL

4.1. Preliminaries

As was mentioned earlier, one of outstanding features of photoionization cross sections of, and photoelectron angular distributions from, encaged atoms in doped fullerenes is the presence of new types of resonances, termed confinement resonances [21], in these parameters, due to the interference of the photoelectron waves going directly out of, and those scattered off the inner and outer walls of the confining carbon cage(s). To date, confinement resonances in photoionization spectra of encaged atoms have been studied extensively with the help of various approximations: (a) single-electron and multi-electron approximations both in nonrelativistic (HF and RPAE) and relativistic (Dirac HF and RRPA) versions, (b) the frozen-cage and (c) dynamical-cage models both at the Δ- and δ-potential model approximations. A detailed review of results of these studies is given in this and subsequent sections.

Following the previous discussion, the following notations are maintained in this section: calculated results obtained within the Δ-potential model at the frozen-cage approximation level are marked as $\sigma_{nl}^{@\Delta}$, $\beta_{nl}^{@\Delta}$, $\gamma_{nl}^{@\Delta}$ and $\delta_{nl}^{@\Delta}$ to distinguish them from the results of the δ-potential model, $\sigma_{nl}^{@\delta}$, $\beta_{nl}^{@\delta}$, $\gamma_{nl}^{@\delta}$ and $\delta_{nl}^{@\delta}$, respectively.

4.2. Confinement resonances in photoionization cross sections

A good case to illustrate confinement resonances in the photoionization cross section of the atom A from a doped fullerene $A@\mathrm{C}_n$ could be the Xe 4d photoionization of Xe@C$_{60}$ in the area of the 4d giant resonance [33,37]. These calculations were performed at the RPAE approximation level, since former studies for free Xe found the decisive role of electron correlation in forming the 4d giant resonance [55]. The corresponding calculated RPAE results for the encaged Xe, obtained both in the Δ-potential model, $\sigma_{4\mathrm{d}}^{@\Delta}(\omega)$ [33], and the δ-potential model, $\sigma_{4\mathrm{d}}^{@\delta}(\omega)$ [37], are depicted in Figure 4 along with the 4d photoionization cross section of free Xe, $\sigma_{4\mathrm{d}}^{\mathrm{free}}(\omega)$.

Both $\sigma_{4\mathrm{d}}^{@\delta}(\omega)$ and $\sigma_{4\mathrm{d}}^{@\Delta}(\omega)$ yield the 4d photoionization cross section of the encaged Xe atom with maxima and minima centered roughly about the 4d photoionization cross section of free Xe; these are confinement resonances. There are four strong confinement resonances seen in $\sigma_{4\mathrm{d}}^{@\delta}(\omega)$ versus two strong (but weaker) resonances in $\sigma_{4\mathrm{d}}^{@\Delta}(\omega)$ at about 85 and 95 eV. This difference is an illustration of the importance of the finite C$_{60}$ cage thickness, an effect ignored in the δ-potential model. The δ-potential model is applicable when the photoelectron wavelength λ is much greater than the thickness Δ of the C$_{60}$ cage, $\lambda \gg \Delta$. This happens only very near the ionization threshold, where $\lambda \propto \epsilon^{-1/2}$ is large because the photoelectron energy ϵ is small. At these, very near threshold, energies the calculated $\sigma_{4\mathrm{d}}^{@\delta}(\omega)$

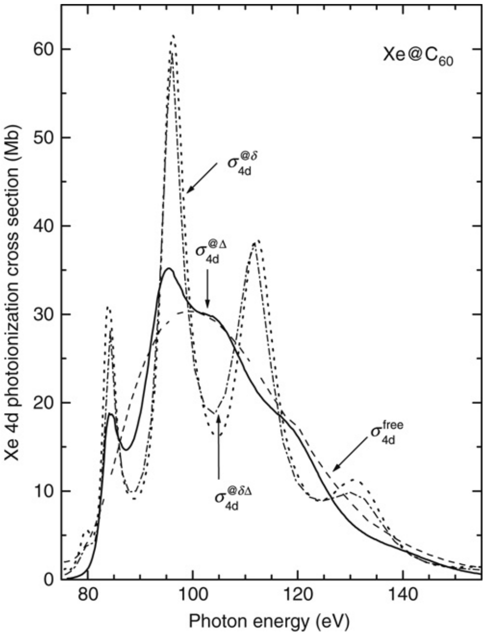

Figure 4 RPAE calculated results for the Xe 4d photoionization cross section of free Xe, $\sigma_{4d}^{\text{free}}$, as well as of Xe@C_{60} calculated in the framework of both the δ-potential model, $\sigma_{4d}^{@\delta}$ [37] and Δ-potential model, $\sigma_{4d}^{@\Delta}$ [33]. Also shown, for comparison, are calculated data [33], marked $\sigma_{4d}^{@\delta\Delta}$, obtained for the 4d photoionization cross section of Xe@C_{60} with an artificially reduced thickness of the C_{60} cage from $\Delta = 1.9$ au to $\Delta = 0.5$ au, deepened potential depth, $U_{60}^{0} = 25.9$ eV, and changed inner radius $R_c = 6.389$ au, in order to simulate the δ-potential model but keep the binding strength of the cage potential unchanged (see the main text body).

and $\sigma_{4d}^{@\Delta}(\omega)$ are practically identical. With an increase of photon energy λ decreases and, well above threshold, λ is no longer much greater than Δ, so that the δ-potential model loses its adequacy. This is seen to result in a considerable overestimate of the "strength" of confinement resonances in the photoionization of encaged atoms found in the framework of the δ-potential model. It is evident from the comparison of the calculated results obtained using the two models that the inclusion of the thickness of the confining cage diminishes the amplitudes of the confinement resonances. As an indisputable proof of this statement, also plotted are calculated data in Figure 4, marked $\sigma_{4d}^{@\delta\Delta}$, for the Xe@C$_{60}$ 4d photoionization cross section obtained [33] in the Δ-potential model with an artificially reduced thickness Δ ($\Delta = 0.5$ au), and, correspondingly, a deepened depth U_{60}^{0} ($U_{60}^{0} = 25.9$ eV) in order to keep the binding strength of the potential unchanged, and appropriately an increased inner radius R_c ($R_c = 6.389$ au) to keep the distance from the center of C$_{60}$ to the middle part of the cage unaltered.

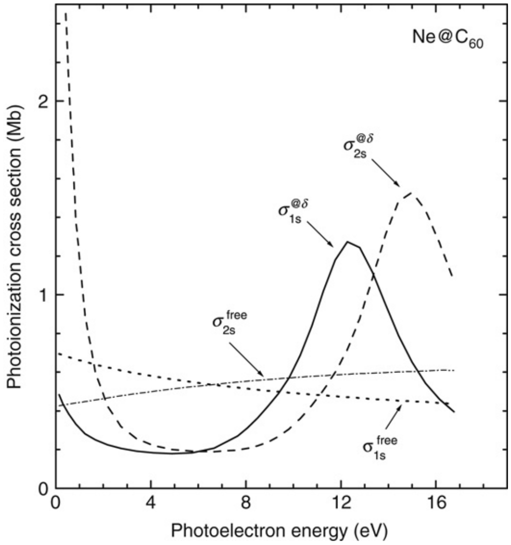

Figure 5 1s and 2s photoionization cross sections of free Ne ($\sigma_{1s}^{\mathrm{free}}$ and $\sigma_{2s}^{\mathrm{free}}$) and Ne from Ne@C$_{60}$ ($\sigma_{1s}^{@\delta}$ and $\sigma_{2s}^{@\delta}$) calculated [34] within the δ-potential model.

One can see, that the thus obtained results, $\sigma_{4d}^{@\delta\Delta}$, are almost identical to those obtained using the δ-potential model, $\sigma_{4d}^{@\delta}$. Hence, the finite thickness of the C$_{60}$ cage does matter greatly. Zeroing the thickness of C$_{60}$ results in such significant quantitative changes in the amplitudes of the confinement resonances that it is clear that finite cage thickness introduces qualitative differences in the photoionization cross sections of the encaged atom as compared to the δ-potential model. Indeed, the finite cage thickness effect essentially eliminates the two prominent confinement resonances predicted by the δ-potential model in $\sigma_{4d}^{@\delta}$ at approximately 118 and 130 eV, turning them into the two insignificant shoulders seen in $\sigma_{4d}^{@\Delta}$ at about 105 and 120 eV. Thus, even the number of confinement resonances predicted by the two models in the 4d photoionization cross section of Xe@C$_{60}$ "seem" to be different.

The dependence of confinement resonances on quantum numbers of the ionized subshell *nl* can be illustrated by the δ-potential model calculated data [34] for the Ne 1s and 2s photoionization cross sections from Ne@C$_{60}$, see Figure 5.

The presented data illustrate the noticeable sensitivity of threshold values of the photoionization cross sections of confined atoms to the principal quantum number *n*. Indeed, as seen from Figure 5, the photoionization cross section $\sigma_{2s}^{@\delta}$ noticeably increases, whereas $\sigma_{1s}^{@\delta}$ decreases, at threshold, compared to the free Ne atom. As a result, for confined Ne, the threshold

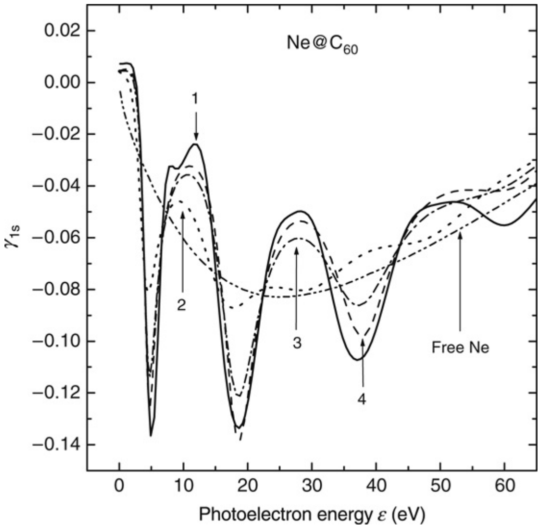

Figure 6 Nondipole asymmetry parameter $\gamma_{1s}(\varepsilon)$ as a function of the photoelectron energy ε for the Ne 1s photoionization from $\mathrm{Ne@C_{60}}$ calculated [36] in two different approximations: 1, the δ-potential model. 2, 3 and 4, the Δ-potential model with the following values for R_{60}, U_{60}^{0} and Δ (all in au): $2, R_{60} = 5.75, U_{60}^{0} = 0.3027, \Delta = 1.89$, as should be; $3, R_{60} = 6.139, U_{60}^{0} = 0.5099, \Delta = 1.0$; $4, R_{60} = 6.389, U_{60}^{0} = 0.9515, \Delta = 0.5$.

value of $\sigma_{2s}^{@\delta} \approx 2.4$ Mb is almost a factor of six greater than that of $\sigma_{1s}^{@\delta} \approx 0.4$ Mb. Note, also, that, away from the threshold, the confinement resonances in $\sigma_{1s}^{@\delta}$ and $\sigma_{2s}^{@\delta}$ emerge at different energies and have different resonance amplitudes. Caution: since the data displayed in Figure 5 were obtained in the δ-potential model, the predicted amplitudes of confinement resonances in these photoionization cross sections are, most likely, overestimated, as in the case of $\mathrm{Xe@C_{60}}$.

4.3. Confinement resonances in photoelectron angular distributions

As an illustration, calculated data [36] for the Ne 1s, 2s and 2p photoelectron angular asymmetry parameters from $\mathrm{Ne@C_{60}}$, both in the δ- and Δ-potential models, are depicted in Figures 6–8. Note, the dipole parameter $\beta_{ns} = 2$, i.e., is constant, whereas a nondipole parameter $\delta_{ns} = 0$ for photoionization of ns subshells of the atom, by definition. Therefore, only calculated data for the $\mathrm{Ne@C_{60}}$ 1s and 2s nondipole photoelectron angular parameters $\gamma_{ns}(\omega)$ are displayed in Figures 6 and 7.

Both models demonstrate sizable oscillations, i.e., confinement resonances, in the energy dependence of photoelectron angular distribution parameters. The resonances fade away rapidly with an increasing energy of the photoelectrons. The decrease in the resonance amplitudes with increasing

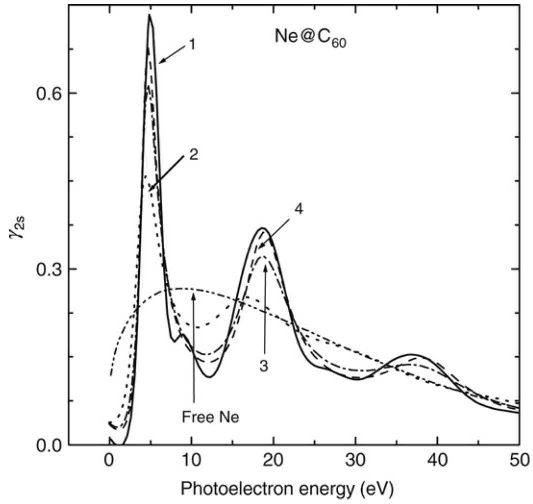

Figure 7 Nondipole asymmetry parameter $\gamma_{2s}(\varepsilon)$ for the Ne 2s photoionization from Ne@C$_{60}$ calculated [36] in the δ-potential model (line 1) and the Δ-potential model (lines 2, 3, and 4) with the same choice of R^{in}, Δ, and U^0_{60} as in Figure 6.

photoelectron energy occurs because the C$_{60}$ cage becomes more and more transparent to the photoelectron, thereby decreasing reflection and, thus, interference.

In addition, to illustrate the importance of the finite thickness Δ of the C$_{60}$ cage in predicting confinement resonances in photoelectron angular asymmetry parameters from encaged atoms, the Δ-potential model calculations were performed with three decreasing values of Δ, namely, $\Delta = 1.9, 1.0$, and 0.5 au, to explore the convergence of photoelectron angular asymmetry parameters to those calculated within the δ-potential. For each calculation with the changed Δ, the depth U^0_{60} of the potential well and its inner radius R_{60} were changed appropriately as well, to keep the 1s electron affinity in a negatively singly charged C$_{60}$ constant and equal to its experimental value $I = 2.65$ eV. Adjusted values of U^0_{60} and Δ are given in figure captions. These figures demonstrate that, with decreasing Δ, results of calculations performed within the Δ-potential model gradually converge to results obtained within the δ-potential; the best agreement with the latter is achieved for the smallest considered Δ, $\Delta = 0.5$ au The performed comparison shows that all four calculations for each particular photoelectron angular distribution parameter agree with each other almost ideally only very near threshold. This is not surprising because of large, compared to Δ, photoelectron wavelengths $\lambda \gg \Delta$ at such energies. This, in turn, demonstrates, once more, the very near threshold applicability of the δ-potential theory. At energies only 5 eV farther from the threshold,

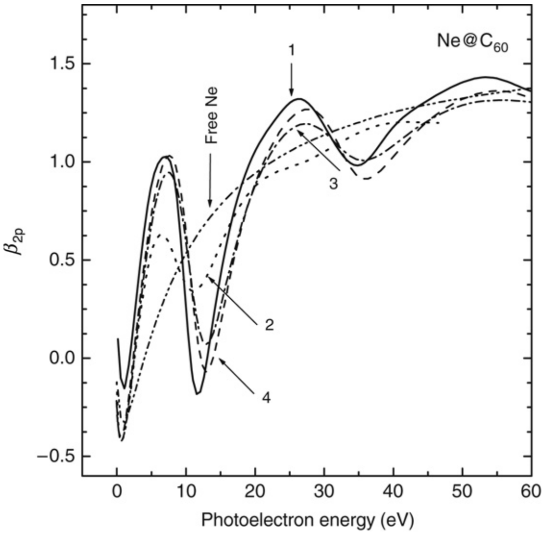

Figure 8 Dipole asymmetry parameter $\beta_{2\mathrm{p}}(\varepsilon)$ for the Ne 2p photoionization from $\mathrm{Ne@C_{60}}$ calculated [36] in the δ-potential model (line 1) and the Δ-potential model (lines 2, 3, and 4) with the same choice of R^{in}, Δ and U_{60}^{0} as in Figure 6.

differences between the δ-potential model (lines 1 in the above figures) and Δ-potential model, accounting for the actual thickness of the carbon cage $\Delta = 1.9$ au (lines 2 in the above figures), are quite sizable, in that the amplitudes of confinement resonances are much lower in the Δ-potential theory than in the δ-theory. One can, actually, talk about a lesser number of "detectable" confinement resonances predicted by the Δ-potential theory (compare, e.g., lines 1 and 2 in Figure 8). Consequently, similar to angle-integrated photoionization cross sections, the δ-potential theory greatly overestimates the strength (and number) of confinement resonances in the photoelectron angular asymmetry parameters of confined atoms.

The discovery of confinement resonances in the photoelectron angular distribution parameters from encaged atoms may shed light [36] on the origin of anomalously high values of the nondipole asymmetry parameters observed in diatomic molecules [62]. Following [36], consider photoionization of an inner subshell of the atom A in a diatomic molecule AB in the gas phase, i.e., with random orientation of the molecular axis relative to the polarization vector of the radiation. The atom B remains neutral in this process and is arbitrarily located on the sphere with its center at the nucleus of the atom A with radius equal to the interatomic distance in this molecule. To the lowest order, the effect of the atom B on the photoionization parameters can be approximated by the introduction of a spherically symmetric potential that represents the atom B smeared over the surface of this sphere. Here, the situation for this molecule becomes, to a large extent, similar to the situation discussed for an encaged atom A from $A@C_{60}$. For an isolated atom A the ratio between the quadrupole and dipole matrix elements, Q_2/D_1, has a value of the order of the radius of the ionized atomic subshell, r_{ns}, while, in the δ-potential model, for the same atom in the molecule $Q_2/D_1 \propto G_2/G_1$; this follows from Equation (28) with G_l $(l = 1, 2)$ being the modulation function, Equation (16). The values of G_1 and G_2, which are defined by the conditions of reflection and refraction of the photoelectron wave function on the potential sphere, are such that this ratio can be significantly more than one, as demonstrated in Figure 7. This resonant enhancement is the likely qualitative explanation for the significant increase in the nondipole asymmetry parameter observed in the N_2 molecule [62]. These considerations apply to an ensemble of randomly oriented molecules, thereby being equally valid for both hot (high-J rotational states) and cold (low-J rotational states) gases.

4.4. Photoionization of doped fullerene anions: Coulomb confinement resonances

The Δ-potential model calculated results [28] for a Ne 1s photoionization cross section $\sigma_{1s}^{@\Delta}(\omega)$ from the Ne@C_{60}^{z} fullerene anion ($z = -1, -2, -3$, and -5) are displayed in Figure 9 along with calculated data for neutral Ne@C_{60} ($z = 0$) and free Ne.

For free Ne, one can see a monotonically decreasing $\sigma_{1s}(\omega)$ with a threshold value of about 0.56 Mb, whereas for neutral Ne@C_{60} one gets the confinement resonances that were discussed previously, to be termed regular confinement resonances. For a Ne@C_{60}^{z} ($z < 0$) anion, the situation is dramatically affected by an increasing negative charge z on C_{60}^{z}. One can see, that as the negative charge on C_{60} is increased just to $z = -1$, a new, strong, resonance structure appears in a lower energy wing of $\sigma_{1s}^{@\Delta}(\omega)$, at $\omega \approx 890$ eV. As z continues to grow, the resonance structure slowly broadens while slightly decreasing in height and, starting from $z = -3$, a new, sharp resonance emerges in $\sigma_{1s}^{@\Delta}(\omega)$ at a yet lower energy, $\omega \approx 885$ eV. Just like the formerly discussed strong resonance structure, the new resonance becomes lower and broader with increasing negative z (compare results for $z = -3$ and $z = -5$). In addition, and this is quite striking, each subsequent increase in negative z is seen to add a new, lower energy part to the former curve of $\sigma_{1s}^{@\Delta}(\omega)$ versus photon energy while leaving the higher energy part of the graph almost intact. The implication is, that the effect of placing a negative charge onto the C_{60} surface is to move some of the oscillator strength of the encaged atom from the discrete excitation region into the continuum. In a sense, a negatively charged shell C_{60}^{z} ($z < 0$) acts as if it were a “magnifying glass (the shell itself) with adjustable index of refraction (the negative charge on the anion)”, because it lets one “see” the part of the oscillator strength of a confined atom that otherwise is hidden from the observer. Note, this effect

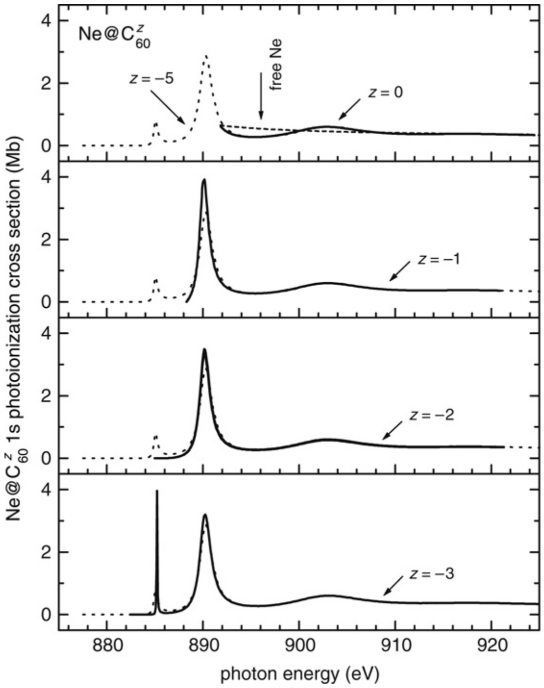

Figure 9 The Δ-potential model calculated results [28] for the 1s photoionization of free Ne, as well as that of Ne from neutral Ne@C$_{60}$ ($z = 0$) and from the Ne@C$^z_{60}$ anion with $z = -1, -2, -3$, and -5 (dotted line), as indicated.

is similar, but opposite, to the effect found in the photoionization of inner shells of free *positive* ions [63]. In the latter case, the effect of the increasing positive charge of the ion by removal of outer electrons, as compared to neutral atoms, is to move some of the oscillator strength of the atom from the continuum into the discrete excitation region.

The behavior of $\sigma^{@\Delta}_{1s}(\omega)$ with increasing negative z can be understood [28] by exploring the evolution in the potential $V^{\mathrm{eff}}(r)$, Equation (4), "seen" by an ejected Ne 1s photoelectron versus various values of z. The direct (Hartree) part of V^{eff} versus z is shown in Figure 10. V^{eff} is seen to be characterized not only by a standard Δ-potential between $R_{60} = 5.8$ and $R_{60} + \Delta = 7.7$ au that models the C$_{60}$ cage itself [(see Equation (1))], but also by the potential *barrier* (split by the well) in the positive plane of $V^{\mathrm{eff}}(r)$. The latter is due to the extra potential $V^z(r)$, Equation (5), which is due to the negative charge z on the outer surface of C$_{60}$. This causes reflection of the continuum photoelectron wave from the split Coulomb barrier creating new kinds of confinement resonances (resonances at $\omega \approx 890$ and 885 eV in Figure 9). These new type resonances, logically termed Coulomb confinement resonances [28], owe

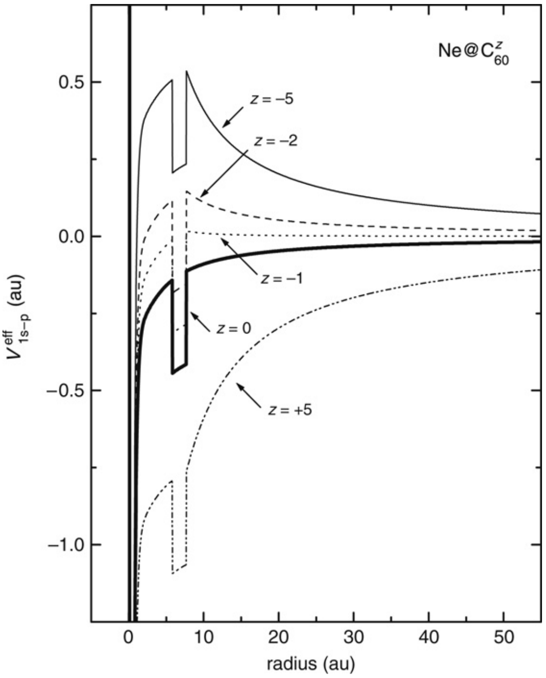

Figure 10 Direct (Hartree) part of the effective potential $V^{\mathrm{eff}}(r)$, Equation (4), "seen" by a $\epsilon\mathrm{p}$ photoelectronic wave arising from Ne 1s photoionization of $\mathrm{Ne@C}^{z}_{60}$ for $z = -5, -2, -1, 0$, and $+5$, as in [28].

their existence to the confinement brought about by the Coulomb potential barrier of the charged cage. Coulomb confinement resonances dominate the regular confinement resonances (compare, e.g., the latter at $\omega \approx 903$ eV with the Coulomb confinement resonance around 890 eV). It is clear that the position and shape of Coulomb confinement resonances intimately involve the C_{60} cage as well. Thus, Coulomb confinement resonances are the result of the interference between the direct photoelectron wave, the reflected wave from the Coulomb *barrier*, and the reflected wave from the C_{60} cage. Sharp Coulomb confinement resonances occur when the photoelectron energy is less than the barrier height, see Figures 9 and 10. In addition, results for $z = -3$ and $z = -5$ indicate that in the energy region where the continuum wave has to penetrate the wider part of the Coulomb barrier, Coulomb confinement resonances are narrow, whereas they are much broader at higher energy, when the wave penetrates the narrow (near the top) part of the barrier. Further, when the energy gets above the barrier height, one gets both types of resonances in the continuum, the large Coulomb confinement resonances at lower energies, and the regular confinement resonance at higher energies. Clearly, this is a general phenomenon and will be in evidence in the photoionization of any atom, molecule or ion, encapsulated in a negatively charged cage. For energies below the potential barrier height (Figure 10), the Ne 1s photoionization cross sections is vanishingly small, as seen in Figure 9, except for the Coulomb confinement resonances. This phenomenology is due to the Coulomb barrier, which does not allow the continuum wave functions to penetrate into the inner region where the 1s wave function has appreciable amplitude, thereby causing the overlap in the dipole matrix elements to be negligible. This should be a general feature of photoabsorption by an object encapsulated by a negatively charged confinement. Note, that the assumption that the encaged atom is at the center of a fullerene cage might not be entirely appropriate for the case of $A@\mathrm{C}_{540}$. This is because the radius of C_{540} exceeds 1 nm, which, combined with the attractive van der Waals force in this region, makes it highly likely that the center-of-cage position of a confined atom becomes unstable. Consequently, the confined atom should move off the center of C_{540} in order to create a weak bond to the C_{540} inner surface. Therefore, the calculated data presented in this paper for $A@\mathrm{C}_{540}$ should be considered more as a mathematical investigation into the problem rather than data susceptible of actual measurement. As regards doped fullerene onions, it is reasonable to assume that the inner C_{60} effectively screens the atom A from the influence of the outer giant C_{240} and/or C_{540}. Therefore, the confined atom is expected to remain sitting at the center of a fullerene onion.

Calculated data [28] of the 1s nondipole photoelectron angular asymmetry parameter $\gamma_{1s}^{@\Delta}(\omega)$ for Ne from the Ne@C_{60}^{z} anion ($z < 0$), along with data for neutral Ne@C_{60}, are presented in Figure 11. Similar to the situation with the photoionization cross section, the neutral cage C_{60} exhibits the regular confinement resonances in $\gamma_{1s}^{@\Delta}(\omega)$ that are centered roughly about the free Ne result. With increasing negative charge z on C_{60}, the threshold value of $\gamma_{1s}^{@\Delta}(\omega)$ is shifted to lower photon energies where the additional resonance structure — the Coulomb confinement resonance — is seen at about 887 eV. Both the ordinary and Coulomb confinement resonances in $\gamma_{1s}^{@\Delta}(\omega)$ of Ne from Ne@C_{60}^{-z} turn out to be due to confinement resonances just in *quadrupole* photoionization [28]. This is evident from Figure 12. Indeed, it shows, that (a) $\gamma_{1s}^{@\Delta}(\omega) \approx \gamma_{1s}^{@\Delta}(\omega)/\cos\Delta$, i.e., $\gamma_{1s}^{@\Delta}(\omega)$ is approximately independent of $\cos\Delta$ and (b) resonances themselves are positioned at precisely the same energies as resonances in the quadrupole photoionization amplitude Q.

4.5. Photoionization of doped fullerene cations

Calculated results [28] for the 1s photoionization of Ne from Ne@C_{60}^{+z} for $z = 0$, $z = +2$, $+5$ and $+10$ are depicted in Figure 13.

In this case, the photoionization cross section possesses no Coulomb confinement resonances. This is because the fullerene cation's potential $V^{\mathrm{eff}}(r)$ seen by an outgoing photoelectron does not exhibit a Coulomb potential barrier (see Figure 10 for $z = +5$ for illustration purposes).

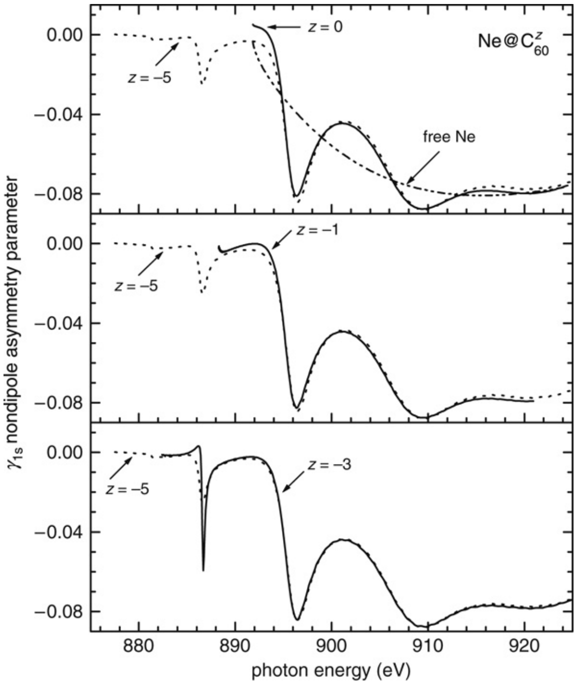

Figure 11 Nondipole photoelectron angular asymmetry parameter $\gamma_{1s}^{@\Delta}(\omega)$ for 1s photoionization of free Ne, Ne from neutral Ne@C$_{60}$ as well as Ne from the fullerene anion Ne@C$^{z}_{60}$ ($z < 0$) [28], as indicated.

In addition, charging the cage positively (by removal of some electrons from the neutral C$_{60}$ surface) is seen to do nothing to the photoionization cross section (as a function of photon energy) except to increase the threshold energy. The implication is that, in direct opposition to the case of a fullerene anion, the only effect of positive C$^{z}_{60}$, as compared to neutral C$_{60}$, is to move some of the oscillator strength of the confined atom from the continuum into the discrete excitation region. Interestingly, this is a precise analogy to the case of *free* positive ions, where the same effects have been observed [63].

4.6. Photoionization of doped giant single-walled and multiwalled fullerenes

The above discussion was focused on confinement resonances, whether regular or Coulomb, in the photoionization spectra of atoms encaged in a neutral or charged C$_{60}$ carbon cage.

In this subsection, confinement resonances emerging upon photoionization of an atom A encaged in giant single-walled spherical fullerenes C$_{240}$ and C$_{540}$, as well as in multiwalled giant spherical fullerene onions C$_{60}$@C$_{240}$

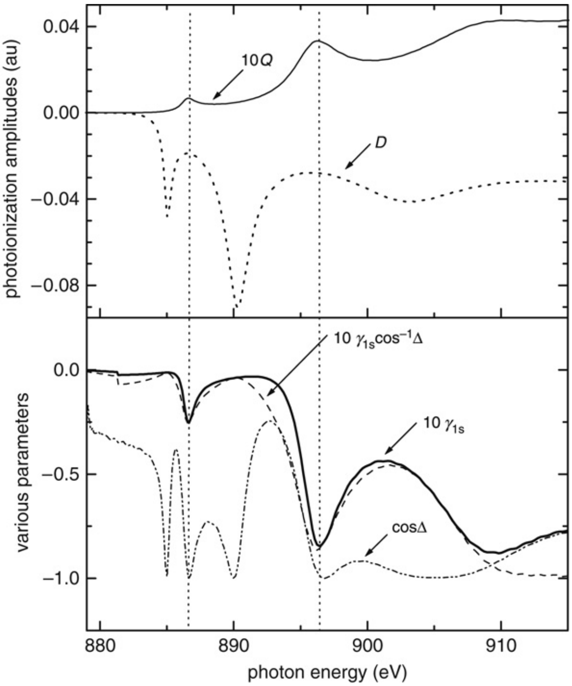

Figure 12 Ne 1s nondipole photoelectron angular asymmetry parameter $\gamma_{1s}^{@\Delta}(\omega)$ for the $\mathrm{Ne@C}_{60}^{-5}$ anion along with the dipole D and quadrupole Q amplitudes and $\cos\Delta$ ($\Delta = \xi_2 - \xi_1$) [28].

and C_{60}@C_{240}@C_{540} are reviewed, following the results of [32]. In the latter, the Δ-potential model was employed. The confining potential $V_n(r)$ was defined by Equation (6). The 1s photoionization of the thus encaged Ar atom was chosen as a case study. The calculated results [32] for the Ar 1s photoionization cross sections for free Ar, as well as for Ar@C_{60}, Ar@C_{240}, Ar@C_{540}, Ar@C_{60}@C_{240} and Ar@C_{60}@C_{240}@C_{540} are depicted in Figure 14. For free Ar, $\sigma_{1s}(\omega)$ monotonically decreases from a threshold value of about 0.19 Mb. For single-walled Ar@C_{60}, however, $\sigma_{1s}^{@\Delta}(\omega)$ acquires an oscillating profile reminiscent of shallow resonances structures. These are regular confinement resonances discussed above. Note a resonance increase of the threshold value of the photoionization cross section by approximately a factor of 2.5 in the confined atom compared to that in free Ar.

For giant doped fullerenes Ar@C_{240} and Ar@C_{540}, a clear tendency in the number, sharpness, and amplitudes of emerging confinement resonances in $\sigma_{1s}^{@\Delta}(\omega)$ is evident; the larger the size of a carbon cage, the greater both the number, sharpness, and amplitudes of the confinement resonances in the photoionization cross section. The strongest qualitative and quantitative changes in $\sigma_{1s}^{@\Delta}(\omega)$ occur in the near threshold energy region. For example,

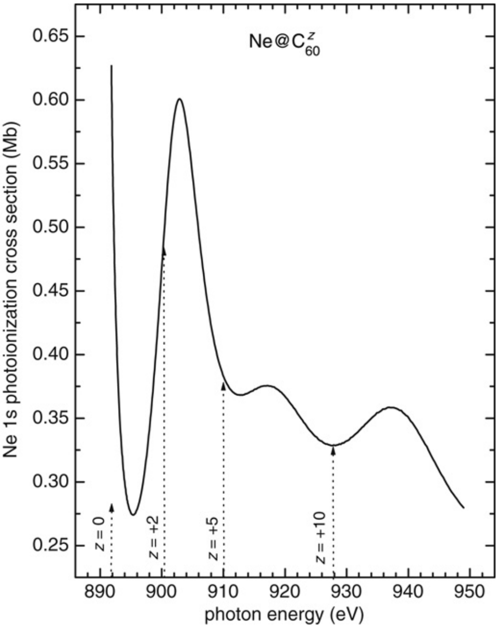

Figure 13 Calculated results [28] for the $\sigma_{1s}^{@\Delta}(\omega)$ of Ne in neutral Ne@C$_{60}$ (represented by the curve on the whole span of the graph), as well as of Ne in Ne@C$_{60}^{+2}$ (the part of the graph starting at the threshold energy of $\approx$ 900 eV and extending towards higher energies), Ne@C$_{60}^{+5}$ (the part of the graph starting at the threshold energy of $\approx$ 910 eV and extending towards higher energies), and Ne@C$_{60}^{+10}$ (the part of the graph with a threshold energy of $\approx$ 928 eV).

compared to Ar@C$_{240}$, an additional sharp confinement resonance emerges in the Ar@C$_{540}$ photoionization cross section, in close proximity to threshold, whereas the very threshold value of $\sigma_{1s}(\omega)$ drops almost to zero.

For Ar confined in a double-walled fullerene C$_{60}$@C$_{240}$, $\sigma_{1s}^{@\Delta}(\omega)$ does not differ much from that in single-walled C$_{240}$ except near threshold. This is understandable in view of a greater number of confinement resonances of larger amplitudes in the photoionization cross section induced by C$_{240}$ than by C$_{60}$ confinement, as follows from the discussion above. Near threshold, however, not only resonances due to C$_{240}$, but also due to C$_{60}$, are significant. Correspondingly, the combined effect of the two nested carbon cages on Ar photoionization is appreciable; most noticeable is a significant drop in the value of $\sigma_{1s}^{@\Delta}(\omega)$ at threshold compared to that in single-walled C$_{60}$ and C$_{240}$.

Encaging doped Ar@C$_{60}$@C$_{240}$ inside a larger giant carbon cage C$_{540}$ results in rather dramatic changes in $\sigma_{1s}^{@\Delta}(\omega)$, compared to that for Ar@C$_{60}$@C$_{240}$ or single-walled fullerenes, in a broad near-threshold energy region, up to about 3240 eV. In this region, $\sigma_{1s}^{@\Delta}(\omega)$ for Ar@C$_{60}$@C$_{240}$@C$_{540}$ differs from those for smaller sized double-walled Ar@C$_{60}$@C$_{240}$ and single-

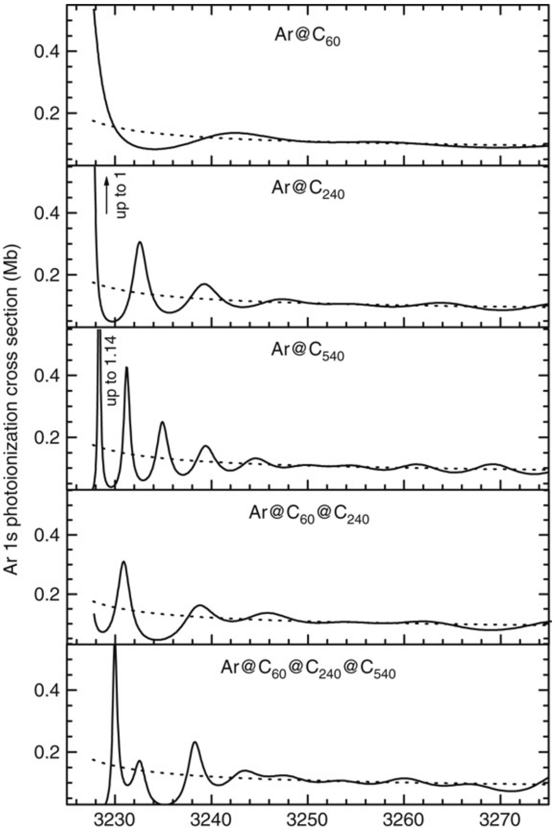

Figure 14 Calculated results [32] for 1s photoionization cross sections $\sigma_{1s}^{@\Delta}$ of Ar from $Ar@C_{60}$, $Ar@C_{240}$, $Ar@C_{540}$, $Ar@C_{60}@C_{240}$ and $Ar@C_{60}@C_{240}@C_{540}$ systems, as indicated, as well as of free Ar (dashed line).

walled C_{60}, C_{240} and C_{540}. It exhibits only three resonances, one of which is weak, in contrast to four strong resonances seen in $Ar@C_{540}$, thereby indicating an appreciable combined effect of the photoelectron waves reflected from each of carbon cages in the fullerene onion $C_{60}@C_{240}@C_{540}$.

Calculated results for the Ar nondipole 1s photoelectron angular-asymmetry parameter $\gamma_{1s}(\omega)$ for free Ar, $Ar@C_{60}$, $Ar@C_{60}@C_{240}$ and $Ar@C_{60}@C_{240}@C_{540}$ are shown in Figure 15 (the nondipole parameter δ_{ns} vanishes, by definition, and the dipole parameter $\beta_{ns} = 2$, i.e., is constant, nonrelativistically for the photoionization of ns-states).

The confinement resonance pattern in $\gamma_{1s}^{@\Delta}(\omega)$ generally displays the same trends as in $\sigma_{1s}^{@\Delta}(\omega)$. In particular, an increasing size of a carbon cage increases the number, sharpness, and amplitudes of the confinement resonances in $\gamma_{1s}^{@\Delta}$ for single-walled fullerenes, whereas

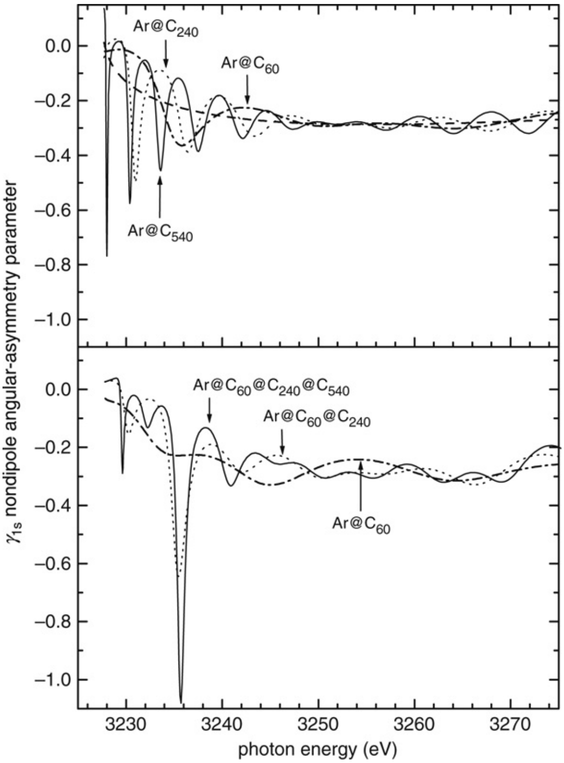

Figure 15 Calculated results [32] for a nondipole photoelectron angular-asymmetry parameter $\gamma_{1s}^{@\Delta}(\omega)$ for the 1s photoionization of Ar@C$_{60}$, $\mathrm{Ar@C_{60}@C_{240}}$ and $\mathrm{Ar@C_{60}@C_{240}@C_{540}}$, as indicated, as well as of free Ar (dashed line).

changing the confinement to a multiwalled fullerene onion alters $\gamma_{1s}^{@\Delta}(\omega)$ quite dramatically at lower photon energies; the tendency being the lower the energy, the greater the change. All this shows the importance of the interference effect between photoelectron waves reflected from the inner and outer edges of each of the carbon cages in the fullerene onion. This also results in a "beating domain" in $\gamma_{1s}^{@\Delta}(\omega)$ which occurs in about the same energy region as in $\sigma_{1s}^{@\Delta}(\omega)$. Note that the oscillations in $\gamma_{1s}^{@\Delta}$ produced by the confinement resonances are sizable enough in their amplitudes to be well within existing measurement capabilities. Moreover, at approximately 3235.7 eV, $\gamma_{1s}(\omega)$ is seen to be about 50% of the value of the dipole asymmetry parameter $\beta_{ns} = 2$, thereby indicating the breakdown of the dipole approximation; at this energy the dipole approximation alone is inadequate to describe the photoelectron angular distribution.

Looking at the calculated results for $\gamma_{1s}^{@\Delta}(\omega)$, a natural question arises how differently confinement resonances show up in dipole photoionization

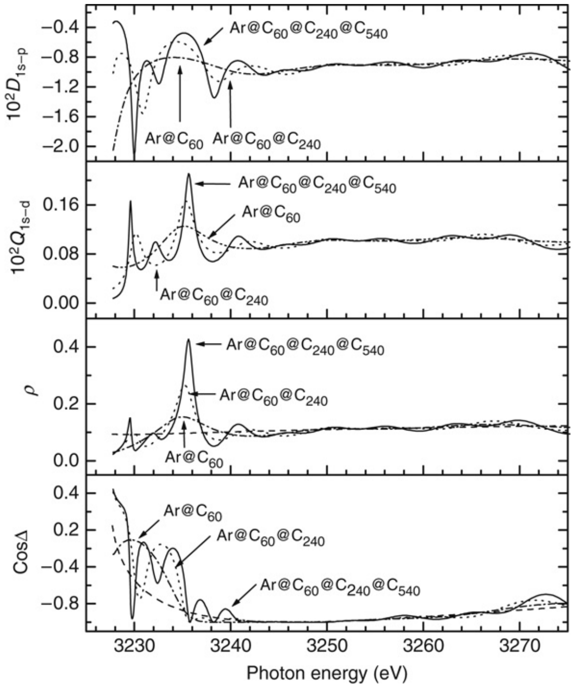

Figure 16 Calculated results [32] for the dipole $D_{1s\to\epsilon p}$ and quadrupole $Q_{1s\to\epsilon d}$ photoionization amplitudes (in atomic units), the ratio $\rho = |D_{1s\to\epsilon p}|/|Q_{1s\to\epsilon d}|$, as well as $\cos\Delta$ (here, Δ being the phase difference between the dipole and quadrupole photoionization amplitudes) for confined Ar, as indicated. A dashed line, when present, relates to the calculated data for free Ar.

amplitudes compared quadrupole photoionization amplitudes. Equally, an important question to answer is whether the primary avenue for the manifestation of confinement resonances in $\gamma_{1s}^{@\Delta}(\omega)$ is through the dipole or quadrupole photoionization amplitudes, or through their phase shifts, or through a combination of these parameters. Answers [32] to these questions come up from Figure 16, where calculated results for $D_{1s\to\epsilon p}$, $Q_{1s\to\epsilon d}$, $\rho \equiv |Q_{1s\to\epsilon d}/D_{1s\to\epsilon p}|$, and $\cos\Delta \equiv \cos(\eta_d - \eta_p)$ for 1s photoionization of Ar@C$_{60}$, Ar@C$_{60}$@C$_{240}$, and Ar@C$_{60}$@C$_{240}$@C$_{540}$ are depicted.

The confinement resonances are seen to be as well developed in the quadrupole amplitudes and in $\cos\Delta$ as in dipole amplitudes. Both of these amplitudes generally get sharper and higher with an increasing number of nested carbon cages. Remarkably, although accidentally, in a broad photon energy region near threshold, from about 3262 to 3236 eV, the resonances in $D_{1s\to\epsilon p}$ and $Q_{1s\to\epsilon d}$ are pretty much in-phase, but become abruptly out-of-phase at lower energy, closer to threshold. As a result, the ratio of these amplitudes ρ develops a sharply pronounced maximum at about 3235.6 eV. At the same time, $\cos\Delta$ reaches its lowest negative amplitude of about -1.0 at the same energy. As a result of the combined action of appreciable confinement resonances in $D_{1s\rightarrow\epsilon p}$, $Q_{1s\rightarrow\epsilon d}$, and $\cos\Delta$, the nondipole photoelectron angular asymmetry parameter γ_{1s} acquires the deepest negative minimum at the same energy. The next lowest negative drop of $\cos\Delta$ to $\cos\Delta \approx -1$ occurs at about 3230 eV, precisely where $\gamma_{1s}^{@\Delta}$ shows another narrow lower energy resonance. Consequently, the results displayed in Figure 16 lead to the conclusion that there is no single factor dominating the detailed behavior of the confinement resonances in $\gamma_{1s}^{@\Delta}$; rather they are determined by all three parameters: $D_{1s\rightarrow\epsilon p}$, $Q_{1s\rightarrow\epsilon d}$, and $\cos\Delta$.

To summarize, clear tends are seen in the behavior of inner-shell, near-threshold confinement resonances along the path from the free atom A to $A@C_{60}$ to a giant single-walled fullerene to giant multiwalled fullerenes: Ar $\rightarrow$Ar@C$_{60}$ $\rightarrow$ Ar@C$_{240}$ $\rightarrow$ Ar@C$_{540}$ $\rightarrow$ Ar@C$_{60}$@C$_{240}$ $\rightarrow$ Ar@C$_{60}$@C$_{240}$@C$_{540}$. The major trends are as follows: (a) In single-walled fullerenes $A@C_n$, a larger sized confining cage results in a greater number of confinement resonances emerging in the inner-shell photoionization cross section of the confined atom; the resonances are more closely spaced, sharper, and have greater amplitudes compared to those for smaller sized fullerenes; (b) In multiwalled fullerene onions, near threshold confinement resonances are altered appreciably due to a combined effect from all nested carbon cages compared to single-walled fullerenes; the alteration effect gets stronger with an increasing number of nested carbon cages in the fullerene onion; (c) In the nondipole photoelectron angular asymmetry parameter $\gamma_{1s}^{@\Delta}$ the (appreciable) confinement resonances are due to a combination of confinement resonances in the relevant dipole and quadrupole photoionization amplitudes as well as in the related phase shifts; none of these quantities may be singled out as the major inducer of confinement resonances in the nondipole photoelectron angular distribution alone.

5. RESULTS: THE DYNAMICAL-CAGE MODEL

5.1. Preliminaries

The above discussion signifies the quintessence of confinement resonances occurring in the photoionization of encaged atoms at photon energies far exceeding the C$_{60}$ dipole surface giant resonance energy, $\omega \gg 20$ eV. There, the frozen-cage model is applicable. This is suitable for photoionization of inner atomic subshell.

For outer subshells of the encaged atom, the ionization thresholds of which vary from a few eV to a few tens eV, the dynamical-cage model is required. The photoionization cross section of the encaged atom in the dynamical-cage approximation will be marked with a tilde sign: $\tilde{\sigma}_{nl}^{@\delta}$ and

$\tilde{\sigma}_{nl}^{@\Delta}$ for the δ-potential and Δ-potential model, respectively. Recall, the photoionization cross section $\tilde{\sigma}_{nl}^{@}$ of the encaged atom in the dynamical cage model, Equation (30), is separable with regard to the screening factor $F(\omega)$ of the incoming radiation by the C_n cage, see Figure 2, and the photoionization cross section $\sigma_{nl}^{@}(\omega)$ of the atom obtained at the frozen-cage approximation level: $\tilde{\sigma}_{nl}^{@} = F(\omega)\sigma_{nl}^{@}$.

5.2. Giant confinement resonances

The effects of dynamical screening of the incoming radiation by the C_n cage can drastically change the photoionization cross section of the encaged atom compared to that obtained at the frozen-cage approximation level. On one occasion, specifically in the Xe 5p photoionization of Xe@C_{60}, the dynamical screening effect was found [40,64] to be so strong, that corresponding confinement resonances were appropriately termed giant confinement resonances [40]. The corresponding RPAE calculated photoionization cross section, obtained both in the δ-potential model, $\tilde{\sigma}_{5p}^{@\delta}(\omega)$ [40], and Δ-potential model, $\tilde{\sigma}_{5p}^{@\Delta}(\omega)$ [64], is depicted Figure 17 along with the screening factor $F(\omega)$ and the 5p photoionization cross section of both free Xe, $\sigma_{5p}^{\text{free}}(\omega)$, and encaged Xe at the frozen-cage model level, $\sigma_{5p}^{@\delta}(\omega)$ and $\sigma_{5p}^{@\Delta}(\omega)$.

At the frozen-cage approximation level, both the δ-potential and Δ-potential calculated photoionization cross sections $\sigma_{5p}^{@\delta}$ and $\sigma_{5p}^{@\Delta}$ predict a noticeable confinement resonance in the Xe 5p photoionization cross section near threshold. The differences in the confinement resonance energy between the two models are, most likely, due to replacing the encaged ground state energies by those of the *free* atom in the δ-potential model, in contrast to the Δ-potential model which makes use of the ground state energies of the actually *encaged* atom; the latter is entirely consistent with the concept of an encaged atom, the former is not. In addition, the predicted confinement resonance in the Xe 5p photoionization is noticeably stronger in the δ-potential model than in the Δ-potential. This is because, as was shown previously, the δ-potential model tends to overestimate the strengths of confinement resonances due to neglecting the C_{60} cage thickness.

Accounting for the dynamical-cage effect results in an impressive enhancement of the Xe 5p photoionization cross section, compared to the frozen-core model calculated data, in a broad photon energy region of about 30 eV above threshold. According to work [40], the total oscillator strength of the huge resonance maximum is about 25 (in the δ-potential model), thus exceeding by a factor of 2.5 the oscillator strength of the giant 4d resonance in free Xe [40]. Consequently, the huge confinement resonance brought about by the dynamical-cage effect in the 5p photoionization cross section of encaged Xe is appropriately termed giant confinement resonance [40]. Obviously, giant confinement resonances in photoionization cross sections of encaged atoms will emerge whenever strong confinement resonances

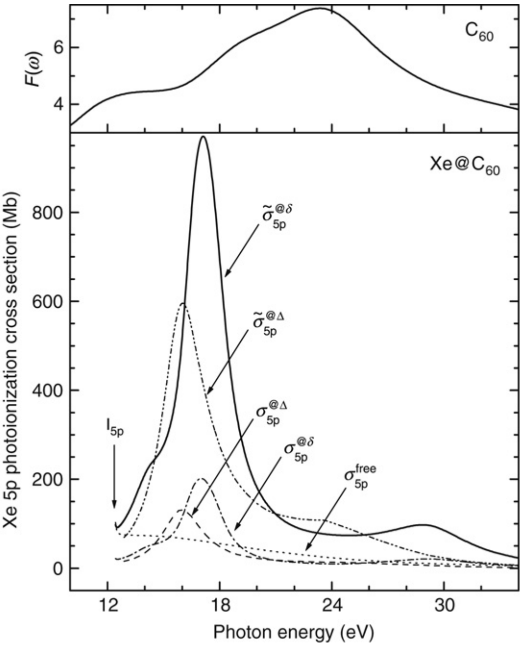

Figure 17 The C_{60} dynamical screening function $F(\omega)$ [40] along with the RPAE calculated 5p photoionization cross section of free Xe, $\sigma_{5p}^{free}(\omega)$, encaged Xe both at the frozen-cage approximation level, $\sigma_{5p}^{@\delta}(\omega)$ [40] and $\sigma_{5p}^{@\Delta}(\omega)$ [64], and dynamical-cage approximation level, $\tilde{\sigma}_{5p}^{@\delta}(\omega)$ [40] and $\tilde{\sigma}_{5p}^{@\Delta}(\omega)$ [64].

brought about by either the frozen C_n cage, or purely atomic resonances, or both, fall into the region of photon energies where $F(\omega)$ is appreciably large.

5.3. Correlation confinement resonances

So far, the discussion has been focused on cases where electron correlation effects in photoionization of encaged atoms were either irrelevant, or largely irrelevant, or significant but unaltered by a confining cage compared to the free atoms, as, e.g., in the Xe 4d photoionization of Xe@C_{60}. However, there have been a number of cases found [20,29,30,33] where electron correlation in encaged atoms, first, *does* matter and, second, *is* remarkably modified by the carbon cage compared to that in the free atoms. The consequences of modified electron correlation for the photoionization spectra of encaged atoms can be dramatic. Corresponding examples are subject to discussion in this and subsequent subsections of this section.

One one occasion, for the Xe 5s photoionization cross section of Xe@C_{60} in a photon energy region of the encaged Xe 4d giant resonance, modified

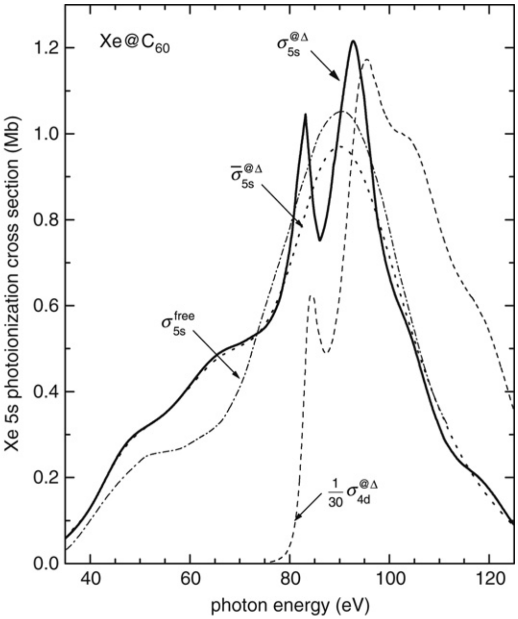

Figure 18 Calculated [33] RPAE results for the Xe 5s photoionization cross section of $\mathrm{Xe@C_{60}}$ obtained in the Δ-potential model at the frozen-cage approximation level. (a) $\sigma_{5s}^{@\Delta}(\omega)$, complete RPAE calculation accounting for interchannel coupling between photoionization transitions from the Xe $4d^{10}$, $5s^2$ and $5p^6$ subshells; (b) $\bar{\sigma}_{5s}^{@\Delta}(\omega)$, the same as in (a) but with the $4d \rightarrow f, p$ transitions being replaced by those of free Xe, for comparison purposes; (c) $\sigma_{4d}^{@\Delta}(\omega)$, complete RPAE calculations for the 4d photoionization cross section of encaged Xe; (d) σ_{5s}^{free}, complete RPAE calculated data for the 5s photoionization cross section of free Xe.

electron correlation has recently led to the discovery [33] of a new type of a confinement resonance, termed correlation confinement resonance. The corresponding RPAE calculated data, $\sigma_{5s}^{@\Delta}$, obtained at the frozen-cage model level, are depicted in Figure 18. The displayed $\sigma_{5s}^{@\Delta}$ was obtained at the following levels of approximations with regard to the RPAE theory: (a) accounting for the most important part of electron correlation in the atom in the form of interchannel coupling between photoionization transitions from the $4d^{10}$, $5p^6$ and $5s^2$ subshells of Xe, termed complete RPAE calculation, and (b) artificially replacing the actual $4d \rightarrow \epsilon p, \epsilon f$ photoionization transitions in the encaged atom by the same transitions from the free atom calculations, to eliminate confinement resonances in the transition, for illustration purposes. The corresponding 5s photoionization cross section is designated as $\bar{\sigma}_{5s}^{@\Delta}(\omega)$. In addition, displayed data in Figure 18 include the complete RPAE calculated results for the 5s photoionization cross section of free Xe, $\sigma_{5s}^{free}(\omega)$, as well as for the 4d photoionization cross section of encaged Xe, $\sigma_{4d}^{@\Delta}(\omega)$.

From the comparison of $\sigma_{5s}^{@\Delta}(\omega)$ and $\sigma_{5s}^{\rm free}(\omega)$, it is evident that resonances seen in $\sigma_{5s}^{@\Delta}(\omega)$ at about 85 and 95 eV are brought about by the confinement. Another comparison, between $\sigma_{5s}^{@\Delta}(\omega)$ and the 4d photoionization cross section $\sigma_{4d}^{@\Delta}(\omega)$, suggests that these resonances in $\sigma_{5s}^{@\Delta}(\omega)$ are reflections of the confinement resonances in $\sigma_{4d}^{@\Delta}(\omega)$ at approximately the same energies; the energies are not exactly the same because the RPAE photoionization amplitude of the 5s $\rightarrow$ p transition is not directly proportional to $\sigma_{4d}^{@\Delta}(\omega)$ but is a solution of a system of coupled integral equations (26) that involve various transitions. Finally, the comparison of $\sigma_{5s}^{@\Delta}(\omega)$ and $\bar{\sigma}_{5s}^{@\Delta}(\omega)$ (the latter was calculated with the exclusion of confinement resonances in the 4d $\rightarrow$ f, p transitions), dots the *i*'s and crosses the *t*'s with regard to the answer about the origin of the two resonances at approximately 85 and 95 eV in $\sigma_{5s}^{@\Delta}(\omega)$; they are definitely induced by the confinement resonances in the 4d $\rightarrow$ f, p transitions in encaged Xe through the interchannel coupling with the 5s $\rightarrow$ p transition. Thus, these resonances in the Xe 5s photoionization cross section of Xe@C_{60} are new types of confinement resonances that are multielectron in nature; they are absent without interchannel coupling, thus they are termed *correlation confinement resonances* [33].

As the next step, the above calculated data, $\sigma_{5s}^{@\Delta}$, must be upgraded by accounting for the dynamical-cage screening factor $F(\omega)$, because a part of them falls into the photon energy region, where $F(\omega)$ is appreciable. The corresponding RPAE calculated data [64], obtained at the dynamical-cage level approximation, marked $\tilde{\sigma}_{5s}^{@\Delta}$, are plotted in Figure 19 along with similar calculations performed in the δ-potential model, $\tilde{\sigma}_{5s}^{@\delta}$ [38]. In addition, for comparison, the calculated data both in the Δ-potential model [64] and δ-potential model [38] performed at the frozen-cage approximation level, $\sigma_{5s}^{@\Delta}$ and $\sigma_{5s}^{@\delta}$, respectively, are depicted in this figure as well.

Both the δ-potential and Δ-potential models demonstrate the significance of the dynamical-cage effects in the 5s photoionization cross section of encaged Xe in a low photon energy region. However, the Δ-potential calculated data demonstrate a much stronger significance of the dynamical-cage effect in the 5s photoionization of encaged Xe over a broader energy region compared to the δ-potential model data. This is because the screening factor $F(\omega)$ used in [38] differs strongly, for unexplained reasons, from the $F(\omega)$ used in subsequent works by the same authors [39,40]; the latter $F(\omega)$, see Figures 3 and 17, was used in the present [64] Δ-potential model calculations. Note, the marked differences in the 5s photoionization cross section of encaged Xe between the δ- and Δ-potential models exist even at the frozen-cage approximation level. This is already no surprise in view of the reasons for such differences that were revealed and explained in previous subsections. However, now there emerges a new important disagreement between the two models, namely, the absence of the discovered correlation confinement resonances in the Xe 5s photoionization cross section calculated in the δ-potential model. To understand this, recall that the

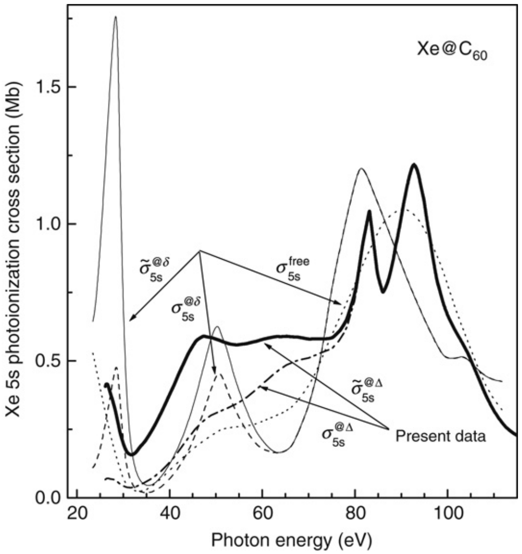

Figure 19 RPAE 5s photoionization cross section of encaged Xe, as marked. (a) $\sigma_{5s}^{@\Delta}$ [33], the Δ-potential model at the frozen-cage approximation level; (b) $\tilde{\sigma}_{5s}^{@\Delta}$ [64], the Δ-potential model at the dynamical-cage approximation level; (c) $\sigma_{5s}^{@\delta}$ [35], the δ-potential model at the frozen-cage approximation level; (d) $\tilde{\sigma}_{5s}^{@\delta}$ [38], the δ-potential model at the dynamical-cage approximation level; (e) $\sigma_{5s}^{\text{free}}$, free Xe.

photoionization cross section of an encaged atom in the δ-potential model is determined as $\sigma_{nl}^{@\delta}(\omega) = G_l^2(\omega)\sigma_{nl}^{\text{free}}(\omega)$, Equation (29). The function $G_l(\omega)$, Equation (16), accounts only for the interference between the outgoing photoelectron wave from the ionized atom and the photoelectron wave scattered off the C_{60} cage. This interference is irrelevant to electron correlation in the atom itself. In addition, the photoionization cross section of a free atom $\sigma_{nl}^{\text{free}}(\omega)$ is, by definition, independent of the presence of a carbon cage. One readily concludes that the δ-potential model is totally incapable of predicting and studying correlation confinement resonances in the photoionization of encaged atoms.

In summary, correlation confinement resonances in the photoionization of encaged atoms are expected to emerge whenever the photoionization transition(s) from an ionizing subshell of the encaged atom are coupled appreciably with strong photoionization transitions from deeper subshells possessing sizable ordinary confinement resonances. Cs and Ba atoms, e.g., might be just such atoms since they possess 4d giant resonances similar to that in Xe [55]. Thus, one may expect that correlation confinement resonances are quite a general effect and will be exhibited in a broad range of encaged atoms and molecules.

5.4. Reversed electron correlation

It turns out [20,29], that electron correlation may work in the "opposite direction" in encaged atoms compared to that in the free atoms, thus termed reversed electron correlation.

The quintessence of the reversed electron correlation effect is illustrated in Figure 20 by nonrelativistic HF and RPAE calculated data of the 4s photoionization cross section of free Ca and encaged Ca, Ca@C_{60} near threshold, both at the frozen-cage approximation level, $\sigma_{4s}^{@\Delta}$, [20] and dynamical-cage approximation level, $\tilde{\sigma}_{4s}^{@\Delta}$ [64].

The shallow spike in $\sigma_{4s}^{@\Delta}$ between approximately 10 and 25 eV is an ordinary confinement resonance. Of importance, however, is that, at the frozen-cage approximation level, (a) electron correlation decreases the threshold magnitude of the photoionization cross section $\sigma_{4s}^{\mathrm{free}}$ of free Ca (see the inset in Figure 20) but increases that of encaged Ca, $\sigma_{4s}^{@\Delta}$ (upper main panel in Figure 20); (b) in the same energy region, the Cooper minimum seen in the photoionization cross section of both the free and encaged Ca atom is moved (from its HF position) by correlation to lower energies in free Ca but towards higher energies in encaged Ca (upper main panel in Figure 20); (c) beyond the Cooper minimum electron correlation noticeably increases (compared to HF results) the magnitude of $\sigma_{4s}^{\mathrm{free}}$ whereas it decreases that of $\sigma_{4s}^{@\Delta}$. The conclusion is that electron correlation in the encaged Ca atom "works" in the opposite direction to that in free Ca, i.e., the electron correlation effect in encaged Ca is reversed compared to the free atom.

At the dynamical-cage approximation level (see the lower main panel in Figure 20), the role of the dynamical screening of the incoming radiation by the C_{60} cage is tremendous [64], resulting in the impressively enhanced 4s photoionization cross section $\tilde{\sigma}_{4s}^{@\Delta}$ compared to that calculated at the frozen-cage approximation level.

The reversed electron correlation effect in encaged atoms was further theoretically studied in [29] with an eye to trends in the modification of electron correlation in ns valence shell photoionization cross sections of a sequence of atoms with increasing nuclear charge Z, namely, Mg, Ca, Sr and Ba, where relativistic effects are not negligible. The calculations were performed in the framework of relativistic Dirac–Fock and RRPA theories, combined with the Δ-potential model for the encaged atom at the frozen-cage approximation level. A key finding was the evolution of reversed electron correlation with changing Z. This was shown to be due to, increasing with Z, alterations of valence ns orbitals in the encaged atoms by the C_{60} cage. As an illustration, the relativistic Dirac–Fock calculated data for the valence ns orbitals in the encaged and free atoms in question are displayed in Figure 21.

From this figure, it is evident, that, for the free atoms, the peak of the valence ns probability distribution moves to larger r with increasing Z. For this reason the valence ns probability density in the encaged atoms is progres-

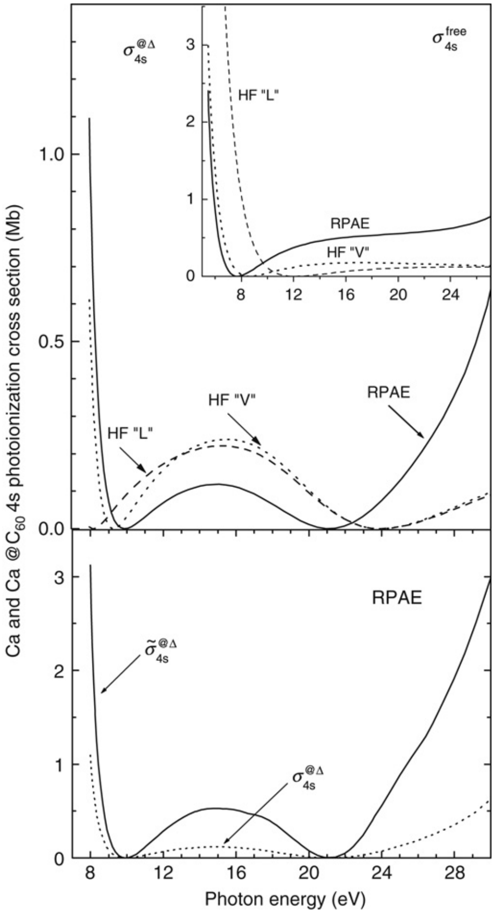

Figure 20 HF and RPAE calculated data for the Ca 4s photoionization cross section of free Ca, $\sigma_{4s}^{\rm free}$, and encaged Ca, calculated at the frozen-cage, $\sigma_{4s}^{@\Delta}$ [20] and dynamical-cage, $\tilde{\sigma}_{4s}^{@\Delta}$ [64] approximation levels in the framework of the Δ-potential model. HF-L and HF-V stands for the HF calculation of the photoionization cross section in the "length" or "velocity" form, respectively. In RPAE [55] the "length" and "velocity" forms are equivalent.

sively affected more strongly with increasing Z. For all the encaged atoms in question, except Mg, the overlap between the electron charge density distribution and the cage becomes so strong that more of the electron density moves into the potential well with increasing Z. Hence, the electron correlation in the valence 3s photoionization of @Mg must be qualitatively different from that for other encaged atoms, @Ca 4s, @Sr 5s and @Ba 6s.

The RRPA calculated [29] valence ns photoionization cross sections for both the free and encaged atoms, at the frozen-cage approximation level, are displayed in Figures 22–24. To demonstrate the importance of electron

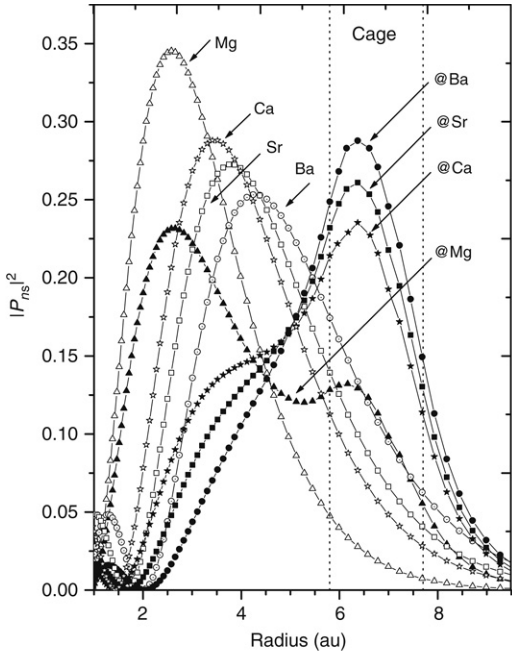

Figure 21 Relativistic Dirac–Fock calculated data [29] of the valence $n\mathrm{s}$ radial electron probability densities $|P_{n\mathrm{s}}|^2$ for free Mg, Ca, Sr and Ba as well as for the atoms encaged in C_{60}, marked @Mg, @Ca, @Sr and @Ba, respectively. The domain of the C_{60} potential well is encompassed by the dashed vertical lines in this figure.

correlation itself, RRPA calculations were performed accounting both for two interacting channels (this brings in an insignificant amount of electron correlation in the calculation), marked "2ch", and for nine interacting channels, "9ch" (this includes the dominant part of electron correlation in the atom).

For all atoms, except Mg, the effect observed is qualitatively the same as that discovered in the nonrelativistic RPAE calculations of Ca@C_{60} [20], discussed above. Namely, in @Ca, @Sr and @Ba the near-threshold Cooper minimum is moved by electron correlation towards higher energies in contrast to that in free Mg, Ca, Sr and Ba. This is the same reversed electron correlation effect in encaged atoms that has been discussed above. As is seen from the RRPA calculated data, Figures 23 and 24, the tendency in the strength of reversed electron correlation is that the heavier the encaged atom, the stronger the reversed electron correlation effect. The physics behind this was detailed in [29]. In accordance with [29], in encaged atoms, whose valence $n\mathrm{s}$ orbitals move appreciably into the potential well of C_{60}, the interchannel coupling matrix elements between transitions from the $n\mathrm{s}$ and $(n-1)\mathrm{p}$ subshells change their signs, in contrast to atoms whose valence $n\mathrm{s}$ orbitals remain, or largely remain, within the atom, as in @Mg. Therefore, the interchannel

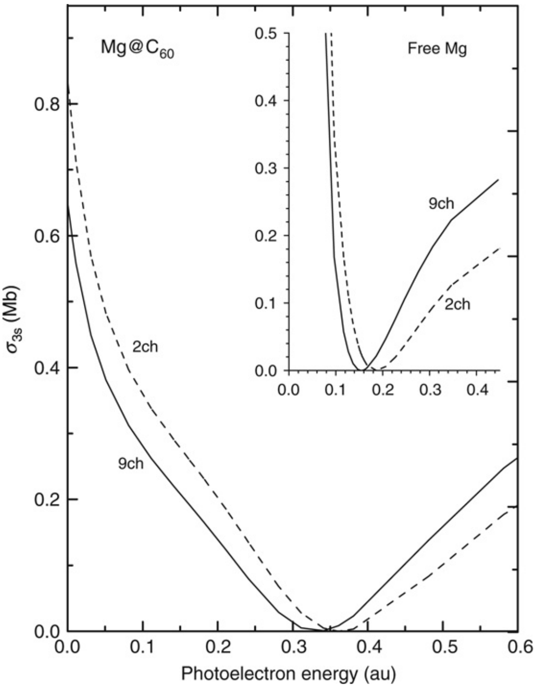

Figure 22 RRPA calculated data [29] for the Mg 3s photoionization cross section of free Mg and $\mathrm{Mg@C_{60}}$ Mg, marked @Mg, as a function of photoelectron energy. The data were obtained at two levels of the RRPA calculations, namely accounting for, (a) only two RRPA interacting channels ("2ch") and (b) nine RRPA channels ("9ch").

coupling in the former has just the reverse effect compared to that in the latter (or free atoms), thereby moving the Cooper minimum to higher energies instead of lower energies. However, in more compact atoms, such as Mg, that transfer only a small portion of the electron density into the potential well of C_{60}, the electron correlation is expected to "work" in the same direction in encaged atoms as in the free atoms; this, indeed, is supported by the calculated data for Mg and $\mathrm{Mg@C_{60}}$. Note, in conclusion, data shown in Figures 22–24 were obtained without accounting for the dynamical-cage screening factor $F(\omega)$. The latter, however, is appreciable in the near-threshold photon energy region considered. Therefore, the presented RRPA calculated data for the photoionization cross sections displayed in Figures 22–24 should have been multiplied by the screening factor $F(\omega)$, Figure 3, to finalize the study; this, however, was not be done in [29].

5.5. Redistributed oscillator strengths

A remarkable modification of oscillator strengths in encaged atoms, $A@C_{60}$, compared to free atoms, and the consequences of such modification for the

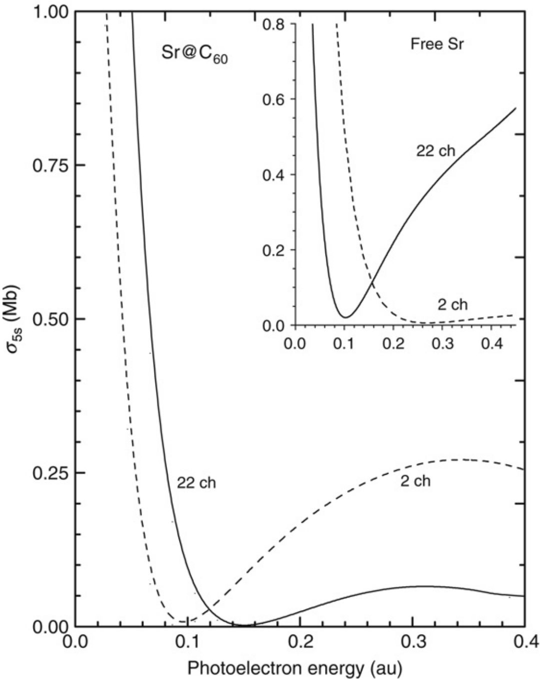

Figure 23 The same as in Figure 22, but for the free (Sr) and encaged (@Sr) strontium atom [29].

autoionizing resonance spectra of encaged atoms were discovered in [20]. The finding was exemplified by the Ca 4s photoionization of Ca@C$_{60}$. A similar study was later performed for La@C$_{60}$ [65]. A key, fundamental, result of both works is the discovery of a behavior, beyond conventional wisdom, of the encaged atom electron charge density within the hollow space of C$_{60}$. Normally, one expects some charge density of an encaged atom to be pulled into the attractive potential well of C$_{60}$ (as in the just discussed @Ca, @Sr and @Ba atoms). However, in the phenomenon in question a reversed behavior was discovered, namely, the *attractive* cage largely pushed the electron charge density of the excited 4d orbital of @Ca [20] and that 5d of @La [65] into the inner hollow space of C$_{60}$, thereby increasing the excited state electron density nearer the atomic core.

To demonstrate the phenomenon, HF calculated results [20] for the ground-state 4s orbital as well as for the excited 3d, 4d and 5d orbitals (resulting due to 3p → *n*d transitions) of free Ca and Ca in Ca@C$_{60}$ are depicted in Figure 25. The calculations for the encaged Ca atom were performed in the framework of the Δ-potential model.

It follows from Figure 25 that the excited 4d orbital in @Ca is largely packed into the hollow space of the C$_{60}$ cage. The mean radius of this orbital

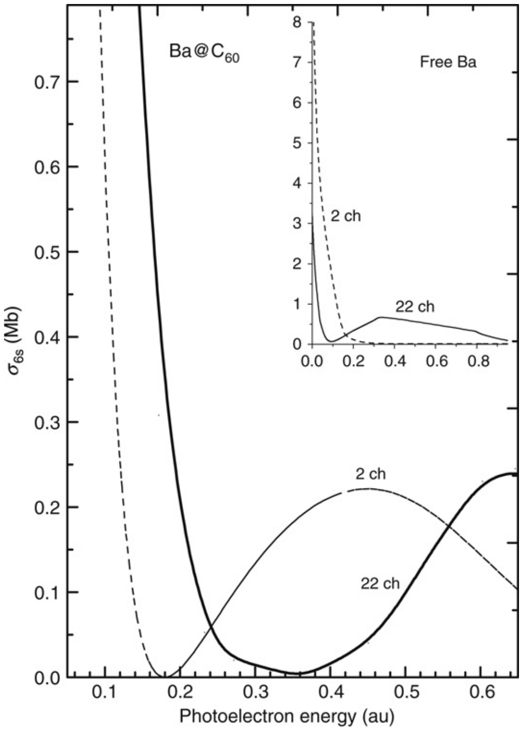

Figure 24 The same as in Figures 22 and 23, but for the free (Ba) and encaged (@Ba) barium atom [29].

shrinks [20] from about 14 au in free Ca to only 4.3 au (less than the size of C_{60} itself!) in @Ca. In contrast, the excited 3d orbital, that used to be collapsed into the inner core of free Ca, expands greatly into the outer region of @Ca. Thus, it is now the 4d orbital, not the 3d orbital, which has the largest electron density near the atomic core of @Ca, in contrast to free Ca. This results [20] in a dramatic tenfold increase of the 3p → 4d transition oscillator strength from 0.27 in free Ca to 2.6 in @Ca, which now exceeds the 3p → 3d transition oscillator strength; the latter was reduced from 2.4 in free Ca to 1.5 in @Ca. Hence, in @Ca the dominant transition is no longer 3p → 3d but 3p → 4d; the effect is termed redistribution of oscillator strength in @Ca [20]. A qualitative explanation for such a spectacular phenomenon is given in the original work [20].

The effect of the oscillator strength redistribution phenomenon on the @Ca 4s photoionization cross section in a region of the 3p → 3d, 4d and 5d autoionizing resonances is illustrated by Figure 26. In this figure, RPAE calculated results [20,64], accounting for interchannel coupling between the autoionizing resonance transitions and 4s photoionization transition $4s \rightarrow \epsilon p$, are depicted. The C_{60} confinement was accounted for in the Δ potential

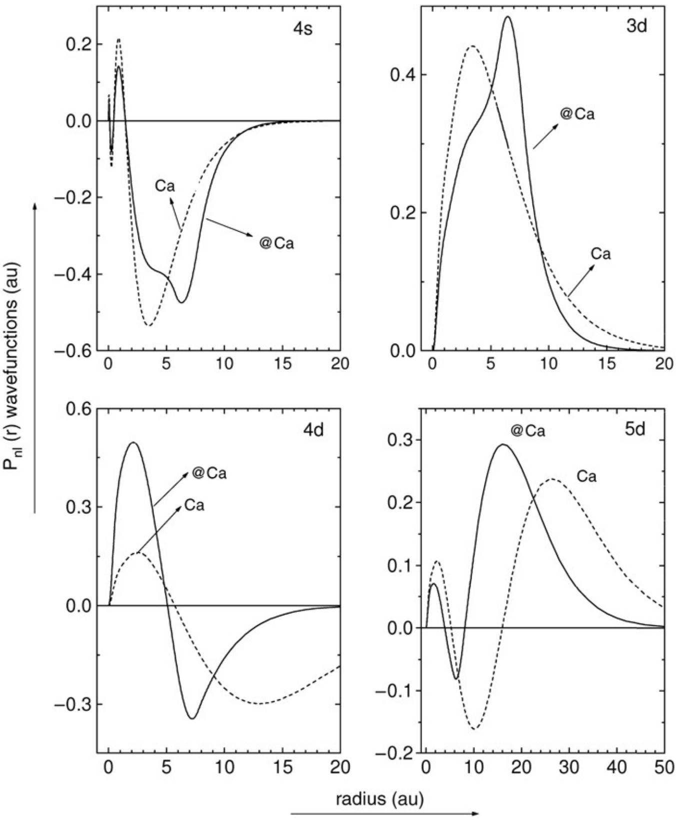

Figure 25 Radial orbitals $P_{nl}(r)$ of free Ca and Ca in Ca@C$_{60}$ (@Ca) [20]. Note the collapse of the 4d orbital in a dipole 3p → 4d excited state of @Ca into a hollow space of C$_{60}$ but significant electron density transfer of the 3p → 3d excited orbital in @Ca into the C$_{60}$ potential well.

model both at the frozen-cage approximation level, $\sigma_{4s}^{@\Delta}$ [20], and dynamical-cage approximation level, $\tilde{\sigma}_{4s}^{@\Delta}$ [64].

One can see, from the upper panel of this figure, that the C$_{60}$ confinement makes the 3p → 4d resonance in @Ca incomparably broader and much higher in its amplitude compared to free Ca. At the same time, the 3p → 3d resonance in @Ca becomes noticeably narrower compared to free Ca. Qualitatively, the 3p → 3d and 3p → 4d resonances in $\sigma_{4s}^{@\Delta}$ become almost equal, to a reasonable approximation, and both have little to resemblance to those in free Ca.

In [20], the dynamical screening of the incoming radiation by the C$_{60}$ cage was not accounted for, since the dynamical screening effect was not yet unraveled at that time. Updated, accounting for the dynamical screening effect, results of a new study [64] of the Ca 4s photoionization cross section of

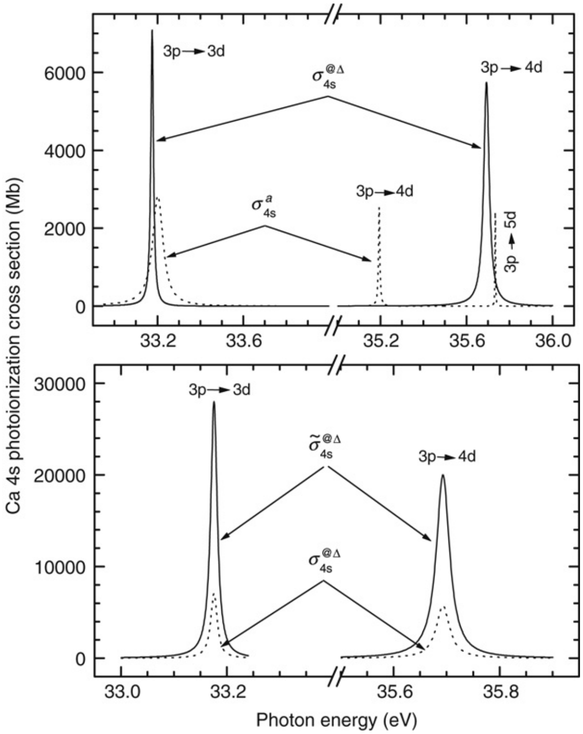

Figure 26 RPAE calculated results for the $3\mathrm{p} \rightarrow nd$ autoionizing resonances in the 4s photoionization cross section of free Ca, σ^{a}_{4s}, and Ca from $\mathrm{Ca@C_{60}}$. The results were obtained within the Δ-potential model both at the frozen-cage approximation level, $\sigma^{@\Delta}_{4s}$ [20] and dynamical-cage approximation level, $\tilde{\sigma}^{@\Delta}_{4s}$ [64].

$\mathrm{Ca@C_{60}}$, $\tilde{\sigma}^{@\Delta}_{4s}$, are displayed in the lower panel of Figure 26. The dynamical screening effect is seen to increase very much quantitatively, although does not alter qualitatively, the photoionization probability of @Ca at the autoionizing resonance energies compared to the predictions of the frozen-cage approximation.

6. RELATIVISTIC EFFECTS

6.1. Preliminaries

Relativistic effects in photoionization of atoms encaged in $\mathrm{C_{60}}$, $A\mathrm{@C_{60}}$, have fallen under theoretical scrutiny in [29,30], where the photoionization spectra of valence ns subshells in encaged alkaline-earth-metal atoms (@Mg, @Ca, @Sr and @Ba) were detailed. The corresponding key results of [29,30] are highlighted in this section.

Table 1 RRPA calculated [29] photoelectron energy positions of the Cooper minima (au) for the free and encaged Ca, Sr and Ba

Transitions	Ca		@Ca	
	2ch	9ch	2ch	9ch
$4s \to p_{3/2}$	0.1647	0.0807	0.0337	0.0667
$4s \to p_{1/2}$	0.1537	0.0747	0.0337	0.0667
Difference	0.0110	0.0060	0	0
Transitions	Sr		@Sr	
	2ch	22ch	2ch	22ch
$5s \to p_{3/2}$	0.2977	0.1087	0.0935	0.1475
$5s \to p_{1/2}$	0.2127	0.0817	0.0935	0.1475
Difference	0.0850	0.0270	0	0
Transitions	Ba		@Ba	
	2ch	22ch	2ch	22ch
$6s \to p_{3/2}$	0.5638	0.1088	0.1797	0.3577
$6s \to p_{1/2}$	0.2128	0.0558	0.1797	0.3577
Difference	0.351	0.0530	0	0

6.2. Obliterated relativistic effects

The above discussed Cooper minima in the valence ns photoionization of free Mg, Ca, Sr and Ba and encaged @Mg, @Ca, @Sr and @Ba are, actually, effective Cooper minima in the sense that each of them is a mixture of Cooper minima in corresponding relativistic $ns \to \epsilon p_{3/2}$ and $ns \to \epsilon p_{1/2}$ transitions, respectively. Relativistic effects, when present, are known [66] to cause different energy positions of Cooper minima in the corresponding partial photoionization cross sections $\sigma^{@\Delta}_{ns \to \epsilon p_{3/2}}$ and $\sigma^{@\Delta}_{ns \to \epsilon p_{1/2}}$; in free atoms, the difference $\Delta_{1/2,3/2}$ between the two energy positions uniquely increases with increasing Z. Surprisingly, at a first glance, a unique increase in $\Delta_{1/2,3/2}$ versus Z was found [29] to cease in encaged @Ca, @Sr and @Ba. There, no splitting whatsoever between the Cooper minima in $\sigma^{@\Delta}_{ns \to \epsilon p_{3/2}}$ and $\sigma^{\Delta}_{ns \to \epsilon p_{1/2}}$ was found for the all encaged atoms in question, in contrast to the free atoms; this is demonstrated by calculated data [29] presented in Table 1.

Thus, another key, fundamental, finding of [29] is that relativistic effects in encaged atoms can be (and *are* in the case of @Ca, @Sr and @Ba) obliterated by the confining cage, a result which is entirely contrary to the conventional wisdom that the relativistic splitting between $\sigma_{ns \to \epsilon p_{1/2}}$ and $\sigma_{np \to \epsilon p_{3/2}}$ increases with increasing Z. According to [29], the physics behind the, thus obliterated, relativistic effects in @Ca, @Sr and @Ba is the concentration of a significant part of the ns charge density in the C_{60} potential well, see Figure 21. This implies a much larger radius of the ground state valence

ns orbital in the encaged atom compared to the free atom. Correspondingly, the spin-orbit interaction, which behaves as $1/r^3$, becomes so small in the encaged atom that it does not affect the Cooper minima at all. Therefore, the seemingly counter-intuitive behavior of relativistic effects for the higher-Z encaged atoms results entirely from the C_{60} confinement-induced alteration of their valence ns orbitals. In @Mg the alteration is negligible, and for this reason it behaves in a manner similar to free Mg.

6.3. ns photoelectron angular distributions

Nonrelativistically, the dipole ns photoelectron angular asymmetry parameter $\beta_{n\mathrm{s}}(\omega)$ is independent of the photon energy ω; $\beta_{n\mathrm{s}}(\omega) = 2$. This is because, nonrelativistically, there is only one dipole photoionization transition $n\mathrm{s} \to \epsilon\mathrm{p}$ possible in the atom due to the selection rules. Then, referring to Equation (21), one readily finds $\beta_{n\mathrm{s}}(\omega) = 2$. The implication is that, nonrelativistically, the ns photoelectron angular distribution is isotropic. However, relativistically, near the Cooper minima in photoionization amplitudes, $\beta_{n\mathrm{s}}(\omega)$ has long been known to be a sensitive function of the photon energy [66]. This is because relativistic effects in the form of spin-orbit interaction in the continuum spectrum result in two different photoionization transitions, $n\mathrm{s} \to \epsilon\mathrm{p}_{1/2}$ and $n\mathrm{s} \to \epsilon\mathrm{p}_{3/2}$, rather than in a single transition $n\mathrm{s} \to \epsilon\mathrm{p}$, as nonrelativistically.

The question of how relativistic effects show up in the $\beta_{n\mathrm{s}}$ parameter of an encaged atom, and how electron correlation in the encaged atom can influence the $\beta_{n\mathrm{s}}$, was originally studied in [30], where relativistic RRPA combined with the Δ-potential model was employed to study $\mathrm{Hg@C_{60}}$. The calculation was performed at two different levels of truncation with regard to RRPA interchannel coupling: (1) including two transitions from the valence $6\mathrm{s}^2$ subshell alone, marked $\beta_{6\mathrm{s}}^{@\Delta a}$, and (2) including transitions from the $6\mathrm{s}^2$ and $5d^{10}$ subshells, marked $\beta_{6\mathrm{s}}^{@\Delta b}$. This is needed in order to learn how electron correlation may influence $\beta_{n\mathrm{s}}$ in the encaged atom. RRPA calculated results [30] are displayed in Figure 27, where the $\beta_{6\mathrm{s}}$ parameters for the free Hg is compared with the $\beta_{6\mathrm{s}}^{@\Delta b}$ of @Hg, as well as in Figure 28, where $\beta_{6\mathrm{s}}^{@\Delta a}$ and $\beta_{6\mathrm{s}}^{@\Delta b}$ are compared.

The complicated physics behind various structures in the energy dependence of $\beta_{6\mathrm{s}}^{@\Delta}$ for @Hg was revealed in [30]. The key reasons are discussed below.

(a) Purely relativistic effect

From Figure 27, one can see that the $\beta_{6\mathrm{s}}$ parameter, both for free Hg, $\beta_{6\mathrm{s}}$, and @Hg, $\beta_{6\mathrm{s}}^{@\Delta}$, acquires a strong photoelectron energy dependence near threshold. This is due to an exchange of oscillator strengths in the two relativistic channels $ns \to \epsilon\mathrm{p}_{1/2}$ and $ns \to \epsilon\mathrm{p}_{3/2}$. Thus, this is a relativistic effect.

(b) Combined confinement-correlation effect

In addition, as seen in the same Figure 27, (i) the positions of deep (Cooper) minima in $\beta_{6\mathrm{s}}$ of free Hg and $\beta_{6\mathrm{s}}^{@\Delta b}$ of @Hg are noticeably different with regard to each other and (ii) $\beta_{6\mathrm{s}}$ has a noticeably deeper and

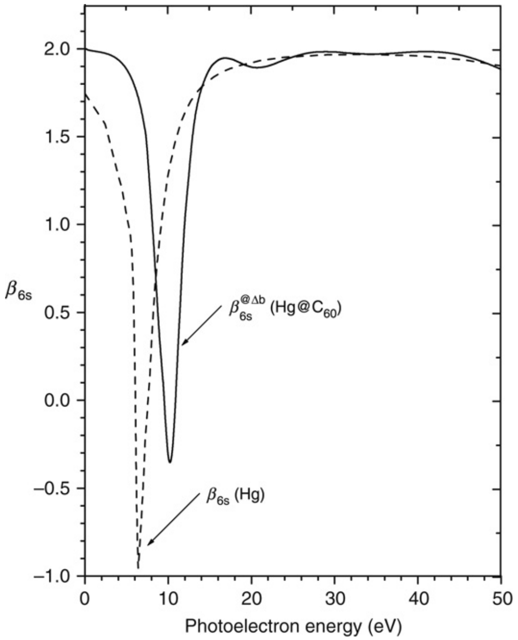

Figure 27 Relativistic RPAE calculated results [30] of the 6s dipole photoelectron angular distribution parameter $\beta_{6s}(\omega)$ from free Hg and @Hg, $\beta_{6s}^{@\Delta b}$. The RRPA calculations included interchannel coupling between transitions from the $6s^2$ and $5d^{10}$ subshells of the atom. Confinement effects were accounted for in the Δ-potential model at the frozen-cage approximation level.

narrower minimum than that in $\beta_{6s}^{@\Delta b}$. This is due to changes in electron correlation in @Hg brought about by the confining cage, i.e., this is a combined confinement-correlation effect.

(c) Purely confinement effect

One can see from the same figure, that $\beta_{6s}^{@\Delta b}$ is an oscillating function of ω beyond the deep minimum in $\beta_{6s}^{@\Delta b}$. These oscillations are confinement resonances discussed earlier. Thus, this is a purely confinement effect.

(d) Purely electron correlation effect

From Figure 28, the $\beta_{6s}^{@\Delta a}$ parameter, calculated with the minimum amount of electron correlation, is quantitatively and qualitatively much different from that $\beta_{6s}^{@\Delta b}$, calculated by including the dominant part of electron correlation in the atom. This is a purely electron correlation effect, demonstrating the importance of electron correlation in the 6s photoionization of @Hg.

Note, as in the discussed case of the ns photoionization cross sections of @Mg, @Ca, @Sr and @Ba, the presented $\beta_{6s}^{@\Delta a}$ and $\beta_{6s}^{@\Delta b}$ parameters for @Hg must be corrected by accounting for the dynamical-cage effect, since the

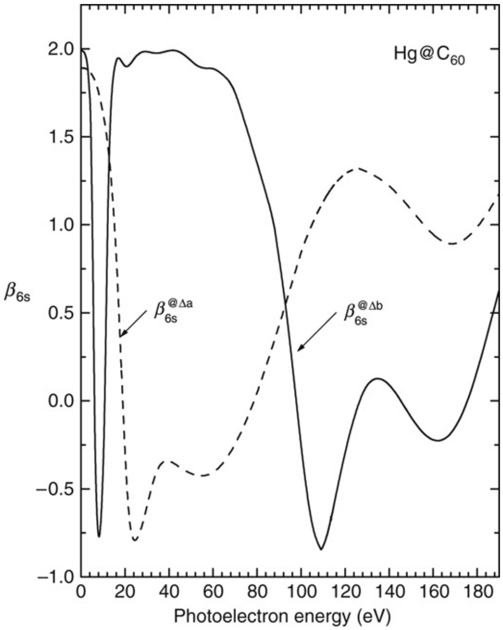

Figure 28 Relativistic RPAE calculated results [30] of the 6s dipole photoelectron angular distribution parameter of @Hg at two different levels of truncation with regard to RRPA interchannel coupling: (a) including channels from the $6s^2$ subshell alone, $\beta_{6s}^{@\Delta a}$, and (b) including channels from the $6s^2$ and $5d^{10}$ subshells of @Hg, as in Figure 27. Confinement effects were accounted for in the Δ-potential model at the frozen-cage approximation level.

phenomenon occurs in the photon energy region where the dynamical screening factor $F(\omega)$ cannot be omitted; this was not done in [30].

7. CONCLUSION

The present paper has focused on novel systems, doped fullerenes, with the emphasis on their photoionization spectra. While the photoionization problem of gas phase doped fullerenes has been experimentally addressed only recently in pioneering works [12,13], there has been much more activity on the theoretical side of the problem; this has far outstripped experiment. In the present paper, only those results obtained on the basis of simple semiempirical models, the Δ-potential [15,20–22,27–33,43,44] and δ-potential [34–41] models have been highlighted. Surprisingly, even within the framework of these simple models a rich variety of novel effects, particularly the confinement resonances and their manifestations in the photoionization spectra of doped fullerenes has been unraveled. Although the approximations made are indisputably reasonable for trusting the existence of, and trends in, the predicted confinement resonances, and thereby urging their experimental verification, they still omit significant physics and should be, and have been, regarded as a useful starting point for experimental or more sophisticated theoretical work. In particular, the assumption of the fullerene cage C_n as a continuous homogeneous medium omits the dependence of the photoionization spectra on the actual multicenter molecular nature of the cage. This molecular aspect results in new resonances, in addition to the confinement resonances, in the photoionization spectra of confined atoms. The new resonances have been investigated in a number of studies [18,19,23–25]. The approximation of the at-the-center position of the encapsulated atom inside the C_n hollow space omits the corresponding off-the-center effects due to the breakdown of the spherical nature of the $A@C_n$ system when the off-center-position occurs. Off-the-center effects result in new and significant features in the spectra, as was found in subsequent works [24,25]. Breaking the $A@C_n$ fullerene into two independent, or nearly independent parts, the ground state encaged atom and the fullerene cage itself, and/or neglecting the polarizability of the encaged atom compared to that of the fullerene cage, as in semiempirical models [38,39,43,44], does not take full account of the electron correlation in the system $A@C_n$, particularly for the interaction between the dipole moment of the encaged atom and the dipole moment of the C_n cage induced due to their interaction with the incoming electromagnetic radiation. Recently this difficulty has been partially addressed within the framework of a time-dependent local density approximation that includes coupling between all the dipole-allowed final state channels [45,46], where new and dramatic effects in the photoionization spectra of doped fullerenes, compared with the semiempirical models, have been predicted and examples of which: Ar@C_{60} [45] and Mg@C_{60}, [46] have been reported. In particular, the theory predicts the breakdown of the universal (i.e., regardless of the structure of an encaged atom) photon energy dependence of the dynamical polarization factor $F(\omega)$ [38,39,43,44]. These more sophisticated photoionization theories for doped fullerenes are not without their own drawbacks; the discussion of these theories, however, is outside of the scope of the present paper. Note that the doped fullerene problem is a sister problem to the study of metallic clusters in general. A critical assessment of the obstacles in the way to understanding these forms of matter can be found elsewhere [67]. Drawing together the threads of the research activities in the area of photoionization of doped fullerenes, one sees how multifaceted is the problem in its complexity for theory. Although all listed and/or cited theoretical studies in this paper have contributed considerably to the current level of understanding the problem, there is clearly a rich variety of new phenomena waiting to be uncovered in the fascinating area of the study of the photoionization and structure of doped fullerenes. Research activities, both experimental and theoretical, in this direction will definitely grow rapidly over the coming years, especially with the impetus of the recent breakthrough in experimental techniques that have made experiments on gas phase doped fullerenes possible [12,13].

ACKNOWLEDGEMENTS

The author is grateful to A. S. Baltenkov, P. C. Deshmukh & H. R. Varma, and S. Lo & A. V. Solovyov for sharing electronic data files of their research, elements of which have been used in many original figures in the present paper. This work was supported by NSF Grant No. PHY-0652704 and a Research Grant from the University of North Alabama.

REFERENCES

[1] H.W. Kroto, J.R. Heath, S.C. O'Brian, R.F. Curl, R.E. Smalley, Nature 318 (1985) 162.

[2] H. Shinohara, Rep. Prog. Phys. 63 (2000) 843.

[3] A.L. Buchachenko, J. Phys. Chem. B 105 (2001) 5839.

[4] L. Forró, L. Mihály, Rep. Prog. Phys. 64 (2001) 649.

[5] P. Moriarty, Rep. Prog. Phys. 64 (2001) 297.

[6] L. Becker, R.J. Poreda, T.E. Bunch, Proc. Natl. Acad. Sci. U.S.A. 97 (2000) 2979.

[7] F.A. Gianturcoa, G.Yu. Kashenock, R.R. Lucchese, N. Sanna, J. Chem. Phys. 116 (2002) 2811.

[8] J.P. Lu, W. Yang, Phys. Rev. B 49 (1994) 11421.

[9] E. Dietel, A. Hirsch, B. Pietzak, M. Waiblinger, K. Lips, A. Weidinger, A. Gruss, K. Dinse, J. Am. Chem. Soc. 121 (1999) 2432.

[10] W. Harneit, Phys. Rev. A 65 (2002) 032322.

[11] J. Kou, T. Mori, M. Ono, Y. Haruyama, Y. Kubozono, K. Mitsuke, Chem. Phys. Lett. 374 (2003) 1.

[12] A. Müller, S. Schippers, R.A. Phaneuf, M. Habibi, D. Esteves, J.C. Wang, A.L.D. Kilcoyne, A. Aguilar, S. Yang, L. Dunsch, J. Phys.: Conf. Series 88 (2007) 012038.

[13] K. Mitsuke, T. Mori, J. Kou, J. Chem. Phys. 122 (2005) 064304.

[14] W. Jaskólski, Phys. Rep. 271 (1996) 1.

[15] V.K. Dolmatov, A.S. Baltenkov, J.P. Connerade, S.T. Manson, Radiat. Phys. Chem. 70 (2004) 417.

[16] M.J. Pushka, R.M. Niemenen, Phys. Rev. B 47 (1993) 1181.

[17] G. Wendin, B. Wästberg, Phys. Rev. B 48 (1993) 14764.

[18] P. Decleva, G. De Alti, M. Stener, J. Phys. B 32 (1999) 4523.

[19] M. Stener, G. Fronzoni, D. Toffoli, P. Colavita, S. Furlan, P. Decleva, J. Phys. B 35 (2002) 1421.

[20] J.P. Connerade, V.K. Dolmatov, S.T. Manson, J. Phys. B 32 (1999) L395.

[21] J.P. Connerade, V.K. Dolmatov, S.T. Manson, J. Phys. B 33 (2000) 2279.

[22] J.P. Connerade, V.K. Dolmatov, S.T. Manson, J. Phys. B 33 (2000) L275.

[23] A.S. Baltenkov, V.K. Dolmatov, S.T. Manson, Phys. Rev. A 64 (2002) 062707.

[24] A.S. Baltenkov, V.K. Dolmatov, S.T. Manson, Surface Review and Letters 9 (2002) 1143.

[25] A.S. Baltenkov, V.K. Dolmatov, S.T. Manson, Phys. Rev. A 66 (2002) 023202.

[26] A.S. Baltenkov, V.K. Dolmatov, S.T. Manson, A.Z. Msezane, V.A. Pikhut, Phys. Rev. A 68 (2003) 043202.

[27] V.K. Dolmatov, J.P. Connerade, A.P. Lakshmi, S.T. Manson, Surface Review and Letters 9 (2002) 39.

[28] V.K. Dolmatov, S.T. Manson, Phys. Rev. A 73 (2006) 013201.

[29] H.R. Varma, P.C. Deshmukh, S.T. Manson, V.K. Dolmatov, Phys. Rev. A 76 (2007) 012711.

[30] H.R. Varma, T. Banerjee, S. Sunilkumar, P.C. Deshmukh, S.T. Manson, V.K. Dolmatov, J. Phys.: Conf. Series 80 (2007) 012025.

[31] P. Brewer, Photoionization of atoms confined inside fullerenes and fullerene onions, Report on Student Research Work, 2008, University of North Alabama (unpublished).

[32] V.K. Dolmatov, P. Brewer, S.T. Manson, Phys. Rev. A 78 (2008) 013415.
[33] V.K. Dolmatov, S.T. Manson, J. Phys. B 41 (2008) 165001.
[34] A.S. Baltenkov, J. Phys. B 32 (1999) 2745.
[35] M.Ya. Amusia, A.S. Baltenkov, U. Becker, Phys. Rev. A 62 (2000) 012701.
[36] M.Ya. Amusia, A.S. Baltenkov, V.K. Dolmatov, S.T. Manson, A.Z. Msezane, Phys. Rev. A 70 (2004) 023201.
[37] M.Ya. Amusia, A.S. Baltenkov, L.V. Chernysheva, Z. Felfi, A.Z. Msezane, J. Phys. B 38 (2005) L169.
[38] M.Ya. Amusia, A.S. Baltenkov, Phys. Rev. A 73 (2006) 062723.
[39] M.Ya. Amusia, A.S. Baltenkov, Phys. Lett. A 360 (2006) 294.
[40] M.Ya. Amusia, A.S. Baltenkov, L.V. Chernysheva, JETP Lett. 87 (2008) 230.
[41] M.Ya. Amusia, A.S. Baltenkov, L.V. Chernysheva, Cent. Eur. J. Phys. 6 (2008) 14.
[42] A. Lyras, H. Bachau, J. Phys. B 38 (2005) 1119.
[43] J.P. Connerade, A.V. Solov'yov, J. Phys. B 38 (2005) 807.
[44] S. Lo, A.V. Korol, A.V. Solov'yov, J. Phys. B 40 (2007) 3973.
[45] M.E. Madjet, H.S. Chakraborty, S.T. Manson, Phys. Rev. Lett. 99 (2007) 243003.
[46] H.S. Chakraborty, M.E. Madjet, J.M. Rost, S.T. Manson, Phys. Rev. A 78 (2008) 013201.
[47] Y.B. Xu, M.Q. Tan, U. Becker, Phys. Rev. Lett. 76 (1996) 3538.
[48] M. Saunders, H.A. Jimenez-Vasques, R.J. Cross, R.J. Poreda, Science 259 (1993) 1428.
[49] T. Almeida murphy, T. Pawlik, A. Weidinger, M. Höhne, R. Alcala, J.M. Spaeth, Phys. Rev. Lett. 77 (1996) 1075.
[50] L.S. Wang, J.M. Alford, Y. Chai, M. Diener, R.E. Smalley, Z. Phys. D 26 (1993) S297.
[51] J.M. Cabrera-Trujillo, J.A. Alonso, M.P. Iñiguez, M.J. López, A. Rubio, Phys. Rev. B 53 (1996) 16059.
[52] O. Hemmers, R. Guillemin, D.W. Lindle, Radiat. Phys. Chem. 70 (2004) 123.
[53] V.K. Dolmatov, S.T. Manson, Phys. Rev. Lett. 83 (1999) 939.
[54] J.W. Cooper, Phys. Rev. A 47 (1993) 1841. Note that in Table XII the coefficient $A_{l+1,l-2}$ has the incorrect sign.
[55] M.Ya. Amusia, Atomic Photoeffect, Plenum, New York, 1990.
[56] W.R. Johnson, C.D. Lin, Phys. Rev. A 20 (1979) 964.
[57] S.W.J. Scully, E.D. Emmons, M.F. Gharaibeh, R.A. Phaneuf, A.L.D. Kilcoyne, A.S. Schlachter, S. Schippers, A. Müller, H.S. Chakraborty, M.E. Madjet, J.M. Rost, Phys. Rev. Lett. 94 (2005) 065503.
[58] C.F. Bohren, D.R. Huffman, Absorption and Scattering of Light by Small Particles, Wiley, New York, 1998, pp. 148–150 and 251–257.
[59] D. Östing, P. Apell, A. Rosén, Z. Phys. D 26 (1993) 1794.
[60] I.V. Hartel, H. Steger, J.de. Vries, C. Menzel, B. Kamke, W. Kamke, Phys. Rev. Lett. 68 (1992) 784.
[61] J. Berkowitz, J. Chem. Phys. 111 (1999) 1446.
[62] O. Hemmers, H. Wang, P. Focke, I.A. Sellin, D.W. Lindle, J.C. Arce, J.A. Sheehy, P.W. Langhoff, Phys. Rev. Lett. 87 (2001) 273003.
[63] S.T. Manson, in: A. Dalgarno, R.S. Freund, P.M. Koch, M.S. Lubell, T.B. Lucatorto (Eds.), The Physics of Electronic and Atomic Collisions, American Institute of Physics, New York, 1990, p. 189.
[64] V.K. Dolmatov, present work.
[65] J.P. Connerade, R. Semauone, J. Phys. B 33 (2000) 869.
[66] S.T. Manson, C.J. Lee, R.H. Pratt, I.B. Goldberg, B.R. Tambe, A. Ron, Phys. Rev. A 28 (1983) 2885.
[67] J.P. Connerade, Phys. Scripta 68 (2003) C25.

CHAPTER 3

DFT Study of Molecules Confined Inside Fullerene and Fullerene-like Cages

O.P. Charkin[a], **N.M. Klimenko**[b] and **D.O. Charkin**[c]

Contents

[a] Institute of Problems of Chemical Physics, Russian Academy of Sciences, Institutskii pr. 18, Chernogolovka, Moscow oblast, 142432 Russia

[b] Lomonosov State Academy of Fine Chemical Technology, pr. Vernadskogo 86, Moscow, 117571 Russia

[c] Chemical Department, Moscow State University, Vorob'evy gory, Moscow, 119992 Russia

E-mail addresses: charkin@icp.ac.ru (O.P. Charkin), nmklimenko@mitht.ru (N.M. Klimenko), charkin@inorg.chem.msu.ru (D.O. Charkin).

Advances in Quantum Chemistry, Vol. 58
ISSN: 0065-3276, DOI: 10.1016/S0065-3276(09)00707-2

1. INTRODUCTION

In recent years, the search has continued for new endohedral endoclusters with atoms and molecules encapsulated in carbon (or fullerene-like inorganic and hybrid) cages of different sizes and shapes, which are promising for different areas of engineering [1–7]. One of the important issues here is how the interaction between the host cage and the inserted guest molecule is displayed in the structural, energetic, and spectroscopic properties of the endocluster as compared to those for the isolated guest molecule and the empty cage. In a general case, insertion of a molecule L into a cage C_n can lead to geometric contraction and deformation of the guest, expansion and deformation of the cage, changes in their mutual polarization, and redistribution of electron density. An overwhelming majority of studies have been focused on endohedral metallofullerenes in which a strong transfer of electrons takes place from the atoms of an electropositive metal, which is characterized by a low ionization potential (*IP*), to a C_n carbon cage, which has a high electron affinity (*EA*). To date, more than a hundred endofullerenes encapsulating one or several atoms of lanthanides and electropositive metals, as well as more complicated metal-containing molecules, such as nitrides $Sc_iLn_{3-i}N@C_{80}$, $Sc_3N@C_{68}$, and $Sc_3N@C_{78}$, acetylide $Sc_2C_2@C_{84}$, and others, have been synthesized and experimentally studied (see, e.g., the reviews of experimental and theoretical work [6,7] and references therein).

Endohedral fullerenes with encapsulated covalent molecules and ions that do not contain electropositive metals have received considerably less attention. In such systems, electron transfer between the guest and the cage is significantly less pronounced and the interaction is determined by the steric match between the guest and cavity shapes and sizes, and by the interplay of the noncovalent attraction and repulsion of their filled electron shells. Experimental studies of similar endoclusters face serious problems at all three stages, i.e., opening of the fullerene cages, introducing covalent guests into them, and, finally, closing the cages (it is evident that arc discharge, laser evaporation, ion implantation, and other extreme methods used in the synthesis of metallofullerenes are inefficient in this case). Endofullerenes with one ($Ng@C_{60}$ with Ng = He, Ne, Ar, Kr, Xe) [8–10] or two ($Ng_2@C_{60}$, Ng = He [11] and Ne [12]) encapsulated atoms of light noble gases, as well as a series of hydrogenated fullerenes of the $He@C_{60}H_{36}$ type [13], have been experimentally obtained (at high temperatures and pressures) and fairly well studied. Interest in these fullerenes stems from the fact that the ^{3}He NMR of the encapsulated helium atom, in combination with ab initio calculations, turned out to be an efficient method for studying the isomerism, internal magnetic field, aromaticity, and chemical behavior [14, 15]. Clusters $Ng@C_n$ and $Ng@C_nH_m$ with one noble gas atom (usually, helium) have been studied in numerous theoretical works [16–21], mainly dealing with the structure and aromaticity of different carbon cages. Ab initio calculations of the $Ng@C_{60}$ [15–20], $He_n@C_{60}$ ($n = 1$–4), and $Ne_n@C_{60}$ ($n = 1, 2$) [21] series showed that the introduction of one *Ng* atom or even several light He and Ne atoms has little effect on the properties of the "very rigid" (toward to radial expansion) C_{60} cage, which is spacious for these *Ng* atoms. Conversely, upon the introduction of *Ng* into tighter cages, the steric effect can be significant. For example, ab initio calculations of model endoclusters $Ng@M_{12}H_{12}^{2-}$ (Ng = He, Ne, Ar, and Kr; M = Al and Ga) [22,23] show that the introduction of the Ar or Kr atom into the *closo*-alane or *closo*-gallane anions, whose radii are ~1.0 Å smaller than the radius of C_{60}, leads to significant inflation of the "soft" [Al_{12}] and [Ga_{12}] cages, long-wavelength ("red") shifts of the *M*–H and *M*–*M* stretching vibration frequencies, a sharp increase in the magnetic shielding constants on the metal atoms $\sigma(M)$, and a decrease in σ(H) for the H atoms as compared to the corresponding values of these properties of isolated (empty) dianions. These changes can be, in principle, experimentally monitored by IR and Raman spectroscopy and NMR.

Recently [24,25], a mild method was suggested for obtaining open-cage bowl-shaped bistriazoline and bislactam fullerene C_{60} derivatives with an orifice through which an Li^+ ion, an He atom, or a hydrogen molecule were inserted into the cage with high yield (100% for H_2). In [25], it was shown that the ^{1}H NMR signal of the H_2 molecule encapsulated into a bowl-shaped fullerene experiences a considerable upfield shift (by 7.2 ppm) due to the shielding effect of the cage. In [26], the rate constant of He escape from open-cage endofullerenes synthesized by Rubins's group (ROCF) [24] and Komatsu's group (KOCF) [25] was measured and the activation barriers to He escape from ROCF (24.6 kcal/mol) and to He and H_2 escape from KOCF (22.8 and 34.3 kcal/mol, respectively) were estimated. In [27], the opening of fullerenes was considered based on the Woodward–Hoffmann rules. Morokuma and coworkers [28] studied, using the ONIOM approximation, the mechanism of insertion of the Li^+ cation through the orifice of the hexahydro, hexamethyl, bistriazoline, and bislactam derivatives of fullerene C_{60} and found that the barrier is very high (~45–60 kcal/mol) for the first two derivatives and decreases to ~20 kcal/mol or more for the last two compounds. In [29], a derivative containing a 20-membered ring orifice in the C_{60} cage was synthesized, and a conclusion was drawn, based on NMR spectra, that this compound encapsulated one water molecule. There is a hope that bulkier guests, such as ammonia, methane, and others, may also be introduced into open fullerene cages (presumably, more spacious than the C_{60} and C_{70}). At the same time, the problems of the opening of large cages, the removal of the bistriazoline or similar "collar", and closure of the orifices to recover the initial closed cage containing the encapsulated guest, still remain to be experimentally solved.

One hopes that first principles calculations that compare the properties of the endoclusters with the properties of the isolated guest and cage molecules can be useful in solving the problem of the guest-cage interaction and its influence on the structural, energetic, and spectroscopic properties of endofullerenes. This paper is focused on DFT studies of the potential energy surfaces (PESs) of several families of model (as yet unsynthesized) endofullerenes in which the guest is a small- or middle-size molecule or atomic cluster with a high *IP* and a large gap between the HOMO and LUMO, and in which the interaction is mainly determined by the steric match between the guest and cavity shapes and sizes, and by the interplay of the noncovalent attraction and repulsion of their filled electron shells. The following endocluster families are considered: (1) with the encapsulated methane molecule and isoelectronic tetrahedral hydrides $MH_4^{0,\pm}$ with 10 valence electrons (M = B, C, N, Al, Si, P) [30,31], as well as with tetrahedral Ng_4 "clusters" (Ng = He, Ne, Ar, Kr, Xe) [32] inside the tetragonal $C_{60}H_{36}(T)$, $C_{60}H_{24}(T)$, and $C_{84}(T_d)$ cages; (2) with linear triatomic (CO_2, CS_2, BeF_2, SiO_2) and tetratomic (acetylene, HBNH) molecules inside the prolate rugby-shaped $C_{70}(D_{5h})$ cage [33]; (3) with planar benzene C_6H_6, borazole $B_3N_3H_6$, and C_6O_6 molecules inside the oblate spheroidal $C_{84}(D_{6h})$ cage [34]; (4) with the onion-like icosahedral doped aluminide clusters $L@Al_{12}$ inside dodecahedral metal-polyoxide cages like $Al_{20}O_{30}$ and $V_{20}O_{50}$ [35]; (5) with atoms and atomic ions L inside the "supertight" icosahedral $[He_{12}]$ box with very short fixed radius R (LHe), etc. Some of these results have been partially reviewed in [36]. Earlier, in [37,38] "moderately spacious" endohedral complexes containing diatomic molecules were calculated at the Hartree-Fock level, and it was found that the bond length of the guest slightly decreased, and the stretching frequency slightly increased, due to confinement. The "moderately tight" cluster $CH_4@C_{60}$ [39,40] and the highly endothermic clusters $ScH_{15}@C_{60}$, $ZrH_{16}@C_{60}$ and $2TiH_{16}@C_{114}$ were also calculated recently [41]. In the present paper we expand the analysis made in [30–36] and include our results for new types of "tight" and "very tight" endoclusters. As in [30–36], our aim is to examine relative changes in the structure, energy, normal frequencies, magnetic shielding constants, and other properties of the endoclusters as compared with the corresponding properties of free guests and empty cages, and to reveal the trends in these properties as a function of the shape and size of the guest and cage, external charge, and other characteristics of endoclusters. The results for clusters with inserted organic molecules are discussed first and those for the related clusters with inorganic guests are considered next. Noble gas atoms are indicated by symbol Ng.

2. COMPUTATIONAL DETAILS

In this paper, we consider results of calculations performed in the framework of the hybrid Becke–Lee–Yang–Parr density functional method (B3LYP)

[42,43], which is thought at the moment to be one of the most adequate approximations for fullerenes. Geometry optimization and calculations of vibrational frequencies of endoclusters and isolated (free) guest molecule and empty cages were firstly carried out at the B3LYP/6-31G level, then their geometries were reoptimized within the B3LYP/6-31G* approximation. Energetic characteristics were calculated at the B3LYP/6-31G*//B3LYP/6-31G* + ZPE(B3LYP/6-31G level and magnetic shielding constants on atoms σ (within the GIAO method [44,45]) at the B3LYP/6-31G*//B3LYP/6-31G* level. The influence of the calculation level used on the accuracy of computed characteristics was considered in detail in [30–34]. Here we restrict ourselves to several typical examples.

It was demonstrated in [36] that the geometrical parameters of the $C_{60}F_{18}$ and $C_{60}F_{48}$ molecules optimized at the B3LYP/6-31G* level reproduce the corresponding X-ray diffraction data [46,47] within the error 0.01–0.02 Å. The vibrational frequencies ν_i of the C_{60} and C_{70} molecules and fluorofullerenes $C_{60}F_{20}$ calculated at the B3LYP/6-31G level, with the use of the scaling factor $k = 0.971$, reproduce the experimental values [48–50] to within 10–30 cm^{-1}. Our B3LYP/6-31G* calculations [31,36], within the GIAO approach, more or less systematically underestimate the experimental NMR chemical shifts δ_i [51] of the T and C_3 isomers of $C_{60}H_{36}$ by 2–3 ppm for the C atoms and by 0.2–0.3 ppm for the hydrogen atoms; the sequences of the chemical shifts for atoms of different symmetry types are reproduced correctly. The calculated chemical shift $\delta(\text{He}) = -8.7$ ppm (relative to $\sigma(\text{He})$ of the free He atom) in the He@$C_{60}H_{36}$ (T) cluster [31] exceeds the experimental values -7.7 [12] by only $\sim$1 ppm. The calculated chemical shift $\delta(\text{Xe}) = 186.3$ ppm (relative to $\sigma(\text{Xe})$ of the free Xe atom) in the Xe@C_{60} (I_h) cluster [36] is in reasonable agreement with the experimental value 179.2 ppm [10]. The calculated vertical ionization potential (*VIP*) and vertical electron affinity (*VEA*) of the C_{60} molecule (7.24 and 1.96 eV, respectively) [31] underestimate experimental values by $\sim$0.3 and -0.7 eV; however, both errors decrease to $\sim$0.2 eV when the basis set is augmented with diffuse functions (6-31+G*) [31,36]. As a rule, B3LYP calculations with the 6-31G and 6-31G* basis sets adequately describe the experimental geometries, vibrational frequencies, σ constants, and some other fullerene properties. The accuracy of the estimates for the dissociation energy E_{diss} of the endofullerenes under consideration into separate guest and cage molecules remains the most challenging problem. Since relevant experimental data are almost completely absent, the only possible sources of information on E_{diss} for these complex objects are density functional theory (DFT) and second-order Møller–Plesset perturbation theory (MP2) calculations, inasmuch as higher level methods of the coupled cluster (CCSD(T)) type are inapplicable in this case. It was stated in [51] that, for systems with noncovalent interactions (presumably including the endofullerenes under consideration), B3LYP calculations can underestimate the bonding component and, hence, the guest–cage bonding energies and introduce some errors into librational (rotational) and translational frequencies of guest vibrations inside the cage. Our calculations of endoclusters $MH_4@C_{60}H_n, MX_2@C_{70}$, $C_2H_2@C_{70}$ and others performed in parallel at different levels show that – among the DFT variants – B3LYP/6-31G* calculations give the most reasonable results; however, systematically underestimating E_{diss} as compared with the MP2 results. Differences between estimates of E_{diss} obtained by the B3LYP, MP2, and the modified MPWB95 methods with the 6-31G* basis set (this MPWB95 approximation was assumed to better consider noncovalent interactions [51]) can vary from several to ten kcal/mol or sometimes even more; and in cases of small E_{diss} values, the different methods can produce different signs. Surely, for "tight" and "very tight" endofullerenes with bulky guests all approximations are equivocal in prediction of negative values of E_{diss} (high endothermicity). The situation is less clear for spacious and moderately tight fullerenes with small guests, for which B3LYP gives small negative, and MP2 small positive, E_{diss} values, while MPWB95 predicts even higher exothermicity than MP2. For such cases, none of the methods used can pretend to the quantitative accuracy of calculations of absolute E_{diss} values, and their consideration at the moment seems be mostly of a semiquantitative or even qualitative nature.

The present paper is mainly devoted to the tight endothermic model endoclusters with a predominating repulsive interaction between a guest molecule and a cage, where the aforementioned deficiency of the DFT approximation (neglecting of the attractive noncovalent interactions) is less significant as compared with that for low-exothermic systems. Use of the more consistent MP2 approximation, in most of our cases, was not feasible due to the large size of the clusters and limited capacities of our computers. As earlier [30–36], we focused not on absolute values, but rather on the relative changes ("shifts" Δ) of the calculated molecular properties of endoclusters as compared to the properties of free guest molecules and pristine fullerenes or fullerene-like inorganic cages, in the hope that relative shifts still keep a high degree of accuracy. Most interesting are the geometry deformation and electronic polarization of a guest molecule, as well as shifts in its vibrational and magnetic properties. The corresponding changes in cages are also briefly discussed, specifically in charged clusters in which a mutual polarization and electron density redistribution between the guest and the cage, inside the guest, and inside the cage are important.

Noteworthy is a series of works (see [52,53] and references therein) in which the geometry of endofullerenes $MH_n@C_{60}$ and $Hal_2@C_{70}$ was optimized in the framework of the semiempirical PM3 and AM1 methods; however, in our opinion, the energy characteristics calculated therein should be treated with caution. For example, the negative E_{diss} energy for $AlH_3@C_{60}$ (248 kcal/mol) deduced from data in [52] turns out to be four times lower than that obtained by B3LYP calculations (56 kcal/mol, our data).

Calculations show that the optimized structures of all endoclusters surveyed in this paper correspond to local minima of the PES (all vibration frequencies are real) and are energetically more favorable than other guest-to-cage orientations. For these structures, calculations predict considerable shifts of stretching frequencies and magnetic shielding constants. Thus, these systems seem to be suitable models to monitor manifestations of the guest–cage interactions in various series of related endoclusters as well as for calibration of approximate physical models describing atoms and molecules under confined conditions.

3. TETRAHEDRAL GUESTS INSIDE TETRAGONAL CAGES

3.1. CH_4 and He_4 moieties inside the moderately tight $C_{60}H_{36}(T)$, $C_{60}H_{24}(T)$ and the spacious $C_{84}(T_d)$ Cages

Our calculations show that the endofullerenes $CH_4@C_{60}H_{36}$ and $He_4@C_{60}H_{36}$ have similar properties. For both systems, the structure of symmetry T, in which the C–H bonds or the o–He lines (o is the center of the He_4 tetrahedron) are directed toward the centers of the hydrogenated faces [C_6H_6], corresponds to a PES minimum and to the most favorable orientation of the guest in the cage (Figure 1).

The shape of the carbon cage in $C_{60}H_{36}$ (T) can be approximated by two radii, the short (inner) radius R_1 and the long (outer) radius R_2, which connect the center of the cage with the carbon atoms of the non-hydrogenated [C_6] and hydrogenated [C_6H_6] rings, respectively. The inner radius R_1 is ~0.34 Å shorter and the outer radius R_2 is ~0.47 Å longer than the radius of bare fullerene C_{60} (~3.55 Å).

Encapsulation of CH_4 and He_4 slightly deforms the cage in the same manner although the four He atoms fill the cage slightly more tightly than CH_4. The lengths of the outer C–H bonds remain unaltered, the C–C bonds are elongated by only a few thousandths of an angstrom. The cage deformation energy $E_{\mathrm{def}}(C_{60}H_{36})$, electron-density redistribution between guest and cage and the shifts of the stretching frequencies of the cage are minor.

Contrary to the weak cage response, the guests properties experience considerable changes. In the encapsulated CH_4 molecule, the C–H bonds are 0.014 Å shorter than in the free molecule (Table 1). This entails a considerable increase in the C–H stretching frequencies a and t (by ~140–150 cm^{-1}) and a small increase in the deformation frequencies e and t (by ~10–12 cm^{-1}) (Table 2). For the stretching frequencies, similar shift values (138 cm^{-1} for symmetrical and 152 cm^{-1} for antisymmetrical modes) were calculated for the $CH_4@C_{60}$ cluster in Ref. [39] within the MP2 approximation.

Among the vibrational frequencies of the $He_4@C_{60}H_{36}$ cluster, the normal modes $e \sim 380\ cm^{-1}$, $t \sim 416\ cm^{-1}$, and $a \sim 479\ cm^{-1}$ appear to be mainly contributed by displacements of the He atoms (see Table 7). These modes

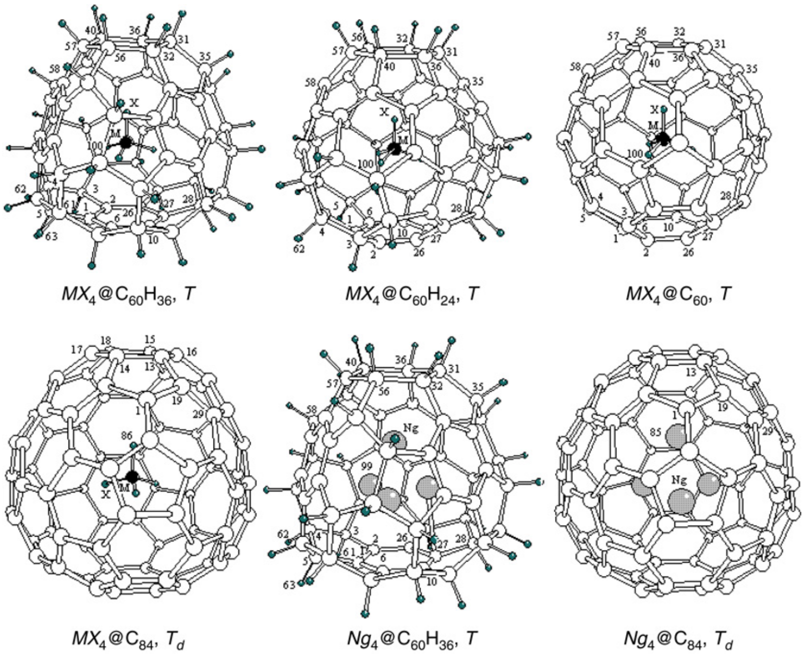

$MX_4@C_{60}H_{36}$, T $MX_4@C_{60}H_{24}$, T $MX_4@C_{60}$, T

$MX_4@C_{84}$, T_d $Ng_4@C_{60}H_{36}$, T $Ng_4@C_{84}$, T_d

Figure 1 The structures of endohedral fullerenes with encapsulated tetrahedral $MX_4^{0,\pm}$ molecules and ions, and Ng_4 clusters.

can be assigned to the vibrations of the “artificial” (or “forced”) He_4 cluster formed inside the cage due to the repulsion of the He atoms from the cage walls. Similar artificial clusters can oscillate and rotate as a structural unit inside the cage, much like chemically bound molecules, such as P_4. The interplay of two competing repulsive interactions of the compressed He atoms with one another and with the cage atoms leads to the fact that the force constants calculated for the e and a modes of the He_4 cluster are considerable ($\sim$0.40–0.55 mdyn/Å) and are only 2–2.5 times lower than the corresponding force constants for the isolated P_4 molecule. The frequencies of weak translational (ν_{tr}) and librational (ν_{libr}) vibrations of the guest inside the cage fall within an extremely long-wavelength spectral range. In $CH_4@C_{60}H_{36}$, both modes are strongly coupled to the nonrigid deformation vibrations of the carbon skeleton (Table 2). In $He_4@C_{60}H_{36}$ (see Table 7), they are also coupled to each other. The magnetic shielding constants σ of the endohedral C, H, and He atoms increase by 5.4–7.0 ppm compared to their values for the free CH_4 molecule (Table 3) and He atom (see Table 8), which is caused by an additional shielding due to the ring currents in benzenoid rings [C_6]. The clusters with one and four He atoms inside the $C_{60}H_{36}$ cage have close σ (He) constants. The approximate localization of transition states indicates that the

Table 1 Optimized geometric parameters of free $C_{60}H_{36}$ (T) and $C_{60}H_{24}$ (T) molecules and their MH_4 endohedral clusters (B3LYP/6-31G*) [30,31]

Cage		$MH_4@C_{60}H_{36}(T)$							$CH_4@C_{60}H_{24}(T)$	
Parameter	Face	–	BH_4^-	CH_4	NH_4^+	AlH_4^-	SiH_4	PH_4^+	–	CH_4
$R(MH)$[a]	–	–	1.210	1.079	1.020	1.575	1.448	1.386	–	1.086
$R(CH)$	–	1.100	1.102	1.100	1.098	1.103	1.100	1.098	1.095	1.096
$R(H_{100}C_1)$	$[C_6]$	–	2.832	2.825	2.787	2.810	2.800	2.772	–	3.024
$R(H_{100}C_2)$	$[C_6]$	–	2.600	2.619	2.588	2.503	2.523	2.507	–	2.865
$R(H_{100}C_3)$	$[C_6H_6]$	–	2.813	2.930	2.985	2.522	2.627	2.694	–	2.934
$R(H_{100}C_4)$	$[C_6H_6]$	–	2.921	3.050	3.112	2.618	2.732	2.811	–	2.932
$R(H_{100}C_5)$	–	–	3.189	3.257	3.292	3.044	3.096	3.123	–	2.909
$R(C_1C_2)$	$[C_6]$	1.387	1.391	1.391	1.391	1.396	1.395	1.394	1.402	1.403
$R(C_1C_6)$	$[C_6]$	1.377	1.378	1.380	1.382	1.380	1.381	1.383	1.398	1.399
$R(C_{31}C_{32})$	$[C_6H_6]$	1.593	1.592	1.595	1.596	1.593	1.595	1.597	1.591	1.592
$R(C_{31}C_{36})$	$[C_6H_6]$	1.567	1.572	1.571	1.571	1.571	1.573	1.574	1.585	1.586
R_1[b]	$[C_6]$	3.207	3.304	3.267	3.216	3.336	3.312	3.274	3.485	3.494
R_2[b]	$[C_6H_6]$	4.024	3.991	4.010	4.032	3.983	3.998	4.016	3.890	3.891
ϕ_1[b]	$[C_6]$	168.5	165.3	166.6	168.4	164.4	165.0	166.4	158.5	158.3
ϕ_2[b]	$[C_6H_6]$	120.9	124.3	122.9	120.9	125.2	124.4	123.0	129.0	129.2
θ_1[b]	$[C_6]$	2.2	2.0	1.6	2.1	1.1	1.3	1.3	3.5	3.7
θ_2[b]	$[C_6H_6]$	−17.2	−14.3	−15.4	−17.1	−13.5	−14.1	−15.3	0.0	0.2

[a] In the isolated molecules and $MH_4^\pm$ ions, the $R(M\text{–}H)$ distance calculated at the same B3LYP/6-31G* level is (in Å) 1.241 (BH_4^-), 1.093 (CH_4), 1.029 (NH_4^+), 1.648 (AlH_4^-), 1.486 (SiH_4), and 1.400 (PH_4^+).

[b] The numbering of atoms is shown in Figure 1. The nonplanar $[C_6]$ and $[C_6H_6]$ rings have a chair conformation and are characterized by pairs of distances between the face atoms and the cage center – R_1, R_1' and R_2, R_2' – and by pairs of angles ϕ, ϕ' and θ, θ'. In the benzoid rings, the difference $R_1 - R_1'$ is small; for the hydrogenated faces, the difference $R_2 - R_2'$ is no more than 0.12 Å for $C_{60}H_{36}$ and decreases to 0.03 Å for $C_{60}H_{24}$. For the sake of simplicity, we restrict our consideration to the distances R_1 and R_2 from the center to the most distant atoms of the $[C_6]$ and $[C_6H_6]$ rings, as well as to those of the ϕ_1, ϕ_2 and θ_1, θ_2 angles that undergo the largest changes upon encapsulation of the guest. For $C_{60}H_{36}$, $R_1 = R(MC_1)$ and $R_2 = R(MC_{31})$; for $C_{60}H_{24}$, $R_1 = R(MC_2)$ and $R_2 = R(MC_{32})$; for both cages, $\phi_1 = (C_{28}\text{–}C_{27}\text{–}C_1)$, $\phi_2 = (C_{58}\text{–}C_{57}\text{–}C_{31})$, $\theta_1 = (C_1\text{–}C_6\text{–}C_{10}\text{–}C_{27})$, and $\theta_2 = (C_{31}\text{–}C_{36}\text{–}C_{40}\text{–}C_{57})$.

Table 2 Vibrational frequencies $\nu_i\,(\mathrm{cm}^{-1})$ and IR intensities (km/mol, in parentheses) of the $C_{60}H_{36}$ (T) and $C_{60}H_{36}$ (T) cages and their MH_4 endoclusters[a]

Symmetry	MH_4@$C_{60}H_{36}(T)$							CH_4@$C_{60}H_{24}(T)$	
	–	BH_4^-	CH_4	NH_4^+	AlH_4^-	SiH_4	PH_4^+	–	CH_4
Guest modes $\nu(MH_4)$[b]									
t_{def}	–	1193(24)	1415(21)	1539(195)	939(196)	962(34)	895(6)	–	1408(1)
e_{def}	–	1277	1613	1711	910	1026	1032	–	1607
A_{str}	–	2476	3186	3463	2039	2401	2607	–	3144
T_{str}	–	2491(183)	3321(7)	3575(27)–	1984(230)	2432(39)	2679(3)	–	3250(3)
Highest ν_{str}(CH) frequencies of outer C–H bond vibrations									
A	3075	3040	3074	3101	3035	3073	3100	3065	3065
T	3073(380)	3035(678)	3071(377)	3100(187)	3030(754)	3070(378)	3099(180)	3064(219)	3065(221)
T	3066(59)	3025(105)	3063(60)	3094(30)	3019(114)	3061(62)	3092(30)	3049(39)	3049(39)
A	3016	2927	3013	3047	2976	3012	3043	3008	3009
T	3014(126)	2924(82)	3012(120)	3046(56)	2951(20)	3011(106)	3042(55)	3008(2)	3009(1)
Highest [C60] cage modes ν_{str}(CC)									
T	1720(1.0)	1709(2)	1705(0.9)	1702(1)	1694(3)	1693(2)	1690(1)	1697(0.7)	1694(0.5)
T	1527(20)	1514(18)	1514(20)	1514(14)	1498(18)	1499(20)	1499(20)	1450(20.0)	1445(19.9)
A	1509	1491	1492	1494	1477	1478	1479	1443	1436

(*continued on next page*)

Table 2 (continued)

Symmetry	$MH_4@C_{60}H_{36}(T)$							$CH_4@C_{60}H_{24}(T)$	
	–	BH_4^-	CH_4	NH_4^+	AlH_4^-	SiH_4	PH_4^+	–	CH_4
Lowest [C60] cage modes $\nu_{def}(CC)$									
T	166(0.6)	$168(6)^t$	$166(0.5)^t$	$165(0)^t$	180(4)	$161(0)^{t,l}$	$140(2)^t$	206(0.2)	$219(0.1)^{t,l}$
E	214	225	226	223	228	228	226	238	243
A	221	264	256	239	281	277	265	305	321
T	260(0)	$273(0)^l$	255^l	$278(0)^l$	$279(0)^l$	$268(0)^l$	$308(0)^l$	305(0.1)	$314(0.1)^l$
E	312	321	319	314	323	323	320	352	353
T	312(0)	$318(1)^l$	$314(0.0)^l$	$315(0)^l$	$319(0)^l$	$317(0)^l$	$327(0)^l$	339(0)	341(0)
T	329(1.6)	$368(1)^t$	$362(2.8)^t$	$346(3)^t$	$369(10)^t$	$372(7)^t$	$364(4)^t$	350(0.4)	353(0.3)
Translational ν_{tr} and librational ν_{libr} modes of the guest									
t_{tr}	–	307(20)	269(0.0)	230(17)	264(0)	264(0)	250(8)	–	181(0.1)
t_{libr}	–	494(0)	342(0.0)	279i	642	497(0.1)	221i	–	242(0.1)

[a] The superscript indices t and l mean a considerable admixture of, respectively, translational and librational (rotational) vibrations of the guest.

[b] For isolated molecules and ions, the frequencies calculated at the same approximation are:BH_4^-: t_{def} = 1126(44), e_{def} = 1240, a_{str} = 2280 and t_{str} = 2282(528) cm^{-1}; CH_4: t_{def} = 1404(25), e_{def} = 1602, a_{str} = 3047 and t_{str} = 3170(31) cm^{-1}; NH_4^+: t_{def} = 1522(188), e_{def} = 1753, a_{str} = 3363 and t_{str} = 3484(199) cm^{-1}; AlH_4^-: t_{def} = 753(417), e_{def} = 746, a_{str} = 1681 and t_{str} = 1625(524) cm^{-1}; SiH_4: t_{def} = 869(120), e_{def} = 959, a_{str} = 2163 and t_{str} = 2190(161) cm^{-1}; PH_4^+: t_{def} = 946(0), e_{def} = 1126, a_{str} = 2444 and t_{str} = 2509(17) cm^{-1}.

Table 3 Mulliken effective charges $Z(e)$ and magnetic shielding constants σ (ppm) of the atoms in the $C_{60}H_{36}$ and $C_{60}H_{24}$ molecules and their MH_4 endofullerenes[a]

Atom	Face	$MH_4@C_{60}H_{36}(T)$														$CH_4@C_{60}H_{24}(T)$			
		–		BH_4^-		CH_4		NH_4^+		AlH_4^-		SiH_4		PH_4^+		–		CH_4	
		Z	σ	Z	σ	Z	σ	Z	σ	Z	σ	Z	σ	Z	σ	Z	σ	Z	σ
M		–	–	+0.05	148.9	−0.54	198.4	−0.83	260.4	+1.15	458.5	+0.93	446.7	+0.61	466.8	–	–	−0.56	194.6
H		–	–	−0.21	37.8	+0.13	38.7	+0.41	34.5	−0.41	33.1	−0.22	33.6	+0.04	31.2	–	–	+0.14	39.9
C_1	$[C_6]$	+0.05	60.9	+0.07	58.4	+0.06	58.1	+0.04	57.6	+0.04	58.5	+0.04	56.7	+0.04	55.3	+0.02	55.4	+0.02	54.3
C_2		+0.06	57.7	+0.07	52.4	+0.04	55.2	+0.00	56.6	+0.05	48.8	+0.03	51.7	+0.00	53.5	+0.02	50.3	+0.03	49.4
C_3	$[C_6H_6]$	−0.18	154.2	−0.17	150.9	−0.18	153.5	−0.19	155.7	−0.16	149.5	−0.18	152.0	−0.19	154.4	−0.17	148.2	−0.17	148.5
C_4		−0.10	137.5	−0.08	139.1	−0.11	139.4	−0.12	138.3	−0.08	139.1	−0.12	140.6	−0.13	140.5	−0.18	147.0	−0.17	146.9
C_5		−0.18	143.6	−0.17	143.2	−0.18	144.1	−0.18	144.4	−0.16	143.5	−0.17	144.6	−0.18	145.0	+0.01	57.3	+0.004	57.3
H_{61}	$[C_6H_6]$	+0.14	29.0	+0.10	29.0	+0.14	28.9	+0.19	28.7	+0.10	29.0	+0.14	28.8	+0.17	28.6	+0.14	28.7	+0.14	28.7
H_{62}		+0.10	28.6	+0.08	28.7	+0.11	28.5	+0.13	28.3	+0.08	28.8	+0.11	28.5	+0.14	28.2	+0.14	28.7	+0.14	28.7
H_{63}		+0.12	28.6	+0.09	28.7	+0.13	28.5	+0.16	28.3	+0.09	28.7	+0.13	28.5	+0.16	28.3	–	–	–	–

[a] For the isolated molecules and ions, the charges and constants σ (calculations at the same level) are: BH_4^-: $Z(B) = -0.14$ and $Z(H) = -0.22\ e$, $\sigma(B) = 155.2$ and $\sigma(H) = 32.4$ ppm; CH_4: $Z(C) = -0.58$ and $Z(H) = +0.14\ e$, $\sigma(C) = 193.1$ and $\sigma(H) = 31.9$ ppm; NH_4^+: $Z(N) = -0.84$ and $Z(H) = +0.46\ e$, $\sigma(N) = 241.7$ and $\sigma(H) = 27.4$ ppm; AlH_4^-: $Z(Al) = +0.10$ and $Z(H) = -0.28\ e$, $\sigma(Al) = 540.5$ and $\sigma(H) = 29.1$ ppm; SiH_4 :$Z(Si) = +0.39$ and $Z(H) = -0.10\ e$, $\sigma(Si) = 483.1$ and $\sigma(H) = 28.5$ ppm; PH_4^+: $Z(P) = +0.41$ and $Z(H) = +0.15\ e$, $\sigma(P) = 471.4$ and $\sigma(H) = 26.2$ ppm.

rotation of the He_4 cluster inside the $C_{60}H_{36}$ (T) cage should be forbidden, or severely hindered, due to high activation barriers (above 20 kcal/mol). For $CH_4@C_{60}H_{36}$, these barriers are considerably lower so that rotation of the encapsulated methane molecule around the threefold axes seem to be possible at elevated temperatures.

For tetrahedral guests, the $C_{60}H_{24}$ (T) cage is more spacious than $C_{60}H_{36}$ (T). The inner radius of the carbon cage in $C_{60}H_{24}$ (T) is 0.28 Å longer and the outer radius is 0.13 Å shorter than in $C_{60}H_{36}$ (T). Correspondingly, the shifts of cage deformation frequencies decrease, whereas ν_{str} (CH) of the outer C–H bonds, ν_{str}(CC) and constants σ of the $C_{60}H_{24}$ (T) cage are virtually insensitive to the encapsulation of CH_4 and He_4. The short-wavelength ("blue") shifts of the stretching frequencies of methane in $CH_4@C_{60}H_{24}$ decrease by a factor of 1.5–2 compared to $CH_4@C_{60}H_{36}$ (Table 2); however, they remain considerable and can easily be detected by spectroscopic methods. The translational and librational modes of CH_4 and He_4 in the $L@C_{60}H_{24}$ clusters are less coupled to the deformation vibrations of the cage, and their frequencies, ν_{tr} and ν_{libr}, are 80–100 cm^{-1} lower than those for $L@C_{60}H_{36}$. Librations of the methane molecule in the $C_{60}H_{24}$ cage are less hindered than those in the $C_{60}H_{36}$ cage and presumably can transform to quasi-free internal rotation at moderately elevated temperatures. Conversely, inner rotation for $He_4@C_{60}H_{24}$ remains hindered.

The diameter of the tetrahedral $C_{84}(T_d)$ cage (Figure 1) is 1.07 Å larger than that of $C_{60}H_{36}(T)$. Accordingly, the geometric parameters (Table 4), magnetic shielding constants σ(C), and vibrational frequencies of the C_{84} cage in corresponding endofullerenes are virtually unchanged as compared with those of the isolated $C_{84}(T_d)$ molecule. In the spacious cluster $He_4@C_{84}$ (see below Table 9), the distance R(He–He) and the shortest R(He–C) distances are, respectively, ~0.24 and ~0.3–0.5 Å longer than in the tight cluster $He_4@C_{60}H_{36}$, and the constant $\sigma(\mathrm{He}) = 69.5$ ppm for $He_4@C_{84}$ is roughly the same as for the $He@C_{84}(T_d)$ cluster containing one endohedral He atom (Table 8). In the methane cluster $CH_4@C_{84}$, the C–H bonds in the guest are only 0.003 Å shorter than in the free CH_4 molecule. Accordingly, the blue $\Delta\nu_{\mathrm{str}}$ (CH) shifts decrease nearly threefold, but are still 45–50 cm^{-1} (Table 5).

Another significant change is in the intensities of IR active vibrations t of the encapsulated CH_4 molecule.These vibrations for $CH_4@C_{84}$ are an order of magnitude weaker than for $CH_4@C_{60}H_{36}$ due to the contributions of the outer C–H bonds in the latter to the spectral transition probabilities. Therefore, an IR study of the host–guest interaction in hydrogenated endofullerenes should be more informative than in clusters with bare carbon cages.

In $He_4@C_{84}$, the He_4 vibrations with frequencies of ~175–215 cm^{-1} are virtually not coupled to the cage vibrations and are roughly half as large as those in $He_4@C_{60}H_{36}$ (Table 7). The translational and librational frequencies of He_4 inside the C_{84} cage, 90–95 cm^{-1}, are reduced by a factor of

Table 4 Optimized geometric parameters of the free cage $C_{84}(T_d)$ molecule and endohedral clusters $MH_4@C_{84}(T_d)$[a]

Cell		$MH_4@C84(T_d)$				
Parameter	Face	C_{84}	BH_4^-	CH_4	NH_4^+	SiH_4
$R(MX)$	–	–	1.235	1.091	1.028	1.476
$R(X_{86}C_1)$	–	–	3.501	3.578	3.614	3.391
$R(X_{86}C_{13})$	Upper	–	3.258	3.390	3.450	3.045
$R(X_{86}C_{19})$	–	–	3.326	3.421	3.464	3.182
$R(X_{86}C_{29})$	–	–	3.333	3.393	3.417	3.264
$R(C_{47}C_{48})$	Lower	1.461	1.459	1.461	1.462	1.461
$R(C_{47}C_{66})$	Lower	1.468	1.467	1.469	1.469	1.469
$R(C_{13}C_{14})$	Upper	1.458	1.457	1.458	1.458	1.458
$R(C_{13}C_{16})$	Upper	1.380	1.380	1.380	1.380	1.380
R_1	Lower	3.947	3.944	3.950	3.949	3.953
R_2	Upper	4.405	4.402	4.404	4.408	4.404
ϕ_1^c	Lower	159.2	159.2	159.1	159.1	159.0
ϕ_2^c	Upper	143.9	143.9	143.9	143.8	143.9

[a] See Figure 1 and the detailed description of the $MH_4@C_{84}(T_d)$ structure in [30,31]. The upper and lower $[C_6]$ rings are planar, $\theta_1 = \theta_2 = 0$. The distances from all atoms of these faces to the center (o) are the same: $R_1 = R_1' = R(MC_{47})$ and $R_2 = R_2' = R(MC_{13})$. The angles $\phi = \phi'$, $\phi_1 = (C_{58}–C_{66}–C_{79})$, and $\phi_2 = (C_{19}–C_{13}–C_{18})$. The C_{84} structure has four symmetry-unique C atoms: C_1, C_{13}, C_{19}, and C_{29}. The upper ring consists of C_{13}-type atoms, and the lower ring is composed of C_{29}-type atoms.

Table 5 Vibrational frequencies ν_i (cm^{-1}) and their IR intensities (km/mol, in parentheses) of the $MH_4@C_{84}(T_d)$ endoclusters[a]

Symmetry	$MH_4@C_{84}(T_d)$			
	BH_4^-	CH_4	NH_4^+	SiH_4
	Guest modes $\nu(MH_4)$[b]			
t_{2def}	1131(2)	1410(1)	1607(15)	882(5)
e_{def}	1263	1610	1789	966
a_{1str}	2316	3085	3397	2219
t_{2str}	2319(19)	3213(1)	3520(7)	2259(6)
	Translational and librational modes of the guest			
t_{2tr}	100(2)	143(0)	128(2)	103(0)
t_{1libr}	225	181	339[c]	180(0)

[a] B3LYP/6-31G//B3LYP/6-31G calculations [30,31].

[b] The vibrational frequencies for the isolated MH_4 molecules and ions are given in the note to Table 6.

[c] Virtually mixed with the frequency 344 cm^{-1} of the cage.

3–4. Analogously, the frequencies $\nu_{libr} \sim 150$ cm^{-1} and $\nu_{tr} \sim 190$ cm^{-1} of methane in $CH_4@C_{84}$ are lower than those in $CH_4@C_{60}H_{36}$; however, these frequencies remain considerably larger than the frequencies of methane librational and translational vibrations measured in inert gas matrices and hydrate clathrates, where they are 7–10 (free rotation) and 30–60 cm^{-1}, respectively [54]. The estimated barriers to internal rotation of CH_4 and He_4 are reduced to a few kcal/mol, and CH_4 and He_4 librations are assumed to transform to quasi-free rotation at ambient and elevated temperatures, respectively. The magnetic shielding constants σ(C) and σ(H) of the methane atoms and σ(He) of the He atoms in the $L@C_{84}$ clusters are 2.8–3.0 ppm larger than the corresponding values in $L@C_{60}H_{36}$ due to the stronger shielding of the C_{84} cage. In principle, in the case of C_{84} and larger cages, the CH_4 molecule, like the ^{3}He atom [14,15] and H_2 molecule [25], can serve as a internal magnetic and spectroscopic probe for monitoring the behavior of fullerenes in different chemical reactions by spectroscopic methods. The blue shifts of its frequencies ν and the shifts of the shielding constants σ are rather large and, in addition, the ν and σ values of the guest and cages lie in significantly distant (separated) areas of the corresponding spectra.

3.2. Other $MH_4^{0,\pm}$ Hydrides inside the $C_{60}H_{36}(T)$, $C_{60}H_{24}(T)$, and $C_{84}(T_d)$ cages

As follows from Table 1, the character of deformation of the $MH_4@C_{60}H_{36}$ (T) persists when $MH_4^{\pm}$ ions are encapsulated. In going along the isoelectronic series from bulkier anions to more compact cations, the deformation effects are getting weaker. Due to redistribution of electron density between the charged guest and the outer C–H bonds (electronic factor), the outer C–H bonds are elongated or shortened by a few thousandths of an angstrom when, respectively, an anion or cation is encapsulated. When a light hydride ($M^{II}H_4$) is exchanged for its heavier analogue $M^{III}H_4$ (M^{II} and M^{III} are elements of the second and third period, respectively), the contraction of the guest becomes stronger by a factor of 1.5–2, while the cage radius enlarges by 0.08–0.09 Å.

The data in Table 3 point to noticeable charge transfer from the central M atom of the guest to the hydride shell $[H_{36}]$ of the cage in the anions $MH_4^-@C_{60}H_{36}$ and to the reverse $[H_{36}] \rightarrow MH_4$ charge transfer in the cations $MH_4^+@C_{60}H_{36}$. In both cases, induced polarization inside the cage is also predicted, i.e., redistribution of about one electron between the $[C_{60}]$ cage and the $[H_{36}]$ shell. In the negative ions $MH_4^-@C_{60}H_{36}$, the hydride shell exhibits acceptor properties, while the carbon cage is a donor; in the positive ions $MH_4^+@C_{60}H_{36}$, the opposite situation occurs: $[H_{36}]$ is a donor and $[C_{60}]$ is an acceptor. In clusters of heavy hydrides $M^{III}H_4@C_{60}H_{36}$, the guest – cage charge transfer is more significant but the cage polarization is weaker than in their light congeners (Table 3). The constants σ(H) of the cage H atoms decrease roughly linearly in going from an anion to a cation, but are barely sensitive to an increase in the size of the guest. Changes of some vibrational frequencies of the cage are also significant (Table 2). The largest shifts are observed for the ν_{str}(CH). When neutral hydrides are exchanged for anions and cations, the ν_{str}(CH) correspondingly decrease by ~40–90 cm^{-1} and increase by ~30–35 cm^{-1}. Due to their high intensity, these frequencies are suitable for studying charged hydrogenated endofullerenes by IR spectroscopy. The steric factor has a considerably weaker effect on the ν_{str}(CH) shifts as compared to the electronic factor. An analogous pattern was found in our calculations of other charged endofullerenes $L^{n\pm}@C_{60}H_{36}$ with encapsulated alkali and alkali-earth metal cations [31] and tetrahedral oxoanions MO_4^{n-} with 32 valence electrons (see below), as well as in the small and tight alane $L^{n\pm}@Al_{12}H_{12}^{2-}$ and gallane $L^{n\pm}@Ga_{12}H_{12}^{2-}$ clusters with the internal cations of Li, Na, Be, Mg, Al and anions of H, F, Cl, and Br [55,56]. The ν_{str}(CC) frequencies of the $C_{60}H_{36}$ cage are barely sensitive to the nature of the guest (Table 2). One can deem that these tendencies are rather typical for other charged endoclusters with various cages and substituents as well.

When light guests $M^{II}H_4^{0,\pm}$ are introduced into the $C_{60}H_{36}$ cage, the constant σ(B) decreases by ~6 ppm compared to the isolated BH_4^- ion, in line with the decrease in electron density on the B atom. When $M^{III}H_4^{0,\pm}$ hydrides are inserted, $\sigma(M)$ decreases in all cases; this decrease rapidly builds up from –5 ppm for P to –82 ppm for Al, also in accord with the decrease in the electron density on the central atom and the increase in the paramagnetic contributions to σ with an increase in the size of the guest.

When the BH_4^- anion is encapsulated instead of CH_4, the hypsochromic shifts $\Delta\nu_{str}$(BH) increase to 180–200 cm^{-1}. For encapsulated NH_4^+, the $\Delta\nu_{str}$(NH) shifts are smaller, 90–100 cm^{-1}. The t_{str} vibration in the charged clusters is significantly more intensive than in their methane analogue.

For $M^{III}H_4$ in the place of $M\ ^{II}H_4$, the shifts $\Delta\nu_{str}(M\text{H})$ increase by a factor of 1.5–2. The behavior of $\Delta\nu_{str}(MH_4)$ with a change of the central Matom in going along a subgroup is basically determined by the steric factor. The deformation frequencies ν_{def} of the encapsulated cations are red shifted in contrast to the blue ν_{def} shifts for the anions and neutral guests (Table 2), in accord with the results of Mulliken's population analysis indicating some charge transfer from the cage to the antibonding MO of the guest, which is accompanied by the elongation and weakening of M–H bonds. The translational ν_{tr} frequencies lie within the range ~230–310 cm^{-1} and are rather intensive. The librational ν_{libr} frequencies of neutral and negatively charged guests are approximately twice as large (~500–640 cm^{-1}) and increase with an increase in the size of the guest and in going from neutral guests to anions. Both modes, ν_{tr} and ν_{libr}, are strongly coupled to the deformation vibrations of the carbon skeleton.

The estimates of activation barriers show that the internal rotation of the bulky anions BH_4^- and AlH_4^- and the SiH_4 molecule is hindered or forbidden, but is possible for the smallest ammonium cation.

The above trends persist when the more spacious $C_{60}H_{24}$ (T) cage is used, but the shifts of the guest frequencies ν and constants σ are noticeably smaller than for $MH_4@C_{60}H_{36}$.

The sphericity of the C_{60} cavity complicates the search for the optimal structure of the $MH_4@C_{60}$ clusters, since their PESs are flattened and only slightly sensitive to the orientation of the guest. The symmetric structures are very close in energy, but at the B3LYP/6-31G level all of them have several imaginary frequencies corresponding to the rotation of the guest. Optimization without constraints imposed on symmetry leads to the asymmetric structures C_1, with the energy difference being hardly perceptible. It is likely that the inner rotation of small guests in C_{60} should be considerably less hindered than in $C_{60}H_{36}$.

The C_{84} cage lacks the hydride shell, the guest–cage charge transfer in $MH_4@C_{84}$ is several-fold smaller than in $MH_4@C_{60}H_{36}$. Accordingly, the geometric parameters (Table 4) and other properties of C_{84} (Table 5) turn out to be hardly sensitive to the presence of the MH_4 guests, both neutral and charged. The steric compression and $\Delta\nu_{str}$ and $\Delta\sigma$ shifts of the inserted MH_4 entities in $MH_4@C_{84}$ are also severalfold smaller than those in $MH_4@C_{60}H_{36}$, but nevertheless remain to be tangible for spectroscopic detection.

It is worth noting that the short-wavelength shifts $\Delta\nu(a)$ and $\Delta\nu(t)$ of the a and t stretching vibration frequencies of the guest in $NH_4^+@C_nH_m$ clusters sharply increase from ~35 cm^{-1} for $NH_4^+@C_{84}$ to 55–65 cm^{-1} for $NH_4^+@C_{60}H_{24}$ and 90–100 cm^{-1} for $NH_4^+@C_{60}H_{36}$ as the cavity size decreases and the "internal pressure" in the cage increases. These calculated shifts can be correlated to the experimental blue shifts $\Delta\nu(a)$ for the NH_4^+ cation measured by Raman spectroscopy for crystalline ammonium perchlorate under increasing static pressure [57]. Neglecting small effects caused by rearrangement of the net of hydrogen bonds, the measurements indicate that, as the pressure increases up to 5.1 GPa, the $\Delta\nu(a)$ shift monotonically increases by approximately 50 cm^{-1}, $\Delta\nu(a) \sim k_{ext}P_{ext}$, at the approximate rate $k_{ext} \sim 10$ cm^{-1}/GPa (see [57] for the plotting of the change in the frequency against pressure), so that the blue shift $\Delta\nu(a)$ can serve as a criterion for estimating the external pressure P_{ext}. Analogously, we may speculate that the blue shifts of the stretching frequencies $\Delta\nu(a)$ and $\Delta\nu(t)$ of the tetrahedral guests in $MH_4@C_nH_m$ clusters can be useful characteristics for estimating the pressure P_{int} inside the fullerene cages by the analogous relationship $\Delta\nu(a) \sim k_{int}P_{int}$. According to this criterion, as applied to the methane endofullerenes, the "internal pressure" in the series of cages C_{84}–$C_{60}H_{24}$– $C_{60}H_{36}$ increases in the approximate proportion 1:1.8:3.5. However, it is clear that these estimates are rough and need further refinement. It is also pertinent to note that the calculated librational frequencies ν_{libr} of the guest (~340 and ~224 cm^{-1}) for the $NH_4^+@C_{84}$ and $BH_4^-@C_{84}$ ions are comparable to the experimental frequencies of ammonium librations in solid salts of the $NH_4^+ \cdot X^-$ type with $X = Hal$, AlF_4, SnF_3, and so on (~300–400 cm^{-1}) and borohydride librations in salts of the $CsBH_4$ type ($\sim$270 cm^{-1}) [54]. Obviously, this comparison is qualitative, since, on the one hand, B3LYP calculations give only approximate estimates of ν_{libr}, and, on the other hand, the experimental ν_{libr} frequencies in salts depend on the symmetry and chemical nature of the surrounding atoms. Nevertheless, we can assume that, in the case of small MX_4 tetrahedra, their hindered librations inside C_{84} and more spacious cages can transform, as in ammonium and borohydride salts, to quasi-free rotation at ambient and moderately elevated temperatures; the barriers to this rotation are no more than a few kcal/mol. This should be manifested in tunnel splitting of the vibrational frequencies of the tetrahedral guest.

The Mulliken population analysis for the neutral radicals $MH_4@C_{60}$, $MH_4@C_{60}H_{24}$, $MH_4@C_{60}H_{36}$, and $MH_4@C_{84}$ produced by both electron elimination (ionization) from the HOMO of the endohedral anions and electron acceptance on the LUMO of the endohedral cations, demonstrate that the spin densities on the guest atoms *M* and H in all these radicals are close to zero, and the unpaired electron is fully delocalized over the atoms of the cages. Thus, we believe that relaxation effects are not very strong in these systems and that their *VIP*s and *VEA*s should be close to adiabatic. The encapsulation of the anions BH_4^- and AlH_4^- decreases the *IP*s of all four cages by $\sim$2.8–3.4 eV, whereas the encapsulation of the NH_4^+ and PH_4^+ cations increases the *EA*s of the cages by roughly the same value. The changes in the *IP*s of these cages caused by the insertion of singly charged cations of alkali, alkaline-earth, and other electropositive metals fall within the same range. By contrast, the introduction of neutral molecules CH_4 and SiH_4 and inert gas atoms has little effect on *IP*s and *EA*s. The results of the calculations are consistent with the conclusions of the charged sphere model.

Similar trends are observed in the behavior of orbital energy levels ε_i. The encapsulation of the MH_4^+ cation leads to a decrease in the energy of the $\Delta\varepsilon 1s(C)$ levels of the cage by 2.85–3.40 eV, whereas the encapsulation of the MH_4^- anion forces this level upward on the energy scale. The shifts $\Delta\varepsilon 1s(C)$ therein are virtually insensitive to the substitution of the ammonium cation by PH_4^+ or Li^+, or to the substitution of the hydroborate anion by AlH_4^-, and are mainly determined by the charge sign and magnitude. The $\varepsilon 1s(M)$ levels of the atoms *M* are forced upward by 1.3–4.4 eV for the encapsulated cations and go down by 0.55–1.55 eV for the anions, and the $\Delta\varepsilon 1s(M)$ shifts depend on the type of cage. For the NH_4^+ cation, $\Delta\varepsilon 1s(N)$ is the largest for the tightest $C_{60}H_{36}$ cage and the smallest for the spacious C_{84}. The reverse situation was found for the BH_4^- anion.

3.3. Oxoanions MO_4^{n-} inside the $C_{60}H_{36}(T)$ Cage

Now we discuss results of our DFT study of another series of model endofullerenes containing tetrahedral anions MO_4^{n-} (M = Si, P, S, Cl, Ar and N) with 32 valence electrons inserted into the $C_{60}H_{36}$ (T) cage [58], where the $R(\mathrm{OC})$ distances between oxygen atoms and their nearest carbon neighbors shorten along the series by 0.10–0.15 Å. The dominant factor of the guest–host interaction here should be strong redistribution of electron density between the guest and the cage, inside the anions and inside the cage. On the contrary to the CH_4- and He_4-clusters (Section 3.1) where the charge transfer is minor, for the $M\mathrm{O}_4^{n-}@\mathrm{C}_{60}\mathrm{H}_{36}$ series one can expect large shifts of frequencies $\Delta\nu_i$ and constants $\Delta\sigma$ both for the guest and the cage atoms. At the first step, geometry optimization and calculations of vibrational frequencies were carried out within the B3LYP approximation with the "combined" basis set Gen = 6-31G*(MO_4) + 6-31G ($C_{60}H_{36}$), where the polarized 6-31G* basis was included only for the guest atoms. At the second step, geometries were reoptimized and magnetic screening constants were computed at the B3LYP/6-31G* level with a polarization function on all atoms. As other tetrahedral guests, discussed above in Sections 3.1 and 3.2, the structure T (Figure 1), where M–O bonds are directed toward centers of hydrogenated faces [C_6H_6], corresponds to a local minimum on the PES (all vibrational frequencies are real) and is most favorable as compared to other orientations of the anions. The calculated results are presented in Table 6 and Figures 2 and 3.

The insertion of the smallest perchlorate anion leads to a moderate contraction of the Cl–O bond by 0.034 Å and 0.2 e charge transfer from the anion to the $C_{60}H_{36}$ cage. In the $\mathrm{ClO}_4^- - \mathrm{SO}_4^{2-} - \mathrm{PO}_4^{3-} - \mathrm{SiO}_4^{4-}$ row, both effects, steric and electronic, rapidly and nearly linearly increase with an increasing of the external charge. For the ortho-silicate ion they become quite significant, as the Si–O bond is shortened by 0.082 Å and the charge transfer is ~1.7 e. The charge removed from the central atom M is usually by 0.2–0.4 e larger than that removed from four oxygen atoms and, as a result, the electron density inside the encapsulated guest polarizes and the M–O bonds are more polar than those in free $M\mathrm{O}_4^{n-}$. The electronic factor clearly dominates in this series, however, both factors can play a role in the guest–host interaction.

The insertion of ClO_4^- also results in an increase of magnetic shielding constants on both Cl and O atoms ($\Delta\sigma(\mathrm{Cl}) = +75$ and $\Delta\sigma(\mathrm{O}) = +33$ ppm) which can be attributed to shielding due to ring currents of the cage. As the contraction of the guest and the charge transfer from the MO_4 to the cage increase, one can see a sign change and a rapid decrease of $\Delta\sigma(M)$ and especially $\Delta\sigma(\mathrm{O})$ in the $\mathrm{ClO}_4^- < \mathrm{SO}_4^{2-} < \mathrm{PO}_4^{3-} < \mathrm{SiO}_4^{4-}$ series. For instance, in the *ortho*-silicate cluster, $\Delta\sigma(\mathrm{Si})$ and $\Delta\sigma(\mathrm{O})$ are 11.5 and −315 ppm, respectively.

Frequency shifts of the endohedral anions are much larger as compared to those of the inserted CH_4 molecule and vary in the range of 15–80 cm^{-1} for deformational t and e, and 80–185 cm^{-1} for the bond stretching a and t vibrations. The largest shifts, from 120 $\mathrm{cm}^{-1}(\mathrm{ClO}_4^-)$ to 185 $\mathrm{cm}^{-1}(\mathrm{SiO}_4^{4-})$, are found for the symmetric vibration a, which practically does not mix with cage vibrations. The deformational vibration e is also weakly coupled and its shift $\Delta\nu(e)$ shows an opposite trend and decreases along the same series

Table 6 Selected characteristics of MO_4^{n-} guests in endohedral clusters MO_4^{n-}@$C_{60}H_{36}(T)$[a]

Parameter	Face	ClO_4^-	SO_4^{2-}	PO_4^{3-}	SiO_4^{4-}
$R(MO)$[a]	–	1.465	1.492	1.551	1.641
$R(CH)$	–	1.102	1.109	1.112	1.120
$R(O_{100}C_1)$	[C_6]	2.856	2.855	2.850	2.844
$R(O_{100}C_2)$	[C_6]	2.581	2.563	2.597	2.481
$R(O_{100}C_3)$	[C_6H_6]	2.619	2.592	2.540	2.468
$R(O_{100}C_4)$	[C_6H_6]	2.706	2.679	2.629	2.560
$R(O_{100}C_5)$	–	3.087	3.072	3.048	3.017
$R(C_1C_2)$	[C_6]	1.400	1.399	1.400	1.402
$R(C_1C_6)$	[C_6]	1.383	1.381	1.380	1.381
$R(C_{31}C_{32})$	[C_6H_6]	1.597	1.594	1.590	1.588
$R(C_{31}C_{36})$	[C_6H_6]	1.578	1.574	1.570	1.567
R_1[b]	[C_6]	3.372	3.373	3.375	3.377
R_2[b]	[C_6H_6]	3.985	3.980	3.978	3.982
ϕ_1[b]	[C_6]	163.2	163.5	164.3	165.3
ϕ_2[b]	[C_6H_6]	126.2	126.1	125.7	125.0
θ_1[b]	[C_6]	1.3	2.9	5.6	8.9
θ_2[b]	[C_6H_6]	–12.3	–12.5	–12.8	–13.2
$\nu_{str}(CC)$ of the [C_{60}] cage	*t*	1676(2.8)	1681(6.2)	1679(13.1)	1670(50.0)
	t	1480(18.0)	1485(16.6)	1485(13.7)	1480(12.3)
	a	1459	1466	1471	1472
$\nu_{tr}(MO_4^{n-})$	*t*	271(2.3)[c]	268(13)[c]	261(40)[c]	256(90)[c]
$\nu_{libr}(MO_4^{n-})$	*t*	204(0)[c]	208(0)[c]	202(0)[c]	196(0)[c]
$Z(M)$		1.49	1.62	1.70	1.77
$Z(O)$		−0.56	−0.75	−0.89	−0.92
$\sigma(M)$		34.8	217.4	353.1	441.9

[a] In the isolated MO_4^{n-} ions the $R(MO)$ distance calculated at the same B3LYP/6-31G* level is (in Å): 1.499 (ClO_4^-), 1.525 (SO_4^{2-}), 1.599 (PO_4^{3-}), 1.723 (SiO_4^{4-}), respectively; $Z(M)$, $Z(O)$ and $\sigma(M)$ (in *e* and *ppm*) are 1.22, −0.56, −40.1 for M = Cl, 1.18, −0.80, 186.6 for M = S, 0.99, −1.00, 344.8 for M = P, 0.58, −1.15, 453.4 for M = Si. The related characteristics of the empty $C_{60}H_{36}$ cage see in Tables 1–3.

[b] See footnotes to Table 1.

[c] ν_{tr} and ν_{libr} are coupled with the cage vibrations.

from 80 to 35 cm^{-1}. In contrast, the IR active *t* vibrations exhibit a notable mixing with the motions of cage atoms, and their shifts (Figure 3) reach the minimal values for the PO_4^{3-} and SO_4^{2-} clusters.

Insertion of the anions does not significantly affect the carbon skeleton geometry. From ClO_4^- to SiO_4^{4-}, the C–C bond elongations do not exceed 0.01 Å. The most substantial structural changes from ClO_4^-@$C_{60}H_{36}$ to SiO_4^{4-}@$C_{60}H_{36}$ involve elongation of C–H bonds by almost 0.02 Å. In addition to the guest-to-host charge transfer, the Mulliken population analysis shows a significant polarization of the cage, i.e., electron density

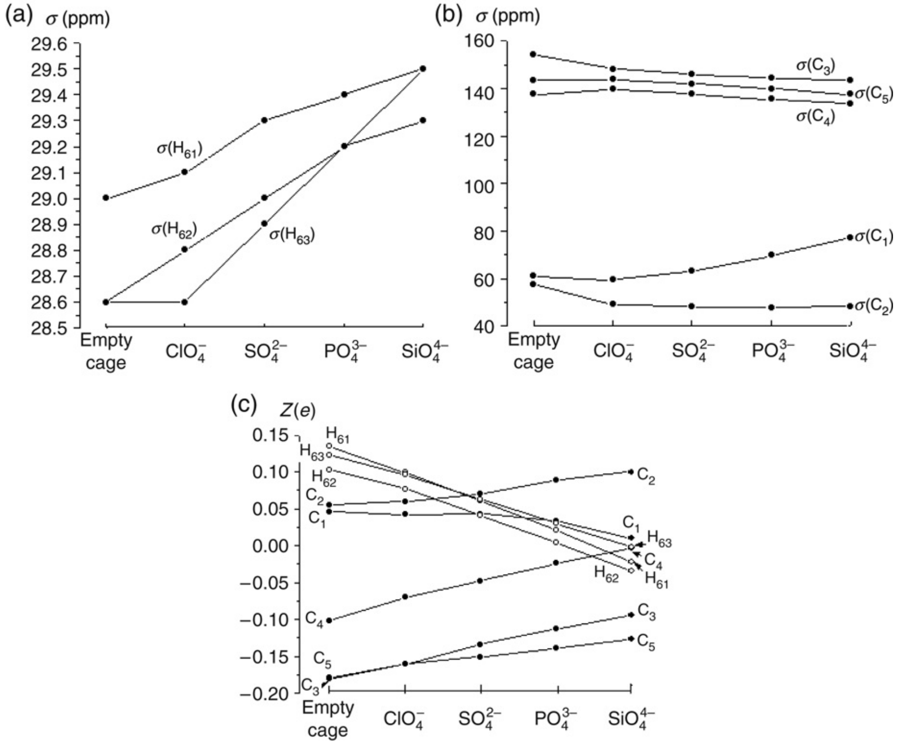

Figure 2 Magnetic shielding constants σ (ppm) on H (a) and C (b) cage atoms and their Mulliken's effective charges (c) in $MO_4^{n-}@C_{60}H_{36}(T)$ clusters.

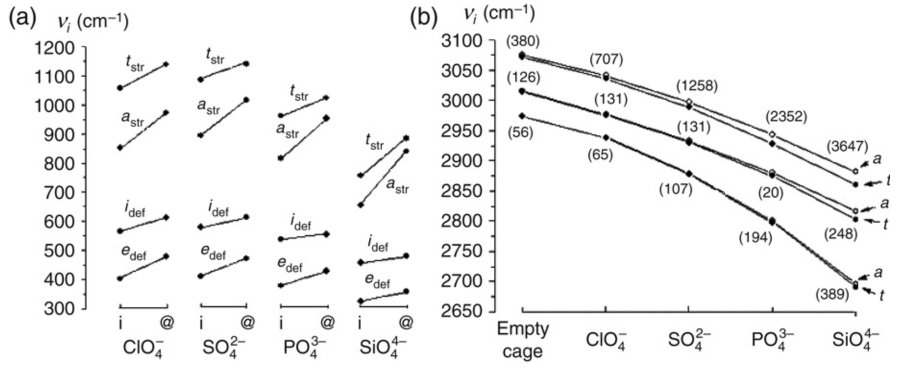

Figure 3 Blue shifts of vibrational frequencies of the guest MO_4^{n-} (a), and red shifts of $\nu_{str}(CH)$ of the cage (b) in $MO_4^{n-}@C_{60}H_{36}(T)$ clusters (i — isolated MO_4^{n-}, @—MO_4^{n-} inside $C_{60}H_{36}$).

redistribution between the carbon skeleton [C_{60}] and hydrogen shell [H_{36}]. The former serves as a donor (mostly on account of hydrogenated faces), and the hydrogen shell accumulates electron density, which is donated both by the guest and by the carbon skeleton. Both components rapidly increase with the external charge and the electron density taken from [C_{60}] is comparable with, or even exceeds, the density donated by the inserted guest. Because of such redistribution, hydrogen atoms change the sign of their effective charge from positive to negative and C–H bonds become more polar, longer, and weaker as compared to those in the isolated molecule $C_{60}H_{36}$. This result is in line with the behavior of magnetic shielding constants σ(H) (Figure 2) and frequencies ν_{str}(CH). The $\Delta\sigma$(H) shifts increase monotonically up to 0.6–1.0 ppm and the red $\Delta\nu_{str}$(CH) shifts rises 220–230 cm^{-1} when the anion changes from ClO_4^- to SiO_4^{4-}. The red shifts for ν_{str}(CC) are smaller as compared to those for ν_{str}(CH), but in the 1400–1700 cm^{-1} range they are still significant (45–50 cm^{-1}).

In order to evaluate the possibility of the guest internal rotation, we calculated two intermediate structures on the rotational pathway of ClO_4^- and SiO_4^{4-}, inverted (“overturned”) $T(i)$ structure with the same symmetry T but with M–O bonds looking at opposite directions (toward centers of nonhydrated cycles [C_6]), and non-symmetric structure C_1 obtained from T by 30° rotation of the guest around a C_3 axis. The calculations show that the $T(i)$ structure has imaginary frequencies and both intermediate configurations reside much higher in energy than T, indicating that a full-scale rotation of the tetrahedral oxoanions inside the $C_{60}H_{36}$ cage is forbidden.

As our B3LYP calculations predict, in salt-like $Li_4[CO_4@C_{60}H_{36}]$ and $Li_4[NO_4@C_{60}H_{36}]^+$ clusters with the structure of the symmetry T, which corresponds to a local minimum on PES, the influence of external Li^+ countercations on the structure, spectral properties and internal movements of the guest is minor or negligible. The M–O bonds are shortened by 0.005 Å and all the frequencies of the guest are only shifted by 3–8 cm^{-1}. Frequencies ν_{tr} (167–170 cm^{-1}) and ν_{libr} (223–112 cm^{-1}) practically do not change but their intensity in the salt rises by an order of magnitude. The shielding constants σ(N) and σ(O) increase by ~9 and ~5 ppm.

3.4. Noble gas “clusters” Ng_4 inside the $C_{60}H_{36}(T)$ and $C_{84}(T_d)$ Cages

Figure 4 shows that an increase in the atomic radius $R(Ng)$ in the row Ng = He, Ne, Ar, Kr, and Xe is accompanied by a rapid expansion of the cage [30,32]. As with the alane and gallane endoclusters $Ng@Al_{12}H_{12}^{2-}$ and $Ng@Ga_{12}H_{12}^{2-}$ [22,23], the diameter of the C_{60} cage is a roughly linear function of $R(Ng)$. In the tightest Kr_4- and Xe_4-endoclusters, the ordinary and multiple C–C bonds are elongated by 0.02–0.03 and 0.05–0.06 Å respectively; as a result, the “inflating” C_{60} skeleton takes on a shape close to a spheroid. The deformation energy of the cage dramatically increases from a few kcal/mol for $He_4@C_{60}H_{36}$ to ~90 kcal/mol for $Kr_4@C_{60}H_{36}$. Despite such a strong internal stress, structure T remains a local minimum on the PES for all

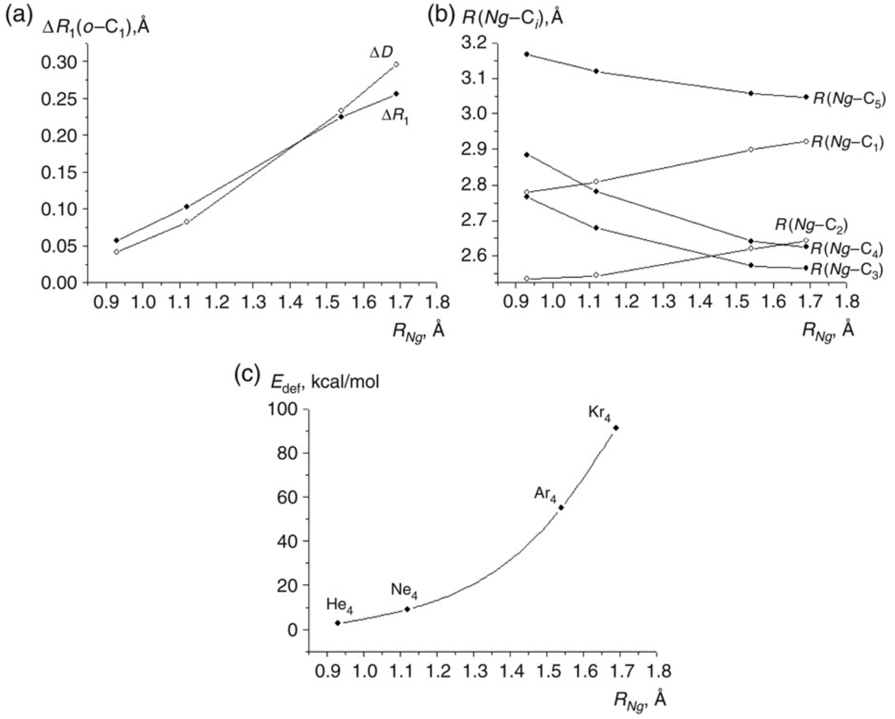

Figure 4 Structural (a, b) and energetic (c) characteristics of the $Ng_4@C_{60}H_{36}(T)$ clusters as a function of the atomic radius $R(Ng)$.

Ng_4-endofullerenes including $Xe_4@C_{60}H_{36}$, which indicates that the carbon cage $[C_{60}]$ is highly stable with respect to isotropic expansion.

For the bulkier Ng, a small but increasing charge transfer from the Ng_4 guest to the cage and distribution of electron density between the C_{60} skeleton (acceptor) and the H_{36} shell (donor) can be noted. For example, the effective electronic configuration of $Kr_4@C_{60}H_{36}$ is described as $Kr_4^{+0.56}@C_{60}^{-0.91}H_{36}^{+0.35}$. One may assume that, in addition to the dominating steric factor, the electronic factor should be also taken into consideration for the $Ng_4C_{60}H_{36}$ clusters.

From Figure 5 and Table 7 one can see that in going from the He_4- to Kr_4-containing cluster, in line with the strengthening of the C–H bonds, their highest $\nu_{str}(CH)$ frequencies undergo a blue shift by 10–35 cm^{-1} and, conversely, the highest $\nu_{str}(CC)$ frequencies of the elongated C–C bonds are red shifted as compared to their values for the isolated $C_{60}H_{36}$ molecule. These shifts increase from 10–15 (He_4) to 125–130 (Kr_4) cm^{-1}. The most intensive frequency t in the region 1400–1500 cm^{-1} is best suited to observation by IR spectroscopy. The longest wavelength frequency $\nu(a)$ of the cage

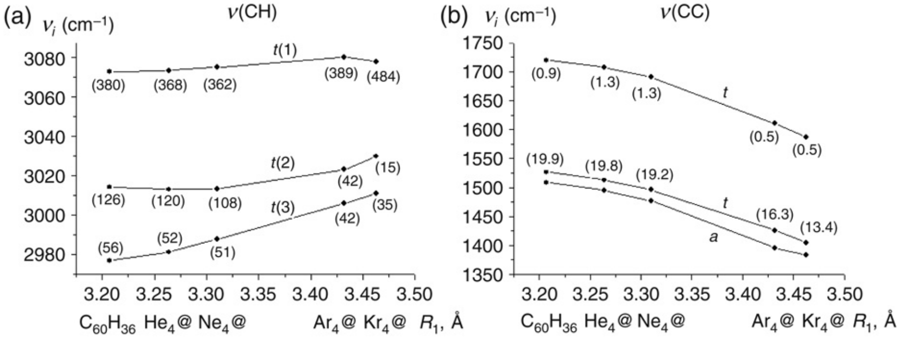

Figure 5 Highest stretching vibration frequencies ν_{str}/R_1 of the C–H (a) and C–C (b) bonds of the cage in the $Ng_4@\mathrm{C}_{60}\mathrm{H}_{36}(T)$ clusters.

Table 7 Frequencies (cm^{-1}) and IR intensities (km/mol, in parentheses) of librational, translational, and deformation vibrations of the Ng_4 guest inside $\mathrm{C}_{60}\mathrm{H}_{36}(T)$ and $\mathrm{C}_{84}(T_d)$ cages[a]

Symmetry	$\mathrm{He}_4@$	$\mathrm{Ne}_4@$	$\mathrm{Ar}_4@$	$\mathrm{Kr}_4@$	Assignment
			$\mathrm{C}_{60}\mathrm{H}_{36}$		
t_1	350(0.1)	182(0.)	156(0.)	120(0.0)	$\nu_{\mathrm{libr}}(Ng_4)$ + cage
t_2	169(0.5)	165(0.7)	210(1.0)	188(1.0)	$\nu_{\mathrm{tr}}(Ng_4)$ + cage
t_2	270(0.1)	241(0.1)	289(1.0)	262(0.7)	$t_{\mathrm{def}}(Ng_4)$ + cage
E	383	269	219	197	$e_{\mathrm{def}}(Ng_4)$ + cage
a_1	479	398	515	360	$a_{\mathrm{def}}(Ng_4)$ + cage
			C_{84}		
t_1	93	61	106	84	ν_{libr}
t_2	94(0.3)	103(0.1)	180(0.7)	157(0.5)	ν_{tr}
t_2	173(0.)	162(0.)	291(0.)	219(0.)	$t_{\mathrm{def}}(Ng_4)$
E	185	125	187	160	$e_{\mathrm{def}}(Ng_4)$
a_1	214	233	364	310	$a_{\mathrm{def}}(Ng_4)$

[a] B3LYP/6-31G calculations [32].

deformation vibration, which is strongly coupled to the *a* vibration of the guest, monotonically increases from 255 cm^{-1} for He_4 to 390 cm^{-1} for Kr_4.

The behavior of σ(C) (Table 8) is dictated by an increase in the paramagnetic contributions from contact C–*Ng* interactions with an increase in the radius $R(Ng)$. The largest shifts $\Delta\sigma$(C) (by ~12–16 ppm) are observed for C_2 and C_3 type atoms nearest to the *Ng* atoms, the smallest shifts on the order of 1 ppm are typical for the most remote atoms of the C_5 type, and the shifts $\Delta\sigma$ for the C_1 and C_4 atoms, separated from the *Ng* atom by intermediate distances, have intermediate values of ~7 ppm. Table 7 summarizes the

Table 8 Magnetic shielding constants $\sigma(Ng)$ and $\sigma(C_i)$ (ppm) in endofullerenes with Ng atoms and Ng_4 clusters inside $C_{60}H_{36}$ (T) and C_{84} (T_d) cages[a]

$\sigma(Ng)$ in endofullerenes with Ng and Ng_4 inside $C_{60}H_{36}(T)$ and $C_{84}(T_d)$

Endocluster	Ng				
	He	Ne	Ar	Kr	Xe[a]
Ng (free atom)	59.8	551.9	1236.8	3235.9	5585.3
$Ng@C_{60}H_{36}(T)$	68.4	550.2	1224.6	3158.8	5518.7
$Ng_4@C_{60}H_{36}(T)$	66.8	478.0	902.6	2423.9	3244.6
$Ng@C_{84}(T_d)$	69.4	560.3	1236.2	3205.1	5535.1
$Ng_4@C_{84}(T_d)$	69.5	547.0	1120	2928.0	4369.3

$\sigma(C_i)$ in $Ng_4@C_{84}(T_d)$

C_i atom	Ng				
	–[b]	He	Ne	Kr	Xe
C_1	53.4	53.4	53.5	53.9	52.6
C_{13}	48.1	48.1	47.7	38.7	30.8
C_{19}	50.7	50.6	50.6	47.7	44.2
C_{29}	57.4	57.4	57.4	53.9	49.4

[a] Calculations at the B3LYP/6-31G*//B3LYP/6-31G* level [32]. For Xe, the DZ + P basis set [59] was used. The numbering of atoms of the C_1, C_{13}, C_{19}, and C_{29} types is shown in Figure 1.

[b] The empty (free) $C_{84}(T_d)$ cage.

calculated frequencies $Ng_4@C_{60}H_{36}(T)$, which correspond to translational and librational vibrations of the Ng_4 guest inside of $Ng_4@C_{60}H_{36}(T)$, as well as to its deformation modes t, e, and a. Rotational and deformation vibrations a and e of the guest are mixed with deformation vibrations of the cage, whereas translational ν_{tr} and deformation t vibrations of the guest are mixed with each other. The ν_{tr} and t_{def} vibrations can be separated only for the smallest guests He_4 and Ne_4.

As follows from Table 8, only $He_4@C_{60}H_{36}$ (T) has the upfield chemical shift δ(He). In tighter Ng_4-encapsulating clusters, the paramagnetic contributions are obviously dominating, and downfield chemical shifts $\delta(Ng)$ rapidly increase in the following order: ~72 (Ne_4), ~334 (Ar_4), and ~812 (Kr_4) ppm. In the more spacious cage $C_{84}(T_d)$, the substitution of He_4 by Ne_4 produces a "feeble" response (Tables 7–9). The shielding constant σ(Ne) in $Ne_4@C_{84}$ is only 5 ppm smaller than σ(Ne) for the free atom. One can suppose that the diamagnetic contributions of "ring" currents and the paramagnetic contributions of the Ne–Ne and Ne–cage contact interactions are comparable in magnitude and partially compensate each other. In the case of a bulkier Ng, the cage diameter in $Kr_4@C_{84}$ and $Xe_4@C_{84}$ increases by 0.07 and 0.15 Å, and all C–C bonds are elongated by 0.006–0.016 and 0.018–0.036 Å, respectively.

Table 9 Optimized geometric parameters of $Ng_4@C_{84}(T_d)$ (B3LYP/6-31G*)[a]

Cage			$Ng_4@C_{84}(T_d)$				
Parameter	face	C_{84}	He_4	Ne_4	Ar_4	Kr_4	Xe_4[b]
$R(oNg)$[c]		-	1.443	1.513	1.719	1.779	1.844
$R(NgNg)$		-	2.357	2.471	2.807	2.904	3.012
$R(Ng_{85}C_1)$		–	3.405	3.374	3.287	3.262	3.253
$R(Ng_{85}C_{13})$	Upper	–	3.074	3.015	2.869	2.841	2.835
$R(Ng_{85}C_{19})$		–	3.201	3.159	3.056	3.030	3.024
$R(Ng_{85}C_{29})$	Lower		3.269	3.246	3.206	3.191	3.203
$R(CC)$	Lower	1.461	1.461	1.460	1.465	1.467	1.479
$R(CC)$	Lower	1.468	1.468	1.468	1.476	1.479	1.493
$R(CC)$	Upper	1.458	1.458	1.458	1.468	1.474	1.490
$R(CC)$	Upper	1.380	1.380	1.380	1.388	1.393	1.406
R_1	Lower	3.947	3.948	3.945	3.958	3.957	3.986
R_2	Upper	4.405	4.405	4.407	4.443	4.468	4.520

[a] The upper and the lower $[C_6]$ rings are planar. The distances between the center of the cage and the C atoms of upper and lower rings are $R_1 = R(oC_{13})$ and $R_2 = R(oC_{29})$. The numbering of atoms is given in Figure 2.

[b] Calculation with the DZ + P basis set for Xe [59].

[c] The distance between the center of the cage and the Ng atoms.

The vibrational frequencies t_2 and a_1 of the guest increase in going from He_4 to Ar_4 by ~85–120 and ~150 cm^{-1} respectively. The long-wavelength t_2 frequencies should be very weak in the IR spectra.

3.5. CF_4, CCl_4, CBr_4, and CLi_4 inside the $C_{60}H_{36}(T)$ Cage

Here we discuss briefly the $C_{60}H_{36}$-endoclusters with neutral halogenated and lithiated molecules CX_4 (X = F, Cl, Br, Li), where the steric repulsion factor should dominate progressively in line with the elongation of the guest C–X bonds [60]. For CX_4 encapsulation, the strong (up to ~0.20 Å) shortening of the distances between X and the nearest C atoms of the cage results in polarization and significant (up to ~0.5 e) redistribution of electron density only inside of the guest. The central C atom plays the role of acceptor and becomes more negatively charged, while the X substituents (donors) become more positively charged. This "inside-guest" charge transfer rises along the series, from small 0.06 e for CF_4 to significant ~0.5 e for CBr_4. The charge transfer between the guest and the cage remains minor for all the endoclusters under discussion.

The blue shifts of the stretching frequencies a and t rise along the series from few tens to few hundreds of wavenumbers, and, like in other endofullerenes considered in Sections 3.1–3.4, the intensity of the IR-active t mode decreases by a factor 4–5. The lithiated CLi_4-endocluster is an exception: due to attractive interaction between the Li cations and the negatively charged

C atoms of the cage, the intensity of the *t* mode in $CLi_4@C_{60}H_{36}$ increases more than by order. Shifts of the constants $\sigma(C)$ and $\sigma(X)$ on the guest atoms rises from 4 and 9 ppm for $CF_4@C_{60}H_{36}$ to ~90 and ~630 ppm for $CBr_4@C_{60}H_{36}$. Lithiated cluster $CLi_4@C_{60}H_{36}$ is again an exception in which both $\sigma(C)$ and $\sigma(Li)$ decrease by 13 and 2 ppm respectively.

Frequencies of translational modes increase along the halogenated series in the range of 160–260 cm^{-1}. Our evaluations of rotational barriers, in the same manner as it was done in Section 3.3, indicate that the rotation of all four guests inside the $C_{60}H_{36}$ is strongly hindered or forbidden. The minimal barrier is predicted for $CLi_4@C_{60}H_{36}$ (about 18 kcal/mol).

3.6. Intermediates and artificial ("forced") tetrahedral molecules inside fullerenes

In Sections 3.1 and 3.4 we underlined that the noble gas Ng_4 units, which are nonbonding in the isolated state, are kept together inside the fullerene cages due to repulsion from the fullerene walls and forced to vibrate as artificial molecules with significant frequencies and force constants like the "real" covalent molecules (P_4) which are able to exist both in endohedral and in isolated states. In a similar manner, inside the fullerene cages one can trap other "artificial" moieties, which are either high-lying intermediates or unstable in an isolated state. In [60] we have performed calculations (at the same B3LYP level as before) for the $L@C_{60}H_{36}$ endoclusters with inserted various intermediates and artificial molecules $L = C_4H_4$, C_4Li_4, ArO_4, O_5^{2-}, N_4, etc. As could be expected, their structure of *T* symmetry corresponds to a local minima of PES for all these guests, and the effects of compressing of the guests, significant shifts $\Delta\nu_{str}$ and $\Delta\sigma$ of the guest frequencies and screening constants follow the same trends which are discussed above in Sections 3.1–3.5.

4. LINEAR MOLECULES INSIDE THE PROLATE SPHEROIDAL $C_{70}(D_{5h})$ CAGE

In endofullerenes $L@C_{70}$ with linear guest molecules *L* inside the prolate spheroidal C_{70} (D_{5h}) cage the pressure exerted on the guest is anisotropic and directed along the principal C_5 axis.

4.1. C_2H_2 and HBNH inside $C_{70}(D_{5h})$

The calculations in [33] show that the structures of $C_2H_2@C_{70}$ (D_{5h}) and $HBNH@C_{70}$ (C_{5v}) (Figure 6, Table 10), in which the linear guest molecules are extended along the principal axis C_5 (*z*), correspond to a minimum of the PES. The contact distances between H atoms and nearest C atoms of the cage in $C_2H_2@C_{70}$ (~2.6 Å) are somewhat shorter than the sum of their van der Waals radii. The C–C and C–H bonds in the encapsulated guest are, respectively, 0.003 and 0.005 Å shorter than in the free molecule C_2H_2, which

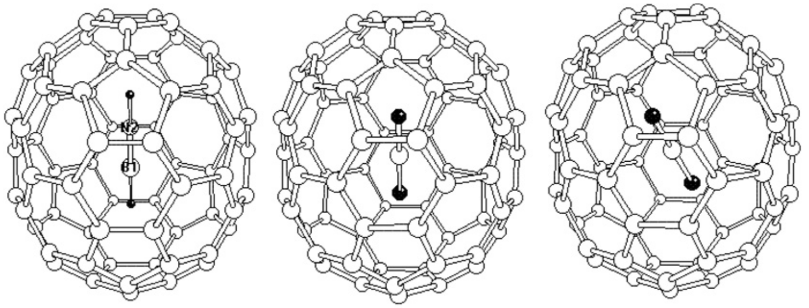

$C_2H_2@C_{70}$, D_{5h}
HB NH$@C_{70}$, D_{5h}

$MX_2@C_{70}$, D_{5h}

$MX_2@C_{70}$, C_2

Figure 6 The structures of endohedral fullerene clusters with linear tri- and tetraatomic guest molecules inside C_{70} (D_{5h}).

is severalfold smaller than the corresponding shortenings of the C–H bond in the methane molecule in $CH_4@C_{60}H_{36}$ (Section 3.1). In the encapsulated acetylene, both stretching and bending vibration frequencies are weakly coupled to the vibrations of the cage and undergo a considerable blue shift. The lowest translational frequencies $e_1' = 114$ cm^{-1} and $a_2'' = 135$ cm^{-1} correspond to the displacements of the guest in the direction perpendicular to the C_5 axis and along this axis, respectively. Due to the axial anisotropy, these frequencies are split; however, the splitting is not very large. The librational mode has a somewhat higher frequency, $e_1'' = 160$ cm^{-1}. Both the translational and librational frequencies for $C_2H_2@C_{70}$ are considerably lower than for $CH_4@C_{60}H_{36}$ (cf. with the data in Table 2). This result, along with weaker effects of geometric contraction and smaller shifts of the stretching and bending vibration frequencies, is evidence that the C_{70} cage for acetylene is more spacious than the $C_{60}H_{36}$ cage for methane. The constants $\sigma(C)$ and $\sigma(H)$ for the C and H atoms of the encapsulated acetylene increase by, respectively, 22.5 and 27 ppm (as compared to the free C_2H_2 molecule) due to strong shielding by the ring currents in the π system of the C_{70} cage. An analogous increase (by ~26 ppm) is also typical of $\sigma(He)$ in the He@C_{70} cluster.

A similar pattern was found for $BNH_2@C_{70}$ (C_{5v}). The difference is that the B–H bond shortens more (by ~0.10 Å) and the N–H bond shortens less (by ~0.03 Å) significantly than the C–H bond in acetylene. Correspondingly, the short-wavelength shift of ν_{str}(B–H) is almost twice as large and the shift of ν_{str}(N–H) is 1.5 times smaller as compared with that of ν_{str}(CH) (Table 10). The translational ($e_1 = 133$ and $a_1 = 154$ cm^{-1}) and librational ($e_2 = 163$ cm^{-1}) frequencies for HBNH exceed those of C_2H_2. The C_{70} cage turns out to be tighter for iminoborane than for acetylene. The character of the electron density polarization in the guest is different for $BNH_2@C_{70}$ and $C_2H_2@C_{70}$. Upon encapsulation, the C–H bonds of acetylene become more covalent, whereas

Table 10 Calculated characteristics of the C_2H_2 and BNH_2 molecules in the isolated state and encapsulated into the C_{70} (D_{5h}) cage [33]

Parameter	C_2H_2	$C_2H_2@C_{70}(D_{5h})$	Parameter	BNH_2	$BNH_2@C_{70}(C_{5v})$
$R(CC)$	1.205	1.202	$R(BN)$	1.239	1.235
$R(CH)$	1.067	1.062	$R(BH)$	1.172	1.161
			$R(NH)$	0.995	0.992
$\nu_i, e''_1\ (\pi_g)$	652	713	$\nu_i, e_1\ (1\pi(HNB))$	597 (172)	622 (4)
$e'_1\ (\pi_u)$	787 (106)	833 (2)	$e_1\ (1\pi(HBN))$	755 (1)	811 (0)
$a'_1\ (1\sigma_g)$	2071	2090	$a_1\ (1\sigma(BN))$	1837 (36)	1861 (1)
$a'_1\ (2\sigma_g)$	3559	3610	$a_1\ (2\sigma(BH))$	2931 (14)	3027 (0.2)
$a''_2\ (\sigma_u)$	3450 (81)	3500 (7)	$a_1\ (3\sigma(NH))$	3906 (169)	3939 (11)
$Z(C)$	−0.188	−0.168	$Z(B)$	+0.118	+0.154
			$Z(N)$	−0.472	−0.502
$Z(H)$	+0.188	+0.162	$Z(H_B)$	+0.032	+0.011
			$Z(H_N)$	+0.322	+0.337
$\sigma(C)$	128.8	151.3	$\sigma(B)$	119.2	143.6
			$\sigma(N)$	174.9	194.3
$\sigma(H)$	31.0	58.0	$\sigma(H_B)$	30.3	57.4
			$\sigma(H_N)$	30.8	57.9

(*continued on next page*)

Table 10 (continued)

Parameter	C_2H_2	$C_2H_2@C_{70}(D_{5h})$	Parameter	BNH_2	$BNH_2@C_{70}(C_{5v})$
$h(C_{70})$[a]	7.942	7.951	$h(C_{70})$[a]	7.942	7.954
$R(C_{70})$[b]	3.564	3.569	$R(C_{70})$[b]	3.564	3.566
$R(CC)$[c]	1.452	1.471	$R(CC)$[c]	1.452	1.471
$R(HC)$[d]		2.623	$R(H_BC)$[d]		2.679
			$R(H_NC)$[d]		2.515
E^e_{diss}		−8.0 (−9.2), +9.5	E_{diss}[e]		−8.3 (−9.6), +9.9

[a] The C_{70} cage height (along the principal molecular axis $C_5(z)$).

[b] The radius of the C_{70} cage in the equatorial *xy* plane.

[c] The length of the cage edges in the equatorial *xy* plane.

[d] The contact (nonbonded) distances between the hydrogen atoms of the guest and the C atoms of the nearest pentagonal face of the cage.

[e] The dissociation energy for $ABH_2@C_{70} \rightarrow ABH_2 + C_{70}$. The first two values were calculated at the B3LYP/6-31G*//B3LYP/6-31G* level without and with (in parentheses) inclusion of ZPEs (B3LYP/6- 31G), and the last values were calculated at the MPWB96/MPWB95 level without inclusion of ZPEs.

the B–N and N–H bonds of iminoborane become more polar due to an increase in the positive effective charge on the B and H_N atoms and an increase in the negative charge on the N atom. The constants σ increase by 24.4 and 19.9 ppm for the B and N atoms, respectively, and by 27.1 ppm for the H_B and H_N atoms, i.e., as much as the $\sigma(H)$ value for the encapsulated acetylene. Both endoclusters are characterized by low dissociation energies on the order of a few kcal/mol.

4.2. CO_2, BeF_2, SiO_2, and CS_2 inside the C_{70} cage

As calculations predicted [33], the C_{70} cage is more spacious for the triatomic CO_2 and BeF_2 guests with moderate distances $R(MX)$ (~1.17 and 1.38 Å, respectively) than for acetylene. At the B3LYP/6-31G level, the symmetric structure D_{5h} of $CO_2@C_{70}$ and $BeF_2@C_{70}$ (Figure 6) has a small imaginary frequency, and a local minimum of the PES in both cases corresponds the structure C_2, in which the central atom (C or Be) remains in the center of the cage while the axis of the guest molecule is inclined to the C_5 axis of the cage at an angle of ~35°–42°. Structures D_{5h} and C_2 are very close in energy, and within the computational error, one may assume that both tilted MX_2 molecules can precess quasi-freely about the C_5 axis. In the encapsulated guests, the changes in $R(MX)$ and $\nu_{\mathrm{str}}(MX)$ do not exceed a few thousandths of an angstrom and 12–22 cm^{-1} respectively (Table 11).

For the $CO_2@C_{70}$ cluster, the translational frequencies $e_1' = 54\ \mathrm{cm}^{-1}$ and $a_2'' = 122\ \mathrm{cm}^{-1}$ are smaller than for $C_2H_2@C_{70}$; both these vibrations are coupled to the deformation vibrations of the guest and the cage. According to the Mulliken population analysis, there is some electron density redistribution and an increase of polarity of the both $M–X$ bonds in the encapsulated guests, as compared to the free molecules BeF_2 and CO_2 (induced polarization).

For the more tight clusters $SiO_2@C_{70}$ and $CS_2@C_{70}$, the local minimum of the PES corresponds to symmetric structure D_{5h}, the R(SiO) and R(CS) distances are, respectively, 0.013 and 0.045 Å shorter and their ν_{str} frequencies experience a blue shift by ~80 cm^{-1} (Si–O) and 145–245 cm^{-1} (C–S). As in the above clusters, the frequency of the deformation vibration π_u (e_1') is red shifted by 78 (SiO_2) and 145 (CS_2) cm^{-1}. Like the C–O and Be–F bonds, the Si–O bonds compressed in the cage become more polar. In the $CS_2@C_{70}$ cluster, a noticeable charge is transferred from the cage to the sulfur atoms, each of which acquires about $0.07e$ (Table 11).

As compared to CO_2 and BeF_2, the translational frequencies for the bulkier guest molecules increase (50 and 175 cm^{-1} for SiO_2, 173 and 229 cm^{-1} for CS_2) and are coupled to deformations of the XMX bond angle. The librational frequency e_1'' for CS_2 is considerably lower than its translational frequencies, whereas, for SiO_2, e_1'' is intermediate between e_1' and a_2''.

With an increase in the mutual repulsion between guest and cage, the $MX_2@C_{70}$ clusters become more endothermic. The calculated energies of

Table 11 Calculated characteristics of MX_2 molecules in the isolated state and encapsulated into the $C_{70}(D_{5h})$ cage [33]

	BeF_2[a]	$BeF_2@C_{70}$	CO_2	$CO_2@C_{70}$	CS_2	$CS_2@C_{70}$	SiO_2	$SiO_2@C_{70}$
$R(MX)$	1.380	1.383	1.169	1.173	1.563	1.518	1.520	1.507
$\varphi(XMX)$	180°	180°	180°	180°	180°	180°	180°	180°
ν_i, e_1' (π_u)	305 (151)	175 (2)	563 (3)	534 (0)	368 (1)	274 (0)	180 (54)	169 (1)
a_1' (σ_g)	709	731	1282	1301	617	762	848	926
a_2'' (σ_u)	1626 (227)	1629 (9)	2283 (460)	2295 (15)	1485 (492)	1732 (32)	1263 (36)	1340 (2)
$Z(M)$	+0.538	+0.595	+0.719	+0.791	−0.050	−0.014	+0.950	+1.095
$Z(X)$	−0.269	−0.275	−0.360	−0.384	+0.025	−0.041	−0.475	−0.546
$\sigma(C)$	111.9	139.3	74.7	98.7	−5.0	30.0	403.4	423.6
$\sigma(X)$	371.3	395.0	223.0	238.6	532.8	562.3	190.6	220.9

(*continued on next page*)

Table 11 (continued)

	BeF_2[a]	$BeF_2@C_{70}$	CO_2	$CO_2@C_{70}$	CS_2	$CS_2@C_{70}$	SiO_2	$SiO_2@C_{70}$
$h(C_{70})$[b]	7.942	7.960	–	7.941	–	8.061	–	7.983
$R(C_{70})$[c]	3.564	3.563	–	3.568	–	3.550	–	3.557
$R(CC)$[d]	1.452	1.453	–	1.454	–	1.469	–	1.445
$R(XC)$[e]	–	2.876	–	3.055	–	2.804	–	2.775
E_{diss}[f]	–	0.2 (0.6)	–	4.6 (−4.6)	–	−70.7 (−70.3)	–	−9.0 (−9.3)
		0.7						−9.5

[a] In the column under the heading BeF_2, the $h(C_{70})$, $R(C_{70})$, and $R(CC)$ for the isolated (empty) C_{70} molecule are given for comparison.

[b] The C_{70} cage height (along the principal molecular axis $C_5(z)$).

[c] The radius of the C_{70} cage in the equatorial xy plane.

[d] The length of the cage edges of the upper and lower pentagonal faces.

[e] The contact (nonbonded) distances between the H atoms of the guest and the C atoms of the nearest pentagonal face of the cage.

[f] The dissociation energy for $MX_2@C_{70} \rightarrow MX_2 + C_{70}$. The upper values were calculated at the B3LYP/6-31G*//B3LYP/6-31G* level with and without (in parentheses) inclusion of ZPEs, and the lower values were calculated at the MPWB96//MPWB95 level.

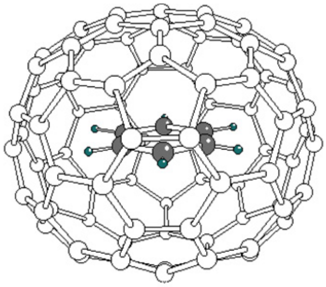

$C_6H_6@C_{84}, D_{6h}$
$B_3N_3H_6@C_{84}, D_{3h}$

Figure 7 The structure of endohedral fullerene clusters with benzene and borazole molecules encapsulated into C_{84} (D_{6h}).

dissociation of $CO_2@C_{70}$ and $BeF_2@C_{70}$ into $MX_2 + C_{70}$ are close to zero, whereas the dissociation of $SiO_2@C_{70}$ and $CS_2@C_{70}$ is accompanied by an energy gain of ∼9 and ∼70 kcal/mol, respectively. One can suppose, that the clusters with a CO_2 molecule inside the C_{70} or larger fullerene cage can, in principle, be synthesized and experimentally studied.

5. PLANAR C_6H_6 AND $B_3N_3H_6$ MOLECULES INSIDE THE OBLATE SPHEROIDAL $C_{84}(D_{6h})$ CAGE

In these clusters, the cage exerts pressure on the guest mainly in the plane perpendicular to the principal molecular axis. As follows from Table 12 and Figure 7 the benzene molecule inside the tight spheroidal C_{84} cage remains planar but undergoes considerable radial contraction [34]. As compared to the isolated C_6H_6, the C–C and C–H bonds in the encapsulated benzene become ∼0.030 Å shorter. According to the Mulliken population analysis (Table 13), this contraction is accompanied by polarization and electron-density redistribution inside the benzene molecule. Each negatively charged C atom loses about 0.05 e while each H atom acquires about 0.08 e, so that the endocluster has the effective electronic configuration $C_6H_6^{-0.14}@C_{84}^{+0.14}$. The $\sigma(C)$ and $\sigma(H)$ constants for the atoms of the encapsulated benzene increase by 15.1 and 12.4 ppm, respectively.

Very large changes are observed in the normal modes of the encapsulated benzene (Table 14). The C–H stretching frequencies ($2a_{1g}$, $3e_{1u}$, $4e_{2g}$, and others) are blue shifted by 400 cm^{-1} or more. The bending vibrations of the guest and the cage are often mixed. The intensities of most IR active modes of the encapsulated benzene obey the general tendency and are almost one order of magnitude lower than those of the free C_6H_6 molecule.

The lowest frequencies, $e_{1g} = 110\ cm^{-1}$ and $2a_{2g} = 160\ cm^{-1}$, correspond to librations of the guest involving its rotations about the x and y axes lying

Table 12 Equilibrium geometric parameters of the C_6H_6, $B_3N_3H_6$, and C_{84} (D_{6h}) molecules in the isolated state and in the endohedral clusters $C_6H_6@C_{84}$ (D_{6h}) and $B_3N_3H_6@C_{84}$ (D_{3h}) [34]

Parameter	Free C_6H_6 and $C_{84}(D_{6h})$ molecules		Endocluster $C_6H_6@C_{84}(D_{6h})$		
	B3LYP 6-31G	B3LYP 6-31G*	B3LYP 6-31G	B3LYP 6-31G*	MPW1B95 6-31G*
$R(CC)^a$	1.400	1.397	1.372	1.367	1.363
$R(CH)^a$	1.086	1.087	1.053	1.054	1.054
$h(C_{84})^b$	7.131	7.111	7.038	7.010	6.918
$d(C_{84})^c$	8.580	8.557	8.716	8.696	8.643
$R(C_eC_e)^d$	1.478	1.472	1.499	1.495	1.481
$R(HC)^e$	–	–	2.226	2.219	2.214

Parameter	Free $B_3N_3H_6$ and C_{84} molecules		Endocluster $B_3N_3H_6@C_{84}(D_{3h})$		
	B3LYP 6-31G	B3LYP 6-31G*	B3LYP 6-31G	B3LYP 6-31G*	MPW1B95 6-31G*
$R(BN)^a$	1.436	1.431	1.395	1.390	1.389
$R(BH)^a$	1.194	1.197	1.122	1.125	1.130
$R(NH)^a$	1.011	1.011	0.994	0.993	0.992
$\varphi(BNB)^a$	122.8	122.8	121.1	120.9	120.9
$h(C_{84})^b$	7.131	7.111	7.017	6.991	6.895
$d(C_{84})^c$	8.580	8.557	8.737	8.716	8.664
$R(C_eC_e)^d$	1.478	1.472	1.503	1.499	1.485
$R(H_BC)^e$	–	–	2.174	2.171	2.144
$R(H_NC)^e$	–	–	2.250	2.251	2.224

[a] The parameters of the benzene and borazole molecules.

[b] The cage height (along the principal molecular axis z).

[c] The diameter of the C_{84} cage (the distance between its opposite atoms) in the equatorial xy plane.

[d] The length of the cage edges in the equatorial xy plane.

[e] The contact (nonbonded) distances between the hydrogen atoms of the guest and the C atoms of the nearest hexagonal face of the cage.

in the benzene plane (e_{1g}) and about the principal axis z (a_{2g}) perpendicular to this plane. Obviously, the rotations about the z axis are more hindered than those about the x and y axes. The next lowest frequencies, $a_{2u} = 170\ \text{cm}^{-1}$ and $e_{1u} = 240\ \text{cm}^{-1}$, are related to the translational vibrations which correspond to the guest displacements along the principal axis (a_{2u}) and along the x and y axes (e_{1u}). The latter are more hindered than the former. The translational vibrations are more hindered than librations. Both types of internal vibrations are weakly coupled to the deformations of the guest and the cage.

Calculations of the borazole endocluster $B_3N_3H_6@C_{84}$ (D_{3h}) [34] give a similar qualitative pattern with some quantitative differences. Upon encapsulation, the B–N bond is 0.01 Å more shortened than the C–C bond.

Table 13 Mulliken effective charges $Z(e)$ and magnetic shielding constants σ (ppm) for the atoms of the C_6H_6 and $B_3N_3H_6$ molecules in the isolated state and encapsulated into the tight C_{84} (D_{6h}) cage[a]

Atom	C_6H_6		$C_6H_6@C_{84}$	
	Z	σ	Z	σ
C	−0.129	67.9	−0.075	83.0
H	+0.129	24.9	+0.052	37.3
	$B_3N_3H_6$		$B_3N_3H_6@C_{84}$	
	Z	σ	Z	σ
B	+0.278	85.3	+0.320	96.9
N	−0.546	137.1	−0.562	153.4
H_B	−0.050	27.3	−0.118	40.4
H_N	+0.318	26.9	+0.346	38.2

[a] Calculations at the B3LYP/6-31G* (Z) and GIAO// B3LYP/6-31G* level (σ).

The shortening of B–H is twice as much, while that of N–H bond is a half as much as the shortening of the C–H bonds in benzene (Table 12). Changes in valence angles φ (BNB) and φ (NBN) do not exceed 2°.

The contraction of borazole leads to an enhancement of the polarity of all bonds (endocyclic B–N and exocyclic B–H and N–H) (Table 13), in contrast to the benzene molecule, whose contraction is accompanied by an increase in the covalent component of the C–H bonds. The charge transfer between the C_{84} cage and the $B_3N_3H_6$ and C_6H_6 guests is small.

The blue shifts of the ν_{str} frequencies of the encapsulated borazole are even greater than those of benzene (Table 14). The e' and a_1' frequencies of the shortened B–H bonds increase by 670–780 cm^{-1}, which is almost 1.5 times larger than the increase found for the C–H bonds in C_6H_6. On the other hand, e' and a_1' frequencies of the less strained N–H bonds increase by 245–255 cm^{-1}, which is 1.5 times smaller than the increase found for C_6H_6. Shifts $\Delta\nu_{\text{str}}$ of the $[B_3N_3]$ and $[C_6]$ rings are close (in the range ~50–110 cm^{-1}). Bending frequencies of borazole are more strongly coupled to cage deformations.

The libration frequencies of borazole are lower than those of benzene; more strongly coupled to borazole bending vibrations and are more split. The lowest frequency $a_2'' = 37\ \text{cm}^{-1}$ corresponds mainly to ring deformation. The next modes, $a_2' = 82\ \text{cm}^{-1}$ and $e'' = 92\ \text{cm}^{-1}$, are related to rotations of the guest about the principal axis $z(C_3)$ and about the perpendicular axes x, y respectively. Translational frequencies are similar for both guests. For borazole, the frequency $a_2'' = 152\ \text{cm}^{-1}$ corresponds to its displacements along the principal z axis, which leads to the ring puckering and deviation of the H atoms from the plane, and $e' = 230\ \text{cm}^{-1}$ is related to its displacements in the xy equatorial plane with moderate in-plane ring deformations.

Table 14 Calculated IR-active $(a_{2u}, e_{1u}, a''_2, e')$[a] and Raman-active $(a_{1g}, e_{1g}, e_{2g}, a'_1)$ normal modes of the C_6H_6 and $B_3N_3H_6$ molecules in the isolated state and encapsulated in the tight C_{84} (D_{6h}) cage [34]

ν_i	C_6H_6		$C_6H_6@C_{84}D_{6h}$	ν_i	$B_3N_3H_6$		$B_3N_3H_6@C_{84}D_{3h}$
	B3LYP 6-31G	B3LYP 6-31G*	B3LYP 6-31G		B3LYP 6-31G	B3LYP 6-31G*	B3LYP 6-31G[b]
$1a_{2u}$	706 (103)	696 (78)	692(1)	$1a''_2$	465 (26)	401 (26)	[b]
$1e_{1u}$	1078 (4)	1069 (3)	1155 (1)	$2a''_2$	744 (62)	733 (61)	[b]
$2e_{1u}$	1542 (9)	1531 (7)	1601 (0.3)	$3a''_2$	996 (366)	936 (247)	[b]
$3e_{1u}$ (CH)	3213 (56)	3201 (52)	3622 (1)	$1e'$	535 (0.3)	524 (0.7)	[b]
$1a_{1g}$	1022	1021	1143	$2e'$	941 (0)	943 (0)	[b]
$2a_{1g}$ (CH)	3227	3211	3630	$3e'$	1095 (0)	1077 (0.2)	1143 (0.6)
$1e_{1g}$	884	866	890	$4e'$	1418 (48)	1401 (13)	1470 (0.6)
$1e_{2g}$	640	622	682	$5e'$	1487 (463)	1494 (493)	1592 (18)
$2e_{2g}$	1232	1208	1310	$6e'$(BH)	2654 (302)	2647 (292)	3330 (7)
$3e_{2g}$	1654	1657	1763	$7e'$(NH)	3621 (27)	3614(35)	3867 (7)
$4e_{2g}$ (CH)	3194	3185	3613	$1a'_1$	865	865	[b]
–	–	–	–	$2a'_1$	960	945	947
–	–	–	–	$3a'_1$(BH)	2666	2657	3336
–	–	–	–	$4a'_1$(NH)	3620	3612	3877

[a] The intensities of the bands in IR spectra (km/mol) are parenthesized.

[b] The moderate- and long-wavelength vibrations of the borazole molecule inside C_{84} are strongly mixed with cage vibrations and their assignment is conjectural.

Thus, the C_6H_6 and $B_3N_3H_6$ molecules inside the tight cages undergo significant radial contraction and electron density redistribution. The stronger bonds are polarized and shortened to a smaller extent, and the weaker bonds to a greater extent. The character of their polarization is different: in benzene, the C–H bonds become more covalent; while in borazole, all bonds become more polar. The contraction and polarization manifest themselves in the very large blue shifts of the frequencies of bond stretches, which can be used for IR and Raman interpretation of the changes in the properties and behavior of the molecules at high and superhigh pressures. Using the same model that we used in Section 3.3, we can suppose that the internal pressure in $C_6H_6@C_{84}$ should be roughly five- to tenfold higher that in $CH_4@C_{84}$.

The encapsulated carbonyl hexamer C_6O_6 represents an example of an "artificial" guest. Within the B3LYP approximation, the isolated (free) C_6O_6 moiety has the elongated R(CC) distances ~1.55 Å and corresponds to a very shallow local minimum on the PES which lies about 6 kcal/mol above the dissociation limit (to 6CO) and is hardly stable. When inserted into the C_{84} cage, the C–O and C–C bonds of the guest are shortened by 0.01 and 0.11 Å, and their stretching frequencies increase by ~270 and ~335 cm^{-1} respectively. In contrast to C_6H_6 and $B_3N_3H_6$, which remain planar both in the isolated and encapsulated states, the D_{6h} structure of C_6O_6 in the $C_6O_6@C_{84}$ cluster has two imaginary frequencies, and after symmetry releasing it transforms into the most favorable "crown"shaped isomer C_{6v}, which lies ~51 kcal/mol lower than D_{6h}. In the structure C_{6v} the gap between the plane containing six O atoms and the plane of the C_6 ring is about 0.50 Å, and all C–O bonds are tilted to the plane of the C_6 ring by an angle ~139°. It is worth mentioning that inside the C_{84} cage, the more traditional "chair" and "boat" conformations of the guest are less favorable in energy compared to the "crown" conformation. The translational frequencies of in-plane (~220 cm^{-1}) and out-of-plane vibrations (~250 cm^{-1}) are moderately split by ~30 cm^{-1}. Rotation of the C_6O_6 guest around the C_5 axes is forbidden.

6. THE "MATRESHKA-LIKE" CLUSTERS $L@Al_{12}Al_{20}O_{30}(I_h)$ AND $L@He_{12}@C_{60}(I_h)$

In this section we discuss another family of high-symmetrical strained clusters in which the icosahedral aluminum "subcluster" Al_{12} with diameter ~5.2 Å and with a "dopant" atoms L or isoelectronic ions in the center ($L = B^-, C, N^+, Al^-$, and Si), is inserted into the dodecahedral cage $Al_{20}O_{30}$ with diameter ~9.5 Å (Figure 8). All calculations were performed at the B3LYP/6-31G* level [61].

The isolated doped aluminum clusters $L@Al_{12}$ with various dopants L have been systematically calculated earlier [62]. In [35] it was predicted that the dodecahedral isomer $Al_{20}O_{30}$ (I_h) is a high-lying intermediate which is, by ~130–150 kcal/mol, less favorable as compared with the more compact

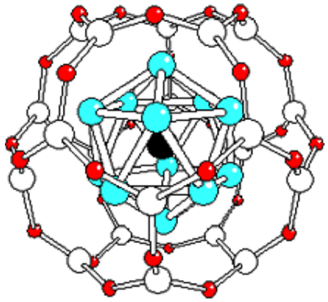

Figure 8 The structure of the "matreshka-like" $L@Al_{12}@Al_{20}O_{30}$ cluster.

"puck"-shaped isomers, where most of Al atoms are five-coordinated and most of O atoms are three- and four-coordinated. Nevertheless, the $Al_{20}O_{30}$ (I_h) has all its vibrational frequencies real, is stabilized kinetically by a barrier and preserves the *closo*-structure under various deformations, asymmetrical solvation by donor molecules like NH_3, etc. (see [35] for detail). The "matreshka"- like clusters $L@Al_{12}@Al_{20}O_{30}$ (I_h) are very endothermic indeed, and they are discussed here as an extremely strained model, where effects of geometry contraction, electron density redistribution and the $\Delta\nu$ and $\Delta\sigma$ shifts should be manifested more distinctly than in previous sections.

One can see from Table 15 that the diameter $D(Al_iAl_i)$ of the encapsulated $L@Al_{12}$ is shortened by 0.20–0.30 Å (as compared with that of $L@Al_{12}$). This compression increases in the row of $L = N^+ < C < B^- < Si < Al^-$ and is accompanied by significant (about $1 - 2e$) charge transfer between the guest and the external cage. The $Al_{20}O_{30}$ cage donates and the icosahedral guest accepts electrons. The charge transfer is maximal in the case of the light dopants (C and especially B^-), and decreases when going from the anions to the isoelectronic neutral clusters and when the light dopants are substituted by the heavier analogs Si and Al^-. The external diameters $D(AlAl)$ and $D(OO)$ of the $Al_{20}O_{30}$ cage are increased by 0.10–0.20 and 0.20–0.30 Å respectively in the opposite manner to the compressing of the $L@Al_{12}$ guest.

In addition to the cage-to-guest donation, a significant electron density inside the inserted $L@Al_{12}$ guest should be noted. In the case of $L = Al^-$ and Si, the aluminum Al_{12} shell accepts electrons both from the external $Al_{20}O_{30}$ and from the internal dopant. The effective charge of the latter increases significantly by ~1.5 e (Al^-) and ~0.8 e (Si) as compared with its effective charge in the free $L@Al_{12}$ molecules. In the neutral $Si@Al_{12}@Al_{20}O_{30}$ the charge transfer to Al_{12} shell from the $Al_{20}O_{30}$ cage is larger than that from the dopant, while in the anion $Al@Al_{12}@Al_{20}O_{30}^-$, in contrast, the dopant donates more charge than $Al_{20}O_{30}$. In the case of the light dopants $L = B^-$ and C, practically all the electron density is donated from the external cage, increasing

Table 15 Geometrical parameters and vibrational frequencies of the icosahedral $L@\mathrm{Al}_{12}$ guest and the dodecahedral $\mathrm{Al}_{20}\mathrm{O}_{30}$ cage in the isolated state (A) and in the matreshka-like $L@\mathrm{Al}_{12}@\mathrm{Al}_{20}\mathrm{O}_{3}$ clusters (B)[a]

	Internal guest $L@\mathrm{Al}_{12}$									
	$\mathrm{B@Al}_{12}^{-}$		$\mathrm{C@Al}_{12}$		$\mathrm{Al@Al}_{12}^{-}$		$\mathrm{Si@Al}_{12}$		$\mathrm{N@Al}_{12}^{+}$	
	A	B	A	B	A	B	A	B	A	B
$D(\mathrm{Al}_i\mathrm{Al}_i)$	5.246	4.980	5.228	4.984	5.536	5.228	5.505	5.220	5.258	5.020
$R(\mathrm{Al}_i\mathrm{Al}_i)$	2.758	2.618	2.748	2.620	2.910	2.748	2.895	2.744	2.765	2.638
$R(\mathrm{Al}_i\mathrm{Al}_e)$		3.122		3.144		3.094		3.109		3.160
$R(\mathrm{Al}_i\mathrm{O}_e)$		3.110		3.094		3.067		3.045		3.061
ν_i, $1t_{1u}$	240	333	223	328	132	220	153	230	111	190
$2t_{1u}(L)$	343	460	287	378	358	470	354	459	266	343

	External cage $\mathrm{Al}_{20}\mathrm{O}_{30}$					
	A	B				
		$\mathrm{B@Al}_{12}^{-}$	$\mathrm{C@Al}_{12}$	$\mathrm{Al@Al}_{12}^{-}$	$\mathrm{Si@Al}_{12}$	$\mathrm{N@Al}_{12}^{+}$
$R(\mathrm{AlO})$	1.716	1.768	1.762	1.742	1.767	1.757
$D(\mathrm{AlAl})$	9.305	9.421	9.471	9.466	9.499	9.525
$D(\mathrm{OO})$	9.560	9.896	9.844	9.930	9.877	9.792
$\varphi(\mathrm{AlOAl})$	150.7	143.9	147.2	144.3	147.0	150.5
$\varphi(\mathrm{OAlO})$	118.8	119.8	119.4	119.7	119.0	118.9
ν_i, $4t_{1u}$	1114	939	953	913	936	969
h_g	1102	943	962	925	946	977

[a] In the upper part of the table, $R(\mathrm{Al}_i\mathrm{Al}_i)$ and $D(\mathrm{Al}_i\mathrm{Al}_i)$ are length of an edge and diameter of the $L@\mathrm{Al}_{12}$ guest, $R(\mathrm{Al}_i\mathrm{Al}_e)$ and $R(\mathrm{Al}_i\mathrm{O}_e)$ are distances between atom Al_i of the guest and the nearest Al and O atoms of the $\mathrm{Al}_{20}\mathrm{O}_{30}$ cage. The $2t_{1u}$ mode frequency corresponds to vibration of the central L dopant atom inside the Al_{12} subshell. See also notes to the previous tables.

sharply in the row $L = \mathrm{B}^{-}$ to C to N^{+} from ~1.35 e for the anion to ~2.75 e for the cation.

The charge redistribution of the external cage is also significant. As compared with the isolated $\mathrm{Al}_{20}\mathrm{O}_{30}$, in $L@\mathrm{Al}_{12}@\mathrm{Al}_{20}\mathrm{O}_{30}$ (I_h) each O atom looses about 0.33 e and each Al atom accepts about 0.40–0.45 e. In contrast to the guest, in the external cage these "partial" changes of the atomic effective charges are almost insensitive to the nature of the dopant. Although values of the effective charges evaluated within the Mulliken population analysis can be approximate, the tendency of electron transfer from more electronegative to more electropositive atoms in strongly strained onion-like clusters seems to be correct.

The lowest frequencies $\nu(1t_{1g}) \sim$ 100–110 cm^{-1} and $\nu(1t_{1u}) \sim$ 120–127 cm^{-1} correspond to rotational and translational vibrations of the icosahedral $L@\mathrm{Al}_{12}$ guest as a whole inside the $\mathrm{Al}_{20}\mathrm{O}_{30}$ cage. The largest IR-active frequency $\nu(t_{1u})$ within the range ~340–470 cm^{-1} is related mostly to vibration of the central dopant atom L inside the icosahedral Al_{12} subshell and increases significantly (by $\sim$ 80–120 cm^{-1}) as compared with its value in the isolated $L@Al_{12}$ cluster. This blue shift rises in the row of $L = N^+ < C < Si < B^- < Al^-$, which is similar to the "compression row" (see above) with a minor difference (permutation of the close-standing Si and B^- neighbors). In other (intermediate) t_{1u} modes, vibrations of the guest L atom and Al_{12} shell are strongly coupled both with each other and with vibrations of the cage.

Other extreme models are "supertight" icosahedral clusters $He_{12}@C_{60}$ and $L@He_{12}@C_{60}$ (I_h) calculated by us within the same B3LYP approximation [63]. All these structures were found to be local minima on PES. The latter clusters contain a central atom (ion) $L = He, Kr, Be, Na^+, Mg^{2+}$, etc. inside the icosahedral He_{12} subshell, which in turn is highly compressed inside the C_{60} shell. The qualitative picture here is quite similar to that described above for $L@Al_{12}@Al_{20}O_{30}$. The calculated diameter and distance R(HeHe) of the He_{12} "subcluster" in $He_{12}@C_{60}$ are extrashort ($\sim$3.18 and $\sim$1.67 Å), the frequencies $\nu(1t_{1g})$ and $\nu(1t_{1u})$ of rotation and translation of the He_{12} moiety as a whole inside C_{60} are $\sim$90 and $\sim$410 cm^{-1} respectively. In $He@He_{12}@C_{60}$ (I_h), where the diameter and R(HeHe) are elongated to $\sim$3.26 and $\sim$1.71 Å, these frequencies vary only slightly, and the frequency $\nu(4t_{1u})$ of translation of the central He atom is $\sim$750 cm^{-1}. The distance R(HeC) between helium and carbon atoms of the cage in $He@He_{12}@C_{60}$ is only $\sim$0.03 Å longer than that in $He_{12}@C_{60}$.

7. ATOMS CONFINED INSIDE THE SUPERTIGHT [He_{12}] ICOSAHEDRAL "BOX"

It is also worthwhile mentioning the results of our calculations [63] for the "very abstract model" systems $L@[He_{12}]$ (I_h), which are "cut off" from the above discussed matreshka-like $L@He_{12}@C_{60}$ clusters, and which contain atoms (ions) L in the center of the "rigid" helium icosahedral "box" [He_{12}] with fixed values of the radius $R(L\mathrm{He})$. Total and relative (ionization potentials IP and s → p promotion energies $E(\mathrm{s} \rightarrow \mathrm{p})$) energies of the $L@[He_{12}]$ clusters were compared with those of the isolated (free) atoms L, calculated at the same level, to follow trends in decreasing IP and $E(\mathrm{s} \rightarrow \mathrm{p})$ with decreasing of the radius $R(L\mathrm{He})$ and compression of the [He_{12}] box from "moderately tight" to "very tight". Due to the small size of these systems, the single-point calculations of their total energies and relative energies have been performed in parallel within two approximations, B3LYP and CCSD(T), with the 6-311++G** basis set, for atoms and single charged ions of the first three rows of the Periodic table (from Li to Kr) at the following fixed values of the radius $R(L\mathrm{He})$ (in Å): 3.00, 2.50, 2.00, and 1.71. Two conclusions [63] are of the most interest here.

Ionization potentials $IP(L) = E_{\mathrm{tot}}(L) - E_{\mathrm{tot}}(L^+)$ and s → p promotion energies ($E(s \rightarrow \mathrm{p}) = E_{\mathrm{tot}}(L, \mathrm{s}^2\mathrm{p}^m) - E_{\mathrm{tot}}(L, \mathrm{sp}^{m+1})$, calculated within the

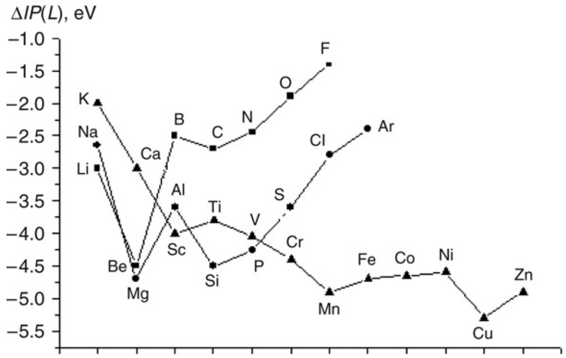

Figure 9 Differences (negative shifts) of ionization potentials of atoms L constrained in the center of the "supertight" [He_{12}] box with a fixed radius $R(L\mathrm{He}) = 2.00$ Å, as compared with IP of the free atoms L.

B3LYP and the coupled clusters CCSD(T) approximations, are in a reasonable semiquantitative agreement each with other both for isolated atoms L from the first two rows (L = Li–Ar) and for their clusters L@[He_{12}]. The trends in behavior of the IP and $E(\mathrm{s} \rightarrow \mathrm{p})$ values, when L is changing along a period or a subgroup of the Periodic table, as well as their decrease ΔIP and $\Delta E(\mathrm{s} \rightarrow \mathrm{p})$ when going from the isolated L atoms to those encapsulated inside the L@[He_{12}] clusters, are reproduced in quite a similar manner in both approximations within the range of $R(L\mathrm{He})$ from 3.00 to 2.00 Å. The difference between the B3LYP and CCSD(T) data for the absolute IP, $E(\mathrm{s} \rightarrow \mathrm{p})$, ΔIP, and $\Delta E(\mathrm{s} \rightarrow \mathrm{p})$ values does not exceed a few tenths eV for the moderately tight [He_{12}] box and ~0.5–1.0 eV for the "very tight" one. This agreement gives a hope that the trends, calculated for the larger endoclusters at the B3LYP level only and discussed in the previous sections of the present paper, will not change significantly when more sophisticated calculations become possible in the future.

In Figure 9 the differences (negative shifts) $\Delta IP = IP(L@[\mathrm{He}_{12}]) - IP(L)$ of ionization potentials when going from the free L atoms of the first three rows to those inserted inside L@[He_{12}] at $R(L\mathrm{He}) = 2.00$ Å are drawn (the $IP(L)$ values of the isolated L atoms are referenced as zero). One can see that when L atoms are encapsulated in the very tight [He_{12}] box, their IP decrease by ~2–5 eV. For the atoms from the first two rows, this negative shift ΔIP is more significant in the first half of the rows (with the maximum, by absolute value, for Be and Mg (s^2 shell), the intermediate minimum for B an Al (s^2p shell)) and decrease monotonically along their second half along with decreasing of polarizability of the s^2p^m shell. For the bulkier atoms from the second row the ΔIP shifts are more significant (by ~1.5–0 eV) than those for their analogs from the first row, with the exception of alkali and alkali-earth metals, where the differences do not exceed 0.3 eV. For atoms of the third row (calculated at the B3LYP level only), ΔIP is minimal for potassium and, more or less monotonically, slowly increases along the row with small intermediate maxima for Sc (ds^2), Mn(d^5s^2), and Cu ($d^{10}s$).

In accord with calculations, the negative shifts ΔIP for the single-charged positive ions L^+ as a rule are larger than those for the isoelectronic neutral atoms L by ~1–2 eV. As regard to change of the promotion $E(\mathrm{s} \rightarrow \mathrm{p})$ energy, the calculations of $E(\mathrm{s} \rightarrow \mathrm{p}) = E_{\mathrm{tot}}(L, \mathrm{s}^2) - E_{\mathrm{tot}}(L, \mathrm{sp})$ for the isolated and inserted atoms of the second group of the Periodic table predict that, upon L encapsulation, this energy also decrease by ~1.8 eV for Be and by ~2.6–2.9 eV for Mg, Ca, and Zn, thus indicating that the valence s-level is destabilized more significant than the p-level upon L encapsulation.

The most dramatic perturbations were predicted for the $L@[\mathrm{He}_{12}]$ clusters with L inside the "supertight" $[\mathrm{He}_{12}]$ box with the shortest $R = 1.71$ Å, which corresponds to the equilibrium value of the internal radius in $\mathrm{He@He}_{12}@\mathrm{C}_{60}$. The calculated ionization potentials of all negative atomic ions and neutral alkali metal atoms inserted in this box decrease so much that their (*IP* values) appear to be negative. This conclusion can be drawn both from B3LYP and from CCSD(T) calculations, indicating that both negative atomic ions and neutral-most electropositive atoms could undergo a "self-ionization" procedure under these extremal conditions. In the more spacious $[\mathrm{He}_{12}]$ box, with fixed $R(L\mathrm{He}) = 3.00$ Å, the negative shifts of *IP* and $E(\mathrm{s} \rightarrow \mathrm{p})$ are much weaker manifested, and as a rule do not exceed a few tenths of eV. However, these predictions should be treated as qualitative.

We restricted our consideration to a few families, which model a rather wide range of endoclusters, from spacious to tight and very tight, from neutral to positively and negatively charged, with isotropic or anisotropic compression of the encapsulated guest along or perpendicular to the principal molecular axis, etc. They all correspond to local minima of PES. The endoclusters for which the insertion of the guest is accompanied by a small or modest energetic effect, in principle, can exist and be experimentally studied. The highly endothermic ones could be treated as extreme models of strained molecules under high or superhigh pressure, in which the host–guest interaction effects clearly manifest themselves in geometric deformations and in shifts of spectroscopical properties. In the charged ions, not only charge transfer between the guest and the cage, but also electron density redistributions inside the guest and inside the cage can be important, and both steric and electronic factors should be taken into account. Ab initio calculations of their PESs may be useful for testing and calibrating various semiempirical models (for spherical cages and cages of other shapes) dedicated to describing the changes in the molecular properties under high pressures. Similar cage models have been extensively developed in recent years because of the prospects of obtaining new materials under high pressures (see, e.g., [64–66] and other papers in this book). We hope that our calculations and qualitative conclusions will stimulate both experimental and more sophisticated theoretical investigations in this rather poorly studied area.

NOTE ADDED IN PROOF

The referee attracted our attention to a few recent publications we had missed when submitting the manuscript. In the interesting paper by A. Krapp and G. Frenking (Chemistry-A European J., **13**, 8256 (2007)), a family of $Ng_2@C_{60}$ clusters (Ng = He, Ne, Ar, Kr, and Xe) was calculated with the DFT, MP2 and SCS-MP2 approximations and the nature of the interaction between two endohedral *Ng* atoms was analyzed with charge- and energy-partitioning methods as well as with a topological analysis of the electron density. The authors found significant (about one electron) charge transfer from the inserted Xe_2 moiety to the C_{60} cage and suggested formation of a "genuine chemical bond" between two short-distant Xe atoms which are enforced by the internal compression. Their conclusion is consistent with the results of our papers [32,36], in which a similar significant charge transfer ($\sim 0.6\ e$ from the Kr_4 and more than $1.0\ e$ for Xe_4) to the $C_{60}H_{36}$ cage was found for $Ng_4@C_{60}H_{36}$ clusters by using Mulliken population analysis (see also Section 3.4 of this paper). For the heaviest (and least "electronegative") noble gas atoms as well as for other related species with moderate *IP* values, the Coulombic attraction between positively charged guest and negatively charged cage should be important.

In another paper by C.N. Ramachandran, D. Roy, and N. Sathyamurthy (Chem. Phys. Letters, **461**, 87 (2008)),which was issued after our paper was submitted, the host-guest interaction between C_{60} fullerene and inserted H^+, H^-, He, and Li ions and atoms, and the H_2 molecule was also examined within the MP2 approximation and using Bader's theory of atoms-in-molecules.

ACKNOWLEDGEMENTS

Calculations were performed in the Institute of Atomic and Molecular Science of Academia Sinica in Taipei (Taiwan). The authors thank Prof. S.H. Lin and Dr. A.M. Mebel for invitations to visit IAMS, and the Computer Center of Academia Sinica for computer time and help in performing calculations.

REFERENCES

[1] R. Dagani, Chem. Eng. News 80 (24) (2002) 32.
[2] M. Takata, E. Nishibori, M. Inakuma, et al., Phys. Rev. Lett. 83 (1999) 2214.
[3] S. Stevenson, G. Rice, T. Glass, et al., Nature 401 (1999) 55.
[4] S. Stevenson, P.W. Fowler, T. Heine, et al., Nature 408 (2001) 428.
[5] C.-R. Wang, T. Kai, T. Tomiyama, et al., Angew. Chem., Int. Ed. Engl. 20 (2001) 397.

[6] K. Gluch, S. Feil, S. Matt-Leubner, et al., J. Phys. Chem. A 108 (2004) 6990; H. Shinohara, Rep. Progr. Phys. 63 (2000) 843.
[7] S. Nagase, K. Kobayashi, T.J. Akasaka, T. Wakahara, in: K.M. Kadish, R.S. Ruoff (Eds.), Fullerenes: Chemistry, Physics, and Technology, Wiley, New York, 2000.
[8] M. Saunders, H.A. Jimmenez-Vazquez, R.J. Cross, et al., Nature 367 (1994) 256.
[9] M. Saunders, R.J. Cross, H.A. Jimmenez-Vazquez, et al., Science 271 (1996) 1693.
[10] M.S. Syamala, R. Cross, M. Saunders, J. Am. Chem. Soc. 124 (2002) 6216.
[11] T. Sternfeld, R.E. Hoffman, M. Saunders, et al., J. Am. Chem. Soc. 124 (2002) 8786.
[12] J. Laskin, T. Peres, C. Lifshitz, et al., Chem. Phys. Lett. 285 (1998) 7.
[13] W.E. Billups, A. Gonzalez, C. Gesenberg, et al., Tetrahedron Lett. 38 (1996) 175.
[14] M. Saunders, H.A. Jimmenez-Vazques, R.J. Cross, et al., J. Am. Chem. Soc. 117 (1995) 9305.
[15] M. Buehl, W. Thiel, H. Jiao, et al., J. Am. Chem. Soc. 116 (1994) 6005.
[16] J. Cioslowski, Chem. Phys. Lett. 227 (1994) 361.
[17] M. Buehl, W. Thiel, Chem. Phys. Lett. 233 (1995) 585.
[18] M. Buehl, W. Thiel, U. Schneider, J. Am. Chem. Soc. 117 (1995) 4623.
[19] M. Buehl, S. Patchkovskii, W. Thiel, Chem. Phys. Lett. 275 (1997) 14.
[20] D.N. Sears, C.J. Jameson, J. Chem. Phys. 118 (2003) 9987.
[21] R.B. Darzynkievicz, G.E. Scuseria, J. Phys. Chem. A 101 (1997) 7141.
[22] O.P. Charkin, N.M. Klimenko, D. Moran, et al., Russ. J. Inorg. Chem. 46 (2001) 110.
[23] O.P. Charkin, N.M. Klimenko, D. Moran, et al., Inorg. Chem. 40 (2001) 6913.
[24] Y. Rubin, T. Jarosson, G.-W. Wang, et al., Angew. Chem., Int. Ed. Engl. 40 (2001) 1543.
[25] Y. Murata, M. Murata, K. Komatsu, J. Am. Chem. Soc. 125 (2003) 7152.
[26] C.M. Stanisky, R.J. Cross, M. Saunders, et al., J. Am. Chem. Soc. 127 (2005) 299.
[27] E. Kemner, A. Hirsch, F. Zerbetto, J. Phys. Chem. A 108 (2004) 7135.
[28] S. Irle, I. Rubin, K. Morokuma, J. Phys. Chem. A 106 (2002) 680.
[29] S.-I. Iwamatsu, T. Uozaki, K. Kobayashi, et al., J. Am. Chem. Soc. 126 (2004) 2668.
[30] O.P. Charkin, N.M. Klimenko, D.O. Charkin, A.M. Mebel′, Russ. J. Inorg. Chem. 49 (2004) 723.
[31] O.P. Charkin, N.M. Klimenko, D.O. Charkin, A.M. Mebel′, Russ. J. Inorg. Chem. 49 (2004) 868.
[32] O.P. Charkin, N.M. Klimenko, D.O. Charkin, A.M. Mebel′, Russ. J. Inorg. Chem. 49 (2004) 1382.
[33] O.P. Charkin, N.M. Klimenko, D.O. Charkin, A.M. Mebel′, Russ. J. Inorg. Chem. 50 (2005) 1903.
[34] O.P. Charkin, N.M. Klimenko, D.O. Charkin, A.M. Mebel′, Russ. J. Inorg. Chem. 50 (2005) 1702.
[35] O.P. Charkin, N.M. Klimenko, D.O. Charkin, Russ. J. Inorg. Chem. 53 (2008) 624.
[36] O.P. Charkin, N.M. Klimenko, D.O. Charkin, A.M. Mebel, S.H. Lin, Russ. J. Inorg. Chem. Suppl. 1 51 (2006) S1.
[37] J. Cioslowski, E.D. Fleischman, J. Chem. Phys. 94 (1991) 3730.
[38] J. Cioslowski, J. Am. Chem. Soc. 113 (1991) 4139.
[39] O. Shameema, C.N. Ramachandran, N. Sathyamurthy, J. Phys. Chem A. 110 (2006) 2.
[40] A. Rehaman, L. Gagliardi, P. Pyykko, Int. J. Quant. Chem. 107 (2007) 1162.
[41] L. Gagliardi, J. Chem. Theory Comput. 1 (2005) 1172.
[42] A.D. Becke, J. Chem. Phys. 98 (1993) 5648.
[43] C. Lee, W. Yang, R.G. Parr, Phys. Rev. B: Condens. Matter 37 (1988) 785.
[44] R. Ditchfield, Mol. Phys. 27 (1974) 789.
[45] K. Wolinski, J.F. Hilton, P. Pulay, J. Am. Chem. Soc. 112 (1990) 8251.
[46] I.S. Neretin, K.A. Lyssenko, M.Yu. Antipin, et al., Angew. Chem. 39 (2000) 3273.
[47] S.I. Troyanov, P.A. Troshin, O. Boltalina, et al., Angew. Chem. 40 (2001) 2285.
[48] V. Schettino, M. Pagliai, L. Ciabini, G. Cardini, J. Phys. Chem. A 105 (2001) 11192.
[49] V. Schettino, M. Pagliai, G. Cardini, J. Phys. Chem. A 106 (2002) 1815.
[50] A.A. Popov, A.A. Goryunkov, I.V. Goldt, et al., J. Phys. Chem. A 108 (2004) 11456.
[51] Y. Zhao, D.G. Truhlar, J. Phys. Chem. A 108 (2004) 6908.
[52] L. Turker, J. Mol. Struct. (THEOCHEM) 619 (2002) 107.

[53] L. Turker, J. Mol. Struct. (THEOCHEM) 634 (2003) 195.
[54] D. Smith, Chem. Rev. 94 (1994) 1567.
[55] O.P. Charkin, N.M. Klimenko, P.V.R. Schleyer, Russ. J. Inorg. Chem. 45 (2000) 1539.
[56] O.P. Charkin, N.M. Klimenko, D. Moran, et al., J. Phys. Chem. A 106 (2002) 11594.
[57] S.M. Peiris, G.I. Pangilinan, T.P. Russel, J. Phys. Chem. A 104 (2000) 11188.
[58] O.P. Charkin, N.M. Klimenko, D.O. Charkin, A.M. Mebel, Unpublished results.
[59] N. Godbout, D.R. Salahub, J. Andzelm, E. Winner, Can. J. Chem. 70 (1992) 560.
[60] O.P. Charkin, N.M. Klimenko, D.O. Charkin, Unpublished results.
[61] O.P. Charkin, Unpublished results.
[62] O.P. Charkin, D.O. Charkin, N.M. Klimenko, A.M. Mebel, Chem. Phys. Letters 365 (2002) 494.
[63] O.P. Charkin, N.M. Klimenko, D.O. Charkin, Russ. J. Inorg Chem., 54(2009) (in press).
[64] R.J. Hemley, Ann. Rev. Phys. Chem. 51 (2000) 763.
[65] S.A. Cruz, J. Soullard, Chem. Phys. Lett. 391 (2004) 138.
[66] T. Saki, I. Chernusak, G.H.F. Dierksen, J. Phys. B: At. Mol. Opt. Phys. 37 (2004) 1091.

CHAPTER 4

Spectroscopy of Confined Atomic Systems: Effect of Plasma

A.N. Sil[a], **S. Canuto**[b] and **P.K. Mukherjee**[c]

Contents

[a] Max Planck Institute for the Physics of Complex Systems, Nöthnitzer Str. 38, 01187 Dresden, Germany
[b] Instituto de Física, Universidade de São Paulo, CP 66318, São Paulo, SP 05315-970, Brazil
[c] Department of Spectroscopy, Indian Association for the Cultivation of Science, Jadavpur, Kolkata-700 032, India

---

Advances in Quantum Chemistry, Vol. 58
ISSN: 0065-3276, DOI: 10.1016/S0065-3276(09)00708-4

1. INTRODUCTION

A quantum mechanical solution to the energy spectrum of the particle in a box reveals, in its simplest form, the difference between the energy spectrum of a free particle and that of a confined particle. However, the meaning of confinement becomes much more general as experimental techniques have been developed gradually, particularly, in relation to layered semiconductor structure, in which the concept of quantum dots, quantum wires and quantum wells has been originated [1–5]. Specially interesting is the case of a quantum dot where spatially confined electrons are responsible for new physical phenomena of technological importance [3–6]. There are ample examples in nature of atoms and molecules residing inside cavities, such as zeolite sieves [7,8], fullerenes [9–13], solutes under solvent environments [14–17] and the reversible storage of ions in certain solids [18]. A large number of other classes of confined systems occur in nature and also can be produced in laboratories. A good review in this line is due to Jaskolski [19]. If the potential felt by an electronic charge cloud of an atom is different from that experienced by a free atom we may consider this as a confined atomic system. We will focus only on bound state properties of the system and collisional aspects from other interesting potentials are not in the present scope. It is obvious that the physico-chemical properties of the confined system will alter depending on the nature of the confining potential. In addition to spatial confinement, environmental effects also influence the properties of atomic systems embedded in them through the presence of different interactions. Spatial confinement usually produces a barrier and thus alters the boundary conditions imposed on the wavefunctions. The problem of an atom confined within a sphere was considered first by Michels et al. [20]. Sommerfeld and Welker [21] investigated in detail the binding energy of a hydrogen atom placed at the center of a cavity of a given radius, taken as a first approximation to a Wigner-Seitz cell, which is assumed to be an impenetrable cage. The variation of the binding energy with change of the cavity radius is analyzed. It was observed that the binding energy diminishes with the decrease of the cage radius and becomes zero at a given radius called the critical radius, indicating instability in the system. For the ground state the critical radius has been estimated as 1.835 au. Sommerfeld and Welker [21] discussed this issue in relation to formation of a conduction band in a solid with the delocalized electron as a free electron in a Wigner-Seitz cell formed outside the cage. Further studies in this line by Boeyens [22] using Hartree-Fock (HF) method provide the critical radii for the ground state of most of the atoms. A large number of theoretical investigations dealing with binding energies and other structural properties along this line are now available [22–41]. Varshni [42] performed detailed calculations on the stability of the excited states of the hydrogen atom for levels up to n=10. Relativistic effects of a cavity embedded hydrogen atom and its isoelectronic series have been analyzed by Huang et al. [43]. Properties of confined quantum chaos were discussed using a model due to Hu et al. [44]. The energy spectra of ground, ionized and excited states of many electron atomic systems in which 3d and 4d orbital collapse occurs [45], have been obtained by Connerade et al. [46,47] using HF configuration averages, modifying thereby the filling of shells in compressed atoms. From the detailed calculations of Connerade and Dolmatov [46] one finds the interesting trend that in a many-electron atom the filling of different shells should be more hydrogen-like with the decrease of cavity radius, thereby increasing the pressure on the atom and hence, in some cases, different from the free system. The atoms belonging to transition series exhibiting orbital collapse are particularly sensitive to environmental changes. Differences in the filling of shells of free transition atoms between successive rows in the periodic table disappear for atoms within a given cavity radius and new regularities appear in the overall organization of the periodic table for confined atoms. When the atom is destabilized the electron is bound by the cavity and is completely delocalized from the atom itself. This may be a primitive description of the formation of a conduction band in a Wigner-Seitz cell. Different theoretical methods to tackle various extended confined systems like zero, one and three dimensional electron gases, semiconductor and metallic quantum wells, several atoms, molecules and excitons etc. with special emphasis on the spatial confinement have been discussed by Bastard [48].

Among the different forms of external confinement, atoms or ions embedded in a plasma also form a class of confined systems. Depending on the coupling strength of the plasma with the atomic electrons, the atomic structural properties may change quite drastically. In a finite density plasma the potential function in the neighborhood of an ion is influenced by its own bound electrons, available free electrons, by neighboring ions and also, to a small extent, by neutral atoms. The time-averaged effect due to such a perturbation on the atomic electrons produces change in the energy levels, their time-dependent effect is responsible for the broadening of the spectral line. The main feature of this perturbation is a lowering of the ionization potential and pressure broadening of the spectral line. In the low density and high temperature limit the randomness of the ion positions in the neighborhood of the atom leads to Debye–Hückel [49,50] potential. The problem of an atom embedded in an electron gas at a temperature T was treated by Feynman et al. [51] using a finite temperature Thomas Fermi model, and later on extended by Cowan and Ashkin [52]. A finite temperature HF scheme was adopted by Husimi [53] to find the electronic states of an atom embedded in plasma. Quantum statistical methods have been adopted by Dharma-Wardana et al. [54] to find the atomic energy levels in a hot dense plasma. Density functional theory as developed by Hohenberg, Kohn and Sham [55,56] has been applied by Gupta and Rajagopal [57] to find atomic properties under a hot dense plasma. Stewart and Pyatt [58] evaluated the reduction of the ionization potential for a number of atoms, using a finite temperature Thomas Fermi model for the electrons, which has previously been employed by Marshak and Bethe [59], Feynman et al. [51] and Latter [60] to calculate the equation of state for high density matter. The plasma potential in the high temperature, low density limit (Debye–Hückel) as well as the high density, low temperature (Ion Sphere) models has also been extracted by Stewart and Pyatt [58]. Besides the case of weakly and strongly coupled plasma, a new frontier is emerging rapidly in the domain of ultracold neutral plasma produced by photoionizing laser cooled atoms near the ionization threshold having electron temperature ~1–1000 K and ion temperature ~1 K [61].

The domain of the calculations based on weakly and strongly coupled plasma can be obtained by defining the coupling constant of a plasma as the ratio of the average Coulomb energy to the average kinetic energy of the plasma particles. For plasma particles obeying classical statistics the average kinetic energy per particle is $\sim kT$ where k is the Boltzmann constant. Let us consider a one-component plasma (OCP) with N particles within a volume V. The characteristic volume is given by $\frac{V}{N} = \frac{4\pi a^3}{3}$ where a is the radius of the sphere encompassing the characteristic volume and is usually called the ion sphere radius or the Wigner-Seitz radius. The Coulomb energy per particle is given by $\frac{(Ze)^2}{a}$. The coupling constant of a plasma obeying classical statistics is given by

$$\Gamma = \frac{(Ze)^2}{akT} = \frac{(Ze)^2}{kT}\left(\frac{4\pi N}{3V}\right)^{\frac{1}{3}}. \tag{1}$$

From this expression one can calculate Γ for a density $n = \frac{N}{V}$ and temperature T. $\Gamma < 1$ corresponds to the case of a weakly coupled plasma and $\Gamma \geq 1$ corresponds to a strongly coupled plasma. Ultracold neutral plasmas can be in the borderline of the strongly coupled plasma domain [61]. Typical examples of weakly coupled plasmas are those occurring in gaseous discharge ($T \sim 10^4$ K, $n \sim 10^{11}/\text{cm}^3$), controlled thermonuclear reactions ($T \sim 10^8$ K, $n \sim 10^{16}/\text{cm}^3$), solar corona ($T \sim 10^6$–$10^8$ K, $n \sim 10^6$–$10^{10}/\text{cm}^3$), laboratory Tokamaks ($T \sim 10^5$–10^7 K, $n \sim 10^8$–$10^{16}/\text{cm}^3$), and doped semiconductors ($T \sim 10^2$ K, $n \sim 10^{17}$–$10^{19}/\text{cm}^3$). In addition, plasmas generated in flames and lightning also fall into the weakly coupled category. Strongly coupled plasma with coupling strength ranging from $\Gamma \sim 1$ to $\gg 1$

can be found in stellar interiors, highly evolved stars (white dwarf) in high density states, interior of Jovian planets, plasma in explosive shock tubes, two dimensional system of electrons trapped in surface states of liquid helium, laser produced plasmas, dusty plasmas and ultracold neutral plasmas [61–65]. Here the density of the plasma may well exceed $10^{23}/\text{cm}^3$ with widely varying temperature ranges. A beautiful pictorial representation of the range of Γ values for different categories of plasma is given by Killan et al. [61]. The details of strongly coupled plasmas and their interactions were reviewed by Ichimaru [66].

The topic of properties of plasma with embedded systems has a pretty long history and an extensive literature. We wish to cover in this short review the current scenario prevailing in the theoretical structure calculations on plasma embedded atomic systems. Special emphasis will be given to the comparison of existing data available from laser plasma and other experiments. In Section 2 we give a brief description of the current experimental techniques in this direction, which will be followed by the theoretical basis for interpreting the available experimental data and the generation of new atomic data in Section 3. In Section 4 we discuss briefly the interpretation of the spectral properties of atoms confined under plasma with special reference to one-, two- and few-body problems, including exotic atoms. In Section 5 we discuss very briefly the interpretation of the spectral properties of atoms under liquid helium. We conclude in Section 6 with a summary and a discussion of the future directions in this field.

2. EXPERIMENTAL TECHNIQUES

Radiative properties of hot and dense plasmas are of substantial interest in different fields such as astrophysics [66], inertial confinement fusion processes [67–69], estimation of stellar opacities useful for studies in stellar structure and evolution [70], in microlithography, time-resolved microscopy and spectroscopic studies of transient physical and chemical phenomena [71, 72]. Interaction of intense ultra-short laser pulses with matter opens up the possibility of generating plasma with solid state density at high temperature $\sim$0.1 to 1 keV [71]. Under these conditions the plasma coupling parameter Γ exceeds unity and the plasma is said to be in a strongly coupled state. The study of such a plasma is essential for a thorough understanding of the compressed materials equation of state [73,74]. While we skip the experiments such as laboratory Tokamaks for the low density and high temperature plasmas, a brief outline of the experimental arrangements for laser produced hot dense plasmas is given below.

2.1. Shock compressed plasmas

Djaoui et al. [74] reported an earlier experiment in which two laser beams were directed on to each side of a sandwich foil target. The resulting shock waves traveled inward to collide in the central layer of the target and produce compression to several times the solid state density and temperature ~several eV. Djaoui et al. [74] performed similar experiments on laser shock compressed aluminium using the Extended X-Ray Absorption Fine Structure (EXAFS) technique and estimated the plasma coupling parameter and plasma density. The laser used had a 40 J pulse of 600 ps duration and wavelength 0.53 μ. The EXAFS technique of Lee et al. [75] to measure the ion correlation effects in dense plasma was used in this experiment. The earlier results of these were discussed by Hall et al. [76]. Measurement of the shock speed and temperature was done using standard methods [77]. The EXAFS arises from oscillations in the photoelectric cross sections above an absorption edge and is absent in monatomic gases. The fine structure is determined from the matrix elements of the dipole operator between the initial and final photoelectron states. The correlation between the positions of the scattering centers is responsible for the fine structure. Comparison of the experimental EXAFS and the theory yields detailed structural information of the plasma. Shock induced shifts in the K absorption edge of aluminium by time-resolved X-ray spectroscopic measurement of DaSilva et al. [73] indicated a red shift of about 7 eV. The density due to shock compression is estimated to be ~2.2 times the normal density of aluminium. In this experiment 25–30 μm aluminium foil was irradiated with a 0.53 μm, 2.3 nsec (FWHM) laser pulses. Aluminium is a fairly common target for experiments as its high pressure equation of state is well-established [78]. Diagnostic determination was done by Ng, Parfeniuk and DaSilva [79]. Such experiments on the study of the electronic structure of radiatively heated and shock compressed KCl by measuring the photoabsorption shift of Cl in a multilayered target was first proposed by Bradley et al. [80].

2.2. Laser irradiated plasmas

The interaction of ultrafast laser pulses with a solid target produces dense plasmas at solid state density. The resulting X-ray emission characteristics reveal strong asymmetry in the line profiles and the possibility of formation of transient molecules, pressure ionization, line merging and line shifts. One of the earlier experiment was due to Laboucher-Dalimier et al. [81] on the broadening of the Lyman $\alpha(\mathrm{Ly}_\alpha)$ lines of F and Al. The existence of ionic molecules like F^{8+}–F^{9+} in highly correlated fluorine plasma has been suggested. The plasma coupling parameter Γ here is ~1.5–2 with an approximate plasma density of $n \sim 10^{23}/\mathrm{cm}^3$ and temperature ~200 eV. This confirms the identification of the special molecular features observed in white dwarfs [82,83] and their interpretation in terms of the formation of molecular structure H–H^+, H–H^+–H^+. In this experiment a Nd glass laser at 0.263 μm with 500 psec pulse duration is used. X-ray heating of a sample opened up new avenues of frequency resolved opacity measurements [84, 85]. Nazir et al. [70] created hot dense iron plasma by irradiating a 1000 Å

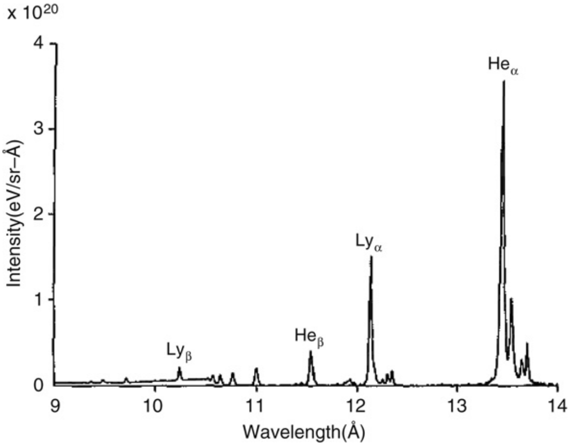

Figure 1 X-ray emission spectrum of highly ionized neon plasma. Reused with permission from [93] © 1992, American Institute of Physics

layer of Fe with a 300 fs pulsed SPRITE KrF laser at 249 nm. The laser intensity is ~10^{17} W/cm^2. The X-ray spectrum is rich in Ne-like transitions in the Fe plasma. High intensity subpicosecond laser pulses with a chirped pulse amplification technique was also used for generating X-rays from solids by Mourou and Umstadter [86] and by Kieffer et al. [87]. The subpicosecond laser interaction keeps the plasma in the solid state density up to several KeV electron temperature [87–89] and the generated X-rays are useful for their diagnostic purpose [87,90]. The experiment by Workman et al. [91] on L edge shifts in plasma generated by a 100 fs Ti:sapphire laser operating at 790 nm and 50 mJ pulses with an intensity of 2×10^{17} W/cm^2 on 1000 Å Al film yields a red-shift of 1.6 ± 0.4 Å. The density estimated is ~1.4 times the solid state density. The pulse duration was measured by the novel technique of jitter-free streak camera averaging. Workman et al. [91] have explicitly shown that the dynamic behavior of this shift is consistent with the relaxation of Al following the compression generated by the shock wave traveling through the film. An experiment on Al plasma was done by Riley et al. [92] using Raman amplified 12 ps pulses from KrF laser of intensity $>10^{15}$ W/cm^2. Analysis of the time-resolved X-ray spectroscopy, showing prominent He$_\alpha$, He$_\beta$ and He$_\delta$ lines, indicates a density ~10^{23}/cm^3. Burkhalter et al. [93] used a Dense Plasma Focus (DPF) device to obtain well-resolved Lyman and Balmer lines (Figure 1) in Ne plasma.

The Ly$_\alpha$ line is at 12.134 Å and the He$_\alpha$ line is at 13.447 Å. Saemann et al. [71] studied in detail the K shell emission from dense Al plasma generated by focusing a high contrast 150 fs laser pulse at 395 nm with intensity of 5×10^{17} W/cm^2 on a tamped Al target. The positions of the resonance lines Ly$_\alpha$, He$_\alpha$ and He$_\beta$ and their He-like and Li-like satellites were

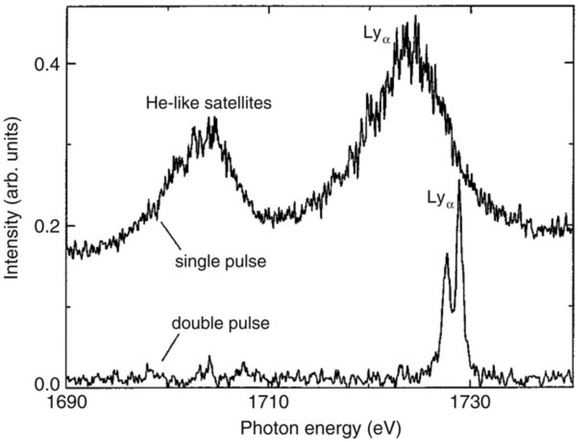

Figure 2 Ly$_\alpha$ line positions of Al plasma in low and high density case. Reprinted with permission from [71] © 1999, American Physical Society

measured. The lines were found to have a large broadening and to show red plasma polarization shifts. The estimated electron temperature was ~300 eV and the electron density ~(5–10) × 10^{23}/cm^3, see Figure 2.

Previously reported resonance lines and their satellites are consistently much less broadened [94–98]. The experiment of Saemann et al. [71] gives a plasma polarization red shift of 3.7 ± 0.7 eV and it gives a good ground for theoretical analysis. Experiments by Nantel et al. [99] with time and space resolved extreme ultraviolet spectra of carbon plasmas produced by 100 fs pulses from a Ti:sapphire laser with 50 mJ energy at 790 nm, show strong pressure ionization and line merging. Diagnostic studies indicate temperatures between 50–80 eV with electron densities ~10^{21} to 10^{23}/cm^3. The estimated plasma coupling parameter is $0.5 < \Gamma < 1.5$. Figure 3 shows the time-resolved spectra taken at time $t = 0$, 50 and 225 ps.

The H- and He-like lines are clearly demonstrated. Results indicated in this particular experiment are very suitable for making theoretical analysis as we will see later.

2.3. Laser imploded plasma

Inertial confinement fusion (ICF) plasma is generated when the inertia of the fuel mass provides the necessary confinement. To make a thermonuclear reaction feasible a capsule containing the fuel mass is compressed by an implosion process to high temperature and density. This may be achieved by direct or indirect processes. In the direct process laser beams impinge on the target material, thereby converting their energy to a plasma process. In the indirect drive the energy from the laser or another ion beam is absorbed

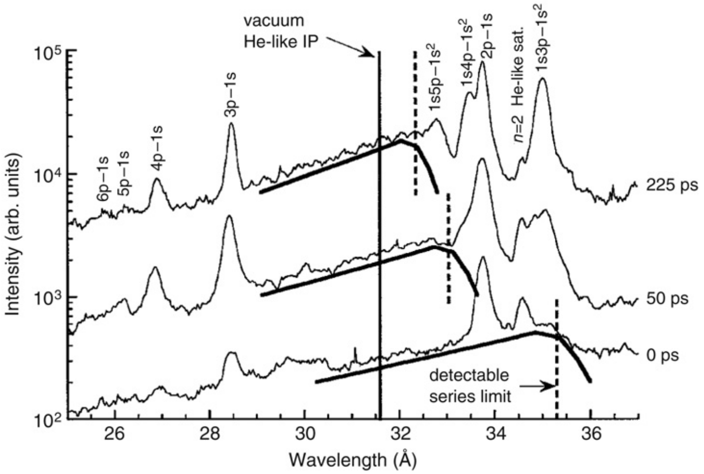

Figure 3 Time-resolved extreme ultraviolet spectra of carbon plasma showing H- and He-like lines. Reprinted with permission from [99] © 1998, American Physical Society

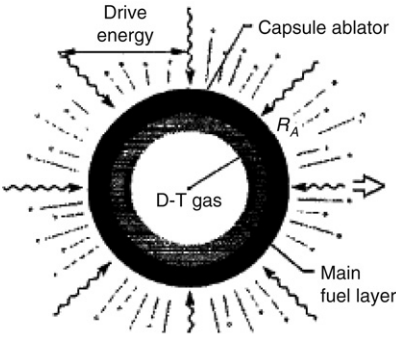

Figure 4 Generation of ICF plasmas by laser implosion. Reprinted with permission (license number 2041481384498) from [69]

by an envelope of a high Z material surrounding the micro-capsule thereby generating X-rays which heat the surface layer [Figure 4].

The layer is ionized and expansion occurs compressing the material of the microsphere. The resulting shock wave compresses and heats the material (mostly deuterium–tritium mixture) inside the microsphere. During compression the gas is ionized by collision and the temperature generated may be sufficient to produce highly stripped ions of medium Z dopants like Ar, a trace of which is added to perform spectroscopic diagnostics of the plasma. A good review of the physics of the ICF process is given by Lindl [69]. The high energy density condition prevailing in an imploded core is of fundamental interest to atomic energy level population kinetics, electron thermal conduction, radiative energy flow and spectral line formation [100], and such emission spectroscopy is capable of providing time-resolved details of an inertially confined core [101–103]. A detailed experimental investigation on the He-like Ar line shape formed in a high density implosion was done by Woolsey et al. [104]. Nova laser beams were used with 1 nsec duration of $\sim$2 kJ of energy per beam at 0.353 nm wavelength. The intensity is $\sim 2 \times 10^{15}\,\mathrm{W/cm^2}$. Time-resolved spectroscopic data shows H- and He-like spectra of Ar. The temperature and density of the plasma are estimated to be $\sim$1 keV and $10^{24}/\mathrm{cm}^3$, respectively.

2.4. Ultracold neutral plasma

Ultracold neutral plasmas may be produced by laser cooling and trapping of different types of neutral atoms [105] such as calcium, strontium, rubidium, cesium etc., by photoionizing Bose condensates [106] and also by spontaneous ionization of dense Rydberg atoms [107,108]. A review on ultracold neutral plasmas due to Killan et al. [61] gives an excellent disposition on the subject.

2.5. Atoms under liquid helium

Electrons, ions, neutral atoms, molecules and clusters can be confined under liquid helium. The confinement is possible because of successful implantation techniques like laser ablation, gas discharge and atomic beams. A beautiful review on the subject is due to Tabbert et al. [109]. Experimental investigations on the spectra of foreign atoms implanted in liquid helium have been done for a wide range of nuclear charges, mostly by using the laser induced fluorescence technique [110–115]. The observation of an unexpected long lifetime of positronium in liquid helium [116,117] indicates a cavity-like structure around the implanted impurity inside the quantum fluid [118]. General observations on the spectra of foreign atoms indicate spectral line shifts in contrast to free atomic lines and change in line shapes. In addition, a general lowering of the ionization potential is also observed. The absorption and emission lines are shifted by different amounts and sometimes in different directions. In light alkali atoms resonance lines in emission are absent when embedded inside liquid helium, and in some cases the lines which are forbidden in free atomic spectra appear in the embedded system [109]. The complex interactions with the surrounding helium atoms are responsible for such behavior. The topic is rich in experimental data but not many theoretical investigations have been done for the interpretation of the available data. The problem can be looked at in terms of cold plasma embedded systems, a theory of which is yet to come.

3. THEORETICAL DEVELOPMENT

The problem of finding the average potential distribution function at a given point from a nucleus of charge Ze immersed in a sea of electrons and other ions at a temperature T is essentially a time dependent phenomena. The surrounding ions may be taken as point charges and the time averaged potential distribution around the nucleus can be assumed to be spherically symmetric to a first approximation. The simplest model to find the potential between two charged particles immersed in such an environment was due to Debye and Hückel [119] and developed in relation to classical electrolytes. Classical statistics is applied in this model and this is valid for high temperature plasmas. Since then, various other models have been developed for high as well as low density plasmas in different temperature ranges. In several models the ions were treated classically while the electrons have been described by quantum statistics. We describe some of these models in the subsequent sections.

3.1. Debye screening model

The electrostatic potential between two charged particles in a plasma is different from the usual Coulomb potential due to the screening effect produced by other charged particles. The dynamic character of this screening is complex because of the motion of other charged particles. A simple picture however follows from the static model [120]. If an ion is placed inside a plasma there is local redistribution of the ions and electrons in its immediate neighborhood. Considering the plasma in local thermodynamic equilibrium (LTE), the electrostatic potential at a given point is determined by the solution of the Poisson equation

$$\nabla^2\phi(\vec{r}) = -4\pi\rho(\vec{r}) \tag{2}$$

where ρ is the total charge density at a given point $\vec{r}$. Here

$$\rho(\vec{r}) = \sum_i e_i n_i \tag{3}$$

where e_i is the charge on the ith particle with density n_i. One should describe the electronic density using the Fermi distribution function and the ionic density by the Boltzmann distribution formula. But a reasonable description may follow by using the Boltzmann formula for both the electrons and the ions.

$$n_i = n_i(\infty)\mathrm{e}^{-\frac{e_i\phi(\vec{r})}{kT}} \tag{4}$$

$n_i\ (\infty)$ is the particle density at $T = \infty$. The neutrality condition

$$\sum_i e_i n_i(\infty) = 0 \tag{5}$$

must be satisfied. Thus we have to solve the equation

$$\nabla^2 \phi(\vec{r}) = -4\pi \sum_i e_i n_i(\infty) \mathrm{e}^{-\frac{e_i \phi(\vec{r})}{kT}}. \tag{6}$$

Assuming a high temperature limit the exponential is expanded, keeping only terms up to first order, resulting in

$$\nabla^2 \phi(\vec{r}) = \left(\frac{4\pi \sum\limits_i e_i^2 n_i(\infty)}{kT} \right) \phi(\vec{r}) = \lambda^2 \phi(\vec{r}) \tag{7}$$

where $\lambda^2 = \frac{4\pi \sum_i e_i^2 n_i(\infty)}{kT}$.

For one-component plasmas (OCP) of ionic charge Ze, one obtains, $\lambda^2 = \frac{4\pi n(1+Z)e^2}{kT}$, where n is the electron density of plasma far from the ionic site.

The spherically symmetric solution of Equation (7) yields

$$\phi(r) = \frac{\mathrm{e}^{-\lambda r}}{r} \tag{8}$$

with

$$\lambda = \sqrt{\frac{4\pi n(1+Z)e^2}{kT}}. \tag{9}$$

This is the screened potential originally developed by Debye and Hückel [119].

The average interaction between two charged particles is now given by

$$V(r_{12}) = e_1 e_2 \frac{\mathrm{e}^{-\lambda r_{12}}}{r_{12}} \tag{10}$$

where λ is called the Debye screening parameter and $r_D = D = \frac{1}{\lambda}$ is called the Debye radius. At $r_D = \frac{1}{\lambda}$ the potential is reduced by $\frac{1}{e}$ times the Coulomb potential. The screening is more effective within a radius determined by r_D.

Using physical values of the parameters we have $r_D \sim 6.9\left(\frac{T}{n}\right)^{\frac{1}{2}}$ cm where T and n are to be measured in units of K and cm^{-3}. For an electron gas with $n \sim 10^8$ and $T \sim 10^4$, $r_D \sim 6.9 \times 10^2$ cm.

The potential is Coulombic at $r \ll r_D$ and at $r > r_D$ the potential screens off exponentially.

Modification of this model to get the potential function is obtained considering the Fermi–Dirac distribution function for the electron density and the Boltzmann distribution for the ionic density. This was done by Stewart and Pyatt [58] to get the energy levels and the spectroscopic properties of several atoms under various plasma conditions. Here the electron density was given by

$$n(r) = n(\infty)\frac{F\left[\left\{\frac{e\phi(r)}{kT}\right\} - \alpha\right]}{F(-\alpha)} \tag{11}$$

$$n_i = n_i(\infty)\mathrm{e}^{-\frac{eZ_i\phi(r)}{kT}} \tag{12}$$

with

$$F(\eta) = \int_0^\infty \frac{t^{\frac{1}{2}}\mathrm{d}t}{\left(\mathrm{e}^{(t-\eta)} + 1\right)}.$$

The boundary conditions $\phi(\infty) = 0$ and $r\phi \rightarrow Ze$ as $r \rightarrow \infty$ are to be satisfied. α is a degeneracy parameter given by the density of the free electrons far from the ion.

Using the value [58]

$$n(\infty) = 2\frac{(2\pi mkT)^{\frac{3}{2}}}{h^3} \times \frac{2}{\sqrt{\pi}} \times F(-\alpha) \tag{13}$$

one gets

$$n(r) = 4\pi\frac{(2mkT)^{\frac{3}{2}}}{h^3} \times F\left[\left\{\frac{e\phi(r)}{kT}\right\} - \alpha\right]. \tag{14}$$

The asymptotic ion densities satisfy the electrical neutrality condition $\sum_i n_i Z_i(\infty) = n(\infty)$. The model developed by Stewart and Pyatt [58] was very general and limiting cases of the Debye screening model, and also that due to strongly coupled plasma, follow as special cases.

3.2. Strongly coupled plasma (ion sphere model)

This particular model of the plasma is based on simple assumptions. One constructs an ion sphere by picking an ion of charge Ze by associating it with a sphere of neutralizing charges that would exactly cancel out the point charge of the ion. As given before, this sphere has the radius $a = \left(\frac{3V}{4\pi N}\right)^{\frac{1}{3}}$, where $\frac{V}{N}$ is the characteristic volume, and the electric charge density is $-\left(\frac{3Ze}{4\pi a^3}\right)^{\frac{1}{3}}$. The characteristic radius is the same as given by the Wigner-Seitz radius in solid state physics. From classical electrostatics it follows that the potential at a point r from the center, due to the negatively charged sphere, is $-\frac{3}{2}\left(\frac{Ze}{a}\right) + \left(\frac{Ze}{2a}\right)\left(\frac{r}{a}\right)^2$.

Thus the total potential at a point r from the center of the sphere is given by

$$\phi(r) = \frac{Ze}{r} + \left(\frac{Ze}{2a}\right)\left[\left(\frac{r}{a}\right)^2 - 3\right]. \tag{15}$$

This potential will be modified if the number of bound electrons N are associated with the ion, then the effective charge to be neutralized is $(Z-N)e$ and the electric charge density of the plasma electrons will be modified accordingly. Thus for an ion with one bound electron the potential is given simply by

$$\phi(r) = \frac{Ze}{r} + \left(\frac{(Z-1)e}{2a}\right)\left[\left(\frac{r}{a}\right)^2 - 3\right]. \tag{16}$$

Thus the interaction energy of an ion with a bound electron is

$$V(r) = -\frac{Ze^2}{r} + \left(\frac{(Z-1)}{2a}\right)e^2\left[3 - \left(\frac{r}{a}\right)^2\right]. \tag{17}$$

For N bound electrons the sum of the particle potential energy given by Equation (17) and the electron repulsion terms are to be taken into account for the total potential energy of the system. An extremely good description of the general properties of strongly coupled plasma is given by Ichimaru [66]. We will adopt the atomic unit (au) for further theoretical descriptions and calculation purpose unless otherwise stated.

3.3. Average atom model

One of the earliest models for estimating the radiative properties of hot and dense plasmas was the average atom model introduced by Rozsnai [121] and subsequently applied for studying the radiative properties of hot dense plasmas [122–125]. The Average Atom (AA) model assumes that the plasma states can be described quantum mechanically as due to that of a selected ion and plasma electrons in its neighborhood with a Wigner-Seitz type of confinement, having identical boundary conditions to that of the ion sphere model, or by an extra potential added to that of the central nucleus (ion correlation model) [125]. For the electrons within the ion sphere, the relativistic Thomas–Fermi–Dirac (TFD) model was applied to find the quantum mechanical solution for the bound states in terms of an independent particle picture. The various one electron states are assumed to be occupied according to the FD distribution and the TFD potential is used as a starting point for the subsequent Hartree-Fock–Slater (HFS) calculation. Fermi statistics and central field approximation is maintained yielding an average atom representation. The relativistic expression for the density is expanded in terms of a power series in kT. The chemical potential appearing in the FD distribution function is determined from the normalization condition applied to the density. Numerical evaluations for the energy levels and populations at different temperatures and densities of several atoms have been performed by Rozsnai [121–125]. The AA model has been implemented successfully in density functional theory and immersed ion models [126,127].

3.4. Inferno model

This is a model developed by Liberman [128] in which an ionic system is embedded in an uniform background of ions and free electrons similar to that assumed in the strongly coupled plasma model. Within a sphere of a given radius the charge neutrality is maintained. The surrounding ions outside the spherical cavity maintain a constant positive charge density also maintaining the electrical neutrality. The orbital wavefunctions ψ_i and the energy ε_i are calculated from self-consistent solutions of the TFD equation and are used to determine the potential self-consistently. Using the Dirac Hamiltonian

$$h = c\vec{\alpha}.\vec{p} + (\beta - 1)c^2 + w(r), \tag{18}$$

the self-consistent solutions of the one particle equation derived from the Kohn-Sham formulation [56] within local density approximation, are sought.

The total energy is expressed in terms of kinetic energy, potential energy including nuclear attraction, Coulomb repulsion and LDA exchange, and correlation energy. Minimization of the free energy $F = E - TS$, with respect to ψ_i, n_i and R, yields [128] the self consistent potential $w(r)$ given by

$$w(r) = -\frac{Z}{r} + \int_0^R \frac{\rho(r')}{\left|\vec{r} - \vec{r'}\right|} \mathrm{d}\vec{r'} - \frac{1}{\pi}\left(3\pi^2\bar{\rho}\right)^{\frac{1}{3}} - \nu \quad \text{for } r < R \tag{19}$$

$$w(r) = -\frac{1}{\pi}\left(3\pi^2\bar{\rho}\right)^{\frac{1}{3}} \quad \text{for } r > R, \tag{20}$$

where $\bar{\rho}$ is the free electron charge that is neutralized by the ionic background. In Equation (19) ν is a Lagrangian multiplier to be determined from the optimization condition [128].

The corresponding Dirac equation to be solved is

$$h\psi_i = \varepsilon_i \psi_i. \tag{21}$$

The electronic density is given by

$$\rho(\vec{r}) = \sum_i n_i \left|\psi_i\right|^2, \tag{22}$$

where n_i is given by the Fermi distribution function $\left[\mathrm{e}^{\frac{(\varepsilon_i - \mu)}{kT}} + 1\right]^{-1}$ in which the chemical potential μ is determined by the requirement

$$\int_0^R \rho(\vec{r})\mathrm{d}\vec{r} = Z, \tag{23}$$

$w(r)$ is obtained from iterative self-consistent solutions.

For the electrons interacting through the mean field the entropy is given by

$$S = -k\sum_i \left[n_i \ln n_i + (1 - n_i)\ln(1 - n_i)\right] N_i, \tag{24}$$

where $N_i = \int_0^R \left|\psi_i\right|^2 \mathrm{d}\vec{r}$.

$\rho(\vec{r})$ given by Equation (22) and the entropy given by Equation (24) used by Liberman are approximate, as in the realistic situation the multi-electronic states are involved in the definitions. Several calculations on the equation of state (EOS) for different atoms are performed by Liberman [128] and the results are compared with the available experimental values.

3.5. Super transition arrays (STA) model

Several extensions to the Inferno model of Liberman [128] were done of which STA is one. This particular model was developed for calculating bound–bound transitions in a hot dense plasma in LTE [129]. The total transition array of a single electron for all possible configurations is described by a smaller number of super transition arrays (STA). The effect of plasma free electrons on the radiating ion was treated by the TF model. The method is consistent with the findings from the AA model. The model is further extended (EOSTA) subsequently to include thermodynamic quantities needed for the description of the equation of state (EOS) of the hot dense plasma [130–134]. In the extended model the relativistic framework is used along with the LDA for the exchange part of the EOS and the optimized effective potential for the calculation of orbital energies necessary for the opacity calculations. A new implementation of Liberman's Inferno model [128] was due to Wilson et al. [135]. The code called Purgatorio, aims at calculating the Helmholtz free energy of plasma electrons over a wide range of temperatures ∼KeV and densities for compressions up to the delocalised limit of most of the bound orbitals. The basic objective of this code is to obtain highly precise results for the pressure and other thermodynamic quantities using numerical differentiation. A further development with the Purgatorio code [136] is the implementation of the Dirac equation for the major and minor components of the wavefunctions normalized to unity over all space, with analytic forms outside an ion sphere radius where the potential is set to zero. EOS quantities are calculated using different exchange and correlation potentials like those of Hedin and Lundqvist [137], the Thomas Fermi based quantum equation of state (QEOS) model of More et al. [138] and the temperature dependent exchange potential due to Gupta and Rajagopal [57], and are found to be dependent on the choice of the exchange and correlation potentials. The Purgatorio code treats the continuum wavefunctions accurately and provides the electron thermal component of the EOS data for use in hydrodynamic modeling.

3.6. Hydrodynamic model

For low values of the Coulomb coupling parameter one can treat the plasma as a single hydrodynamical medium, and the basic equations relating to the plasma density and particle velocity are to be solved to get the evolution of the plasma. The density is usually treated by the continuity equation and the velocity by the Navier–Stokes equation. Collisionless plasma dynamics is more accurately described by the well known Vlasov equations [120]. Solutions of the Vlasov equations have been investigated in a number of cases [61]. In a laser-produced plasma, particularly for short pulse durations, rapid heating of the target material occurs. The flow of the thermal energy through such a plasma is a complex process involving collisional and many other processes. The plasma may be in LTE but departure from LTE is observed, depending on the time scale of the hydrodynamical changes compared to the time scales of the thermodynamic equilibrium. In non-LTE plasma a time dependent solution of the excitations and ionizations in plasma is required. General theoretical discussion on the plasma dynamics in the presence of collisions is given by Killan et al. [61]. Interpretation of laser produced data was done by Djaoui and Rose [139], using their one-dimensional hydrodynamical simulation code. Experiments involving subpicosecond high intensity laser pulses on solid targets yield data on collisional ionization and three-body recombination processes in high temperature dense plasmas. In such a case the hydrodynamic code, including the conventional heat flow due to Spitzer and Fokker-Planck simulations [140] within the average atom model, is more suitable for predicting the ionization rate as a function of time.

3.7. Time dependent methods

Adiabatic time dependent density functional theory (ATDDFT) has been developed and applied for estimating the properties of hot and dense plasma [141–143]. This method is a generalization for the finite temperature immersed ion model developed by Zangwill and Soven [144] and Stott and Zaremba [145] for ground state atoms at zero temperature. The model aims at finding the electronic solutions of the Kohn-Sham equation in a self-consistent manner in the presence of a time dependent external potential. Reasonably good results were achieved by the ATDDFT for atoms and molecules at $T = 0$. A review of this topic is given by Mahan and Subbaswami [146]. The model has the defect of getting an incorrect picture of the asymptotic behavior of the potential function [146]. Finite temperature random phase approximation (FTRPA) formulation was done in terms of a matrix eigenvalue problem by Mermin [147] and Vautherin and Vinh Mau [148], and also by Cloizeaux [149]. FTRPA uses the finite temperature time dependent Hartree-Fock [TDHF] method for calculating the response properties of fermionic systems in the presence of a time dependent external field. FTRPA has been applied for estimating the spectroscopic properties of dense neon plasmas at various temperatures and densities by Colgan et al. [150], in which the effect of temperature is incorporated in the HF density matrix through the Fermi distribution function n_i given by Equation (22). The zero temperature non relativistic formulation uses the time dependent coupled Hartree-Fock (TDCHF) theory and it has been widely used for calculating the response properties of atomic and molecular systems [151]. The TDCHF theory has been shown to be equivalent to RPA and includes part of the electron correlations [152,153]. A brief outline of the TDCHF theory is given below.

The non relativistic Hamiltonian of an atomic system under a plasma environment is given by

$$H_0 = \sum_i \left[-\frac{1}{2}\nabla_i^2 + V_{\text{eff}}(r_i) \right] + \sum_{i<j} V'_{\text{eff}}(r_{ij}), \tag{25}$$

where $V_{\text{eff}}(r_i)$ is the one-body effective potential whose structure depends on the coupling strength of the surrounding plasma. For weakly coupled plasma the coupling constant $\Gamma < 1$ [see Equation (1)], and the Coulomb potential is modified to the screened Coulomb potential [120],

$$V_{\text{eff}}(r_i) = -\frac{Z\mathrm{e}^{-\lambda r_i}}{r_i}, \tag{26}$$

where Z is the nuclear charge and λ, the Debye screening parameter [120], is given by

$$\lambda = \left[\frac{4\pi(1+Z)n}{kT} \right]^{1/2}, \tag{27}$$

which is a function of the temperature T and the number density n of the plasma electrons. A large number of plasma conditions can be simulated by suitably changing the values of T and n. The two-body potential for the weakly coupled plasma model is given by [see Equation (10)]

$$V'_{\text{eff}}(r_{ij}) = \frac{\mathrm{e}^{-\lambda r_{ij}}}{r_{ij}}. \tag{28}$$

In the case of a spatially homogeneous one-component strongly coupled plasma ($\Gamma \geq 1$) surrounding an ion of nuclear charge Z, having N valence electrons, the radius R of the Wigner-Seitz neutralizing sphere is given by

$$R = \left[\frac{Z-N}{\frac{4\pi n}{3}} \right]^{\frac{1}{3}}. \tag{29}$$

The one particle effective potential is given by [see Equation (17)]

$$V_{\text{eff}}(r_i) = -\frac{Z}{r_i} + \left(\frac{(Z-N)}{2R} \right) \left[3 - \left(\frac{r_i}{R} \right)^2 \right]. \tag{30}$$

Here

$$V'_{\mathrm{eff}}(r_{ij}) = \frac{1}{r_{ij}}. \tag{31}$$

To get the ground state energy of the system in the presence of a plasma confinement one has to solve the appropriate Schrodinger equation

$$H_0\Psi = E_0\Psi, \tag{32}$$

subject to the usual normalization condition

$$\langle \Psi | \Psi \rangle = 1. \tag{33}$$

One can impose additional spatial confinement on a Debye plasma such that the potential energy vanishes at the boundary of a given sphere of radius R. For the strongly coupled system, one can assume that no electron current passes through the boundary surface and the wavefunction must vanish at the Wigner-Seitz boundary R [154]. Under such conditions, the radial one-particle wavefunction $\psi(r)$ satisfies

$$\int_0^R \psi^*(r)\psi(r)r^2\mathrm{d}r = 1 \tag{34}$$

and

$$\psi(r) = 0 \quad \text{at } r = R. \tag{35}$$

To incorporate the finite boundary conditions we assume that the radial part of the wavefunction is represented by

$$\psi(r) = (R - r)\chi(r), \tag{36}$$

where $\chi(r)$ is a radial basis set obtained from a linear combination of Slater-type orbitals (STO)

$$\chi(r) = \sum_i C_i r^{n_i} \mathrm{e}^{-\rho_i r}. \tag{37}$$

Usually the nonlinear parameters n_i and ρ_i are preassigned and the linear variation parameters C_i are obtained from the solution of the generalized eigenvalue equation

$$\underline{\underline{H_0}}\,\underline{\underline{C}} = E_0 \underline{\underline{S}}\,\underline{\underline{C}}, \tag{38}$$

which yields the energy E_0 under various plasma coupling strengths which are then functions of the plasma parameters. All the integrals are to be evaluated at the finite domain radius R.

To get excitation properties of the plasma-embedded atomic system, usually a time dependent perturbation approach within linear response theory is used. The response of the systems is studied using an external harmonic perturbation

$$H'(\vec{r}, t) = G(\vec{r})\mathrm{e}^{-\mathrm{i}\omega t} + G^{\dagger}(\vec{r})\mathrm{e}^{\mathrm{i}\omega t}, \tag{39}$$

where $G(\vec{r})$ is a sum of one-particle operators, the angular part of which suggests the nature of one-particle excitations from a given orbital. Under such a perturbation the first order admixture to a given ground orbital oscillates harmonically and the correction to first order is given by

$$\delta\psi(\vec{r}, t) = \delta\psi^{-}(\vec{r})\mathrm{e}^{-\mathrm{i}\omega t} + \delta\psi^{\dagger}(\vec{r})\mathrm{e}^{\mathrm{i}\omega t}. \tag{40}$$

The basis set representing the first order perturbed orbitals should also be chosen such that it satisfies the imposed finite boundary conditions and can be represented by a form like Equation (36) with the STOs having different sets of linear variation parameters and preassigned exponents. The coefficients of the perturbed functions are determined through the optimization of a standard variational functional with respect to, the total wavefunction Φ. The frequency dependent response properties of the systems are analyzed by considering a time-averaged functional [155]

$$J(\Phi) = \frac{1}{T}\int_0^T \mathrm{d}t \frac{\left\langle \Phi(\vec{r}, t) \left| H(\vec{r}, t) - \mathrm{i}\frac{\partial}{\partial t} \right| \Phi(\vec{r}, t) \right\rangle}{\langle \Phi \mid \Phi \rangle}, \tag{41}$$

subject to the optimization condition

$$\delta J(\Phi) = 0. \tag{42}$$

The optimization procedure is usually carried out with respect to linear variational parameters introduced in the perturbed orbitals. Poles of the variational functional yield the excitation properties of the systems. The oscillator strength ($f_{n'n}$) and transition probabilities ($A_{n'n}$) are obtained from standard expressions [156]

$$f_{n'n} = 2\omega_{n'n} \left| z_{n'n} \right|^2 \tag{43}$$

$$A_{n'n} = \frac{4}{3}\omega_{n'n}^{3} \left| \vec{r}_{n'n} \right|^2 , \tag{44}$$

where $\omega_{n'n} = (E_n - E_n')$ and $\vec{r}_{n'n} = \int \psi_{n'}^{*} \sum_i \vec{r}_i \psi_n \mathrm{d}\tau$.

The spatial confinement produces an external pressure on the system, which is given by [157]

$$P = \frac{1}{4\pi R^3} \left[2E - \langle V \rangle \right] , \tag{45}$$

where E and $\langle V \rangle$ are the total energy and potential energy of the system for a given value of R. The spectral properties of atoms under weak and strongly coupled plasma with spatial confinement can readily be obtained using TDCHF theory.

3.8. Other methods

A generalization of the Stewart Pyatt model for estimating the densities in hot plasma was developed by Crowley using the average atom quantum statistical cell model [158]. A novel approach applying percolation theory to a cylindrically symmetric TF model for estimating the lowering of the ionization potential was developed by Stein and Salzmann [159]. The plasma spectroscopy of K shell emitters for a large number of atoms from He to Fe was done by Lee and Larsen [160] by using a time dependent FLY simulation model.

4. INTERPRETATION OF SPECTRAL PROPERTIES AND ATOMIC DATA

Theoretical investigations on the spectral properties of different systems using different plasma models generate a large amount of atomic data. The main focus here is on the interpretation of atomic data generated for atomic, ionic and exotic systems for a small number of electron systems in relation to those produced in experiments on laser produced plasmas. General trends observed for various spectral properties on the coupling strengths of plasma will be given for ready reference.

4.1. Spectral properties of hydrogenic ions

Theoretical investigations on spatial confinement, as well as the screening effect produced by plasma environments of different coupling strengths Γ on the spectroscopic properties of hydrogen-like ions, have been performed

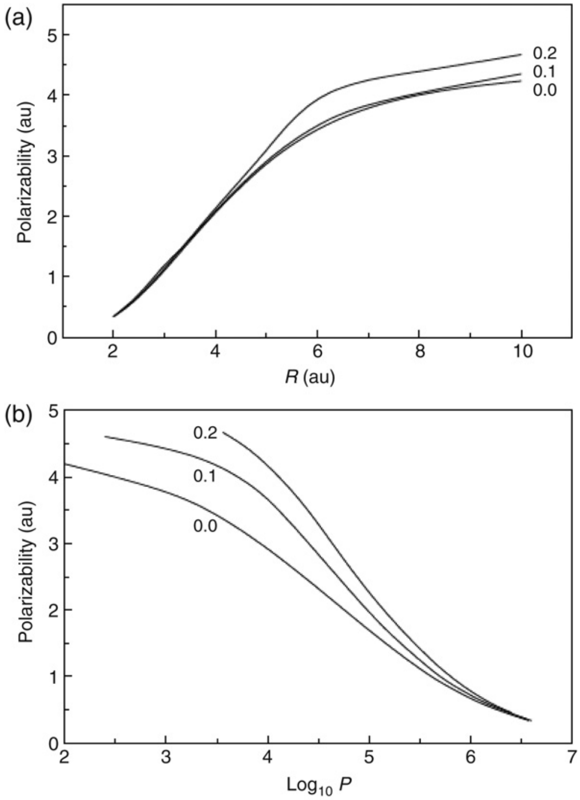

Figure 5 Variation of dipole polarizability against (a) confinement radius, (b) pressure (atm) due to confinement for different Debye screening parameters for a hydrogen atom. Reprinted with permission from Claude Bertout, Editor-in-Chief, A & A (Ref. [172]).

by several authors [21,29,30,36,37,41,42,154,161–177] using numerical and various other methods. While in the Debye model one can impose spatial confinement through additionally imposed boundary conditions, it occurs as a natural consequence of applying the Ion Sphere (IS) model [Section 3.2] for strongly coupled plasmas. Detailed analysis performed by Saha et al. [172] on the effect of Debye screening and spatial confinement on neutral hydrogen reveals that the dipole polarizability increases with the increase of the Debye screening parameter, and diminishes with the decrease of the confinement radius, which increases the pressure generated on the system (Equation (45)). Figure 5 shows the behavior of the polarizability of hydrogen against the screening parameter and confinement radius R and on the pressure P.

The variation of the pressure against the confinement radius is shown in Figure 6. Figure 7 shows the behavior of the 1s–2p transition wavelength against different values of the Debye shielding parameter λ and the

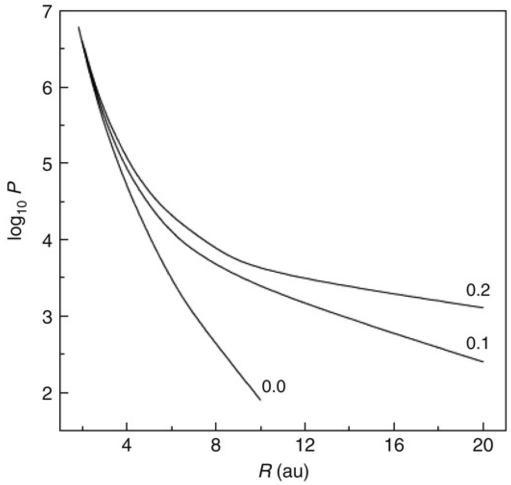

Figure 6 Variation of pressure (atm) vs confinement radius for different screening parameters for the hydrogen atom. Ionization pressure is explicitly indicated. Reprinted with permission from Claude Bertout, Editor-in-Chief, A & A (Ref. [172]).

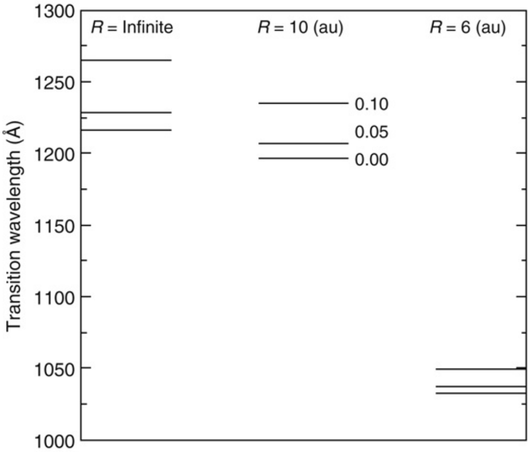

Figure 7 Transition wavelength for the 2p state of a compressed hydrogen atom under different confinement radii and Debye shielding. The screening parameters (au) are indicated along the horizontal lines. Reprinted with permission from Claude Bertout, Editor-in-Chief, A & A (Ref. [172]).

confinement radius R. Figure 8 displays the behavior of the charge density for the 2p state of hydrogen under different values of λ and R. It is interesting to see that the charge density at higher values of λ becomes more and more diffuse and is responsible for the increase in the polarizability at a larger screening. The trends are very general and are also likely to follow for

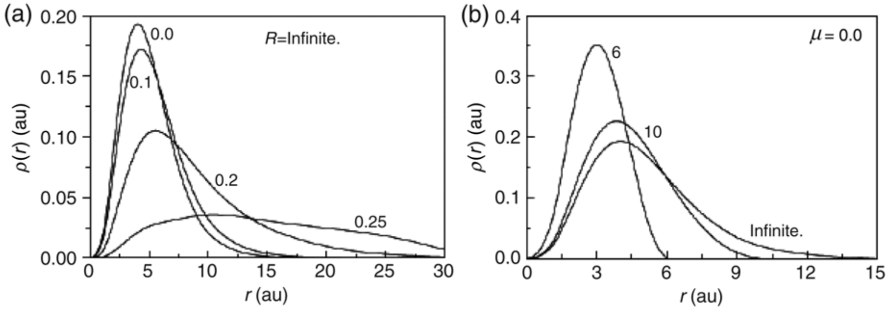

Figure 8 Variation of the charge density of the 2p state of the hydrogen atom against Debye shielding and confinement radius. Reprinted with permission from Claude Bertout, Editor-in-Chief, A & A (Ref. [172]).

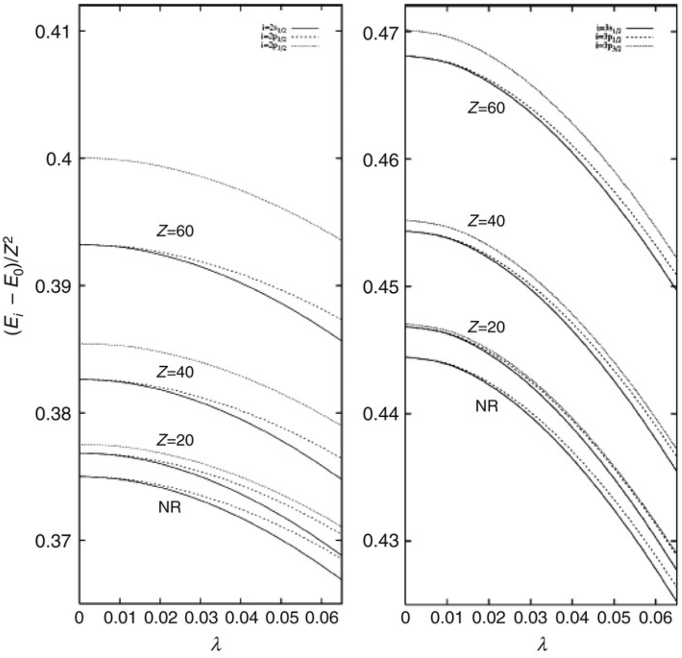

Figure 9 Scaled excitation energies (au) for different hydrogen-like ions against Debye shielding (au) showing explicitly relativistic effects. Reprinted with permission from [173] © 2004, American Physical Society

the case of multi-electron atoms with only minor modifications. Relativistic effects have been incorporated for estimating the spectral energy levels and transition rates for hydrogen-like ions embedded in a Debye plasma by Belinska-Waz et al. [173]. Figure 9 shows explicitly the effect due to relativity for different ions against the screening parameter λ.

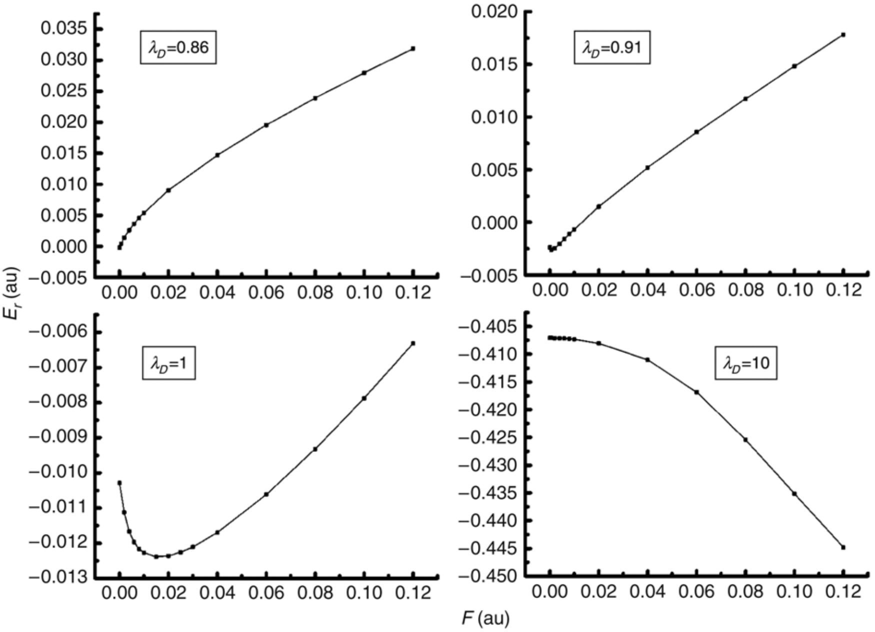

Figure 10 Energy shift of ground state of the hydrogen atom against the applied field for different plasma screening values. Reprinted with permission (license number 2041 490042669) from [178].

Complex coordinate rotation method has been applied by Yu and Ho [178] to find the Stark shifts and widths on the ground state of hydrogen in a Debye plasma for field strengths up to $F = 0.12$ au, and also to estimate the auto-ionization width for different λ values. In this method a complex transformation of the coordinates is performed [179]. The Hamiltonian is modified under such a transformation. The generalized eigenvalue equation for such a Hamiltonian is solved by the basis set expansion technique yielding complex energy eigenvalues from which one can extract the energy and the width simultaneously. Figures 10 and 11 show the Stark shifted energy and the widths for the ground state of hydrogen for different screening constants. The effect of strongly coupled plasmas where $\Gamma \sim 1$, or greater, has been investigated in detail by Sil et al. [174] and by Bhattacharyya et al. [176] using the IS model as described in detail in Section 3.6, using nonrelativistic as well as relativistic Hamiltonians. The influence of the plasma coupling strength, as given by the radius of the ion sphere on the energy levels, frequency dependent polarizabilities, oscillator strengths and transition probabilities, has been estimated. Figure 12 displays the behavior of the orbital energy for a few hydrogenic ions against the ion sphere radius.

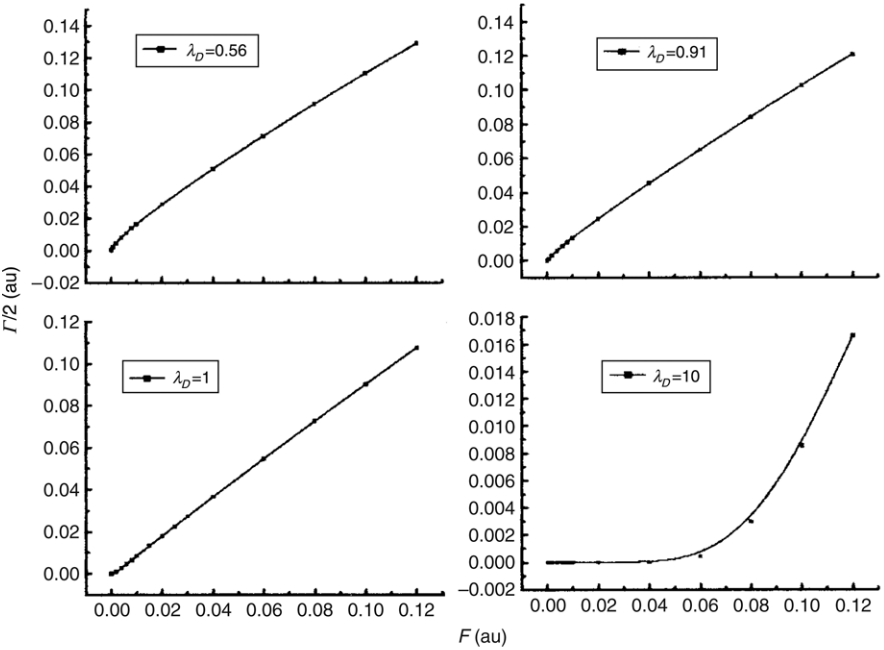

Figure 11 Variation of the energy width of the hydrogen atom against the applied field for different plasma screening. Reprinted with permission (license number 2041 490042669) from [178].

The ionization potential appears to reduce sharply towards zero with decrease of the ion sphere radius indicating the effect of increased plasma coupling strength. Table 1 gives the energy levels of hydrogen-like Ne in a plasma environment for different plasma densities.

The calculated results for Sil et al. [174] agree well with those of Skupski [162] and Nguyen et al. [154]. For hydrogen-like Al the transition energy vs plasma density [176] is plotted in Figure 13.

Figures 14 and 15 show interesting comparison of the results calculated by different methods and those obtained from the laser plasma experiments due to Woolsey et al. [104] and Nantel et al. [99]. Detailed comparison of the theoretical results using an ion sphere model and those from laser plasma experiments [99,104] in Table 2 indicate the viability of the IS model calculations for dense plasmas.

An interesting calculation on the influence of dense plasma to the fine structure levels of hydrogenic ions has been performed by Ray [180], using relativistic methods indicating the removal of the k degeneracy of the Dirac levels. Figures 16 and 17 display the features of the behavior of the fine structure correction of hydrogenic ions and the multiplet structure of a given ion C^{5+} under a dense plasma. Earlier theoretical investigation in this line

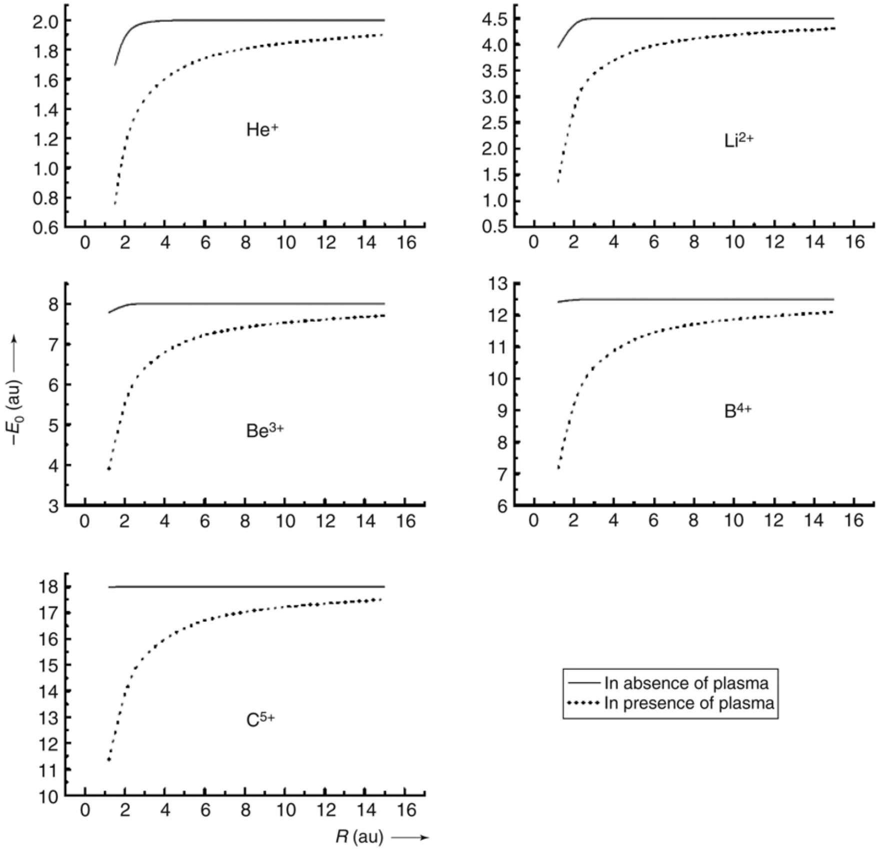

Figure 12 Plot of orbital energy against the ion sphere radius for hydrogenic ions. Reprinted with permission from [174] © 2005, John Wiley & Sons, Inc.

considered the role of the plasma screening on the proton-impact induced fine structure transitions [181,182].

This particular calculation due to Ray [180] gives a new insight into the problem, as the ordering and spacing between the fine structure multiplet components in high density plasma appear to be completely different from that observed for a free system.

4.2. Spectral properties of two electron systems

An early calculation on the effect of the screened Coulomb potential on the energy of the He atom was due to Rogers [183]. Lam and Varshni [184] calculated the ground state energy of the He atom as a function of the

Table 1 Energy levels (in au) of Ne^{9+} at different plasma electron densities. Reprinted with permission from [174]. Copyright 2005, John Wiley & Sons, Inc.

n/cc	$-E$(1s)	$-E$(2p)	$-E$(3p)	$-E$(4p)
6×10^{22}	47.8333[a]	10.3383[a]	3.422[a]	1.0635[a]
	47.7615[b]	10.2705[b]	3.364[b]	1.0280[b]
1×10^{23}	47.4310[a]	9.9394[a]	3.0421[a]	0.723[a]
	47.333[b]	9.848[b]	2.966[b]	0.697[b]
3×10^{23}	46.2971[a]	8.8223[a]	2.0214[a]	
	46.109[b]	8.653[b]	1.895[b]	
6×10^{23}	45.3359[a]	7.8866[a]	1.2096[a]	
	45.055[b]	7.6415[b]	1.081[b]	
1×10^{24}	44.4720[a]	7.0569[a]	0.4494[a]	
	44.094[b]	6.737[b]	0.486[b]	
3×10^{24}	42.0431[a]	4.7930[a]		
	41.353[b]	4.2745[b]		
6×10^{24}	39.9964[a]	2.9053[a]		
	38.990[b]	2.3605[b]		

[a] Ref. [174].
[b] Ref. [154].

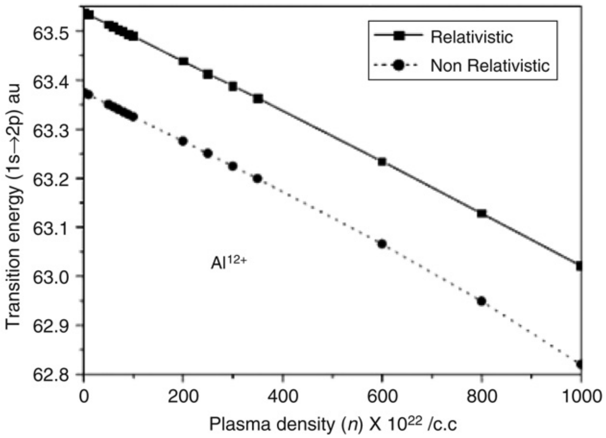

Figure 13 Plot of relativistic and nonrelativistic transition energy ($1s \rightarrow 2p$) for Al^{12+} against the plasma electron density using Ion Sphere model. Reprinted with permission from [176] © 2008, EDP Sciences

Debye screening parameter λ using variational method with correlated basis functions. The numerical results show that the energy diminishes continuously with respect to increased screening and finally becomes zero, giving instability in the system at $\lambda \sim 2.0$. Later on several authors showed their interest in studying the behavior of energy of two-electron systems in

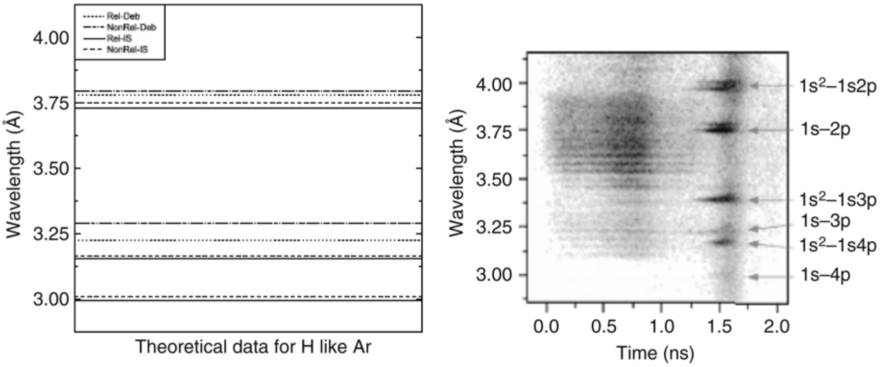

Figure 14 Comparison of the experimental and theoretical results using different models for the transition wavelengths for $1s \rightarrow 2p$, 3p and 4p of Ar^{17+}. The plasma electron density and temperatures are those of Ref. [104]. Reprinted with permission from [176] © 2008, EDP Sciences

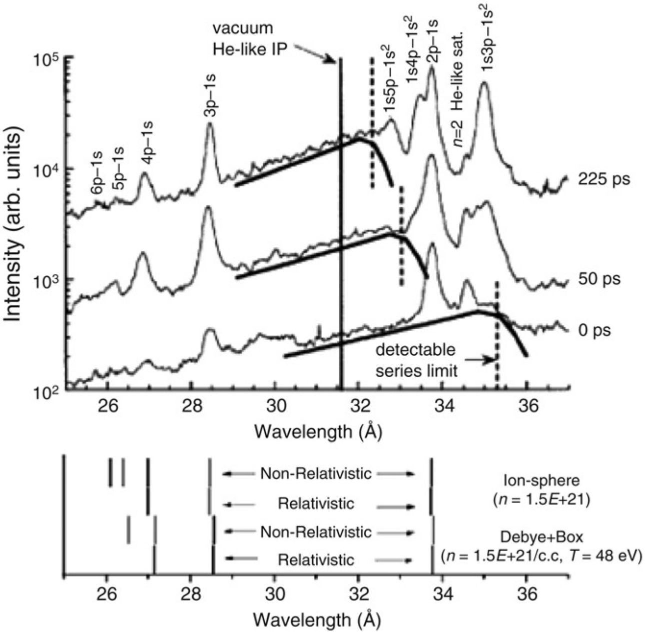

Figure 15 Comparison of experimental [99] and theoretical results using different models for the transition wavelengths for $1s \rightarrow 2p$, 3p, 4p, 5p and 6p of C^{5+}. Reprinted with permission from [176] © 2008, EDP Sciences

a screened Coulomb potential [185–191]. A systematic investigation on the behavior and stability of He isoelectronic ions up to Ar^{16+} was due to Saha et al. [192] and their result is shown in Figure 18.

Table 2 Comparison between experimental and theoretical results of relativistic and nonrelativistic transition wavelengths of C^{5+} and Ar^{17+}. The experimental data have been extracted from Figure 1 of Ref. [99] and Figure 2a of Ref. [104] for C^{5+} and Ar^{17+} respectively. Reprinted with permission from [176]. Copyright 2008, EDP Sciences.

Excitation	Transition wavelength (Å)				
	IS model results		Debye model results		Experimental results
	nonrelativistic	Relativistic	nonrelativistic	Relativistic	
		C^{5+}			
1s → 2p	33.7422	33.7238	33.7878	33.7693	33.7491
1s → 3p	28.4733	28.4589	28.5693	28.5546	28.4667
1s → 4p	27.0055	26.9918	27.1597	27.1427	26.8791
1s → 5p	26.3906		26.5488		26.2104
1s → 6p	26.0926		25.9557		25.7380
		Ar^{17+}			
1s → 4p	3.7498	3.7311	3.7962	3.7767	3.7494
1s → 3p	3.1668	3.1525	3.2882	3.2265	3.2394
1s → 4p	3.0110	2.9969			2.9927

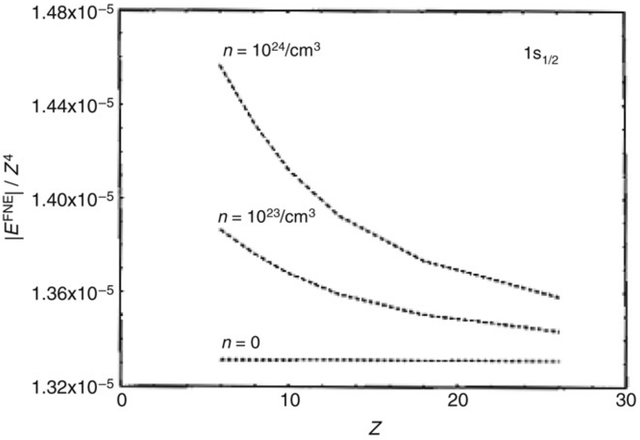

Figure 16 Plot of the scaled fine structure correction for the ground state of hydrogen-like ions for different plasma densities using Ion Sphere model. Reprinted with permission from [180] © 2000, American Physical Society

Wang and Winkler [185] used correlated basis sets to study variationally the stability of the ground state energy of the H^- ion and He and also the behavior of several excited states of He under Debye screening. A general study of the stability of the excited states of the He isoelectronic sequence

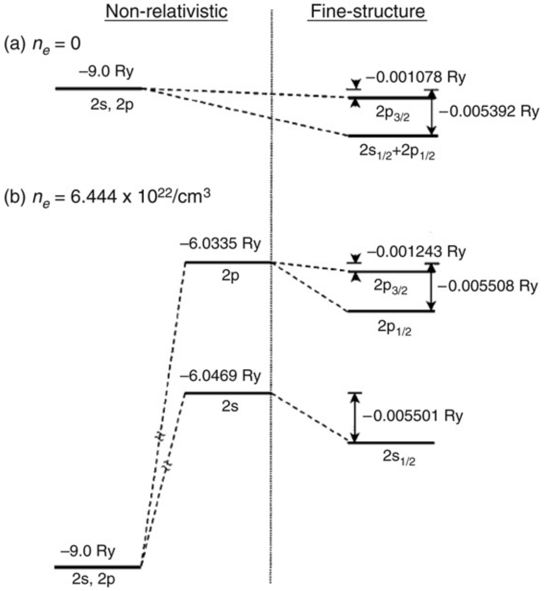

Figure 17 Modification of the $n = 2$ fine structure multiplet of C^{5+} ion in a dense plasma with electron density $6.444 \times 10^{22}/\mathrm{cm}^3$. Reprinted with permission from [180] © 2000, American Physical Society

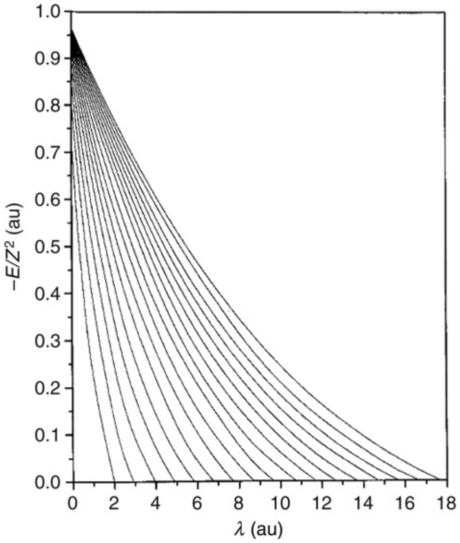

Figure 18 Variation of the ground state energy of helium-like ions against the Debye parameter. The lowermost curve is for He and the uppermost curve is for Ar^{16+}. Reprinted with permission from [192] © 2002, Springer Science + Business Media

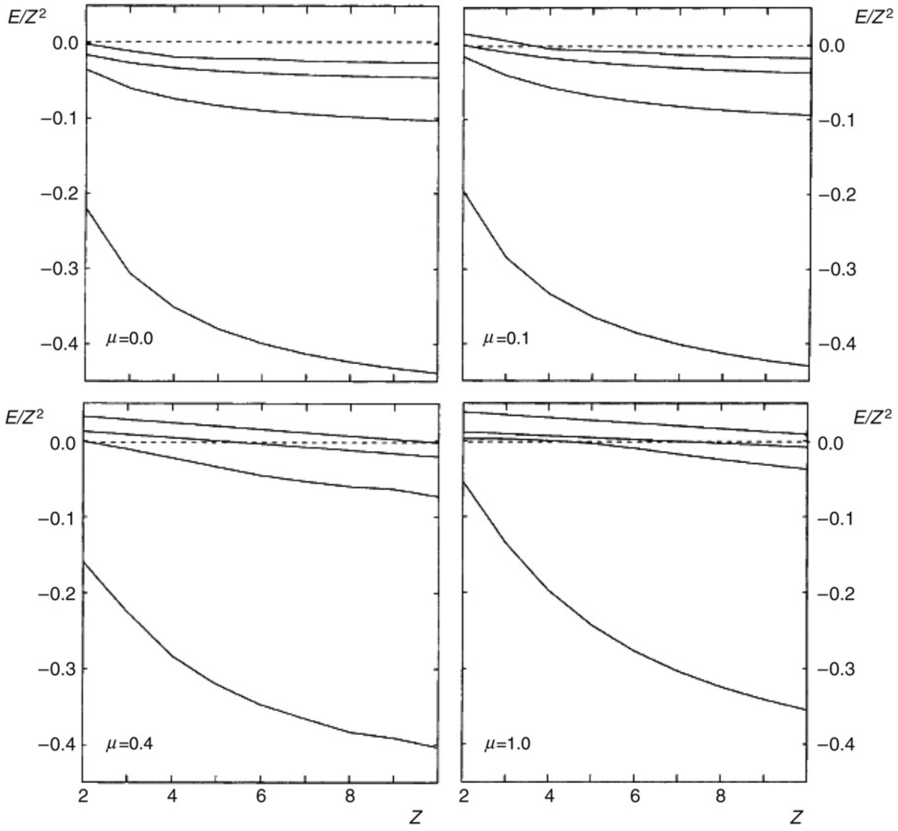

Figure 19 Plot of the lowest four ^{1}S energies (au) of helium-like ions against different Debye parameters (au). The ionization limit is set to zero. Reprinted with permission from [193] © 2002, Elsevier

was due to Mukherjee et al. [193]. Figure 19 shows the pattern for the stability plot of the lowest three excited ^{1}S states of two-electron ions from $Z = 2 - 10$.

The general pattern is likely to be similar for other excited states. It is noted that the high lying excited states rapidly move to the continuum with increased screening. The precise results obtained by Kar and Ho [189] on the energies of the ground and several excited states of He, along with the behavior for the ground state of He$^+$ using accurate basis sets, serve as future reference. Their results for the transition energy (au) between the ground and some low lying excited states are shown in Table 3.

The effect of the Debye screening on the spectra of a few He-like ions was studied by Saha et al. [194] using time dependent perturbation theory. Detailed analysis has been made for the behavior of the orbital energies, polarizabilities; transition energies, oscillator strengths and transition

Table 3 Transition energy (in au) between the ground states and some low-excited states of He. Reprinted with permission from [189]. Copyright 2006, John Wiley & Sons, Inc.

D	$E_{\mathrm{He}(1\mathrm{s}2\mathrm{p}\,^1P)} - E_{\mathrm{He}(1\mathrm{s}1\mathrm{s}\,^1S)}$	$E_{\mathrm{He}(1\mathrm{s}2\mathrm{p}\,^3P)} - E_{\mathrm{He}(1\mathrm{s}1\mathrm{s}\,^1S)}$	$E_{\mathrm{He}(1\mathrm{s}2\mathrm{p}\,^1P)} - E_{\mathrm{He}(1\mathrm{s}2\mathrm{s}\,^1S)}$	$E_{\mathrm{He}(1\mathrm{s}2\mathrm{p}\,^3P)} - E_{\mathrm{He}(1\mathrm{s}1\mathrm{s}\,^3S)}$
∞	0.77988129053	0.77056018624	0.02213095957	0.042065187477
100	0.77967550012	0.77037898679	0.02213672050	0.042053595407
70	0.77946510435	0.77019350249	0.02214253590	0.042041866587
50	0.77907504996	0.76984925985	0.02215309420	0.042020214210
40	0.77863392153	0.76945950648	0.02216467715	0.041995730651
30	0.77769846566	0.76863183473	0.02218797598	0.041943484983
20	0.77511164006	0.76633705514	0.02224355703	0.041794747738
15	0.77162468344	0.76323336469	0.02229832712	0.041581379291
10	0.76214940433	0.75475510509	0.02233279745	0.040914485985
8	0.75299073794	0.74651097989	0.02220686574	0.040138178936
6	0.73398854286	0.72928597345	0.02141390651	0.038071846235
5	0.71531022025	0.71225716925	0.01979445884	0.035346740304

Table 4 Ionization pressures P (atm) and scaled critical radii ZR_c. The screening parameter λ and the radii are in au. Reprinted with permission from [195]. Copyright 2005, Elsevier.

Ion	λ	P	ZR_c	λ	P	ZR_c
He	0.00	3.98×10^7	2.79	0.08	3.03×10^7	2.96
Li^+	0.00	7.32×10^8	2.38	0.25	4.77×10^8	2.60
Be^{2+}	0.00	4.54×10^9	2.22	0.30	3.25×10^9	2.38
B^{3+}	0.00	1.72×10^{10}	2.13	0.50	1.13×10^{10}	2.33
C^{4+}	0.00	4.93×10^{10}	2.08	0.50	3.56×10^{10}	2.22

probabilities for the lowest three excited states $1\mathrm{s}^2 \rightarrow 1\mathrm{s}n\mathrm{p}$: $^1\mathrm{P}$ ($n = 2$–4) against the screening parameter λ. The effects of the Debye screening, as well as the spatial confinement on such properties, have also been investigated by Saha et al. [195]. The general pattern of other structural parameters is given in detail by Saha et al. [195]. The pressure generated by the spatial confinement is calculated, and the ionization pressures generated by critical confinement radii for different ions have been listed in Table 4.

Kar and Ho [196] have estimated the oscillator strengths for different transitions, dipole and quadrupole polarizabilities of He for a wide range of the Debye screening parameters using explicitly correlated wavefunctions. Results presented by Kar and Ho [196] are very accurate and may be of substantial use for comparison with those from laser plasma experiments. The behavior of several singly and doubly excited states of He under screened potential was also accurately estimated by Kar and Ho [197] using correlated basis functions. Variation of the transition wavelength as a

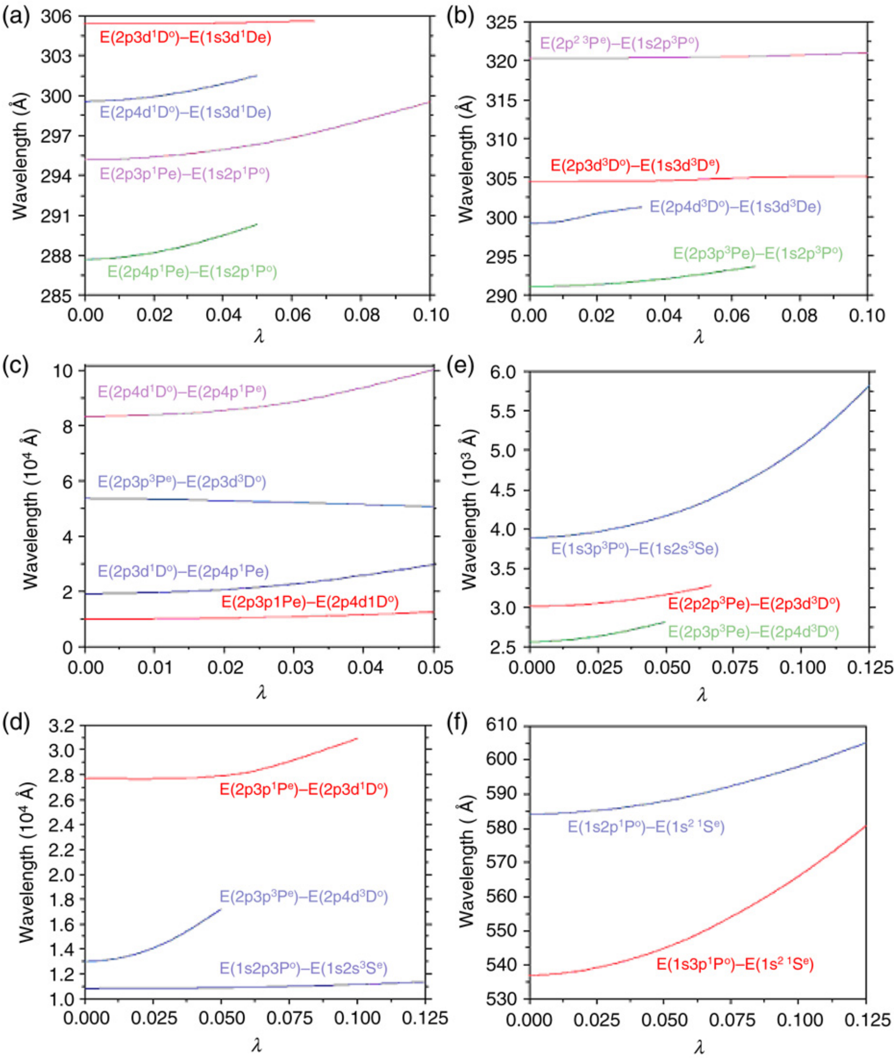

Figure 20 Transition wavelengths of the helium atom immersed in plasmas in terms of the screening parameter λ (au). Reprinted with permission from [197] © 2007, Elsevier

function of the screening parameter for He is displayed in Figure 20. Kar and Ho [198] also investigated interatomic forces between H and He atoms under screened Coulomb potential and estimated the variation of the dispersion coefficient C_6 with respect to the screening parameter using highly correlated basis functions.

Figure 21 displays the nature of the variation of C_6 against the screening parameter λ. The effect of Debye plasma on the atomic diamagnetic level

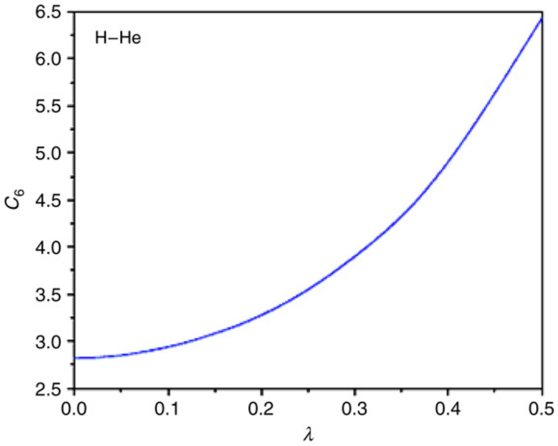

Figure 21 The dispersion coefficient C_6 as a function λ for the interaction between H and He atoms in their ground states (au is used). Reprinted with permission from [198] © 2007, Elsevier

shift of two-electron ion Ne^{8+} has been investigated by Ray [199] within a nonrelativistic framework. The total Hamiltonian is represented by

$$H = H_0 + H_1 \tag{46}$$

$$H_0 = \sum_{i=1,2}\left[\left(\frac{p_i^2}{2}\right) - \left(\frac{Z}{r_i}\right)\exp(-\lambda r_i)\right] + \left(\frac{1}{r_{12}}\right)\exp(-\lambda r_{12}) \tag{47}$$

$$H_1 = \sum_{i=1,2}\left[-\left(\frac{1}{c}\right)\vec{A}_i.\vec{p}_i + \left(\frac{1}{2c^2}\right)\vec{A}_i^2\right]. \tag{48}$$

For an uniform magnetic field this can be transformed into [199]

$$H_1 = \sum_{i=1,2}\left[\left(\frac{1}{2c}\right)\vec{B}.\vec{l}_i + \left(\frac{1}{8c^2}\right)\left|\vec{B}\times\vec{r}_i\right|^2\right]. \tag{49}$$

The first order perturbation energy is calculated and the diamagnetic susceptibility is calculated from

$$\Delta E = -\frac{1}{2}\chi_d^{\text{ion}}B^2. \tag{50}$$

A typical pattern for the variation of diamagnetic susceptibility against the screening parameter is shown in Figure 22.

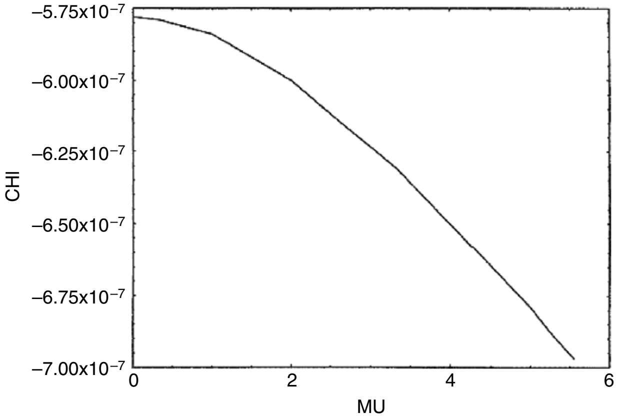

Figure 22 Variation of the diamagnetic susceptibility CHI (χ_d^{ion} in a_B^3) of the ground state $1s^2\ {}^1$S of the Ne^{8+} impurity against the dimensionless screening strength parameter $\mathrm{MU} = \lambda * a_B$ (a_B is the Bohr radius) in a magnetized plasma. Reprinted with permission from [199] © 2000, IOP Publishing Limited

Kar and Ho [200] performed an interesting estimation of the ratio of double to single photoionization cross-sections of plasma embedded helium atoms at X-ray energies under weak coupling. Their reported result for the ratio for the free system is in good agreement with available synchrotron data. The same authors studied in detail the effect of weakly coupled plasma within the Debye model on the photodetachment cross sections of H^- by using the asymptotic form of the bound state wavefunction and a plane wave representation for the final state wavefunction [201]. Highly correlated basis functions have been used in such calculations to predict the nature of the photoionization cross-section against the wavelength in a plasma environment. The effect of a plasma environment under a screened potential has a fairly extensive literature. But the number of calculations on two- or many-electron systems under a strongly coupled plasma is relatively few. Diamagnetic response properties of He-like C^{4+} immersed in a dense plasma have been investigated by Ray [202] using the HF method and first-order perturbation theory. The IS model of the plasma is applied in which the potential term due to external plasma is given by Equation (30) with $N = 2$. The first order Hamiltonian in the presence of a uniform magnetic field is given by Equation (49). The diamagnetic shift of energy E^1, with respect to the strength of the magnetic field at different electron densities, is displayed in Figure 23, and the behavior of the diamagnetic susceptibility as a function of density is shown in Figure 24.

Spectroscopic properties such as the orbital energies, dynamic polarizabilities, low lying excited state energy levels, oscillator strengths and transition probabilities have been evaluated in strongly coupled plasma for the He-like

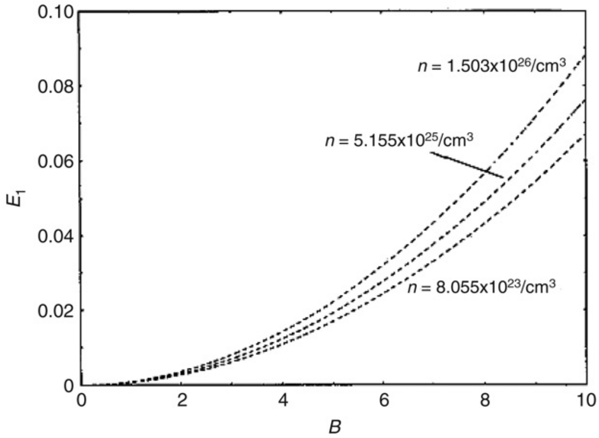

Figure 23 Diamagnetic shift (E_1, in cm^{-1}) of the ground state of a C^{4+} ion as a function of the magnetic field (B, in MG) within dense plasma at plasma electron densities $n = 8.055 \times 10^{23}/\mathrm{cm}^3$, $5.155 \times 10^{25}/\mathrm{cm}^3$ and $1.503 \times 10^{26}/\mathrm{cm}^3$. Reprinted with permission from [202] © 2001, American Physical Society

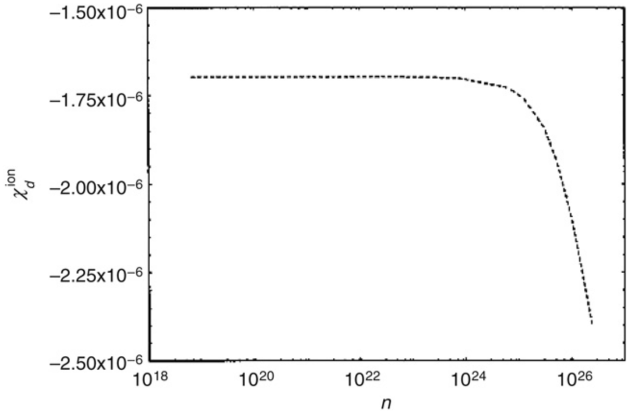

Figure 24 Variation of the diamagnetic susceptibility (χ_d^{ion}, in a_B^3) of a plasma-embedded C^{4+} ion in its ground state against the plasma electron density (n/cm^3). Reprinted with permission from [202] © 2001, American Physical Society

ions Li^+ to Ne^{8+}, using the IS model by Sil and Mukherjee [203]. Figure 25 gives a plot of the orbital energy against the ion sphere radius for Ne^{8+}. A plot of the excitation energy $1\mathrm{s}^2 \rightarrow 1\mathrm{s}2\mathrm{p}$: $^1\mathrm{P}$ for O^{6+} against IS radius is given in Figure 26.

Confinement due to an ion sphere as well as Debye screening with radial confinement, generates pressure on the system, whose critical value at the ionization for different parameters, has been displayed in Table 5.

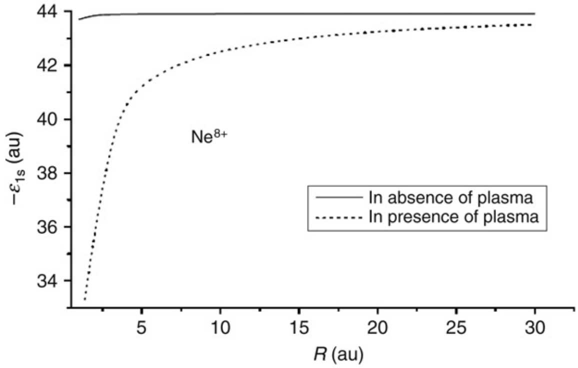

Figure 25 Plot of orbital energy against ion-sphere radius for Ne^{8+}. Reprinted with permission from [203] © 2006, John Wiley & Sons, Inc.

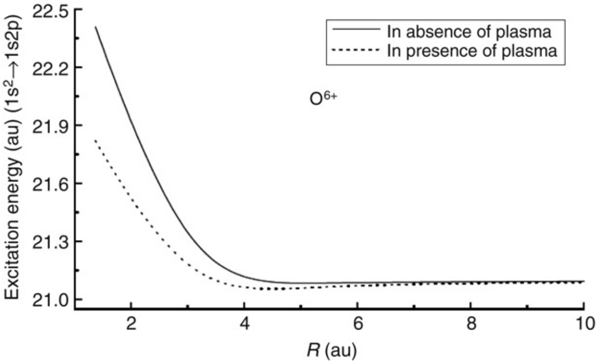

Figure 26 Excitation energy vs IS radius R for O^{6+}. Reprinted with permission from [203] © 2006, John Wiley & Sons, Inc.

Table 5 Comparison of the critical radius R_c (in au), n $(/\mathrm{cm}^3)$ and critical pressure P_c (in atm) between the results obtained by using a Debye–Hückel model and an Ion-Sphere (IS) model. Reprinted with permission from [203] Copyright 2006, John Wiley & Sons, Inc.

Ion	λ	ZR_c	P_c	n(IS)	ZR_c(IS)	P_c(IS)
Li^+	0.00	2.36	7.32×10^8	1.71×10^{24}	2.94	2.71×10^8
	0.25	2.60	4.77×10^8			
Be^{2+}	0.00	2.22	4.54×10^9	7.41×10^{24}	3.03	1.08×10^9
	0.30	2.36	3.25×10^9			
B^{3+}	0.00	2.13	1.72×10^{10}	2.05×10^{24}	3.09	3.19×10^9
	0.50	2.33	1.13×10^{10}			
C^{4+}	0.00	2.08	4.93×10^{10}	4.57×10^{24}	3.12	7.83×10^9
	0.50	2.22	3.56×10^{10}			

*The screening parameter λ is in au.

Table 6 Comparison between experimental and theoretical results of relativistic (R) & non relativistic (NR) transition wavelengths of C^{4+}, Al^{11+} and Ar^{16+}. The experimental data have been extracted from Figure 1 of Nantel et al. [99], Figure 1 of Riley et al. [92] and Figure 2 of Woolsey et al. [104] for C^{4+}, Al^{11+} and Ar^{16+}, respectively. The transition wavelengths have been calculated at the experimentally quoted temperatures and densities

Excitations	Transition wavelength (Å)						
	IS model results		Debye model results				Expt. results
			Only Debye		Debye + Box		
	NR	R	NR	R	NR	R	
C^{4+}							
$1s^2 \rightarrow 1s2p$	40.2079	40.7000	40.2765	40.7851	40.2794	40.7852	40.268
$1s^2 \rightarrow 1s3p$	34.9530	35.3253	35.1182	35.5035	35.1328	35.5035	34.998
$1s^2 \rightarrow 1s4p$	33.4305	33.7728	33.7014	34.0575	33.7036	34.0547	33.469
$1s^2 \rightarrow 1s5p$	32.7996	33.1326	33.1746	33.5217	32.9183	33.3978	32.773
Al^{11+}							
$1s^2 \rightarrow 1s2p$	7.7686	7.7671	7.8222	7.8228	7.8283	7.8228	
$1s^2 \rightarrow 1s3p$	6.6478	6.6458	6.7611	6.7602	6.7465	6.7560	6.63
$1s^2 \rightarrow 1s4p$	6.3344	6.3323	6.5139	6.5129			6.31
$1s^2 \rightarrow 1s5p$	6.2049	6.2120					6.17
Ar^{16+}							
$1s^2 \rightarrow 1s2p$	3.9644	3.9497	4.0187	4.0048	4.0225	4.0048	3.984
$1s^2 \rightarrow 1s3p$	3.3820	3.3703	3.4811	3.4811	3.3919	3.4544	3.365
$1s^2 \rightarrow 1s4p$	3.2255	3.2152	3.3852	3.3852		3.3688	3.168
$1s^2 \rightarrow 1s5p$	3.1523	3.1690	3.3628	3.3628		3.3314	

A general discussion of the results from the different methodologies for one- and two-electron systems was given by Sil et al. [204]. Laser produced plasma experiments on C, Al and Ar plasma performed by Nantel et al. [99], Riley et al. [92], Saemann et al. [71] and Woolsey et al. [104] yield H- and He-like spectral lines of these ions and their profiles. The line positions calculated by Sil et al. [205] using nonrelativistic and relativistic Debye models with spatial confinement as well as an IS model of the plasma at temperatures and densities suggested by the experimental conditions, are in reasonably good agreement indicating the success of the simple models. From the analysis of a host of data it appears that the IS model yields better agreement with the laser produced data. Table 6 gives a comparison of the data calculated by using Debye and IS models of the plasma both in the relativistic and nonrelativistic formalisms and those obtained from laser plasma experiments [205].

4.3. Three body systems under plasma

Several calculations have been performed for systems in which a generalized three body Hamiltonian is solved for studying the energy levels and other properties under plasma, mostly using the Debye screening model. These calculations properly incorporate electron correlations in their framework and are highly precise. Theoretical investigations on the Ps^- ion are of importance as few experimental observations are available for the existence and decay measurements of Ps^- [206]. The stability of Ps^- embedded in a Debye plasma was investigated by Saha et al. [207] using basis functions which include inter-particle coordinates explicitly. The Hamiltonian of the three-body system is given by

$$H = -\sum_{i=1}^{3} \frac{1}{2m_i}\nabla_i^2 + \sum_{i<j=1}^{3} \frac{q_i q_j \mathrm{e}^{-\lambda r_{ij}}}{r_{ij}}, \tag{51}$$

where the q_i 's are the respective charges in atomic units, and λ, as before, is the Debye screening parameter. Again, one has to solve the Schrodinger equation

$$H\,|\Psi\rangle = E\,|\Psi\rangle \tag{52}$$

to get the energy eigenvalue in a given confinement. For the spherically symmetric ground state of a three-body system, momentum conservation leads to a nonrelativistic Hamiltonian, expressible in terms of relative coordinates r_1, r_2 and r_{12}, and the expectation value of the Hamiltonian with respect to a normalized wavefunction $|\Psi\rangle$ can be written as [207]

$$\begin{aligned}
&\langle \Psi\,|\mathrm{H}|\,\Psi\rangle \\
&\quad= \int \left\{ \frac{1}{2}\left(\frac{1}{m_1}+\frac{1}{m_3}\right)\left(\frac{\partial\Psi}{\partial r_1}\right)^2 + \frac{1}{2}\left(\frac{1}{m_2}+\frac{1}{m_3}\right)\left(\frac{\partial\Psi}{\partial r_2}\right)^2 \right. \\
&\qquad + \frac{1}{2}\left(\frac{1}{m_1}+\frac{1}{m_2}\right)\left(\frac{\partial\Psi}{\partial r_{12}}\right)^2 + \frac{1}{m_3}\left(\frac{r_1^2+r_2^2-r_{12}^2}{2r_2r_2}\right)\left(\frac{\partial\Psi}{\partial r_1}\right)\left(\frac{\partial\Psi}{\partial r_2}\right) \\
&\qquad + \frac{1}{m_2}\left(\frac{r_2^2-r_1^2+r_{12}^2}{2r_2r_{12}}\right)\left(\frac{\partial\Psi}{\partial r_2}\right)\left(\frac{\partial\Psi}{\partial r_{12}}\right) + \frac{1}{m_1}\left(\frac{r_1^2-r_2^2+r_{12}^2}{2r_1r_{12}}\right) \\
&\qquad \left. \times \left(\frac{\partial\Psi}{\partial r_1}\right)\left(\frac{\partial\Psi}{\partial r_{12}}\right) + \left(-\frac{\mathrm{e}^{-\lambda r_1}}{r_1} - \frac{\mathrm{e}^{-\lambda r_2}}{r_2} + \frac{\mathrm{e}^{-\lambda r_{12}}}{r_{12}}\right)\Psi^2 \right\} \\
&\qquad \times r_1 r_2 r_{12}\,\mathrm{d}r_1\,\mathrm{d}r_2\,\mathrm{d}r_{12}.
\end{aligned} \tag{53}$$

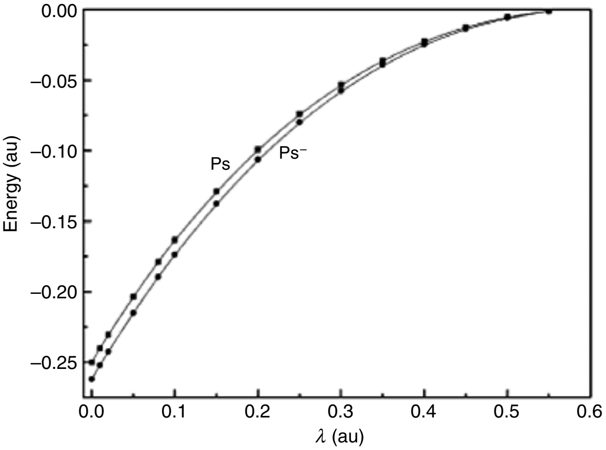

Figure 27 Plot of ground state energy of Ps and Ps$^-$ against the Debye screening (λ). Reprinted with permission from [207] © 2003, Elsevier

The wavefunction is expanded in terms of Hylleraas basis sets incorporating explicitly the electron correlation effects

$$\Psi(r_1, r_2, r_{12}) = \sum_{ij} C_{ij}\chi_i(1,2)\eta_j(12), \tag{54}$$

where

$$\chi_i(1,2) \sim (e^{-\alpha_k r_1} e^{-\alpha_l r_2} + e^{-\alpha_l r_1} e^{-\alpha_k r_2}) \tag{55}$$

gives the radially correlated basis, being expanded in terms of products involving Slater exponents α_i's, and

$$\eta_j(12) \sim e^{-\beta_j r_{12}} \tag{56}$$

involves inter-particle coordinates in the basis set expansion and gives angular correlations.

The generalized eigenvalue equation

$$\underline{\underline{H}}\,\underline{C} = E\underline{\underline{S}}\,\underline{C} \tag{57}$$

is solved to yield the energy eigenvalues and the linear variation parameters. Depending upon the expansion length of the basis set the calculation yields highly accurate estimates of energy and often benchmark results.

Figure 27 shows a plot of the stability of Ps$^-$ against the Debye screening. Several other calculations on plasma embedded Ps$^-$ subsequently

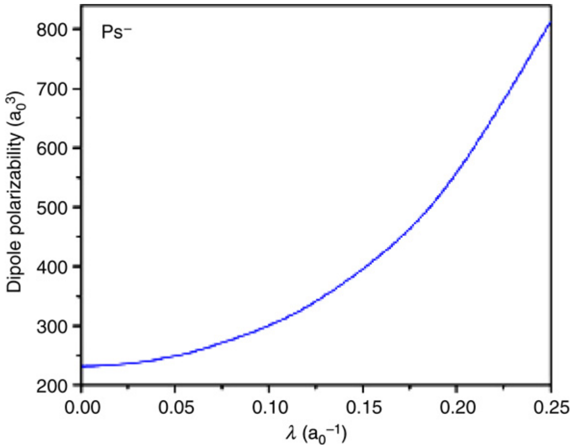

Figure 28 Dipole polarizability of Ps^- in plasma in terms of the screening parameter λ. Reprinted with permission from [210] © 2008, Elsevier

follow [208,209]. The behavior of the dipole polarizabilities of Ps^- and H^- against the Debye screening parameter has been analyzed by Kar and Ho [210] using highly correlated basis functions. As usual the polarizability value increases monotonically with the increase of the screening parameter as shown in Figure 28. The effect of weakly coupled plasma on the photodetachment cross-sections of Ps^- has been investigated by Kar and Ho [211] much along the same lines as it was for H^- [201]. These results are likely to be useful in plasma physics and astrophysics. An interesting calculation on the intermolecular interaction potential between positronium and light atoms in a screened Coulomb potential was performed by Kar and Ho [212]. The variation of the van der Waals coefficient against the Debye screening parameter obtained by them for Ps–He system, is shown in Figure 29.

Correlated calculations on the stability and other properties of plasma embedded H^- using similar techniques exist [213,214]. Stability of the H_2^+ molecular ion under weakly coupled plasma and also the dipole polarizability have been investigated by using correlated basis sets [215,216]. The variation of the ground state energy and the polarizability are similar in nature as observed generally for other existing systems, the numerical values being highly precise.

4.4. Exotic systems under plasma

The effects of plasma environments on the spectral properties of exotic two- and three-body systems have been studied. Influence of the Debye plasma on the stability and spectral properties of spatially confined exotic systems like $p^+\mu^-$ and $\mu^+\mu^-$ was investigated by Sil et al. [217] along the same line as was

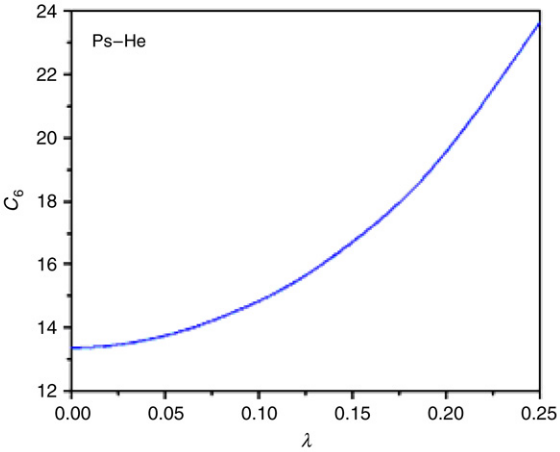

Figure 29 Dispersion coefficient C_6 in terms of the screening parameter λ for the interaction between Ps and He atoms in their ground states. Reprinted with permission from [212] © 2008, Elsevier

Table 7 Ionization pressures at different plasma screening (λ). Reprinted with permission from [217]. Copyright 2004, Elsevier.

Atom	λ (au)	R_0(au)	Ionization pressure (atm)
$p^+ \mu^-$	00.0	0.0099	7.2621(+15)
	10.0	0.0102	6.1743(+15)
$\mu^+ \mu^-$	00.0	0.0178	6.9546(+14)
	10.0	0.0189	5.1767(+14)

done for the H atom [172]. Because of the large reduced mass of the system, the domain of the energy values is larger and the polarizability value is small, indicating a very large value of the screening parameter to destabilize the system. This is shown explicitly by calculating the ionization pressures for such systems and are displayed in Table 7. Further estimates in this line were done by Bhattacharyya et al. [218] on the electron affinity of exotic systems like μ^+ e^- and π^+ e^- by using the general three-body formalism described in Section 4.3.

Electron correlation has been taken care of by using multiple exponent Hylleraas type basis sets. The effect of radial and full correlation on such affinity is analyzed and is reflected in Figure 30.

The calculations have been further extended by Sil et al. [219] for analyzing the stability of exotic systems like ppμ, ddμ and ttμ and also finding the behavior of the hadronic affinity under Debye plasma. An interesting feature emerges from this particular study, namely, a given two-body system becomes unstable at a screening parameter for which the corresponding three-body system is stable. This property depends very much on the

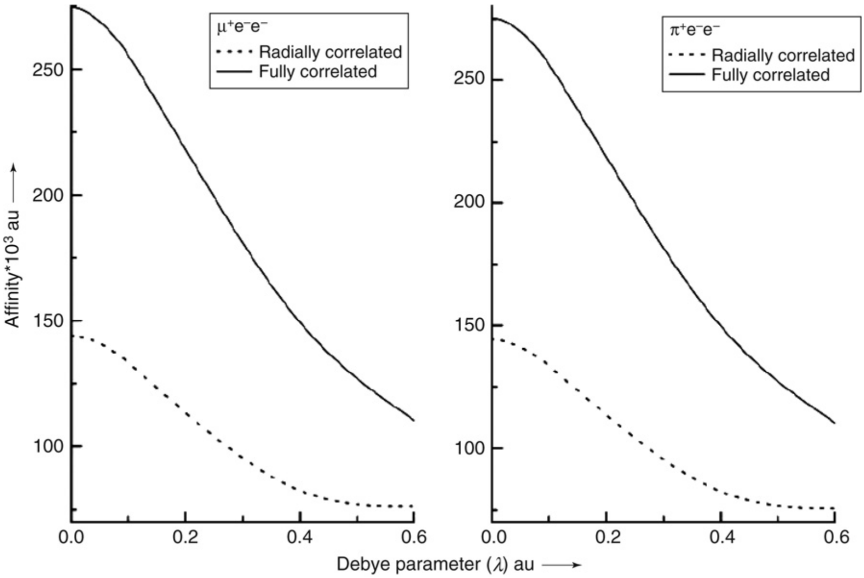

Figure 30 Plot of electron affinity of the exotic systems against the Debye screening parameter λ. Reprinted with permission from [218] © 2007, John Wiley & Sons, Inc.

reduced mass of the systems. This feature is displayed in Figure 31. The critical mass for which a two-body system becomes unbound can be obtained by scaling the result of Gomez et al. [220]. The phenomena where the two particle system is energetically unbound while the corresponding three particle system is bound is known as Thomas collapse [221–223]. These are called Borromean systems as they resemble Borromean rings linked together, although in the absence of any one of them no pair of the others are linked. Further studies on exotic molecular ions tdμ and ddμ under Debye plasma was performed Kar and Ho [224] in relation to both bound and particularly resonance states. This will be detailed in the next section.

4.5. Resonance states under plasma

Investigations on the doubly excited states of two electron systems under weakly coupled plasma have been performed by several authors. Such states usually occur as resonance states in electron atom collisions and are usually autoionizing [225]. Many of these states appear in solar flare and corona [226,227] and contribute significantly to the excitation cross-sections required to determine the rate coefficients for transitions between ionic states in a high temperature plasma. These are particularly important for dielectronic recombination processes which occur in low density high temperature plasma, occurring e.g. in solar corona. Coronal equilibrium is usually guided by the balance between the rates of different ionization and

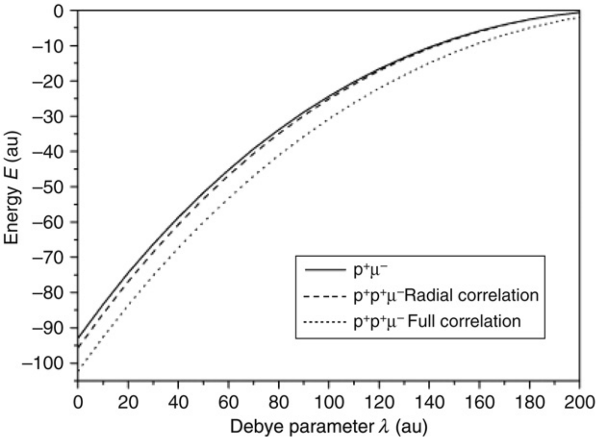

Figure 31 Energy of $\mathrm{p\mu}$ and $\mathrm{pp\mu}$ against the Debye parameter. Reprinted with permission from [219] © 2008, Elsevier

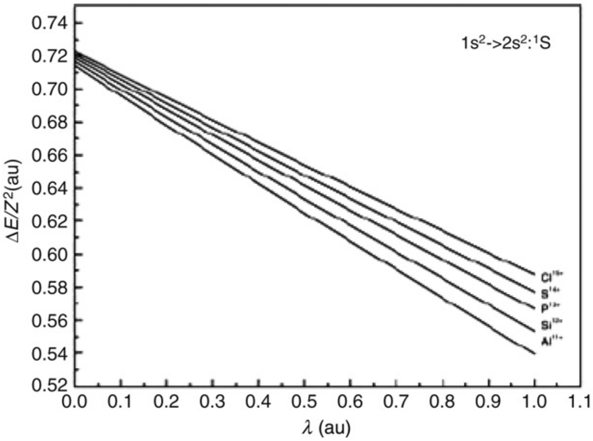

Figure 32 Variation of $\Delta E/Z^2$ with λ for all ions for the transition $1\mathrm{s}^2 \rightarrow 2\mathrm{s}^2$: ^{1}S. Reprinted with permission from [232] © 2005, John Wiley & Sons, Inc.

recombination processes [228,229]. Dielectronic recombination processes are directly linked with doubly excited states [230,231]. Study of doubly excited states and their properties, is thus, an important area for the generation of atomic data. An earlier calculation of plasma embedded doubly excited states was made by Sil and Mukherjee [232]. The calculations were done involving highly stripped ions of the He sequence which normally occur in high temperature plasma. The behavior of the excitation energies of several doubly excited states under screened Coulomb potential was analyzed. Figure 32 displays the variation of the doubly excited state energies against

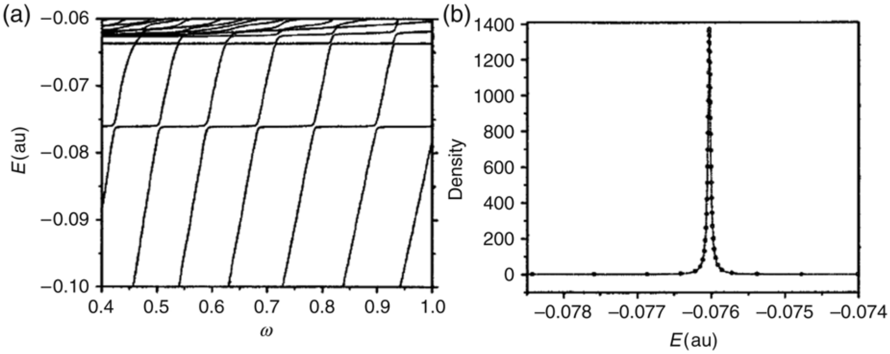

Figure 33 (a) Stabilization plots for the $2s^2\ {}^1S^e$ state of Ps^- in the Debye plasma environments for $D = 10$. (b) Calculated density (circles) and the fitted Lorenztian (solid line) corresponding to the $2s^2\ {}^1S^e$ state of Ps^- for $D = 10$. Reprinted with permission from [235] © 2005, American Physical Society

the screening parameter λ for different ions and gives an idea about the nature of the variation. Pioneering work on the resonance states in positron hydrogen scattering under Debye plasma was done by Kar and Ho [233] using Hylleraas basis sets. The stabilization method [234] was used in their calculation to find the density of resonance states. Similar calculation for the Ps^- resonance state under the Debye plasma was performed by Kar and Ho [235]. The stabilization of the lowest resonance state in Ps^- under a given screening parameter is shown in Figure 33.

The variation of the energy of Ps^- against the Debye screening parameter follows a similar pattern as obtained earlier by Saha et al. [207] but the variation of the width of the resonance level against the screening parameter is instructive. A series of calculations by Ho and co-workers follow in this line for the study of low and high lying resonance states in the plasma embedded H^-, Ps^- and He [191,236–238]. The nature of the variation of the width of ${}^{1,3}P^o$ resonances in Ps^- against the Debye screening parameter due to Ho [238] and shown in Figure 34 is instructive.

Resonance states of tdμ and ddμ molecular ions under plasma have been calculated by Kar and Ho [224] using a generalized three-body formalism discussed in Section 4.3 with highly correlated basis functions. The variation of the ground and ro-vibrational excited state energy with respect to the screening constant follows a similar pattern to that obtained earlier by Sil et al. [219], but the resonance states, as calculated by the stabilization method, give new insight in this line. Figure 35 displays the variation of the resonance state energies against the screening constant λ for the ddμ ion.

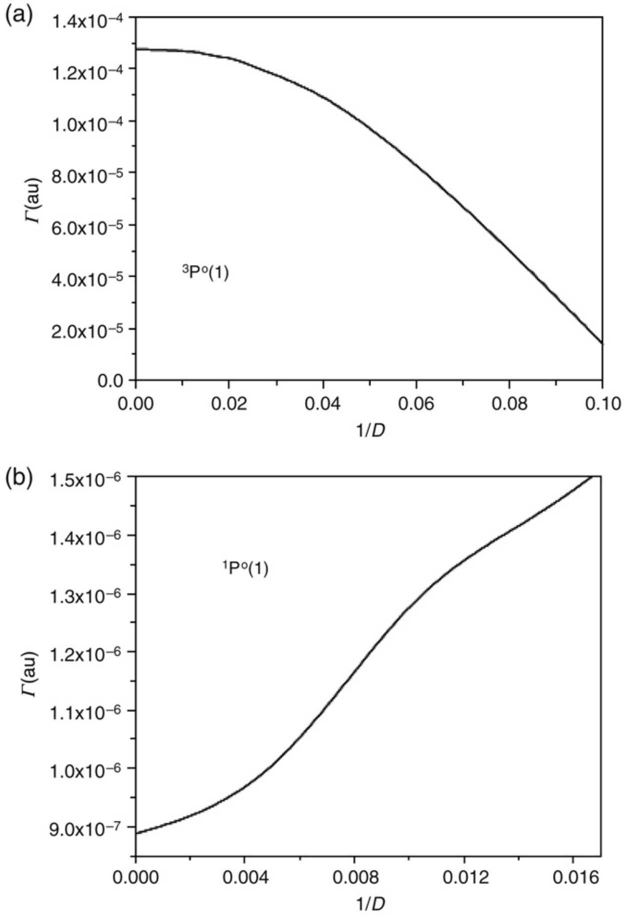

Figure 34 Resonance widths of first $^3\mathrm{P}^\mathrm{o}$ and $^1\mathrm{P}^\mathrm{o}$ of Ps^- as a function of the Debye screening parameter (au). Reprinted with permission from [238] © 2008, Elsevier

4.6. Many electron atoms under plasma

Earlier calculation on many electron atomic systems under plasma was performed by Stewart and Pyatt [58], who estimated the variation of IP of several atoms using a finite temperature TF model. Applications of the density functional theory on these systems were reviewed by Gupta and Rajagopal [57]. The calculations on many electron systems are mostly concerned with the hot and dense plasmas with the application of the IS model, or from general solutions of the Poisson equation for the potential function. The discussions using the average atom model in Section 3.3, Inferno model of Liberman in 3.4, STA model in 3.5, hydrodynamic model in 3.6, time dependent methods using the ATDDFT model and FTRPA methods

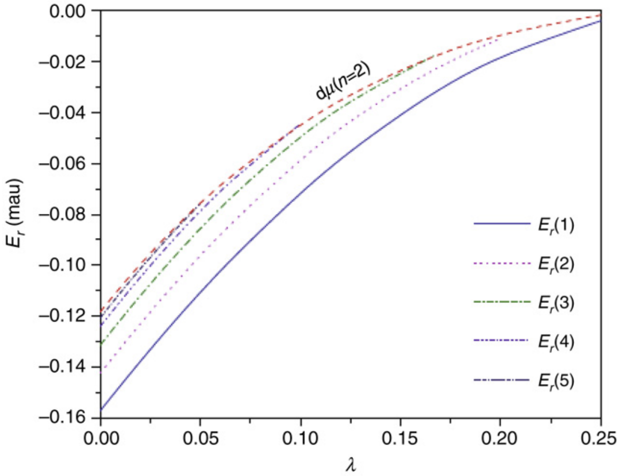

Figure 35 $J = 0$ state resonance energies of the ddμ molecular ion for different screening parameters along with the $n = 0$ threshold energies of dμ. Reprinted with permission from [224] © 2008, EDP Sciences

in 3.7 are all concerned with the properties of many electron systems. Recent calculations due to Silanes et al. [239] on the relative stability of various charge states of several atoms under Debye plasma and also that of Gill et al. [240] using an effective screened potential are very instructive. The influence of plasma screening on the spectral properties of low lying allowed and intercombination lines of Be isoelectronic ions have been investigated by Saha and Fritzsche [241] using the multiconfiguration Dirac-Fock method. The intensity ratio of the allowed to intercombination lines is very useful for the interpretation of astrophysical and tokamak plasma diagnostics [242–245]. In Figure 36 a typical plot of this intensity ratio against the Debye screening parameter for Be-like Fe and Mo is given. These ions are observed in a large variety of astrophysical and laboratory tokamak plasmas [246, 247]. Multiconfiguration Dirac-Fock calculations have also been performed by Saha and Fritzsche [248] for the estimation of the plasma polarization shift of the lowest lying resonance and intercombination transitions of several Be-like ions using a strongly coupled model of the plasma. A typical plot of the energy shift in strongly coupled plasma is shown in Figure 37.

In many electron atomic systems the dynamic screening effect resulting from the time dependent nature of the ion movement appears to be important [249–251]. The effect of the Debye plasma on the photoionization cross-sections of Li and Na has been studied by Sahoo and Ho [252] using the complex rotation method. The photoionization cross-sections appear to be sensitive to the screening due to plasma resulting in a change of the position of the Cooper minimum. Figure 38 displays the behavior of the photoionization cross-section of Na for different screening parameters

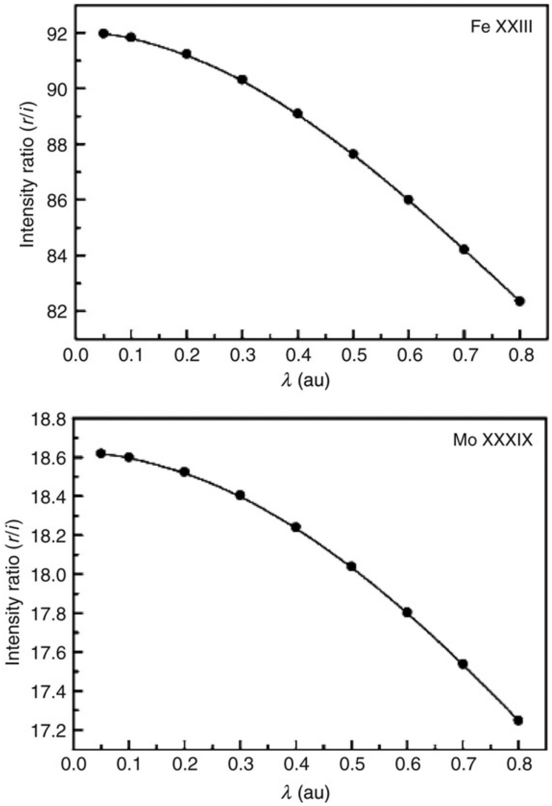

Figure 36 Intensity ratio of the resonance (r) to the intercombination (i) line as function of the plasma screening parameter λ. Results are shown for the two ions Fe XXIII and Mo XXXIX. Reprinted with permission from [241] © 2006, American physical Society

as a function of the ejected electron energy. Finite temperature random phase approximation in conjunction with average atom code has been applied by Colgan et al. [150] for estimating several spectroscopic properties of dense Ne plasma at various temperatures and densities. The method has wide applicability in many electron systems. The effects of strongly coupled plasma on the spectral properties, like the total energy and oscillator strengths for a few members of He isoelectronic series and many electron ions of Fe, have been studied by Rodriguez et al. [253] using the relativistic DFT method. This method utilizes a central analytic potential in lieu of iterative self-consistent calculations.

5. SPECTRA OF ATOMS UNDER LIQUID HELIUM

The spectroscopic properties of atoms change when embedded inside a liquid helium matrix. The common features with respect to plasma

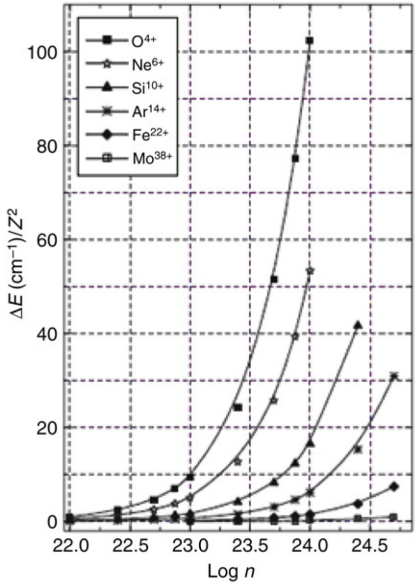

Figure 37 Plasma shift ΔE (scaled by Z^{-2}) for $2s^2\ {}^1S_0 \rightarrow 2s2p\ {}^1P_1^o$ resonance transitions as a function of the electron density (n in cm^{-3}). Reprinted with permission from [248] © 2007, IOP Publishing Limited

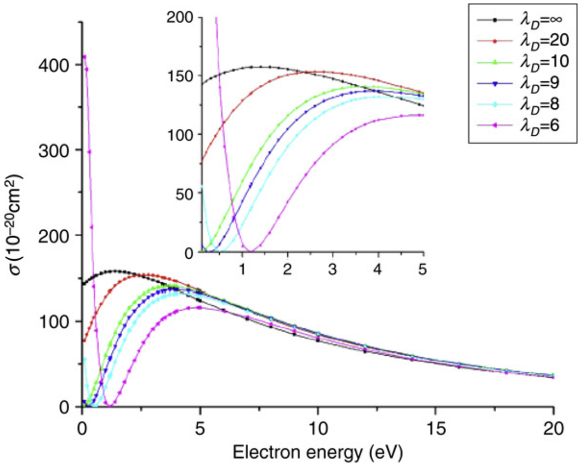

Figure 38 Photoionization cross-section of the sodium ground state for different Debye screenings as a function of the ejected electron energy. λ_D is the Debye screening length in au. Reprinted with permission (license number 2041 490188918) from [252].

embedded atomic systems are the changes in the ionization potentials, shift of the spectral line positions and changes in line shapes compared to those of the free atomic systems. Several extra features are noted like the absence of certain resonance radiations in emission, the existence of transitions not allowed for in free systems, etc. Since the overall embedded system is fairly complex not many theoretical investigations exist. It would appear that tackling this problem from the theoretical standpoint may be through a model potential or making a complete quantum mechanical calculation. We briefly describe the existing methods in next sections.

5.1. Standard bubble model (SBM)

The basic idea of this model is to assume the embedded atom to reside in a cavity inside the liquid helium, the dimension of the cavity being determined by the intermolecular interaction between the bulk liquid and the central atom. The total energy is partitioned into three parts namely, liquid energy, energy of the free atom and the interaction between the liquid and the atom [254,255]. The total Hamiltonian is thus

$$H_{\text{tot}} = H_{\text{liq}} + H_{\text{A}} + H_{\text{int}}. \tag{58}$$

The liquid energy is assumed to be formed by the kinetic energy of helium atoms and the sum of pair potential energies associated with liquid helium. H_{A} is the usual nonrelativistic many electron Hamiltonian and H_{int} is the interaction energy between liquid helium and the embedded atom. It is formed by the pair potential between He atoms and the embedded atom [109]. Usually the liquid energy is approximated in terms of classical pressure volume energy, the surface energy and the volume kinetic energy arising out of the enhanced kinetic energy of the liquid at the bubble margin [254,255]. The liquid helium density $\rho\ (r)$ vanishes at the atomic site and starts to grow at a given radius r_0 reaching the bulk density at a long distance from the atomic site. The effective bubble radius r_b is defined as the center of mass of the density distribution and is determined by [109]

$$\int_0^{r_b} \rho(r).4\pi r^2 \mathrm{d}r = \int_{r_b}^{\infty} [\rho_0 - \rho(r)]\,.4\pi r^2 \mathrm{d}r. \tag{59}$$

The density distribution is assumed to have a profile like

$$\begin{aligned} \rho(r, r_0, \alpha) &= 0; \quad \text{for } r \le r_0 \\ &= \rho_0[1 - [1 + \alpha(r - r_0)]\mathrm{e}^{-\alpha(r-r_0)}]; \quad \text{for } r > r_0 \end{aligned} \tag{60}$$

r_0 and α are parameters related to the size and shape of the bubble and are determined by the optimization of the total energy of the system. In the SBM the interaction energy can be calculated in terms of the pair potential between liquid helium atoms and the central impurity integrated over the density distribution of the liquid. Once the effective interaction potential is known first-order perturbation theory may be applied to find the spectral shift of the atom. As the excitation process is very fast the liquid keeps the same structure during excitation. Thus, knowing the pair potential in the ground and the excited states the first-order shift of the energy of the atom in the ground as well as in the excited states can be calculated, giving the shift of the frequency of the spectral line. The details of the applicability of SBM is discussed by Tabbert et al. [109]. SBM has been applied to the electron bubble problem [256] and several alkaline earth atoms [257,258] using existing pair potentials.

5.2. Other methods

A pseudo potential approach was adopted by Hickman et al. [259] to calculate the excited metastable states of a He atom under liquid He. The density functional approach developed by Dupont-Roc et al. [260] was applied subsequently [261] for the description of the nature of the cavity formed around an alkali atom in the excited state of non-zero angular momentum. The resulting form of the cavity differs very much from the spherical shape. A similar approach was adopted by De Toffol et al. [262] to find qualitatively the first excited states of Na and Cs in liquid He. Earlier work in this direction was given in detail in Ref. [263].

5.3. Ab-initio quantum chemical methods

And now quantum chemical calculations have been performed using a realistic cluster model of the system. Alkali atoms are chosen as foreign atoms as it was found from laser-induced fluorescence (LIF) experiments [109,110] that alkali atoms embedded in liquid He have large spectral shifts. The first such calculation was due to Ludwig et al. [264] in which a Monte Carlo simulation technique was adopted to find the structure of the liquid environment around the central alkali atom. Subsequent quantum chemical calculation using TDDFT yields a blue shift of the Na 3s → 3p resonance line ~14.7 nm and a FWHM ~7.8 nm, in reasonably good agreement with that given by De Toffol et al. [262]. Subsequent quantum chemical calculation using model clusters by SAC-CI calculation on Na in liquid He yields encouraging results [265]. The calculations [266,267] on Na, Rb and Cs in liquid He clusters, using relativistic density functional theory (RDFT), yield very fruitful results and compare well with the existing data of the shifts of D lines in Rb and Cs in liquid He obtained in LIF experiments [110]. Table 8 gives a comparison of the results of the spectral line shifts of alkali atoms in liquid He indicating reasonable success of quantum chemical calculations in this direction.

Table 8 Spectral line shifts (in nm) of alkali atoms embedded in liquid helium. Experimental values are presented together with relativistic RLDA as well as other nonrelativistic (NR) results

Transition	Shift		
	Experiment	Theory	
		RLDA	Other (NR)
Na			
$s_{1/2} \rightarrow p_{1/2}$	Unknown	−22.90	−16.7[a]
$s_{1/2} \rightarrow p_{3/2}$	Unknown	−22.72	−15.0[b]
Average		−22.8	−18.6∼−18.9[c] −16.6[d]
Rb			
$s_{1/2} \rightarrow p_{1/2}$	−16.8±0.5[e]	−14.02	
$s_{1/2} \rightarrow p_{3/2}$	−16.0±0.5[e]	−16.81	
Average	−16.4[e]	−15.4	
Cs			
$s_{1/2} \rightarrow p_{1/2}$	−18.4±0.5[e]	−15.52	−26[b]
$s_{1/2} \rightarrow p_{3/2}$	−18.1±0.5[e]	−17.83	−27[b]
Average	−18.3[e]	−16.7	−26.5[b]

RLDA [266,267].
[a] Ref. [258].
[b] Ref. [262].
[c] Ref. [264].
[d] Ref. [265].
[e] Ref. [110].

6. SUMMARY AND FUTURE DIRECTIONS

In this brief review we have tried to concentrate on the changes in the spectral properties of atoms and ions embedded in weak and strongly coupled plasmas. The theoretical estimates mostly dealt with, are based on simple plasma models rather than by going through the vastly developed subject in terms of its dynamical behavior, which has been well reviewed earlier. Special emphasis has been given to the most recent calculations on plasma embedded properties of atoms, ions and exotic systems connected with their ground, singly and doubly excited states and new observations arising out of them. Current experiments using high power subpicosecond laser pulses have opened up a vast area, producing a wealth of atomic data whose theoretical interpretation with precision is a challenge. Highly accurate correlated calculations including the dynamics of the system are necessary. Properties of confined extended systems like semiconductors and quantum dots are to be explored more accurately, particularly with respect to reduction in the ionization potential, which may be of technological importance. The interpretation of spectral data based on the LIF experiments on foreign atoms embedded in liquid helium is in its early stage and proper interpretation in terms of quantum chemical cluster models or cold plasma models remains a challenge for future theoretical investigations.

ACKNOWLEDGEMENTS

P.K. Mukherjee acknowledges with thanks the financial support received from the Department of Science and Technology and also the Department of Atomic Energy, Govt. of India under Grant Nos: INT/POL/P-4/2004, SR/S2/LOP-05/2005, 2007/37/59/BRNS/436. He also acknowledges financial support from the AvH Foundation, Germany and FAPESP, Brazil where parts of this work was performed in collaboration. PKM wishes to acknowledge the encouragement from his parent Institution IACS, Kolkata, for allowing him all facilities necessary for sustaining research work. S. Canuto acknowledges continuous support of the Brazilian agencies CNPq, CAPES and FAPESP.

REFERENCES

[1] L. Esaki, L.L. Chang, Phys. Rev. Lett. 33 (1974) 495.
[2] R. Dingle, W. Weigmann, C.W. Henry, Phys. Rev. Lett. 33 (1974) 827.
[3] C. Weisbuch, B. Vinter, Quantum Semiconductor Structures Fundamentals and Applications, Academic Press, London, 1991.
[4] S.P. Beaumont, C.M. Sotomayor-Torres (Eds.), Science and Engineering of one and zero dimensional Semiconductors, in: NATO ASI Series B: Physics, vol. 214, Plenum Press, 1990.
[5] M.A. Read, J.N. Randall, R.J. Aggarwal, R.J. Matyi, T.M. Moore, A.E. Wetsel, Phys. Rev. Lett. 60 (1988) 535.
[6] Proceedings of the 10th International Conference on Electronic Properties of Two-Dimensional Systems, Newport, U.S.A. 1993, Surf. Sc., vol. 305, 1994.
[7] P.A. Jacobs, Carboniogenic Activity of Zeolites, Elsevier, Amsterdam, 1997.
[8] Z.K. Tang, Y. Nozue, T. Goto, J. Phys. Soc. Japan 61 (1992) 2943.
[9] H.W. Kroto, J.R. Heath, S.C. O'Brian, R.F. Curl, R.E. Smalley, Nature 318 (1985) 162.
[10] J. Cioslowski, E. Fleischmann, C. Chem. Phys. 94 (1991) 3730.
[11] A.S. Baltenkov, J. Phys. B: At. Mol. Opt. Phys. 32 (1999) 2745.
[12] J.P. Connerade, V.K. Dolmatov, P.A. Lakshmi, S.T. Manson, J. Phys. B: At. Mol. Opt. Phys. 32 (1999) L 239.
[13] J.P. Connrade, V.K. Dolmatov, S.T. Manson, J. Phys. B: At. Mol. Opt. Phys. 32 (1999) L 395.
[14] C. Reichhard, Solvents and Solvent Effects in Organic Chemistry, V. C. H., Germany, Weinheim, 1988.
[15] B. Mennucci, R. Cammi (Eds.), Continuum Solvation Models in Chemical Physics, Wiley, 2007.
[16] K. Coutinho, S. Canuto, J. Chem. Phys. 113 (2000) 9132.
[17] S. Canuto (Ed.), Solvation Effects on Molecules and Biomolecules: Computational Methods and Applications, Springer, 2008.
[18] J.P. Connerade, J. Alloys. Relat. Compounds 255 (1997) 79.
[19] W. Jaskolski, Phys. Rep. 271 (1996) 1.
[20] A. Michels, J. de Boer, A. Bijl, Physica 4 (1937) 981.
[21] A. Sommerfeld, H. Welker, Ann. Phys. 32 (1938) 56.
[22] J.C.A. Boeyens, J. Chem. Soc. Faraday Trans. 90 (1994) 3377.

[23] S.R. de Groot, C.A. Ten Seldam, Physica 12 (1946) 669.
[24] R.B. Dingle, Proc. Camb. Phil. Soc. 49 (1953) 103.
[25] A.D. Buckingham, K.P. Lawley, Mol. Phys. 3 (1960) 219.
[26] B.M. Gimarc, J. Chem. Phys. 44 (1966) 373.
[27] H.C. Graboske Jr., D.J. Harwood, F.J. Rojers, Phys. Rev. 186 (1969) 210.
[28] D. Suriyanarayana, J.A. Weil, J. Chem. Phys. 64 (1976) 510.
[29] E.V. Ludena, J. Chem. Phys. 66 (1977) 468;
E.V. Ludena, J. Chem. Phys. 69 (1978) 1770.
[30] E. Lee-Koo, S. Rubinstein, J. Chem. Phys. 71 (1979) 351.
[31] F.M. Fernandez, E.A. Castro, Int. J. Quantum. Chem. 21 (1982) 741.
[32] G.A. Arteca, F.M. Fernandez, E.A. Castro, J. Chem. Phys. 80 (1984) 1569.
[33] J. Gorecki, W. Bayers Brown, J. Phys. B: At. Mol. Phys. 20 (1987) 5953.
[34] J. Gorecki, W. Bayers Brown, J. Phys. B: At. Mol. Phys. 22 (1989) 2659.
[35] P.L. Goodfriend, J. Phys. B: At. Mol. Opt. Phys. 23 (1990) 1373.
[36] J.L. Marin, S.A. Cruz, J. Phys. B: At. Mol. Opt. Phys. 24 (1991) 2899;
J.L. Marin, S.A. Cruz, J. Phys. B: At. Mol. Opt. Phys. 25 (1992) 4365.
[37] J.L. Marin, S.A. Cruz, Am. J. Phys. 59 (1991) 931.
[38] S. Goldman, C. Joslin, J. Phys. Chem. 96 (1992) 6021.
[39] K.R. Brownstein, Phys. Rev. Lett. 71 (1993) 1427.
[40] R. Dutt, A. Mukherjee, Y.P. Varshni, Phys. Rev. A 52 (1995) 1750.
[41] Y.P. Varshni, J. Phys. B: At. Mol. Opt. Phys. 30 (1997) L589.
[42] Y.P. Varshni, J. Phys. B: At. Mol. Opt. Phys. 31 (1998) 2849.
[43] Y.S. Huang, V.C. Yang, S.S. Liaw, Phys. Rev. A 60 (1999) 85.
[44] B. Hu, B. Li, J. Liu, Y. Gu, Phys. Rev. Lett. 82 (1999) 4224.
[45] J.P. Connerade, Contemp. Phys. 19 (1978) 415.
[46] J.P. Connerade, V.K. Dolmatov, J. Phys. B: At. Mol. Opt. Phys. 31 (1998) 3557.
[47] J.P. Connerade, V.K. Dolmatov, P.A. Lakshmi, J. Phys. B: At. Mol. Opt. Phys. 33 (2000) 251.
[48] G. Bastard, Wave Mechanics Applied to Semiconductor Heterostructure, Les Editions de Physique, Paris, 1990.
[49] P. Debye, E. Hückel, Z. fur Physik. 24 (1923) 185.
[50] H. Greim, Plasma Spectroscopy, Mc Graw Hill, N.Y., 1964.
[51] R.P. Feynman, N. Metropolis, E. Teller, Phys. Rev. 75 (1949) 1561.
[52] R.D. Cowan, J. Ashkin, Phys. Rev. 105 (1957) 144.
[53] K. Husimi, Proc. Phys. Math. Soc. Japan 22 (1940) 264.
[54] M.W.C. Dharma-Wardhana, F. Grimaldi, A. Licowit, J.L. Pellisier, Phys. Rev. A 21 (1980) 2064.
[55] P. Hohenberg, W. Kohn, Phys. Rev. 136 (1964) B864.
[56] W. Kohn, L.J. Sham, Phys. Rev. A 140 (1965) 1133.
[57] U. Gupta, A.K. Rajagopal, Phys. Rep. 87 (1982) 259.
[58] J.C. Stewart, K.D. Pyatt Jr., Ap. J. 144 (1966) 1203.
[59] R.E. Marshak, H.A. Bethe, Ap. J. 91 (1940) 239.
[60] R. Latter, Phys. Rev. 99 (1955) 239.
[61] T.C. Killan, T. Pattard, T. Pohl, J.M. Rost, Phys. Rep. 449 (2007) 77.
[62] H.M. Van Horn, Science 252 (1991) 384.
[63] E. Springate, N. Hay, J.W.G. Tisch, M.B. Mason, T. Ditmire, M.H.R. Hutchinson, J.P. Marangos, Phys. Rev. A 61 (2000) 063201.
[64] C. Hollenstein, Plasma Physics, Control Fusion 42 (2000) 93.
[65] T.C. Killan, S. Kulin, S.D. Bergeson, L.A. Orozco, C. Orzel, S.L. Rolston, Phys. Rev. Lett. 83 (1999) 4776.
[66] S. Ichimaru, Rev. Mod. Phys. 54 (1982) 1017.
[67] C.M. Lee, A. Hauer, Appl. Phys. Lett. 33 (1978) 692.
[68] B.A. Hammel, et al., Phys. Rev. Lett. 70 (1993) 1263.
[69] J. Lindl, Phys. Plasmas 2 (1995) 3933.
[70] K. Nazir, S.R. Rose, A. Djaoui, G.J. Tallents, M.G. Holden, P.A. Norreys, P. Fews, J. Zhang, F. Failles, Appl. Phys. Lett. 69 (1996) 3686.

[71] A. Saemann, K. Eidmann, I.E. Golovkin, R.C. Mancini, E. Andersson, E. Forster, K. Witte, Phys. Rev. Lett. 82 (1999) 4843.

[72] P. Bucksbaum, N. Ceglio (Eds.), OSA Proceedings on Short Wavelength Coherent Radiation: Generation and Applications, Optical Society of America, Washington D.C., 1991.

[73] L. DaSilva, A. Ng, B.K. Godwal, G. Chiu, F. Cottet, M.C. Richardson, P.A. Jaanimagi, Phys. Rev. Lett. 62 (1989) 1623.

[74] A. Djaoui, B. Shiwai, T.A. Hall, R.W. Eason, C. Jackson, Plasma Phys. Controlled Fusion 31 (1989) 111.

[75] R.A. Lee, P.H. Citrin, P. Eisenberger, B.M. Kincaid, Rev. Mod. Phys. 53 (1981) 769.

[76] T.A. Hall, A. Djaoui, R.W. Eason, C.L. Jackson, B. Shiwai, S.L. Rose, A. Cole, P. Apte, Phys. Rev. Lett. 60 (1988) 2034.

[77] F. Cottet, J.P. Romain, R. Fabbro, B. Farral, Phys. Rev. Lett. 52 (1984) 1884.

[78] W.J. Nellis, J.A. Moriarty, A.C. Mitchell, M. Ross, R.G. Dandrea, N.W. Ashcroft, N.C. Holmes, G.R. Gathers, Phys. Rev. Lett. 60 (1988) 1414.

[79] A. Ng, D. Parfeniuk, L. DaSilva, Phys. Rev. Lett. 54 (1985) 2604.

[80] D.K. Bradley, J. Kilkenny, S.J. Rose, J.D. Hares, Phys. Rev. Lett. 59 (1987) 2995.

[81] E. Leboucher-Dalimier, A. Poquérusse, P. Angelo, I. Gharbi, H. Derfoul, J. Quant Spectrosc. Radiat. Transfer 51 (1994) 187.

[82] R. Stamm (Ed.), J. Kielkopf Spectral Line shapes, vol. 7, Nova Science, New York, 1993.

[83] D. Koester, N. Allard, in: R. Stamm (Ed.), Spectral Line Shapes, vol. 7, Nova Science, New York, 1993.

[84] J.M. Foster, D.J. Hoarty, C.C. Smith, P.A. Rosen, S.J. Davidson, S.J. Rose, T.S. Perry, F.J. Serduke, Phys. Rev. Lett. 67 (1991) 3255.

[85] L.B. DaSilva, B.J. MacGowan, D.R. Kania, B.A. Hammel, C.A. Back, E. Hsieh, R. Doyas, C.A. Iglesias, F.J. Rogers, R.W. Lee, Phys. Rev. Lett. 69 (1992) 438.

[86] G. Mourou, D. Umstadter, Phys. Fluids B4 (1992) 2315.

[87] J.C. Kieffer, M. Chaker, J.P. Matte, H. Pepin, C.Y. Cote, Y. Beaudoin, T.W. Jahnson, C.Y. Chien, S. Coe, G. Mourou, O. Peyrusse, Phys. Fluids B5 (1993) 2676.

[88] M.M. Murnane, H.C. Kapteyn, M.D. Rosen, R.W. Falcone, Science 251 (1991) 531.

[89] P. Audebert, J.P. Geindre, A. Rouse, F. Fallies, J.C. Gauthier, A. Mysyrowicz, G. Grillon, A. Antonetti, J. Phys. B 27 (1994) 3303.

[90] J. Workman, A. Maksimchuck, X. Lu, U. Ellenberger, J.C. Coe, C.Y. Chien, D. Umstadter, Phys. Rev. Lett. 75 (1995) 2324.

[91] J. Workman, M. Nantel, A. Maksimchuk, D. Umstadter, Appl. Phys. Lett. 70 (1997) 312.

[92] D. Riley, L.A. Gizzi, F.Y. Khattak, A.J. Mackinnon, S.M. Viana, O. Willi, Phys. Rev. Lett. 69 (1992) 3739.

[93] P.G. Burkhalter, G. Mehlman, D.A. Newman, M. Krishnan, R.R. Prasad, Rev. Sci. Instrum. 63 (1992) 5052.

[94] A. Maksimchuk, M. Kim, J. Workman, G. Korn, J. Squire, D. Du, D. Umstadter, G. Mourou, M. Bouvier, Rev. Sci. Instrum. 67 (1996) 697.

[95] P. Audebert, J.P. Geindre, J.C. Gauthier, A. Mysyrowicz, J.P. Chambaret, A. Antonetti, Europhys. Lett. 19 (1992) 189.

[96] Z. Jiang, J.C. Kieffer, J.P. Matte, M. Chaker, O. Peyrusse, D. Gilles, G. Korn, A. Maksimchuk, S. Coe, G. Mourou, Phys. Plasmas 2 (1995) 1702.

[97] U. Teubner, T. Missalla, I. Uschmann, E. Foerster, W. Theobald, C. Wuelker, Appl. Phys. B62 (1996) 213.

[98] J.C. Gauthier, J.P. Geindre, P. Audebert, S. Bastiani, C. Quoix, G. Grillon, A. Mysyrowich, A. Antonetti, R.C. Mancini, Phys. Plasmas 4 (1997) 1811.

[99] M. Nantel, G. Ma, S. Gu, C.Y. Cote, J. Itatani, D. Umstadter, Phys. Rev. Lett. 80 (1998) 4442.

[100] N.C. Woolsey, A. Asfaw, B. Hammel, C. Keane, C.A. Back, A. Calisti, C. Mosse, R. Stamm, B. Talin, J.S. Wark, R.W. Lee, L. Klein, Phys. Rev. E 53 (1996) 6396.

[101] N.C. Woolsey, B.A. Hammel, C.J. Keane, A. Asfaw, C.A. Back, J.C. Moreno, J.K. Nash, A. Calisti, C. Mosse, R. Stamm, B. Talin, L. Klein, R.W. Lee, Phys. Rev. E 56 (1997) 2314.

[102] N.C. Woolsey, B.A. Hammel, C.J. Keane, A. Asfaw, C.A. Back, J.C. Moreno, J.K. Nash, A. Calisti, C. Mosse, R. Stamm, B. Talin, C. Hooper, L. Klein, R.W. Lee, J. Quant. Spectros. Radiat. Transfer. 58 (1998) 975.

[103] B.A. Hammel, C.J. Keane, M.D. Cable, D.R. Kania, J.D. Kilkenny, R.W. Lee, R. Pasha, Phys. Rev. Lett. 70 (1993) 1263.

[104] N.C. Woolsey, B.A. Hammel, C.J. Keane, C.A. Back, J.C. Moreno, J.K. Nash, A. Calisti, C. Mosse, R. Stamm, B. Talin, A. Asfaw, L.S. Klein, R.W. Lee, Phys. Rev. E 57 (1998) 4650.

[105] H.J. Metcalf, P. van der Stratten, Laser Cooling and Trapping, Springer, New York, 1999.

[106] D. Ciampini, M. Anderlini, J.H. Muller, F. Fuso, O. Morsch, J.W. Thompson, E. Aroimondo, Photoionisation of ultracold and Bose–Einstein condensed Rb atoms, Phys. Rev. A 66 (2002) 043409.

[107] S.L. Rolston, S.D. Bergeson, S. Killin, C. Orzel, Bull. Am. Phys. Soc. 43 (1984) 1324.

[108] G. Vitrant, J.M. Raimond, M. Gross, S. Haroche, J. Phys. B. 15 (1982) 49.

[109] B. Tabbert, H. Gunther, G.zu. Putlitz, J. Low. Temp. Phys. 109 (1997) 653.

[110] Y. Takahashi, K. Sano, T. Kinoshita, T. Yabuzaki, Phys. Rev. Lett. 71 (1993) 1035.

[111] B. Tabbert, M. Beau, H. Guenther, W. Haussler, C. Honninger, H. Hust, K. Mayer, B. Plagemann, G. zu Putlitz, Z. Phys. B 97 (1995) 425.

[112] B. Tabbert, M. Beau, M. Foereste, H. Guenther, C. Honninger, H. Hust, K. Mayer, G. zu Putlitz, T. Schumacher, Z. Phys. B 98 (1995) 399.

[113] T. Yabuzaki, T. Kinoshita, K. Fukuda, Y. Takahashi, Z. Phys. B 98 (1995) 367.

[114] Q. Hui, J.L. Persson, J.H.M. Beijersbergen, M. Takami, Z. Phys. B 98 (1995) 353.

[115] B. Tabbert, M. Beau, H. Guenther, C. Honninger, K. Meyer, G. zu Putlitz, B. Plagemann, W. Haeussler, Z. Phys. B 97 (1995) 425.

[116] W. Wackerle, R. Stump, Phys. Rev. 106 (1957) 18.

[117] C.V. Briscoe, S.I. Choi, A.T. Stewart, Phys. Rev. Lett. 20 (1968) 493.

[118] R.A. Ferrel, Rev. Mod. Phys. 28 (1956) 308.

[119] P. Debye, E. Hückel, Z. Phys. 24 (1923) 185.

[120] A.I. Akhiezer, I.A. Akhiezer, R.A. Polovin, A.G. Sitenko, K.N. Stepanov, Plasma Electrodynamics, Linear Response Theory, vol. 1, Pergamon, Oxford, 1975.

[121] B.F. Rozsnai, Phys. Rev. A 5 (1972) 1137.

[122] B.F. Rozsnai, J. Quant. Spectros. Radiat. Transfer 13 (1973) 1285.

[123] B.F. Rozsnai, J. Quant. Spectros. Radiat. Transfer 15 (1975) 695.

[124] B.F. Rozsnai, J. Quant. Spectros. Radiat. Transfer 27 (1982) 211.

[125] B.F. Rozsnai, Phys. Rev. A 43 (1991) 3035.

[126] M.W.C. Dharma-Wardana, F. Perrot, Phys. Rev. A 26 (1982) 2096.

[127] F. Perrot, Phys. Rev. A 26 (1982) 1035.

[128] D.A. Liberman, Phys. Rev. B 20 (1979) 4981.

[129] A. Bar-Shalom, J. Oreg, W.H. Goldstein, D. Shvarts, A. Zigler, Phys. Rev. A 40 (1989) 3183.

[130] A. Bar-Shalom, J. Oreg, M. Klapisch, J. Quant. Spectros. Radiat. Transfer 99 (2006) 35.

[131] C. Blancard, F. Faussurier, Phys. Rev. E 69 (2004) 016409.

[132] J.C. Pain, G. Dejonghe, T. Blenski, J. Quant. Spectros. Radiat. Transfer 99 (2006) 451.

[133] J.C. Pain, T. Blenski, J. Quant. Spectros. Radiat. Transfer 81 (2003) 355.

[134] A. Bar-Shalom, J. Oreg, High Energy Density Phys. 3 (2007) 12.

[135] B. Wilson, V. Sonnad, P. Sterne, W. Isaacs, J. Quant. Spectros. Radiat. Transfer 99 (2006) 658.

[136] P.A. Sterne, S.B. Hansen, B.G. Wilson, W.A. Isaacs, High Energy Density Phys. 3 (2007) 278.

[137] L. Hedin, B.I. Lundqvist, J. Phys. C 4 (1971) 2064.

[138] R.M. More, K.H. Warren, D.A. Young, G.B. Zimmerman, Phys. Fluids 31 (1988) 3059.

[139] A. Djaoui, S.J. Rose, J. Phys. B 25 (1992) 2745.

[140] R.J. Town, A.R. Bell, S.J. Rose, Phys. Rev. E 50 (1994) 1413.

[141] J. Quant. Spectros. Radiat. Transfer 99 (2006) III–VII. (special issue).

[142] T. Blenski, B. Chichocki, J. Quant. Spectros. Radiat. Transfer 51 (1994) 49.

[143] F. Grimaldi, A. Grimaldi-Lecourtand, M.W.C. Dharma-Wardhana, Phys. Rev. A 32 (1985) 1063.

[144] A. Zangwill, P. Soven, Phys. Rev. A 21 (1980) 1561.
[145] M.J. Stott, E. Zaremba, Phys. Rev. A 21 (1980) 12.
[146] G.D. Mahan, K.R. Subbhaaswamy, Local Density Theory of Polarizability, Plenum Press, New York, 1990.
[147] N.D. Mermin, Ann. Phys. 21 (1963) 99.
[148] D. Vautherin, N. Vin Mau, Phys. Lett. B 120 (1983) 261.
[149] J. des Cloizeaux, in: C. de Witt, R. Balian (Eds.), Many Body Physics, Gordon and Breach, New York, 1968.
[150] J. Colgan, C.J. Fontes, G. Csanak, L.A. Collins, High Energy Density Phys. 3 (2007) 65.
[151] B. Kundu, D. Ray, P.K. Mukherjee, Phys. Rev. A 34 (1986) 62.
[152] T.C. Caves, M. Karplus, J. Chem. Phys. 50 (1969) 3649.
[153] C.W. McCurdy, T. Rescigno, D.L. Yeager, V. Mc Koy, in: H.F. Schaefer III (Ed.), Methods of Electronic Structure Theory, Plenum, New York, 1977, p. 339.
[154] H. Nguyen, M. Koenig, D. Benredjem, M. Caby, G. Couloud, Phys. Rev. A 33 (1986) 1279.
[155] P.O. Lowdin, P.K. Mukherjee, Chem. Phys. Lett. 14 (1972) 1.
[156] H.A. Bethe, E.E. Salpeter, Quantum Mechanics of One and Two Electron Atoms, Academic Press, New York, 1957.
[157] J.O. Hirschfelder, C.F. Curtis, R.B. Bird, Molecular Theory of Gases and Liquids, John Wiley, New York, 1954, p. 264.
[158] B.J.B. Crowley, Phys. Rev. A 41 (1990) 2179.
[159] J. Stein, D. Salzmann, Phys. Rev. A 45 (1992) 3943.
[160] R.W. Lee, J.T. Larsen, J. Quant. Spectros. Radiat. Transfer 56 (1996) 535.
[161] F.J. Rogers, H.C. Grabroske Jr., D.J. Harwood, Phys. Rev. A 1 (1970) 1577.
[162] S. Skupski, Phys. Rev. A 21 (1980) 1316.
[163] H.R. Griem, Spectral Line Broadening by Plasmas, Academic Press, New York, 1974.
[164] H.R. Griem, Phys. Rev. A 38 (1988) 2943.
[165] P.W. Fowler, Mol. Phy. 53 (1984) 865.
[166] D. Singh, Y.P. Varshni, Phys. Rev. A 29 (1984) 2895.
[167] C. Zicovich-Wilson, J.H. Plenelles, W. Jaskolski, Int. J. Quantum. Chem. 50 (1994) 429.
[168] M. Dineykhan, R.G. Nazmitdinov, Phys. Atomic Nuclei 62 (1999) 138.
[169] C. Laughlin, B.L. Burrows, M. Cohen, J. Phys. B, At. Mol. Opt. Phys. 35 (2002) 701.
[170] H.E. Montgomery, Chem. Phys. Lett. 352 (2002) 529.
[171] N.A. Aquino, Int. J. Quantum. Chem. 54 (1995) 107.
[172] B. Saha, P.K. Mukherjee, G.H.F. Diercksen, A& A 396 (2002) 337.
[173] D. Belinska-Waz, J. Karwowski, B. Saha, P.K. Mukherjee, Phys. Rev. E 69 (2004) 016404.
[174] A.N. Sil, B. Saha, P.K. Mukherjee, Int. J. Quantum. Chem. 104 (2005) 903.
[175] J. Siedel, S. Arndt, W.D. Kraeft, Phys. Rev. E 52 (1995) 5387.
[176] S. Bhattacharyya, A.N. Sil, S. Fritzsche, P.K. Mukherjee, Eur. Phys. J. D 46 (2008) 1.
[177] B. Saha, P.K. Mukherjee, Phys. Lett. A 302 (2002) 105.
[178] A.C.H. Yu, Y.K. Ho, Phys. of Plasmas 12 (2005) 043302.
[179] W.P. Reinhardt, Int. J. Quantum. Chem. 21 (1982) 133.
[180] Debasis Ray, Phys. Rev. E 62 (2000) 4126.
[181] K. Scheibner, J.C. Weisheit, N.F. Lane, Phys. Rev. A 35 (1987) 1252.
[182] B. Zeigelman, A. Dalgarno, Phys. Rev. A 35 (1987) 4085;
B. Zeigelman, A. Dalgarno, Phys. Rev. A 37 (1988) 2693.
[183] F.J. Rogers, Phys. Rev. A 10 (1974) 2441.
[184] C.S. Lam, Y.P. Varshni, Phys. Rev. A 27 (1983) 418.
[185] Z. Wang, P. Winkler, Phys. Rev. A 52 (1995) 216.
[186] P. Winkler, Phys. Rev. E 53 (1996) 5517.
[187] D. Ray, P.K. Mukherjee, Eur. Phys. J. D 2 (1998) 89.
[188] D. Ray, P.K. Mukherjee, J. Phys. B 31 (1998) 3479.
[189] S. Kar, Y.K. Ho, Int. J. Quantum. Chem. 106 (2006) 814.
[190] S. Kar, Y.K. Ho, Chem. Phys. Lett. 402 (2005) 544.
[191] S. Kar, Y.K. Ho, New J. Phys. 7 (2005) 141.

[192] B. Saha, T.K. Mukherjee, P.K. Mukherjee, G.H.F. Diercksen, Theor. Chem. Acc. 108 (2002) 305.

[193] P.K. Mukherjee, J. Karwowski, G.H.F. Diercksen, Chem. Phys. Lett. 363 (2002) 323.

[194] B. Saha, P.K. Mukherjee, D. Belinska-Waz, J. Karwowski, J. Quant. Spectros. Radiat. Transfer 78 (2003) 131.

[195] B. Saha, P.K. Mukherjee, D. Belinska-Waz, J. Karwowski, J. Quant. Spectros. Radiat. Transfer 92 (2005) 1.

[196] S. Kar, Y.K. Ho, J. Quant. Spectros. Radiat. Transfer 109 (2008) 445.

[197] S. Kar, Y.K. Ho, J. Quant. Spectros. Radiat. Transfer 107 (2007) 315.

[198] S. Kar, Y.K. Ho, Chem. Phys. Lett. 449 (2007) 246.

[199] D. Ray, J. Phys. B. At. Mol. Opt. Phys. 33 (2000) L21.

[200] S. Kar, Y.K. Ho, Phys. Rev. A 77 (2008) 022713.

[201] S. Kar, Y.K. Ho, Phys. of Plasmas 15 (2008) 013301.

[202] D. Ray, Phys. Rev. E 63 (2001) 027401.

[203] A.N. Sil, P.K. Mukherjee, Int. J. Quantum. Chem. 106 (2006) 465.

[204] A.N. Sil, S. Bhattacharyya, P.K. Mukherjee, Int. J. Quantum. Chem. 107 (2007) 2708.

[205] A.N. Sil, J. Anton, S. Fritzsche, P.K. Mukherjee, B. Fricke, Private Communication.

[206] A.P. Mills Jr., Phys. Rev. Lett. 46 (1981) 717;
A.P. Mills Jr., Phys. Rev. Lett. 50 (1983) 671.

[207] B. Saha, T.K. Mukherjee, P.K. Mukherjee, Chem. Phys. Lett. 373 (2003) 218.

[208] S. Kar, Y.K. Ho, Phys. Rev. A 71 (2005) 052503;
S. Kar, Y.K. Ho, Phys. Rev. A 73 (2006) 032502.

[209] S. Kar, Y.K. Ho, Chem. Phys. Lett. 424 (2006) 403.

[210] S. Kar, Y.K. Ho, Phys. Lett. A 372 (2008) 4253.

[211] S. Kar, Y.K. Ho, Few Body Systems 42 (2008) 73.

[212] S. Kar, Y.K. Ho, Nucl. Instrum. Methods B 266 (2008) 526.

[213] S. Kar, Y.K. Ho, Phys. Rev. E 70 (2004) 066411.

[214] S. Kar, Y.K. Ho, Few Body Systems 40 (2006) 13.

[215] P.K. Mukherjee, S. Fritzsche, B. Fricke, Phys. Lett. A 360 (2006) 287.

[216] S. Kar, Y.K. Ho, Phys. Lett. A 368 (2007) 476.

[217] A.N. Sil, B. Saha, P.K. Mukherjee, Phys. Lett. A 324 (2004) 308.

[218] S. Bhattacharyya, A.N. Sil, T.K. Mukherjee, P.K. Mukherjee, P. Vasu, Int. J. Quantum. Chem. 107 (2007) 946.

[219] A.N. Sil, M. Pawlak, P.K. Mukherjee, M. Bylicki, J. Quant. Spectros. Radiat. Transfer 109 (2008) 873.

[220] O.A. Gomez, H. Chacham, J. Mohallem, Phys. Rev. A 50 (1994) 228.

[221] J. Goy, J.M. Richard, S. Fleck, Phys. Rev. A 52 (1995) 3511.

[222] L.H. Thomas, Phys. Rev. 47 (1935) 903.

[223] V. Effimov, Phys. Lett. B 33 (1970) 563.

[224] S. Kar, Y.K. Ho, Eur. Phys. J. D 48 (2008) 157.

[225] A. Temkin (Ed.), Autoionisation: Recent Developments and Applications, Plenum, New York, 1985.

[226] A.B.C. Walker Jr., H.R. Rugge, Ap. J. 164 (1971) 181.

[227] G.A. Doschek, P. Meekins, R.W. Kerplin, T.A. Chubb, H. Friedman, Ap. J. 164 (1971) 165.

[228] R.D. Cowan, Theory of Atomic Structure and Spectra, University of California Press, Berkley, 1981.

[229] S. Mannervik, Phys. Scr. 40 (1989) 28.

[230] K. Swada, T. Fujimoto, Phys. Rev. E 49 (1994) 5565.

[231] T. Kawachi, T. Fujimoto, Phys. Rev. E 51 (1995) 1440.

[232] A.N. Sil, P.K. Mukherjee, Int. J. Quantum. Chem. 102 (2005) 1061.

[233] S. Kar, Y.K. Ho, J. Phys. B, At. Mol. Opt. Phys. 38 (2005) 3299.

[234] V.A. Mandelshtam, T.R. Ravuri, H.S. Taylor, Phys. Rev. Lett. 70 (1993) 1932.

[235] S. Kar, Y.K. Ho, Phys. Rev. A 71 (2005) 052503.

[236] S. Kar, Y.K. Ho, Phys. Rev. A 72 (2005) 010703;
S. Kar, Y.K. Ho, Phys. Rev. A 73 (2006) 032502.

[237] S. Chakraborty, Y.K. Ho, Chem. Phys. Lett. 438 (2007) 99; Phys. Rev. A 77 (2008) 014502.
[238] Y.K. Ho, Nucl. Instrum. Methods B 266 (2008) 516.
[239] I. Silanes, J.M. Mercero, J.M. Ugalde, Phys. Rev. E 66 (2002) 026408.
[240] J.M. Gill, P. Martel, E. Mnguez, J.G. Rubiano, R. Rodrguez, F.H. Ruano, J. Quant. Spectros. Radiat. Transfer 75 (2002) 539.
[241] B. Saha, S. Fritzsche, Phys. Rev. E 73 (2006) 036405.
[242] D. Porquet, J. Dubau, A & A, Suppl. 143 (2000) 495.
[243] F.P. Keenan, Space Sc. Rev. 75 (1996) 537.
[244] T. Brage, P.G. Judge, C.R. Proffit, Phys. Rev. Lett. 89 (2002) 281101.
[245] D.G. Ellis, I. Martinson, E. Trabbert, Comments At. Mol. Phys. 22 (1990) 241.
[246] D.L. Mc Kenzie, P.B. Landecker, U. Feldman, G.A. Doschek, Ap. J. 289 (1985) 849.
[247] B. Denne, G. Magyar, J. Jacquinot, Phys. Rev. A 40 (1989) 3702.
[248] B. Saha, S. Fritzsche, J. Phys. B, At. Mol. Opt. Phys. 40 (2007) 259.
[249] M.S. Murrilo, J.C. Weisheit, Strongly Coupled Plasma Physics, University of Rochester Press, Rochester, N. Y., 1993, p. 233.
[250] M.S. Murrilo, J.C. Weisheit, Phys. Rep. 302 (1998) 1.
[251] C.G. Kim, Y.D. Jung, Plasma Phys. Controlled Fusion 46 (2004) 1493.
[252] S. Sahoo, Y.K. Ho, Phys. of Plasmas 13 (2006) 063301.
[253] R. Rodriguez, J.M. Gill, R. Florido, Phys. Scr. 76 (2007) 418.
[254] K. Hiroike, N.R. Kestner, S.A. Rice, J. Jortner, J. Chem. Phys. 43 (1965) 2625.
[255] W.T. Sommer, Phys. Rev. Lett. 12 (1964) 271.
[256] A.L. Fetter, Physics of Liquid and Solid Helium I, Wiley, New York, 1976.
[257] H. Bauer, M. Beau, B. Friedl, C. Marchand, K. Miltner, H.J. Reyher, Phys. Lett. A 146 (1990) 134.
[258] M. Beau, H. Guenther, G. zu Putlitz, B. Tabbert, Z. Phys. B, Condens. Matter. 101 (1996) 253.
[259] A.P. Hickman, W. Steets, N.F. Lane, Phys. Rev. B 12 (1975) 3705.
[260] J. Dupont-Roc, M. Himbert, N. Pavlov, J. Treiner, J. Low. Temp. Phys. 81 (1990) 31.
[261] J. Dupont-Roc, Z. Phys. B, Condens. Matter 98 (1995) 383.
[262] G. De Toffol, F. Ancilotto, F. Toigo, J. Low. Temp. Phys. 102 (1996) 381.
[263] Ions and atoms in superfluid helium, Z. Phys. B, Condens. Matter 98 (1995) No. 3.
[264] V. Ludwig, P.K. Mukherjee, K. Coutinho, S. Canuto, Phys. Rev. A 72 (2005) 062714.
[265] B. Saha, R. Fukuda, H. Nakatsuji, P.K. Mukherjee, Theor. Chem. Acc. 118 (2007) 437.
[266] J. Anton, P.K. Mukherjee, B. Fricke, S. Fritzsche, J. Phys. B., At. Mol. Opt. Phys. 40 (2007) 2453.
[267] J. Anton, B. Fricke, P.K. Mukherjee, S. Fritzsche, Phys. Lett. A 372 (2008) 4462.

CHAPTER 5

The Energy Level Structure of Low-dimensional Multi-electron Quantum Dots

Tokuei Sako[a], **Josef Paldus**[b] and **Geerd H.F. Diercksen**[c]

Contents

1. INTRODUCTION

Confined quantum systems of a finite number of electrons bound in a fabricated nano-scale potential, typically of the order of 1 $\sim$ 100 nm, are

[a] Laboratory of Physics, College of Science and Technology, Nihon University, 7-24-1 Narashinodai, Funabashi, 274-8501 Chiba, Japan

[b] Department of Applied Mathematics, University of Waterloo, Waterloo, Ontario N2L 3G1, Canada

[c] Max-Planck-Institut für Astrophysik, Karl-Schwarzschild-Strasse 1, D-85741 Garching, Germany

E-mail addresses: sako@phys.ge.cst.nihon-u.ac.jp (T. Sako), paldus@scienide2.uwaterloo.ca (J. Paldus), ghd@mpa-garching.mpg.de (G.H.F. Diercksen).

URLs: http://www.phys.ge.cst.nihon-u.ac.jp/~sako/ (T. Sako), http://www.mpa-garching.mpg.de/mol_physics/index.shtml (G.H.F. Diercksen).

Advances in Quantum Chemistry, Vol. 58
ISSN: 0065-3276, DOI: 10.1016/S0065-3276(09)00709-6

referred to as quantum dots or artificial atoms [1–4] since they have a discrete energy-level structure following Hund's rules [5,6]. The properties of quantum dots can be controlled by changing the size and/or the shape of the fabricated potential [7–9]. Quantum dots are known to show features in their energy-level structure and their optical properties that are qualitatively different from atoms [10,11]. The differences between quantum dots and atoms are due to the harmonic nature of the confining potential of quantum dots as compared to the Coulomb potential of atoms [4,12,13] as well as to the larger size and the lower dimensionality of quantum dots [14,15].

Computational techniques based on the quantum chemical molecular orbital theory make it possible to calculate the properties of, not only the ground state, but also the low-lying excited states of multi-electron quantum dots for a specific value of the strength of confinement. As the calculated results vary strongly for different strengths of confinement, due to a strong variation of the relative importance of the electron–electron interaction with respect to the change of the strength of confinement [4,12,16–18], it is necessary to develop a unified method for interpreting the complicated energy-level structure of quantum dots for the whole range of the strength of confinement.

In previous studies of this series it was found that the *polyad quantum number* [19], defined by the total number of nodes in the leading configuration of the configuration interaction (CI) wave function, is approximately conserved for harmonic-oscillator quantum dots. The polyad quantum number and its extension can be used to characterize the energy spectra of quasi-one-dimensional quantum dots of two and three electrons for the whole range of the strength of confinement [20,21]. Energy levels belonging to different polyad quantum numbers and having different spin multiplicities converge to nearly degenerate levels as the strength of confinement becomes smaller. This convergence is caused by the increasingly stronger potential walls of the electron–electron interaction potentials that significantly modify the nodal pattern of the wave function of lower spin states while hardly affecting the wave function of the highest spin states [20,21].

In the present contribution the interpretation of the energy-level structure of quasi-one-dimensional quantum dots of two and three electrons is reviewed in detail by examining the polyad structure of the energy levels and the symmetry of the spatial part of the CI wave functions due to the Pauli principle. The interpretation based on the polyad quantum number is applied to the four electron case and is shown to be applicable to general multi-electron cases. The qualitative differences in the energy-level structure between quasi-one-dimensional and quasi-*two*-dimensional quantum dots are briefly discussed by referring to differences in the structure of their *internal space*.

2. COMPUTATIONAL METHODOLOGY

2.1. Theoretical model

The Hamiltonian operator for a confined quantum system is written in atomic units as

$$\mathcal{H} = \sum_{i=1}^{N} \left[-\frac{1}{2} \nabla_i^2 \right] + \sum_{i=1}^{N} w(\mathbf{r}_i) + \sum_{i>j}^{N} \frac{1}{|\mathbf{r}_i - \mathbf{r}_j|}, \tag{1}$$

where N denotes the number of electrons and w denotes the one-electron confining potential [16,22]. In the present study the one-electron confining potential, w, for the quasi-one-dimensional quantum dots is given by

$$w_{q1D}(\boldsymbol{r}) = \frac{1}{2} \omega_{xy}^2 \left(x^2 + y^2 \right) - D \exp\left[-\frac{\omega_z^2}{2D} z^2 \right], \tag{2}$$

and for the quasi-two-dimensional quantum dots it is given by

$$w_{q2D}(\boldsymbol{r}) = -D \exp\left[-\frac{\omega_{xy}^2}{2D} (x^2 + y^2) \right] + \frac{1}{2} \omega_z^2 z^2. \tag{3}$$

The potentials of Equations (2) and (3) represent the sum of harmonic-oscillator and attractive Gaussian potentials. For a sufficiently large value of ω_{xy} in Equation (2) the electrons bound by this potential are strongly compressed along the x and y directions and have degrees of freedom only along the z direction. Therefore, the one-electron potential w_{q1D} of Equation (2) represents the confining potential of quasi-one-dimensional quantum dots with a shape like a 'pipe'. Similarly, for a sufficiently large value of ω_z in Equation (3), the electrons in this potential are strongly compressed along the z direction and have degrees of freedom only in the xy plane. Therefore, the potential w_{q2D} of Equation (3) represents the confining potential of quasi-two-dimensional quantum dots having a shape like a 'disk'. A Gaussian potential has been chosen as the confining potential, among others, because it is approximated in the low energy region by a harmonic-oscillator potential typically used for modeling semiconductor quantum dots [13,12,4]. The values of the parameters ω_{xy} and ω_z are set to 20 a.u. for all the results presented in this contribution and this is not indicated explicitly hereafter.

The *anharmonicity* of the confining potential can be controlled by changing the 'depth' of the Gaussian potential D with respect to ω_z and ω_{xy}, respectively. The parameters ω_z and ω_{xy} represent the frequency of the harmonic-oscillator potential characterizing the strength of confinement of the Gaussian potential. They are obtained by a quadratic approximation to the Gaussian potential in Equations (2) and (3), respectively. When D is much larger than the harmonic frequency the Gaussian potential closely follows the harmonic-oscillator potential in the low energy region. This indicates that the anharmonicity is small. On the other hand, when D is only slightly larger than the harmonic frequency the Gaussian potential deviates strongly from the harmonic-oscillator potential, even in the low energy region. This indicates that the anharmonicity is large. The extent of the anharmonicity may be specified by the parameter α [20], which is defined for the quasi-one-dimensional quantum dots by

$$\alpha_{q1D} = \omega_z / D, \tag{4}$$

and for the quasi-two-dimensional quantum dots by

$$\alpha_{q2D} = \omega_{xy} / D. \tag{5}$$

Introducing anharmonicity is important for simulating realistic confining potentials [23,24].

The total energies and wavefunctions of the Hamiltonian (1) have been calculated as the eigenvalues and eigenvectors of a CI matrix. Full CI has been used for all calculations of quasi-one-dimensional quantum dots and for quasi-two-dimensional quantum dots with $N = 2$, while multi-reference CI has been used for quasi-two-dimensional quantum dots with $N = 3$ and 4. The results are presented in atomic units. They can be scaled by the effective Bohr radius of 9.79 nm and the effective Hartree energy of 11.9 meV for GaAs semiconductor quantum dots [25,26].

2.2. Basis sets employed

In order to properly describe the wave function of electrons confined in the strongly anisotropic potential given by Equations (2) and (3), a set of properly chosen Cartesian *anisotropic* Gaussian-type orbitals (c-aniGTO) [16, 17,22] have been adopted as the basis set spanning the one-electron orbital space. The general form of an unnormalized c-aniGTO function placed at (b_x, b_y, b_z) is given by

$$\chi_{\mathrm{ani}}^{\vec{a},\vec{\zeta}}(\vec{r}; \vec{b}) = x_{b_x}^{a_x} y_{b_y}^{a_y} z_{b_z}^{a_z} \exp\left(-\zeta_x x_{b_x}^2 - \zeta_y y_{b_y}^2 - \zeta_z z_{b_z}^2\right), \tag{6}$$

where the shorthand notation x_{b_x} is used for $(x - b_x)$, etc. Unlike standard Gaussian-type orbitals the c-aniGTO functions can be easily fitted to properly describe the wavefunction of electrons in an anisotropic confining potential by adjusting the three exponents ζ_x, ζ_y, and ζ_z independently. In principle,

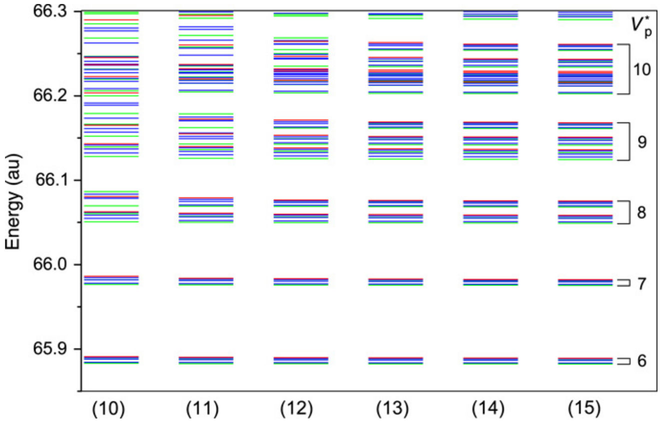

Figure 1 Energy spectrum of the low-lying states of four electrons confined in a quasi-one-dimensional Gaussian potential with $(D, \omega_z, \omega_{xy}) = (4.0, 0.1, 20.0)$ for different-size basis sets. Energy levels of different spin multiplicities are indicated by different colors (See the caption to Figure 2). The number in the round brackets specifies the total number of basis functions and the parameter v_p^* specifies the *extended* polyad quantum number (See the text for details). (For interpretation of the references to color in this figure legend, the reader is referred to the web version of this book.)

a Gaussian basis set of floating standard Gaussian functions could be used for this purpose, but this would require an extremely large number of functions at different points in space in order to properly describe the distribution of the electrons. A c-aniGTO basis set can be transformed into a set of eigenfunctions of the corresponding three-dimensional anisotropic harmonic oscillator [17]. Consequently, such a basis set is also useful in high-accuracy calculations of eigenvalues and eigenfunctions of atoms in strong magnetic fields [27–30] and of semiconductor quantum dots [31,32].

In the present study a c-aniGTO basis set has been placed at the center of the confining potential, i.e. at the origin of the Cartesian coordinate system. The orbital exponents for the harmonic-oscillator potential in the Equations (2) and (3) have been chosen as one half of the strength of the confinement, ω_{xy} and ω_z, respectively, while the exponents for the Gaussian potentials have been determined in the same way as described in a previous study [19]. Since the strength of the confinement for the harmonic-oscillator potential is much larger than that for the Gaussian potential, only functions *without* nodes along the direction of the harmonic-oscillator potential have been selected and used in the basis sets [18–20]. The size of the basis set required for calculating a reliable energy spectrum has been determined by following the convergence of the energies while stepwise increasing its size. The pattern of convergence for the case of four electrons with $(D, \omega_z) = (4.0, 0.1)$ is displayed in Figure 1. The number of basis functions, indicated by the number enclosed in parentheses, was increased stepwise by adding at each step a new function with an additional node. The energy spectrum calculated with 10 basis functions, displayed on the left-hand side of Figure 1, differs for $E \geq 66.1$ significantly from the spectrum calculated by using the next larger basis with 11 functions, indicating the inadequacy of the former basis. It is noted that the basis set with 10 functions already includes a function with the angular momentum quantum number $l = 9$. Thus, a basis set with very high angular momentum functions is clearly required for a reliable description of strongly anisotropic quantum dots. As shown in Figure 1 the energy-level structure becomes stabilized as the number of basis functions increases. The maximum deviation between the energy levels up to the fifth band with $v_p^* = 10$ calculated by using the basis sets with 14 and 15 functions, respectively, is smaller than 5.7×10^{-4}. In the calculations involving four electrons that are presented in this study a basis set consisting of 16 functions has been used. The convergence characteristic has already been given for the case of two electrons in Ref. [20] and for the case of three electrons in Ref. [21].

3. QUASI-ONE-DIMENSIONAL QUANTUM DOTS

3.1. Energy spectrum: General outlook

The confinement strength ω_z of quasi-one-dimensional quantum dots can be classified according to the relative size of the one-electron energy E_1 and the two-electron energy E_2. The one-electron energy of the one-dimensional harmonic oscillator is given by $\omega_z(n + \frac{1}{2})$, with n denoting the harmonic-oscillator quantum number. Thus, it scales linearly with ω_z, i.e., $E_1 \sim \omega_z$. The two-electron energy can be estimated by considering the characteristic length l_z of the system along the z direction [33]. The characteristic length is related to ω_z by $l_z \sim 1/\sqrt{\omega_z}$, since the probability distribution of the one-dimensional harmonic-oscillator ground state with the frequency ω_z is proportional to $\exp\left[-\frac{1}{2}\omega_z z^2\right]$. Thus, the two-electron energy, which is related to l_z by $E_2 \sim 1/l_z$, scales with ω_z as $E_2 \sim \sqrt{\omega_z}$. Consequently, the one-electron energy E_1 dominates the total energy for $w_z \gg 1.0$ (large ω_z). Its contribution to the total energy becomes similar to that of E_2 for $w_z \sim 1.0$ (medium ω_z), while the two-electron energy E_2 dominates the total energy for $w_z \ll 1.0$ (small ω_z) [21].

The energy spectra of N electrons confined by the quasi-one-dimensional Gaussian potentials with $(D, \omega_z) = (200.0, 5.0)$, $(40.0, 1.0)$, and $(4.0, 0.1)$ are displayed in Figures 2(a), (b), and (c) for $N = 2$, 3, and 4, respectively. The ω_z values of 5.0, 1.0, and 0.1, correspond to the three regimes of confinement strength defined above, namely, large, medium, and small. Energy levels with different spin multiplicities are displayed in different colors: for $N = 2$ (Figure 2(a)) the singlets and triplets are displayed in green and red, for $N = 3$ (Figure 2(b)) the doublets and quartets are displayed also in green

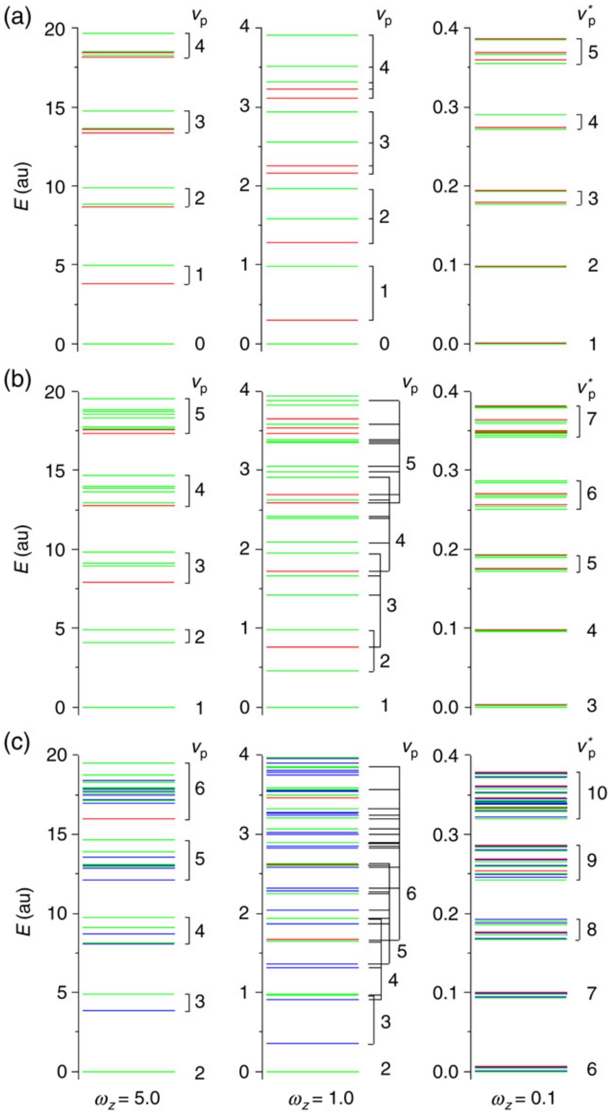

Figure 2 Energy spectrum of N electrons confined by a quasi-one-dimensional Gaussian potential with different strength of confinement ω_z for $N = 2$ (a), 3 (b), and 4 (c), respectively, represented as relative energies from the ground state. The anharmonicity parameter α of the Gaussian potential is 0.025 in all cases. Energy levels for different spin multiplicities are indicated by different colors: in (a), the singlets and triplets are colored by green and red, respectively, in (b), the doublets and quartets by green and red, respectively, and in (c), the singlets, triplets, and quintets by green, blue, and red, respectively. (For interpretation of the references to color in this figure legend, the reader is referred to the web version of this book.)

and red, and for $N = 4$ (Figure 2(c)) the singlets, triplets, and quintets are displayed in green, blue, and red. The anharmonicity parameter α is equal to 0.025 in all cases. This corresponds to an approximately harmonic Gaussian potential. The vertical axis of each of the three energy diagrams for different confinement strengths is scaled by ω_z so that the energy of the ground state and the excitation energy of 4 quanta of ω_z appear on the vertical axis at the same level [20,21]. Therefore in the *absence* of electron–electron interaction all three energy spectra would look identical in this representation.

As shown in Figure 2 the energy level structure changes dramatically for the three regimes of confinement strength ω_z: The energy spectrum for the large confinement regime displayed on the left-hand side of Figure 2 shows a harmonic band structure with a band gap close to ω_z. The energy spectrum for the medium confinement regime displayed in the middle of the figure shows a broader distribution of energy levels. On the other hand, the energy spectrum in the small confinement regime displayed on the right-hand side of the figure again shows a harmonic band structure with a band gap close to ω_z. However, this energy spectrum is characterized by a different number of levels, with different spin multiplicities in each band, as compared to the case of the large confinement regime. These observations apply to all the cases $N = 2$, 3, and 4. In the next section the changes in the energy spectrum due to different confinement strength are interpreted by exploiting the concept of the *polyad quantum number*.

3.2. Polyad structure

The polyad quantum number is defined as the sum of the number of nodes of the one-electron orbitals in the leading configuration of the CI wave function [19]. The name *polyad* originates from molecular vibrational spectroscopy, where such a quantum number is used to characterize a group of vibrational states for which the individual states cannot be assigned by a set of normal-mode quantum numbers due to a mixing of different vibrational modes [19]. In the present case of quasi-one-dimensional quantum dots, the polyad quantum number can be defined as the sum of the one-dimensional harmonic-oscillator quantum numbers for all electrons.

The harmonic-band structure of the energy spectrum of quasi-one-dimensional quantum dots for the large ω_z regime can be understood by exploiting the polyad quantum number. In the large ω_z regime the one-electron energy E_1 dominates the total energy and the electron–electron interaction represents only a small perturbation. Therefore, in a zeroth-order approximation, the Hamiltonian of the system can be written as a sum of N harmonic-oscillator Hamiltonians

$$\mathcal{H}_0 = \sum_{i=1}^{N} \left[-\frac{1}{2} \left(\frac{\partial}{\partial z_i} \right)^2 + \frac{1}{2} \omega_z^2 z_i^2 \right], \tag{7}$$

where the x and y degrees of freedom are ignored and the Gaussian potential along the z direction is approximated by a harmonic oscillator with the frequency ω_z. The energy of the Hamiltonian (7) can then be expressed in terms of the polyad quantum number, denoted hereafter by v_p, as follows

$$E_{\vec{n}} = \omega_z \left[v_p + \frac{N}{2} \right], \tag{8}$$

with

$$v_p = \sum_{i=1}^{N} n_i, \tag{9}$$

where $\vec{n} = (n_1, n_2, \ldots, n_N)$ represents the harmonic-oscillator quantum numbers for the electron $1, 2, \ldots, N$, respectively. Equation (8) shows that energy levels having the same value of v_p are degenerate and that those having different values of v_p are separated by a multiple of ω_z. This explains why the energy-level structure for the large ω_z regime has a harmonic-band structure with a spacing of ω_z, as observed on the left-hand side of Figure 2.

It is noted, however, that not all possible combinations of $(n_1, n_2, \ldots, n_N)$ can be realized as quantum states. Because of the Pauli principle, the total wave function involving both the spatial and spin parts must be antisymmetric with respect to the interchange of any two electron coordinates. In order to construct electronic quantum states for the Hamiltonian (7) satisfying the Pauli principle, it is convenient to impose a restriction on the set $(n_1, n_2, \ldots, n_N)$ by requiring that $n_1 \leq n_2 \leq \cdots \leq n_N$, where the same value of n_i cannot appear more than twice. In order to satisfy the Pauli principle, a chosen $\vec{n}$, representing a spatial orbital configuration, should be coupled with the appropriate spin functions. In the case of two electrons, the configuration (n_a, n_b) $(n_a \neq n_b)$ can be coupled to the singlet and the triplet spin functions. On the other hand, the configuration (n_a, n_a) can be coupled only to the singlet spin function, since the latter configuration is symmetric with respect to the interchange of the electron coordinates 1 and 2, and thus must be coupled with an antisymmetric spin function. For example, in case of the polyad manifold $v_p = 2$ there are two configurations, (0,2) and (1,1). The (0,2) configuration is coupled both to the singlet and triplet spin functions while the (1,1) configuration is coupled only to the singlet spin function, resulting in a total of three electronic states. Similar arguments can be applied to all v_p manifolds, and it can be shown that for the two-electron case the number of levels in each v_p manifold amounts to $(v_p + 1)$, as may be seen in Figure 2(a).

The situation becomes slightly complicated for systems with more than two electrons due to the *spin degeneracy*. In the case of three electrons, for example, one can construct doublet ($S = \frac{1}{2}$) and quartet ($S = \frac{3}{2}$) spin states denoted by $|\frac{1}{2}, M\rangle$ $(M = -\frac{1}{2}, \frac{1}{2})$ and $|\frac{3}{2}, M\rangle$ $(M = -\frac{3}{2}, -\frac{1}{2}, \frac{1}{2}, \frac{3}{2})$, respectively. States with different magnetic quantum numbers M are degenerate in the absence of spin-dependent interactions, such as spin-orbit interaction. It should be noted, however, that for a given $|S, M\rangle$ state there is only one quartet state while there are *two* doublet states. These two doublet spin states are linearly independent and, in general, have different energies. Therefore three spin states will participate in forming the energy-level structure for three electron quantum dots. The three spin functions with the highest M value, namely, $|\frac{3}{2}, \frac{3}{2}\rangle$ and $|\frac{1}{2}, \frac{1}{2}\rangle$ for the quartet and the doublet states, respectively, may be written as $\alpha(1)\alpha(2)\alpha(3)$ for the quartet state, and $\frac{1}{\sqrt{2}}\alpha(1)[\alpha(2)\beta(3) - \beta(2)\alpha(3)]$ and $\frac{1}{\sqrt{6}}[2\beta(1)\alpha(2)\alpha(3) - \alpha(1)\alpha(2)\beta(3) - \alpha(1)\beta(2)\alpha(3)]$ for the two doublet states. In constructing the two doublet spin functions, it has been assumed that the first function $\frac{1}{\sqrt{2}}\alpha(1)[\alpha(2)\beta(3) - \beta(2)\alpha(3)]$ (denoted hereafter by $|\frac{1}{2}, \frac{1}{2}\rangle_a$) forms a *two-electron singlet* for the electron pair 2 and 3. The second doublet spin function $\frac{1}{\sqrt{6}}[2\beta(1)\alpha(2)\alpha(3) - \alpha(1)\alpha(2)\beta(3) - \alpha(1)\beta(2)\alpha(3)]$ (denoted hereafter by $|\frac{1}{2}, \frac{1}{2}\rangle_b$) has been obtained by requiring it be orthogonal to $|\frac{1}{2}, \frac{1}{2}\rangle_a$. The spatial orbital configurations for the three electrons have one of the following forms: (n_a,n_b,n_c), (n_a,n_a,n_b), and (n_a,n_b,n_b) with $n_a \neq n_b \neq n_c$. The latter two configurations have a doubly occupied orbital for the electron pairs (1,2) and (2,3). Thus the spin function which forms a two-electron singlet for the electron pairs (1,2) and (2,3) should be coupled with configurations of the type (n_a, n_a, n_b) and (n_a, n_b, n_b), since it has to be antisymmetric with respect to the exchange of the electron pairs (1,2) and (2,3). It is convenient to impose, on the orbital configuration $(n_1, n_2, \ldots, n_N)$, the restriction that the singly occupied orbitals always precede the doubly occupied ones [34]. With this restriction, the latter two three-electron configurations can be represented by the configuration (n_a, n_b, n_b). The three electron ground state then has the configuration (1,0,0) and has to be coupled with the spin function $|\frac{1}{2}, \frac{1}{2}\rangle_a$, giving rise to one level as shown in Figure 2(b). In the case of $v_p = 2$ the two configurations (0,1,1) and (2,0,0) are possible. Both of these configurations have to be coupled with the spin function $|\frac{1}{2}, \frac{1}{2}\rangle_a$, giving rise to two levels. In the case of $v_p = 3$ the configuration (0,1,2) with three distinct orbitals will appear in addition to the configuration (3,0,0). The configuration (0,1,2) can be coupled with all three spin functions, giving rise to three levels, resulting in four levels in total associated with the polyad manifold of $v_p = 3$. A summary of the number of levels and orbital configurations of low-lying polyad manifolds of three electrons is displayed in Table 1.

The situation becomes more complicated for a system with four electrons, but similar arguments as in the three electron case can be applied. The total spin S in the four electron case can take three distinct values, namely, $S = 0$ (singlet), 1 (triplet), and 2 (quintet). According to the spin branching diagram

Table 1 Orbital configuration, number of levels derived from the configuration, and the total number of levels belonging to each v_p manifold for three electrons

v_p	N_p[a]	Configuration	n[b]
1	1	(1,0,0)	1
2	2	(2,0,0)	1
		(0,1,1)	1
3	4	(3,0,0)	1
		(0,1,2)	3
4	6	(4,0,0)	1
		(0,1,3)	3
		(2,1,1)	1
		(0,2,2)	1
5	9	(5,0,0)	1
		(0,1,4)	3
		(3,1,1)	1
		(0,2,3)	3
		(1,2,2)	1

[a] Number of levels belonging to each v_p manifold.

[b] Number of levels arising from each configuration.

the degree of degeneracy that is associated with the singlet, triplet, and quintet states is 2, 3, and 1, respectively [35]. The ground state of the four electron case has the configuration (0,0,1,1). This configuration belongs to the polyad manifold of $v_p = 2$ and gives rise to one level, since it can only be coupled with the singlet spin function consisting of the two-electron singlets for the electron pairs (1,2) and (3,4). The next polyad manifolds of $v_p = 3$ also involve only one configuration, namely (1,2,0,0), which can be coupled with one singlet and one triplet spin function, forming a two-electron singlet for the electron pair (3,4), giving rise of a total of two levels as shown in Figure 2(c). The same procedure can be applied to the polyad manifold of $v_p = 4$ and 5 giving rise to a total of 5 and 8 levels, respectively. In the case of the polyad manifold of $v_p = 6$ there are five possible configurations: (1,5,0,0), (2,4,0,0), (0,4,1,1), (0,0,3,3), and (0,1,2,3). The first three configurations form a two-electron singlet for the electron pair (3,4), giving rise to one singlet and one triplet level. The fourth configuration forms two-electron singlets for the electron pairs (1,2) and (3,4), giving rise to only one singlet level as in the case of $v_p = 2$ and 3. In the fifth configuration (0,1,2,3) all four orbitals are different and 6 linearly independent spin functions can be coupled with this configuration, giving rise to 6 levels. Thus, a total of 13 levels is associated with this polyad manifold. The number of levels and orbital configurations for the low-lying polyad manifolds of four electrons are summarized in

Table 2 Orbital configuration, number of levels derived from the configuration, and the total number of levels belonging to each v_p manifold for four electrons

v_p	N_p[a]	Configuration	n[b]
2	1	(0,0,1,1)	1
3	2	(1,2,0,0)	2
4	5	(1,3,0,0)	2
		(0,0,2,2)	1
		(0,2,1,1)	2
5	8	(1,4,0,0)	2
		(2,3,0,0)	2
		(0,3,1,1)	2
		(0,1,2,2)	2
6	13	(1,5,0,0)	2
		(2,4,0,0)	2
		(0,4,1,1)	2
		(0,0,3,3)	1
		(0,1,2,3)	6

[a] Number of levels belonging to each v_p manifold.

[b] Number of levels arising from each configuration.

Table 2. The number of levels calculated for each polyad manifold listed in the table agrees with the results displayed in Figure 2(c) for all v_p manifolds.

As the confinement strength ω_z decreases the electron–electron interaction, which represents only a small perturbation for large ω_z, starts to influence the energy spectrum. As a result the splitting of the energy levels belonging to a polyad manifold becomes so large that the energy levels of neighboring polyad manifolds start to overlap, as is apparent from Figure 2 for the medium confinement regime of $\omega_z = 1.0$. When ω_z decreases even further the overlap of the energy levels belonging to different polyad manifolds becomes even larger. Since the polyad quantum number represents an approximately conserved quantity it may be expected that the breakdown of this constant of motion will lead to an irregular energy-level pattern known as quantum chaos. On the other hand, the energy spectra shown in Figure 2 for the small confinement regime of $\omega_z = 0.1$ again show, for all cases of $N = 2$, 3, and 4, a band structure as in the case of the large confinement regime. The reason for the reappearance of such a regular band structure in the energy spectrum for the small confinement regime is examined in detail in the next section.

3.3. Extended polyad structure

The energy spectrum for the small confinement regime ($\omega_z = 0.1$) is displayed on the right hand side of Figure 2. It shows a band structure similar to that of the large confinement regime with $\omega_z = 5.0$ characterized by an energy gap close to ω_z. It should be noticed, however, that the energy spectrum for the small confinement regime differs from that of large confinement regime by the fact that in the small confinement regime the energy spectrum consists of groups of nearly degenerate levels having different spin multiplicities. In the case of $N = 2$, 3, and 4 the number of nearly degenerate levels is 2 (singlet and triplet), 3 (two doublets and one quartet), and 6 (two singlets, three triplets, and one quintet), respectively. Therefore, in the small confinement regime all linearly independent spin states become degenerate. A similar multiplet structure was previously reported for a small number of electrons confined in a large quasi-one-dimensional rectangular potential well [33,36] and may be considered as an indication of the formation of the Wigner lattice [37]. It is also noted that the number of levels belonging to each band of the energy spectrum is different for the small and large ω_z regimes. In the case of $N = 2$, for example, the number of levels belonging to each band, counted from below, is 2, 2, 4, 4, ... for $\omega_z = 0.1$, and 1, 2, 3, 4, ... for $\omega_z = 5.0$.

In order to explain the band structure for the small confinement regime the nature of the potential energy function in the Hamiltonian has been examined in the *internal space*. Since, for quasi-one-dimensional quantum dots, the electrons can only move along the z coordinate, their x and y dependence is neglected in the analysis. The internal space is defined by a unitary transformation from the independent electron coordinates $(z_1, z_2, \ldots, z_N)$ into the correlated electron coordinates $(z_\alpha,\ z_\beta, \ldots)$. The coordinate z_α represents the totally symmetric *center-of-mass* coordinate $z_\alpha = \frac{1}{\sqrt{N}}(z_1 + z_2 + \cdots + z_N)$, and the remaining correlated electron coordinates $z_\beta, \ldots, z_N$ represent the internal degrees of freedom of the N electrons [20,21]. In the case of two electrons the correlated coordinates are defined by

$$\begin{aligned} z_s &= \frac{1}{\sqrt{2}}[z_1 + z_2], \\ z_a &= \frac{1}{\sqrt{2}}[z_1 - z_2]. \end{aligned} \tag{10}$$

The symmetric z_s coordinate describes the center-of-mass degree of freedom for the two electrons, while the antisymmetric z_a coordinate describes the internal degree of freedom. In the case of three electrons the correlated coordinates may be defined by

$$\begin{aligned} z_a &= \frac{1}{\sqrt{3}}[z_1 + z_2 + z_3], \\ z_b &= \frac{1}{\sqrt{6}}[2z_1 - z_2 - z_3], \\ z_c &= \frac{1}{\sqrt{2}}[z_2 - z_3]. \end{aligned} \tag{11}$$

The totally symmetric z_a coordinate describes the center-of-mass degree of freedom and the remaining z_b and z_c coordinates span the internal space [21]. It is noted that the same set of coefficients used to define the internal space, namely, $\frac{1}{\sqrt{6}}(2, -1, -1)$ and $\frac{1}{\sqrt{2}}(1, -1)$ for the z_b and z_c coordinates, also appear as coefficients in the two doublet spin functions of $|\frac{1}{2}, \frac{1}{2}\rangle_b$ and $|\frac{1}{2}, \frac{1}{2}\rangle_a$, respectively. The internal space for the four electron case can be similarly defined. In the following, the internal space for two electrons is analyzed in detail.

The Hamiltonian (1) for quasi-one-dimensional two-electron quantum dots is simplified by neglecting the x and y degrees of freedom and by approximating the confining Gaussian potential by a harmonic-oscillator potential with ω_z

$$\mathcal{H}_{\mathrm{1D}}^{\mathrm{harm}} = -\frac{1}{2}\frac{\partial^2}{\partial z_1^2} - \frac{1}{2}\frac{\partial^2}{\partial z_2^2} + \frac{1}{2}\omega_z^2 z_1^2 + \frac{1}{2}\omega_z^2 z_2^2 + \frac{1}{|z_1 - z_2|}. \tag{12}$$

By introducing the correlated coordinates of Equation (10) this Hamiltonian takes the form

$$\mathcal{H}_{\mathrm{1D}}^{\mathrm{harm}} = -\frac{1}{2}\frac{\partial^2}{\partial z_s^2} + \frac{1}{2}\omega_z^2 z_s^2 - \frac{1}{2}\frac{\partial^2}{\partial z_a^2} + \frac{1}{2}\omega_z^2 z_a^2 + \frac{1}{\sqrt{2}|z_a|}. \tag{13}$$

The first two terms on the right-hand side of Equation (13) represent a harmonic-oscillator Hamiltonian for the z_s coordinate. They contribute the eigenenergy of a one-dimensional harmonic oscillator with frequency ω_z to the total energy. The remaining terms on the right-hand side of Equation (13) represent a harmonic-oscillator Hamiltonian for the z_a coordinate, with an additional Coulomb-type potential originating from the electron–electron interaction potential. These z_a-dependent terms account for the variation of the energy spectrum for different confinement strengths ω_z, as has been observed in Figure 2(a). The potential energy function of these x_a-dependent terms, i.e., the sum of the harmonic-oscillator potential and the Coulomb-type potential, has been plotted in Figure 3 for different strengths ω_z. In this figure the maximum potential height $V_{\max}$ and the domain of the z_a coordinate are $V_{\max} = \omega_z \times 10$ and $|z_a| \le \sqrt{\frac{20}{\omega_z}}$, respectively, for all ω_z. The

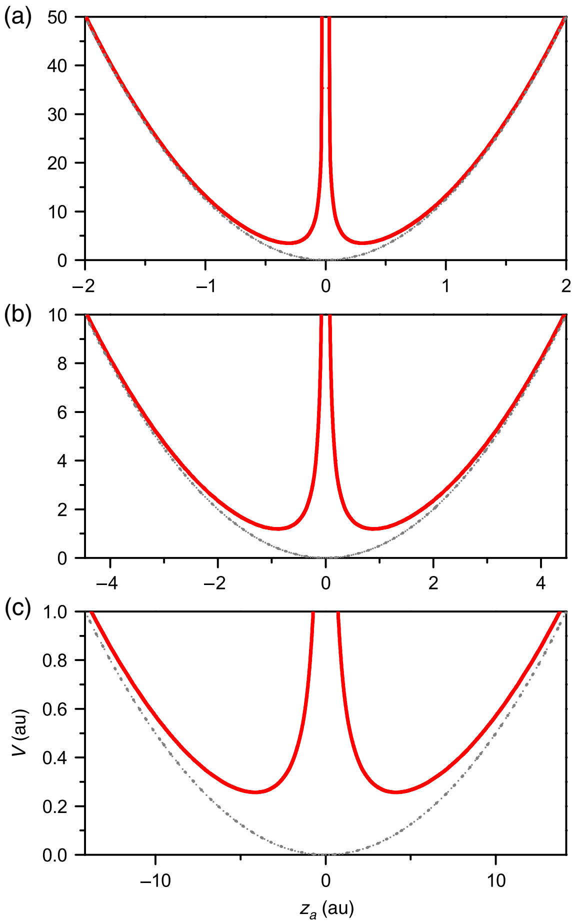

Figure 3 One-dimensional plot of the sum of the harmonic-oscillator and of the electron-repulsion potentials V for two electrons as a function of the internal coordinate z_a for $\omega_z = 5.0$ (a), 1.0 (b), and 0.1 (c). The solid red line represents the sum of the harmonic-oscillator and the electron repulsion potentials, while the dotted grey line represents the harmonic-oscillator potential alone. The maximum potential height $V_{\max}$ and the domain of the z_a coordinate displayed are $V_{\max} = \omega_z \times 10$ and $|z_a| \leq \sqrt{\frac{20}{\omega_z}}$, respectively, for all cases. (For interpretation of the references to color in this figure legend, the reader is referred to the web version of this book.)

harmonic-oscillator part of the potential function is indicated by dotted lines in order that the role of the electron–electron interaction can be clearly seen. It appears to be identical for all ω_z values. The sharp increase at the origin of the solid line representing the diverging contribution of the electron–electron interaction potential divides the region into the two parts separated by a wall. This *potential wall* becomes stronger as ω_z decreases from (a) to (c).

In case (a), corresponding to $\omega_z = 5.0$, the potential wall is rather thin and only acts as a small perturbation to the harmonic-oscillator potential. Consequently, in this case, the eigenenergy of the Schrödinger equation is basically that of the harmonic-oscillator potential modified by a small energy shift. As ω_z becomes smaller, the potential wall becomes thicker, as displayed in Figure 3(b), corresponding to $\omega_z = 1.0$, and the energy shift due to the potential wall becomes larger. This observation agrees with the large splitting of the energy levels within each of the v_p manifolds, as displayed in Figure 2(a) for the medium confinement regime.

It is noted that the eigenstates χ of the one-dimensional harmonic-oscillator with an even quantum number, χ_{even}, are affected more strongly by the potential wall than those with an odd quantum number, χ_{odd}, since the states with an even quantum number have a finite amplitude at the origin, while the states with an odd quantum number have a node at the origin. Since χ_{even} and χ_{odd} are symmetric and antisymmetric with respect to the inversion of the z_a coordinate, respectively, they are symmetric and antisymmetric with respect to the interchange of electrons 1 and 2. This means that χ_{even} and χ_{odd} must be coupled to the singlet and triplet spin functions, respectively. Therefore, as ω_z decreases the triplet states become more stabilized relative to the singlet states. This effect can be clearly seen in the energy spectrum of Figure 2(a), where the triplet levels (colored in red) become lowered as ω_z decreases from 5.0 to 1.0.

When ω_z becomes even smaller, and reaches the small confinement regime corresponding to $\omega_z = 0.1$, the potential wall becomes so thick that the wave function can hardly penetrate it. As a result the amplitude of singlet wave functions in the vicinity of the origin becomes extremely small. Therefore, except for the phase along the z_a coordinate, the nodal pattern of singlet wave functions becomes almost identical to that of the corresponding triplet wave functions having the same number of nodes as the singlet wave functions, except for the node at the origin. This rationalizes the singlet-triplet doublet structure of the energy spectrum of Figure 2(a) for $\omega_z = 0.1$. Another nonrigorous, yet simple, explanation of the doublet structure is given by considering the average distance between the two electrons. In the limit of small confinements, the relative distance between the two electrons becomes very large. Therefore, the total energy hardly depends on the mutual orientation of the electron spins, implying the degeneracy of the singlet and triplet states.

Another observation that needs to be explained is the recovering of the harmonic band structure in the small ω_z regime. As the potential energy function of Figure 3(c) indicates, the potential wall due to the electron–electron interaction is so thick that it divides the internal space into two regions, i.e., $z_a < 0$ and $z_a > 0$. Using the eigenfunctions χ of a particle bound in either of these two regions, χ^- and χ^+, for $z_a < 0$ and $z_a > 0$, respectively, the solution in the entire region of the potential of Figure 3(c) can be approximated by the sum and the difference of the functions χ^- and χ^+, respectively, because the wave function should be localized in both regions and has to satisfy the symmetry condition. The symmetric $\frac{1}{\sqrt{2}}(\chi^- + \chi^+)$ and the antisymmetric $\frac{1}{\sqrt{2}}(\chi^- - \chi^+)$ functions describe the singlet and the triplet states, respectively, as explained earlier. On the other hand, since at $|z_a| \rightarrow \infty$ both functions $\chi^\pm$ satisfy the same boundary condition as the harmonic oscillator and vanish at the origin, the functions $\chi^\pm$ can be approximated by eigenfunctions of the harmonic oscillator with *odd* quantum numbers that have a node at the origin. Consequently, the eigenenergies associated with the symmetric and the antisymmetric solutions are given by the harmonic oscillator energies and produce a harmonic-oscillator type energy spectrum.

Finally, the number of levels in each band displayed in Figure 2(a) for the small ω_z regime can be rationalized by the following considerations. Since in the small ω_z regime the singlet and triplet levels always appear as degenerate doublets, the pattern of the triplet states determines the number of levels. As shown in the previous paragraph, the potential wall of the electron–electron interaction does not strongly affect the nodal pattern of the triplet wave functions. Therefore, the polyad quantum numbers can still be used to classify the triplet levels for small ω_z. On the other hand, the singlet wave functions are affected more strongly by the potential wall for smaller ω_z and, in the limit of weak confinements, result in a 'node' at the origin but keep the phase of a singlet. Therefore, it is convenient to extend the definition of the polyad quantum number for singlet levels by including the node at the origin. For two electrons the *extended* polyad quantum number v_p^* is defined to be identical to v_p for the triplet levels, but to be $(v_p + 1)$ for the singlet levels. Using this definition the doublet pair of singlet and triplet levels has the same v_p^* value. Starting from the smallest v_p^* value of 1 for the lowest configuration of (0,1), the possible triplet configurations are (0,2) for $v_p^* = 2$, (0,3) and (1,2) for $v_p^* = 3$, and, (0,4) and (1,3) for $v_p^* = 4$. Therefore the number of levels belonging to each v_p^* manifold is calculated by using these numbers multiplied by two for a singlet and a triplet state, i.e., as 2, 2, 4, 4 for $v_p^* = 1$, 2, 3, 4, respectively. The results agree with the number of levels displayed in Figure 2(a).

The case of three and four electrons is more complicated, but the two characteristic features of the energy spectra observed for small ω_z, i.e., the nearly-degenerate multiplet structure of the energy levels of different spin multiplicities and the harmonic band structure of these levels, can be rationalized in a similar way. In the case of three electrons, for example, the internal space can be defined by the two correlated coordinates z_b and z_c defined by Equation (11). The potential function becomes a sum of two harmonic-oscillator Hamiltonians for the z_b and z_c coordinates plus *three* Coulomb-type potentials originating from the three electron–electron interaction potentials $\frac{1}{|z_1-z_2|}$, $\frac{1}{|z_2-z_3|}$, and $\frac{1}{|z_3-z_1|}$. As ω_z becomes smaller, these three potential walls become thicker and divide the two-dimensional internal space spanned by z_b and z_c into the six regions [21]. The quartet wave functions for three electrons are not strongly affected by the potential walls, since they have *nodal lines* along the three potential walls in order to satisfy the Pauli principle, as in the case of triplet wave functions for two electrons. The doublet wave functions, on the other hand, have a finite amplitude along the lines of the potential walls, since they do not change their sign with respect to the exchange of any two of the three electron coordinates. Therefore, they are affected more strongly by the potential walls for smaller ω_z as in the case of the singlet wave functions for the two electrons. In the limit of very weak confinement, they have almost no amplitude along the lines of the potential walls and their nodal pattern and energy become almost identical to those of the corresponding quartet states, except for the phase of the wave functions. For the four electron case the situation is similar, except that the internal space is three dimensional and divided by six potential walls.

For three and four electrons, the number of levels belonging to each v_p^* band in the small confinement regime can be calculated by examining the level pattern for the highest spin states, namely, quartet and quintet, respectively. Since the spin function of the highest spin state is totally symmetric with respect to the interchange of any two electrons, it can only be coupled with orbital configurations involving distinct orbitals. The orbital configurations that may be coupled to the triplet, quartet, and quintet spin states of respectively, two, three, and four electrons, are listed in Table 3 for the range of v_p^* values that appear in the energy spectra of Figure 2. The number of levels belonging to each v_p^* manifold can be calculated from this table by counting the number of orbital configurations for each v_p^* and by multiplying this number by the factor of 2, 3, and 6 for two, three, and four electrons, respectively. In the case of four electrons the number of configurations equals 1, 1, 2, 3, and 5 for $v_p^* = 6, 7, 8, 9$, and 10, respectively. Multiplying by the factor of 6, the number of possible levels becomes equal to 6, 6, 12, 18, and 30 for $v_p^* = 6, 7, 8, 9$, and 10, respectively. These results agree with the number of levels appearing in the energy spectrum displayed in Figure 2(c) for $\omega_z = 0.1$.

4. QUASI-TWO-DIMENSIONAL QUANTUM DOTS

The energy spectrum of two electrons confined in a *quasi-two-dimensional* Gaussian potential defined by Equation (3) is presented in Figure 4 for different confinement strengths in a similar form as in Figure 2 (a) for quasi-one-dimensional quantum dots. The displayed energy spectrum, for the large and medium confinement regime of ω_{xy} = 5.0 and 1.0, shows a polyad structure which is similar to that found for quasi-one-dimensional quantum dots shown in Figure 2 (a), except that it involves a larger number of levels

Table 3 Orbital configuration for the highest spin state of two, three, and four electrons belonging to each v_p manifold

v_p	2e	3e	4e
1	(0,1)		
2	(0,2)		
3	(0,3) (1,2)	(0,1,2)	
4	(0,4) (1,3)	(0,1,3)	
5	(0,5) (1,4) (2,3)	(0,1,4) (0,2,3)	
6		(0,1,5) (0,2,4) (1,2,3)	(0,1,2,3)
7		(0,1,6) (0,2,5) (0,3,4) (1,2,4)	(0,1,2,4)
8			(0,1,2,5) (0,1,3,4)
9			(0,1,2,6) (0,1,3,5) (0,2,3,4)
10			(0,1,2,7) (0,1,3,6) (0,1,4,5) (0,2,3,5) (1,2,3,4)

in each polyad manifold due to the increased dimensionality. For the small confinement regime of $\omega_{xy} = 0.1$, on the other hand, the energy spectrum is qualitatively different from that found in the corresponding quasi-one-dimensional case. In the first place, for quasi-two-dimensional quantum dots (cf. Figure 4), the doublet structure, consisting of a pair of singlet and triplet levels, a typical feature found in the case of quasi-one-dimensional quantum dots, indicating the formation of a Wigner lattice, is absent. Moreover, the energy levels of a quasi-two-dimensional quantum dot with $\omega_{xy} = 0.1$ do not seem to form, in the high energy region $E > 0.25$, a clearly defined band structure as in the case of quasi-one-dimensional quantum dots.

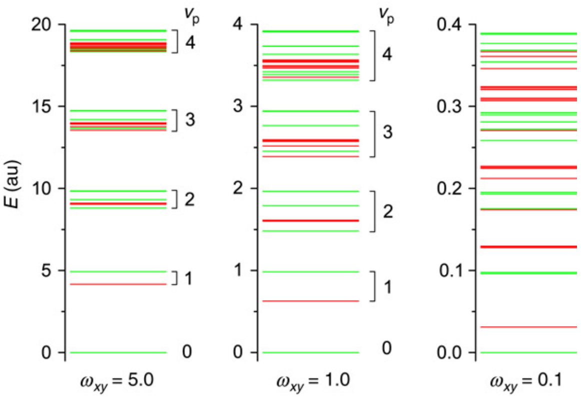

Figure 4 Energy spectrum of the low-lying states of two electrons confined in a quasi-two-dimensional Gaussian potential for different strength of confinement. Energy levels are colored by green for singlet states and red for triplet states, respectively. The parameter v_p specifies the polyad quantum number (See the text for details). (For interpretation of the references to color in this figure legend, the reader is referred to the web version of this book.)

It may be argued that the energy spectrum in the small confinement regime, corresponding to $\omega_{xy} = 0.1$ displayed in Figure 4, shows a tendency to form a Wigner lattice for even smaller values of ω_{xy}. In order to check this, a quasi-two-dimensional quantum dot for confinement strength as small as $\omega_{xy} = 0.01$ has been studied. The resulting energy spectrum is presented in Figure 5. Again, the displayed spectrum shows no singlet-triplet doublet structure. Quite to the contrary, it becomes more difficult to recognize a band structure in the spectrum. Thus, the energy spectrum of quasi-two-dimensional quantum dots in the weak confinement regime seems to be essentially different from that of quasi-one-dimensional quantum dots.

In order to analyze the origin of this difference between the energy spectra of quasi one- and two-dimensional quantum dots in the small confinement regime, the internal space for two electrons is considered as in the quasi-one-dimensional cases. Using a harmonic approximation to the Gaussian confining potential, and neglecting the dependence on the z coordinate, the Hamiltonian of Equation (1) for two electrons takes the form

$$\mathcal{H}_{2D}^{\text{harm}} = -\frac{1}{2}\left[\frac{\partial^2}{\partial x_1^2} + \frac{\partial^2}{\partial y_1^2}\right] - \frac{1}{2}\left[\frac{\partial^2}{\partial x_2^2} + \frac{\partial^2}{\partial y_2^2}\right] + \frac{1}{2}\omega_{xy}^2\left[x_1^2 + y_1^2\right] + \frac{1}{2}\omega_{xy}^2\left[x_2^2 + y_2^2\right] + \frac{1}{\sqrt{(x_1 - x_2)^2 + (y_1 - y_2)^2}}. \tag{14}$$

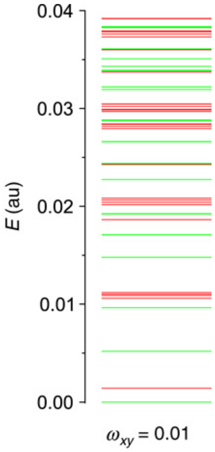

Figure 5 Energy spectrum of the low-lying states of two electrons confined in a quasi-two-dimensional Gaussian potential for $(D, \omega_{xy}) = (0.4, 0.01)$. Energy levels are colored by green for singlets and by red for triplets. (For interpretation of the references to color in this figure legend, the reader is referred to the web version of this book.)

Performing the unitary transformation of the independent electron coordinates (x_1, y_1, x_2, y_2) into the correlated coordinates (x_s, y_s, x_a, y_a),

$$\begin{aligned} x_s &= \frac{1}{\sqrt{2}}[x_1 + x_2], \\ y_s &= \frac{1}{\sqrt{2}}[y_1 + y_2], \\ x_a &= \frac{1}{\sqrt{2}}[x_1 - x_2], \\ y_a &= \frac{1}{\sqrt{2}}[y_1 - y_2], \end{aligned} \tag{15}$$

the Hamiltonian of Equation (14) separates into a sum of two contributions, depending either on the coordinates (x_s, y_s) or (x_a, y_a), i.e.,

$$\mathcal{H}_{\text{2D}}^{\text{harm}} = \mathcal{H}_{\text{c.o.m}}(x_s, y_s) + \mathcal{H}_{\text{int}}(x_a, y_a), \tag{16}$$

where

$$\mathcal{H}_{\text{c.o.m}} = -\frac{1}{2}\left[\frac{\partial^2}{\partial x_s^2} + \frac{\partial^2}{\partial y_s^2}\right] + \frac{1}{2}\omega_{xy}^2\left[x_s^2 + y_s^2\right], \tag{17}$$

and

$$\mathcal{H}_{\text{int}} = -\frac{1}{2}\left[\frac{\partial^2}{\partial x_a^2} + \frac{\partial^2}{\partial y_a^2}\right] + \frac{1}{2}\omega_{xy}^2\left[x_a^2 + y_a^2\right] + \frac{1}{\sqrt{2(x_a^2 + y_a^2)}}. \tag{18}$$

The first part of the Hamiltonian (16), $\mathcal{H}_{\text{c.o.m}}$, describes the center-of-mass contribution, as in the quasi-one-dimensional cases, and contributes the eigenenergy of a two-dimensional isotropic harmonic oscillator to the total energy. The second part of the Hamiltonian, $\mathcal{H}_{\text{int}}$, depends on the antisymmetric coordinates x_a and y_a, and represents the contribution to the total energy due to the internal degrees of freedom.

In order to explain the characteristic feature of the energy spectrum that distinguishes it from the quasi-one-dimensional case, the potential energy function has been plotted for the internal Hamiltonian of Equation (18) for different ω_{xy} values in Figure 6. The maximum height of the potential $V_{\max}$ and the domain of the x_a and y_a coordinates are the same as for the quasi-one-dimensional potential presented in Figure 3. Implying that the harmonic-oscillator part of the potential looks identical for different ω_{xy} values, the effect of the electron–electron interaction becomes apparent. The small red spot at the center of the potential represents a sharp increase due to the electron–electron interaction. It increases in size as ω_{xy} becomes smaller. This indicates that the electron–electron interaction perturbs the harmonic-oscillator potential more strongly for smaller confinement as in the quasi-one-dimensional case. It is noted, however, that the potential energy function has a pole, rather than a potential wall as in the quasi-one-dimensional case, where the wall separates the internal space into two regions. As a consequence, the electron–electron interaction potential in the quasi-two-dimensional case will not strongly modify the nodal pattern of singlet wave functions, since they can avoid the pole. Therefore, there seems to be little reason for the singlet and triplet levels of quasi-two-dimensional quantum dots to form degenerate pairs in the small confinement regime, unlike in the case of quasi-one-dimensional quantum dots.

5. SUMMARY

In the present study the energy-level structure of two, three and four electrons confined in a quasi-one-dimensional Gaussian potential for different strengths of confinement has been examined in detail, by using the accurate computational results of eigenenergies and wave functions obtained in previous studies for two and three electrons and in the present study for four electrons, respectively. The eigenenergies and wave functions have been calculated by using the quantum chemical full configuration interaction method and by employing Cartesian anisotropic Gaussian basis

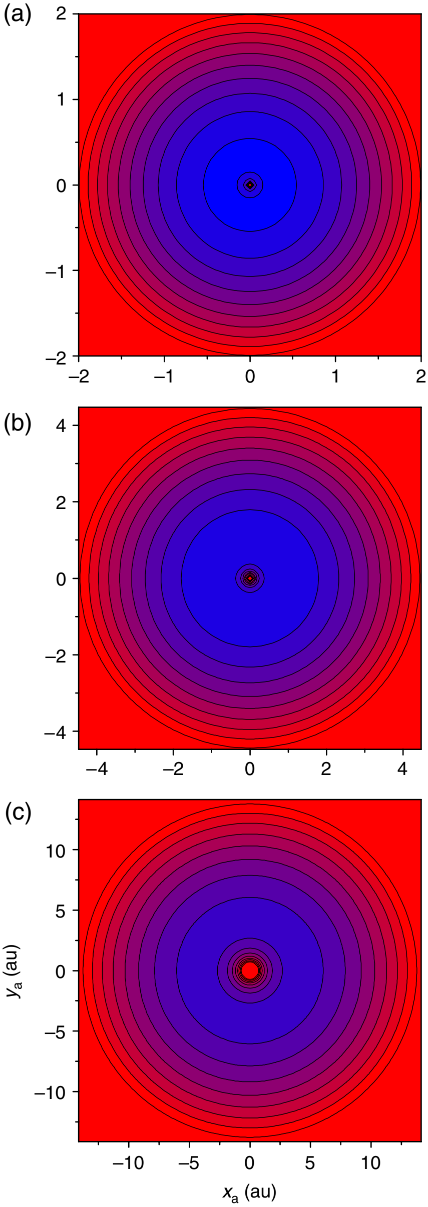

Figure 6 Two-dimensional contour plot of the sum of the harmonic-oscillator and of the electron-repulsion potentials for two electrons in the internal space (x_a, y_a) for ω_{xy} = 5.0 (a), 1.0 (b), and 0.1 (c). The maximum potential height $V_{\max}$ and the domain of the x_a and y_a coordinates displayed are the same as used in Figure 3. The red spot at the origin of the contours represents the *potential pole* of the electron repulsion potential. (For interpretation of the references to color in this figure legend, the reader is referred to the web version of this book.)

sets with high angular momentum functions. The energy-level structure changes qualitatively for different strengths of confinement and is classified by three regimes of the strength of confinement ω_z, namely, large, medium and small. The polyad quantum number v_p has been used to characterize the energy-level structure for large and medium ω_z, while the *extended* polyad quantum number v_p^* has been used for small ω_z. The energy levels in the small ω_z regime form nearly-degenerate multiplets consisting of a set of energy levels having different spin multiplicities. To analyze the effect of the electron–electron interaction on the formation of the degenerate multiplets, the *potential energy function*, defined by the sum of the one-electron potentials and the two-electron potentials, has been introduced and displayed as a function of the internal space for different strengths of ω_z. The plots of the potential energy function for different ω_z clearly show that, for small ω_z, the degeneracy of the energy levels among different spin states is caused by the *potential walls* of the electron–electron interaction potentials within the internal space. A systematic way of obtaining the degeneracy pattern of energy levels for small ω_z is given.

The energy spectrum of two electrons confined in a quasi-*two*-dimensional Gaussian potential has also been studied for the same set of the strengths of confinement as the corresponding quasi-one-dimensional cases, and are compared to them. The energy spectrum of the quasi-two-dimensional quantum dot is qualitatively different from that of the quasi-one-dimensional quantum dot in the small confinement regime. The origin of the differences is due to the difference in the structure of the internal space.

ACKNOWLEDGEMENTS

TS has been supported in parts by the Grants-in-Aid for Scientific Research (No. 20750018) from the Ministry of Education, Culture, Sports, Science and Technology (MEXT), Nihon University Joint Research Grant for 2008, and by Nihon University Strategic Projects for Academic Research. JP thanks the Alexander von Humboldt Foundation for the renewal of his Humboldt Research Award.

REFERENCES

[1] C.B. Murray, D.J. Norris, M.G. Bawendi, J. Am. Chem. Soc. 115 (1993) 8706.
[2] R.C. Ashoori, Nature 379 (1996) 413.
[3] S. Tarucha, D.G. Austing, T. Honda, R.T. van der Hage, L.P. Kouwenhoven, Phys. Rev. Lett. 77 (1996) 3613.
[4] N.F. Johnson, J. Phys.: Condens. Matter 7 (1995) 965.
[5] L.P. Kouwenhoven, T.H. Oosterkamp, M.W.S. Danoesastro, M. Eto, D.G. Austing, T. Honda, S. Tarucha, Science 278 (1997) 1788.
[6] P. Matagne, J.P. Leburton, D.G. Austing, S. Tarucha, Physica E 13 (2002) 679.
[7] A.P. Alivisatos, Science 271 (1996) 933.
[8] T. Ezaki, N. Mori, C. Hamaguchi, Phys. Rev. B 56 (1997) 6428.

[9] G. Cantele, D. Ninno, G. Iadonisi, Phys. Rev. B 64 (2001) 125325.
[10] B. Szafran, J. Adamowski, S. Bednarek, Physica E 5 (2000) 185.
[11] T. Sako, S. Yamamoto, G.H.F. Diercksen, J. Phys. B: At. Mol. Opt. Phys. 37 (2004) 1673.
[12] U. Merkt, J. Huser, M. Wagner, Phys. Rev. B 43 (1991) 7320.
[13] P.A. Maksym, T. Chakraborty, Phys. Rev. Lett. 65 (1990) 108.
[14] J. Hu, T.W. Odom, C.M. Lieber, Acc. Chem. Res. 32 (1999) 435.
[15] M. Rontani, F. Rossi, F. Manghi, E. Molinari, Phys. Rev. B 59 (1999) 10165.
[16] T. Sako, G.H.F. Diercksen, J. Phys. B: At. Mol. Opt. Phys. 36 (2003) 1433.
[17] T. Sako, G.H.F. Diercksen, J. Phys.: Condens. Matter 15 (2003) 5487.
[18] T. Sako, G.H.F. Diercksen, J. Phys.: Condens. Matter 17 (2005) 5159.
[19] T. Sako, P.A. Hervieux, G.H.F. Diercksen, Phys. Rev. B 74 (2006) 045329.
[20] T. Sako, G.H.F. Diercksen, Phys. Rev. B 75 (2007) 115413.
[21] T. Sako, G.H.D. Diercksen, J. Phys.: Condens. Matt. 20 (2008) 155202.
[22] T. Sako, G.H.F. Diercksen, J. Phys. B: At. Mol. Opt. Phys. 36 (2003) 1681.
[23] P. Matagne, J.P. Leburton, Phys. Rev. B 65 (2002) 235323.
[24] J. Adamowski, M. Sobkowicz, B. Szafran, S. Bednarek, Phys. Rev. B 62 (2000) 4234.
[25] M. Wagner, U. Merkt, A.V. Chaplik, Phys. Rev. B 45 (1992) 1951.
[26] J.T. Lin, T.F. Jiang, Phys. Rev. B 64 (2001) 195323.
[27] O. Dippel, P. Schmelcher, L.S. Cederbaum, Phys. Rev. A 49 (1994) 4415.
[28] W. Becken, P. Schmelcher, F.K. Diakonos, J. Phys. B: At. Mol. Opt. Phys. 32 (1999) 1557.
[29] P.S. Drouvelis, P. Schmelcher, F.K. Diakonos, J. Phys.: Condens. Matter 16 (2004) 3633.
[30] P.S. Drouvelis, P. Schmelcher, F.K. Diakonos, Phys. Rev. B 69 (2004) 035333.
[31] M. Braskén, M. Lindberg, D. Sundholm, J. Olsen, Phys. Rev. B 61 (2000) 7652.
[32] S. Corni, M. Braskén, M. Lindberg, J. Olsen, D. Sundholm, Phys. Rev. B 67 (2003) 085314.
[33] G.W. Bryant, Phys. Rev. Lett. 59 (1987) 1140.
[34] W. Duch, J. Karwowski, Comput. Phys. Rep. 2 (1985) 93.
[35] M. Kotani, A. Amemiya, E. Ishiguro, T. Kimura, Table of Molecular Integrals, Maruzen, Tokyo, 1995.
[36] B. Szafran, F.M. Peeters, S. Bednarek, T. Chwiej, J. Adamowski, Phys. Rev. B 70 (2004) 035401.
[37] E. Wigner, Phys. Rev. 46 (1934) 1002.

CHAPTER 6

Engineering Quantum Confined Silicon Nanostructures: Ab-Initio Study of the Structural, Electronic and Optical Properties

Elena Degoli[a] and **Stefano Ossicini**[a]

Contents

1. INTRODUCTION

Understanding and controlling the properties of materials is crucial for improving the information technology on which our modern world is built.

[a] CNR-INFM-S^3 and Dipartimento di Scienze e Metodi dell'Ingegneria - Università di Modena e Reggio Emilia - via Amendola 2 Pad. Morselli, I-42100 Reggio Emilia, Italy

---

Advances in Quantum Chemistry, Vol. 58
ISSN: 0065-3276, DOI: 10.1016/S0065-3276(09)00710-2

The ever increasing demands from distributed information systems are stimulating research and technology development. Theory has a central role because a microscopic understanding represents a fundamental step towards the innovation, design and fabrication of new materials and devices. The ability to describe structural, electronic and optical properties of new materials with accurate first-principle methods is hence of fundamental importance.

In particular silicon microelectronics devices have revolutionized our lives in the second half of the last century. Integration and economy of scale are the two key ingredients for the Si technological success. Si has a band gap of 1.12 eV, which is ideal for room temperature operation, and has an oxide that allows the processing flexibility to place, at this time, more than 10^8 transistors on a single chip. The extreme integration levels reached by the Si microelectronics industry have permitted high speed performance and unprecedented interconnection levels. The present interconnection degree is sufficient to cause interconnect propagation delays, overheating and information latency between single devices. To overcome this bottleneck, photonic materials, in which light can be generated, guided, modulated, amplified and detected, need to be integrated with standard electronic circuits to combine the information processing capabilities of electronic data transfer and the speed of light. In particular, chip to chip or even intra-chip optical communications all require the development of efficient optical functions and their integration with state-of-art electronic functions [1].

Si is the desired material, because Si-based optoelectronics would open the door to faster data transfer and higher integration densities at low cost. Si microphotonics has boomed during recent years. Almost all the various photonic devices have been demonstrated [1,2], but the main limitation of Si photonics remains the lack of any practical Si-based light source. Bulk Si is an indirect band-gap material which emits in the infrared region; radiative lifetimes of excited carriers in Si are very long, causing a predominant de-excitation of carriers via fast non-radiative recombinations. Moreover, Si has significant free carrier absorption and Auger recombination rates which impede population inversion and, hence, optical gain if strongly pumped. Therefore the role of Si as a light source has been ignored up to now.

Several attempts have been employed to engineer luminescing transitions in an otherwise indirect material [1]. After the initial impulse given by the pioneering work of Canham on photoluminescence (PL) from porous Si [3], nanostructured silicon has received extensive attention (for reviews see Refs. [4–15]). This activity is mainly centered on the possibility of getting relevant optoelectronic properties from nanocrystalline Si. The huge efforts made towards matter manipulation at the nanometer scale have been motivated by the fact that desirable properties can be generated just by changing the system dimension and shape. The idea is to confine carriers into small Si-based systems (1–5 nm in size) so that quantum confinement effects start to play a crucial role by changing the physical properties of bulk Si [1,10].

Quantum confinement can act in three spatial directions, thus one has zero-dimensional, one-dimensional, and two-dimensional confined systems.

For zero-dimensional systems, as in the case of Si nanocrystals (Si-NCs) the band-gap increases with decreasing size. Visible luminescence external efficiency in excess of 23% has been obtained in nanostructured Si [1,10,16],

Investigation of phenomena such as the Stokes shift (difference between absorption and emission energies), the PL emission energy vs nanocrystals size, etc. can give a fundamental contribution to the understanding of how the optical response of such systems can be tuned. An interesting amount of work has been done regarding excited Si-NCs [4–15], but a clear comprehension of some aspects is still lacking. The question of surface effects, in particular oxidation, has been addressed in recent years. Both theoretical calculations and experimental observations have been applied to investigate the possible active role of the interface on the optoelectronic properties of Si-NCs. Different models have been proposed: Baierle et al. [17] have considered the role of the surface geometry distortion of small hydrogenated Si clusters in the excited state. Wolkin et al. [18] have observed that oxidation introduces defects in the Si-NC band-gap which pin the transition energy. They claimed the formation of a Si=O double bond as the pinning state. The same conclusion has been recently reached by other authors [19–22], whereas Vasiliev et al. [23] have pointed out that similar results can also be obtained for O connecting two Si atoms (single bonds) at the Si-NC surface.

The optical gain observed in Si-NC embedded in SiO_2 formed by different techniques [24–27] has given a further impulse to these studies. Interface radiative states have been suggested to play a key role in the mechanism of population inversion at the origin of the gain [24,25,28]. However many researchers are still convinced of the pure quantum confinement model and they are focusing their efforts mainly on the self trapped excitonic effects [29,30] in order to explain the differences between their results and the experimental outcomes.

Nevertheless Si-NC remain indirect band-gap materials where structures related to momentum-conserving phonons were clearly observed [1,8,31]. This drawback can be circumvented by introducing into the Si-NCs an isoelectronic impurity [1,10] or by simultaneous *n*- and *p*-type impurity doping [32]. In a series of intriguing papers Fujii and collaborators [32–34] have demonstrated that it is possible to control the PL properties of Si-NCs by simultaneous doping with B and P impurities. They have shown not only that the PL intensity of co-doped Si-NCs is always higher than that of either P– or B doped Si-NCs, but that it is even higher than that of the undoped Si-NCs. In addition, under resonant excitation conditions the co-doped samples did not exhibit structures related to momentum-conserving phonons, suggesting that in this case the quasidirect optical transitions are predominant.

Among the different Si nanostructures, Si nanowires (Si-NWs) have recently attracted a lot of interest. Being one-dimensional structures, they seem potentially as useful as carbon nanotubes and probably more, due to the possibility of tailoring their chemistry and using them to create nanosized lasers. Si-NWs of different controllable sizes and growth directions have been synthesized in recent years through several routes [1,35–39]. Thin Si-NWs down to about 1 nm diameter have been obtained with grown orientation along the [100], [110], [111] and [112] directions and with a very rich surface chemistry. The clear device potential of these Si-NWs has been demonstrated by a wide range of applications [40–43].

Regarding the two-dimensional systems, the optoelectronic properties of Si nanoslabs embedded in calcium fluoride and in silicon dioxide have been experimentally studied [44–52], confirming the role of quantum confinement, even if the discussion is still alive.

In this paper we present a comprehensive first-principles study of the structural, electronic and optical properties of undoped and doped Si nanosystems. The aim is to investigate, in a systematic way, their structural, electronic and stability properties as a function of dimensionality and size, as well as pointing out the main changes induced by the nanostructure excitation. A comparison between the results obtained using different Density Functional Theory based methods will be presented. We will report results concerning two-dimensional, one-dimensional and zero-dimensional systems. In particular the absorption and emission spectra and the effects induced by the creation of an electron–hole pair are calculated and discussed in detail, including many-body effects.

The paper is organized as follows. A complete description of the theoretical methods used is given in Section 2 considering, in the different subsections, the Density Functional Theory (DFT) (Section 2.1), the Δ self-consistent (Δ-SCF) approach (Section 2.1.1), and the Many-Body perturbation theory (Section 2.2) through the GW (Section 2.2.1) and the Bethe–Salpeter (Section 2.2.2) methods.

The study of the physical systems is presented in Sections 3–5. We start from the systems where the quantum confinement acts in all the three spatial dimension, thus considering zero-dimensional systems. Starting from the analysis of hydrogenated Si-NCs (Section 3.1.1) we then consider the effect of oxidation (Section 3.1.2), and finally of an embedding matrix (Section 3.2). The particular case of how doping changes the structural, electronic and optical properties of the nanocrystals is discussed is Section 3.3. Here we study three different regimes: single-doped, co-doped and multi-doped Si nanocrystals (see Sections 3.3.1–3.3.3). Moreover the problem of screening in nanostructures has also been considered in Section 3.3.4.

Next we consider one-dimensional quantum confined systems in Section 4. Here we present the electronic and optical properties of Si and Ge nanowires (see Section 4.1) grown in different directions and with different diameters, considering also the presence of doping impurities (see Section 4.2)

Indeed we study the two-dimensional systems in Section 5. In this section we will analyze the structural, electronic and, in particular, the optical properties of Si and Ge based nanofilms (Section 5.1), of Si superlattices and multiple quantum wells where CaF_2 and SiO_2 are the barrier mediums (Sections 5.2 and 5.3). The quantum confinement effect and the role of symmetry will be considered, changing the slab thickness and orientation, and also the role of interface O vacancies will be discussed.

Conclusions are presented in Section 6.

2. THEORETICAL METHODS

Electronic and optical properties of complex systems are now accessible thanks to the impressive development of theoretical approaches and of computer power. Surfaces, nanostructures, and even biological systems can now be studied within ab-initio methods [53,54]. In principle within the Born-Oppenheimer approximation to decouple the ionic and electronic dynamics, the equation that governs the physics of all those systems is the many-body equation:

$$\begin{aligned}\left(\sum_i -\frac{1}{2}\nabla^2\mathbf{r}_j + V_{\text{ext}} + \frac{1}{2}\sum_{i\neq j}\frac{1}{|\mathbf{r}_i - \mathbf{r}_j|}\right)\Psi(r_1, r_2, \ldots, r_N)\\ = E\Psi(r_1, r_2, \ldots, r_N) \qquad (1)\end{aligned}$$

with V_{ext} being the ionic potential. Unfortunately a direct solution of Equation (1) is a formidable task, not only for realistic systems but even for $N \geq 2$. It is hence necessary to resort to approximations, or to different approaches. The static (Section 2.1) DFT avoids dealing directly with the many-body equation by mapping the interacting system into a fictitious non-interacting system (which is then described by single particle equations); the Green's function approach (Section 2.2.1), instead, maps the many-body electronic problem to a system of quasi-particles, which describe the excitations in terms of a particle of finite lifetime, that represent the extra electron (and/or the extra hole added to the system) plus its screened interaction with the electrons of the system. In next sections, we review the theoretical approaches used to calculate ground state properties, band structures, and optical spectra.

2.1. The density functional theory

Density functional theory (DFT) treats the case of an external, time independent potential, and is based on the Hohenberg and Kohn theorem [55], which proves that all the ground state properties of an interacting electronic system, including, in principle, the many-body wave function, could be expressed as unique functionals of the electronic density alone. In particular this assertion is valid also for the total energy E of the system. For the total energy functional $E[n]$, the variational principle ensures that for a given density $n(r)$, $E[n(\mathbf{r})] \geq E_{\mathrm{GS}}$ where E_{GS} is the ground state energy of the system. The energy functional finds its minimum at the ground state density n_{GS}, for which $E[n_{\mathrm{GS}}] = E_{\mathrm{GS}}$. This theorem leads, in principle, to a straightforward method for computing ground state properties, but the explicit form of the functional in terms of the density is not known and such an explicit functional may not exist. Once given an approximation for the functional dependence of E, the ground state density can be obtained by a minimization procedure of the energy functional. Kohn and Sham [56], introduced an ad hoc separation of the terms contributing to the total energy E: the electron–electron interaction and the kinetic energy T of the interacting N-electron system. The advantages of this separation are: (1) it provides a single particle scheme to obtain the ground state density and total energy, and (2) to have an expression in which the approximations to the unknown part would be, in many cases, not as relevant as before. In the KS scheme the total energy functional of the interacting system is written as:

$$E[n] = T_0[n] + E_H[n] + \int \mathrm{d}\mathbf{r} n(\mathbf{r}) v_{\mathrm{ext}}(\mathbf{r}) + e_{xc}[n], \tag{2}$$

where T_0 is the kinetic energy of a non-interacting system with density n, E_H is the Hartree contribution to the total energy, and E_{xc} is the remaining part of the total energy which contains exchange–correlation contributions plus the difference between the kinetic energy of the interacting N-electron system T and the kinetic energy T_0 of the non-interacting system. The main idea underlying this approach is to map the study of the (complicated) interacting system into the study of a (simpler) non interacting fictitious system whose Hamiltonian is written as:

$$\left[-\frac{1}{2}\nabla^2 + v_{\mathrm{ext}} + v_H + V_{xc}\right] = \varepsilon_i \phi_i(\mathbf{r}) \tag{3}$$

and which has, by construction, the same ground state density of the interacting system:

$$n(r) = \sum_i f_i |\phi_i(\mathbf{r})|^2 \tag{4}$$

with f_i being the occupation number of the state i. In Equation (3) $V_{xc} = \delta E_{xc}[n]/\delta n$ is the exchange and correlation potential of the interacting system. It is now possible, given an approximation for $E_{xc}[n]$, to solve the Kohn-Sham Equations (3) and (4) self consistently and calculate the density of the interacting (real) system via Equation (2). Once the density is known, it is possible to calculate the energy of the ground state of the interacting system and hence, by proper minimization, to find its ground state geometry. The simplest and most common approximation to E_{xc} is the Local Density Approximation (LDA) given by [57]:

$$E_{xc}^{\mathrm{LDA}} = \int \mathrm{d}\mathbf{r}\, n(\mathbf{r})\varepsilon_{xc}^{\mathrm{heg}}(n), \tag{5}$$

where $\varepsilon_{xc}^{\mathrm{heg}}(n)$ is the exchange–correlation energy per electron of a homogeneous electron gas of density n. It is worth noting that the Kohn-Sham equations, representing a fictitious auxiliary system, have in principle no physical meaning. Nevertheless, their eigenvalues are often interpreted as one electron excitation energies corresponding to the excitation spectra of the system upon removal or addition of an electron, and DFT is in this way used to calculate band structures. The qualitative agreement with experiments is often remarkable, but not quantitative: the electronic gaps of semiconductors are, as a matter of fact, always systematically underestimated within DFT.

2.1.1. The Δ-self-consistent approach: Absorption, emission and Stokes shift

What happens when an e–h pair is excited in the system is that the charge density distribution changes, thus perturbing the forces acting on the atoms. The ions follow the excitation relaxing to a new equilibrium geometry, provided that the time taken by this process is shorter than the e–h pair recombination time. Therefore, the excitation and de-excitation processes involve two atomic configurations, that we can call ground-state (GS) and excited-state (EXC) geometries. This gives rise to four possible electronic/atomic configurations with their corresponding total energies, as follows:

1. ground state as the starting point, whose total energy is E_1,
2. one e–h pair induced by the excitation, described by the excited-state level occupation but in the ground-state geometry, whose total energy is E_2,

3. cluster relaxation in the presence of the e–h pair, toward the excited-state minimum energy geometry, whose total energy is E_3,
4. e–h pair recombination, ground-state occupation, excited-state geometry, total energy E_4.

After the recombination the system can eventually relax toward the starting, ground-state geometry. As we will see the excitation can induce significant changes on the electronic and structural properties of the system and, mostly, there is a strong interplay between the electronic level occupation and the cluster geometry. For systems with a spatial confinement, i.e., with free-exciton radii larger than, or, of the order of their spatial extent, the lowest pair-excitation energies ϵ_{ex} can be rigorously expressed in terms of DFT–LDA total energies. Usually one defines $\epsilon_{ex} = E(N+1) + E(N-1) - 2E(N)$ using the ground-state energies E of the $N+1$, $N-1$, and N electron system. However, in this definition the effect of the attractive screened Coulomb interaction of the excited electron and hole pair is missing. In order to account for the excitonic effect, we use the Δ-SCF approach, which is based on the study of two different electronic configurations for the system:

- initial state: Ground State

$$\vec{\gamma}_{\text{gs}} = \begin{cases} \gamma_i = 1 & i = 1, \ldots, N \\ \gamma_i = 0 & i > N \end{cases}$$

- final state: Neutral Excited State

$$\vec{\gamma}_{\text{exc}} = \begin{cases} \gamma_i = 1 & i = 1, \ldots, (h-1), (h+1), \ldots, N \quad \text{and} \quad i = e \ (e > N) \\ \gamma_i = 0 & i = h \quad \text{and} \quad i > N, i \neq e \end{cases}$$

In the last configuration a particle–hole pair is considered in the system promoting an electron from the valence band ($i = h$) to a conduction band ($i = e$). For this reason the method is also called constrained DFT. The excitation energy of the many-electron system is the difference in total energy between two self-consistent calculations with the occupations described above, i.e.:

$$E_{\text{exc}} = E_{\vec{\gamma}_{\text{exc}}} - E_{\vec{\gamma}_{\text{gs}}} \tag{6}$$

and should give the optical gap (since the initial and final states are both neutral). In our particular calculation the total energy $E_{\vec{\gamma}_{\text{exc}}}$ is calculated with the constraint that the HOMO (Highest Occupied Molecular Orbital) of the ground-state system contains a hole h, placing the corresponding electron e into the LUMO (Lowest Unoccupied Molecular Orbital) of the ground-state system. When the atomic geometry of the nanocrystal is optimized in the ground-state configuration, the corresponding calculated pair-excitation energies $\epsilon_{ex}^{A} = E_2 - E_1$ define the optical absorption (A) edges. We also relax the nanostructure with an excited electron–hole pair. At the resulting geometry, the lowest emission (E) energy $\epsilon_{ex}^{E} = E_3 - E_4$ is calculated. The difference of the two energies ($\epsilon_{ex}^{A} - \epsilon_{ex}^{E}$) defines the Stokes or Frank-Condon shift, which is due to the lattice relaxation induced by the electronic excitation. Through this method one can extract the absorption and emission energies that are different with respect to the HOMO–LUMO gaps obtained for both the ground and excited state configurations; the latter are actually affected by the well known problem of the underestimation of the gap by all DFT calculations. Δ-SCF can yield good results when it is possible to simulate the excitations occupying just one-particle orbital; this immediately excludes the possibility of describing those excitations that are not easily described in terms of isolated single particle transitions. Furthermore, this method works in finite systems, but not in infinite ones. This is because the main contribution in Δ-SCF is the Hartree relaxation that for an extended system is negligible, leaving the system energy dominated by other contributions. Through the Δ-SCF method it is not possible to obtain the lineshape of the optical spectra that allow a direct comparison with experimental data, anyway, using the ground and excited state optimized geometry calculated within this scheme we can calculate the absorption and emission spectra, evaluating the imaginary part of the nanostructure dielectric function ($\epsilon_2(\omega)$) through first-principle calculations also beyond the one-particle approach. The emission spectrum is calculated, in a first approximation, as the time reversal of the absorption [58]. Strictly speaking, $\epsilon_2(\omega)$ corresponds to an absorption spectrum in a new structural geometry, the EXC geometry, with the electronic configuration of the GS. For the first time, we also consider the electron–hole interaction in the emission geometry. This different approach, where the many-body effects are combined with the study of the structural bond distortion at the Si-NC surface in the EXC, accounts both for the absorption and PL spectra. Starting from the calculated self-consistent electronic properties, the imaginary part of the dielectric function can be computed in the optical limit:

$$\epsilon_2^{\alpha}(\omega) = \frac{4\pi^2 e^2}{m^2\omega^2} \sum_{v,c} \frac{2}{V} \sum_{k} |\langle \psi_{c,k} | p_\alpha | \psi_{v,k} \rangle|^2 \times \delta[E_c(k) - E_v(k) - \hbar\omega], \qquad (7)$$

where $\alpha = (x, y, z)$, E_v and E_c denote the energies of the valence $\psi_{v,k}$ and conduction $\psi_{c,k}$ band states at a point k, and V is the supercell volume. From the calculated ϵ_2 the real part ϵ_1 is obtained by Kramers-Kronig transformation, after having attached a tail to ϵ_2 for energies greater than

15 eV following Ref. [59]. The optical-absorption coefficient

$$\alpha(\omega) = \frac{\omega}{nc}\epsilon_2(\omega) \tag{8}$$

is directly related to ϵ_2, thus ϵ_2 contains the necessary information about the absorption properties of the material.

2.2. The Many-Body perturbation theory

2.2.1. The GW approach

Underestimation of the electronic gaps in DFT calculations finds its origin not in a deficiency of the theory, but in the incorrect use we make of the Kohn-Sham equations. In fact, even if the Kohn-Sham equations have the form of single-particle Schrödinger-like equations, their eigenvalues are not the excited state energies. DFT is an exact theory for ground state properties, but there is no strict theoretical justification to use it to obtain excitation energies. It is important to note that, in the determination of the electronic band structure, we are dealing with energy differences between the system with N electrons and the system with $N-1$ (direct photoemission spectroscopy) or $N+1$ (inverse photoemission spectroscopy) electrons. It is hence natural to change over to the Green's function formalism [60]. The one-electron Green's function is defined as the probability amplitude that an electron or a hole, created at time t_1 and point r_1 will be detected at time t_2 and point r_2, that is, the probability amplitude of the electron (hole) propagation from r_1 to r_2 in the time interval $(t_2 - t_1)$. Because of this interpretation, the Green's function is also called the one-electron propagator. After a Fourier transform into the frequency domain, the Green's function G can be formally written as

$$G(\mathbf{r}_1, \mathbf{r}_2, \omega) = \sum_s \frac{\Psi_{0s}(\mathbf{r}_1)\Psi^+_{s0}(\mathbf{r}_2)}{\omega - \varepsilon_s - \mu + \mathrm{i}\delta} + \sum_{s'} \frac{\Psi^+_{0s'}(\mathbf{r}_2)\Psi_{s'0}(\mathbf{r}_1)}{\omega + \varepsilon_{s'} - \mu - \mathrm{i}\delta}, \tag{9}$$

where s and s' run over the $N+1$ and $N-1$ electrons excited states, $\Psi_{0s}(\mathbf{r})$ ($\Psi_{0s'}(\mathbf{r})$) is the expectation value of the creation operator of an electron at position $\mathbf{r}$ between the N particle ground state and the $N+1$ ($N-1$) particle excited state labelled by $s(s')$, and $\varepsilon_s(\varepsilon_{s'})$ is the energy of the $N+1$ ($N-1$) excited states; the infinitesimally small imaginary term $i\delta$ is needed for the convergence of the Fourier transform over the time variable. In expression (8) all the main ingredients of photoemission experiments appear, i.e. the photon energy ω and the energy differences between the N electron system and the $N \pm 1$ electron excited system. This explains why Green's functions are the main tools for band structure calculations: the excitation energies of a system are obtained by the determination of the poles of G. The Green's function cannot be calculated exactly for realistic systems. It obeys a Dyson equation of the form

$$G(1,2) = G_0(1,2) + \int d(34) G_0(1,3)\Sigma(3,4)G(4,2), \tag{10}$$

where G_0 is the non-interacting Green's function and Σ is the self-energy, a non-hermitian, non-local and energy dependent operator. In this framework, by introducing the equation of motion for G, we can obtain the so called quasiparticle equation:

$$\left[-\frac{\nabla^2}{2} + V_{\mathrm{ext}}(\mathbf{r}_1) + V_H(\mathbf{r}_1)\right]\phi_s(\mathbf{r}_1,\omega) + \int \mathrm{d}\mathbf{r}_2 \Sigma(\mathbf{r}_1,\mathbf{r}_2,\omega)\phi_s(\mathbf{r}_2,\omega) = \varepsilon_s(\omega)(\mathbf{r}_1,\omega). \tag{11}$$

The energies ε are the poles of the Green's function, so that the solution of Equation (11) directly gives the electronic band structure of the system. It is worth noticing that this equation reduces to the Hartree equations when $\Sigma = 0$, to the Hartree-Fock ones when $\Sigma = \mathrm{i}GV$, and to the Kohn-Sham equations when, instead of Σ, a local, hermitian and energy independent operator is taken: $\Sigma \to V_{xc}^{\mathrm{KS}}(r)$. This observation gives an *a posteriori* justification of the use of the Kohn-Sham equations to calculate the excitation energies; the qualitative agreement between DFT and experimental band structure comes from the fact that, somehow, the Kohn-Sham equations already carry a lot of physics, containing, at least approximately, exchange and correlation effects. In other words, $V_{xc}^{\mathrm{KS}}(r)$ is often a quite good approximation for the *true* self-energy Σ. In the same way in which in DFT we have to use an approximation for V_{xc}^{KS}, we now have to face the problem of finding a suitable expression for Σ. But at odds with the DFT case, within the Many-Body theory we have a closed set of equations, the Hedin Equations [61], which together with Equation (10) define implicitly the self-energy Σ:

$$\begin{aligned}
\Sigma(12) &= \mathrm{i}\int G(13)\Gamma(324)W(41)d(34);\\
W(12) &= v(12) + \int v(13)P(34)W(42)d(34);\\
P(12) &= -\mathrm{i}\int G(13)G(41)\Gamma(342)d(34);\\
\Gamma(123) &= \delta(12)\delta(13) + \int \frac{\delta\Sigma(12)}{\delta G(45)}G(46)G(75)\Gamma(673)d(4567),
\end{aligned} \tag{12}$$

where Γ is called vertex function, P is the polarization operator and W is the dynamically screened potential, $W = \varepsilon^{-1}v$.

In principle, the Hedin equations could be solved self-consistently, with an iterative procedure; in practice full self-consistency is never achieved for realistic systems. As a first step we can neglect the vertex corrections by assuming $\Gamma(123) = \delta(12)\delta(13)$; in this way the self-energy operator takes the form $\Sigma = \mathrm{i}GW$, which is the famous GW approximation [62,63]. At present computing quasiparticle energies within the GW approximation represents the most refined method for band structure calculation. The GW method can be applied to the calculation of the band structures of solids and surfaces, and to the determination of the energy levels of molecules and of atoms. In order to describe optical spectra, we have to take into account excited states of a completely different nature with respect to the ones involved in photoemission spectroscopy. In the latter, the final state of the system is charged, since one electron has been removed or added to it; in the former, instead, the system exchanging energy with the probe, is left in what is called a neutral excited state (see Figure 1c). Excitons are examples of neutral excited states that are commonly detected by optical spectroscopy; in a very schematic way excitons can be thought as bounded electron–hole states. The physical quantity which is directly connected to this spectrum is the macroscopic dielectric function ε_M that, following the derivation of Adler and Wiser [64], is given, in terms of the microscopic dielectric function, $\varepsilon_{G,G'}(q,\omega)$ by:

$$\varepsilon_M(\omega) = \lim_{q\to 0} \frac{1}{(\varepsilon(q,\omega))^{-1}_{G=0,G'=0}}. \tag{13}$$

The absorption spectrum is proportional to the imaginary part of the macroscopic dielectric function. Adopting the same level of approximation that we have introduced to obtain GW quasiparticle energies, i.e. neglecting the vertex correction by putting $\Gamma = \delta\delta$, we get the so called random phase approximation (RPA) for the dielectric matrix. Within this approximation, neglecting local field effects, the response to a longitudinal field, for $q \to 0$, is:

$$\varepsilon_M(\omega) = 1 - \lim_{q\to 0} v(q) \sum_{vc} \frac{|\langle v|\mathrm{e}^{-\mathrm{i}qr}|c\rangle|^2}{\omega - (\varepsilon_c - \varepsilon_v) - \mathrm{i}\eta}, \tag{14}$$

where $|v\rangle(|c\rangle)$ represent the valence (conduction) single particle state and $\varepsilon_v(\varepsilon_c)$ is its corresponding energy. From Equation (14) we see that the sum of all possible independent transitions gives rise to the spectra, its structures are located at quasiparticle energy differences and the line shape is determined by the matrix elements of $\mathrm{e}^{\mathrm{i}qr}$ between a valence state and a conduction state independently for each transition. In fact, in a non interacting quasiparticle scheme, the neutral excited state can be seen to be a sum of independent excitations of one electron from the valence to the conduction band. The spectrum may also be strongly dependent on local field effects, which must be included for highly anisotropic systems such as surfaces, nanowires and clusters. Even including local field effects the optical spectra of solids obtained within RPA are often not even in qualitative agreement with experiments. Due to some fortuitous cancellation of errors, DFT-RPA can sometimes yield very good agreement with experiment, but it should be stressed, however, that such good quantitative agreement is not generally found.

2.2.2. The Bethe–Salpeter equation

The vertex corrections cannot be completely neglected if we want to obtain optical spectra in agreement with experiments. Neglecting vertex corrections means to neglect the interaction between the hole and the electron that are formed within the polarization processes of the system. In fact putting $\Gamma = \delta\delta$ in the Hedin equation for P, leads to an expression for it, namely $P = -\mathrm{i}GG$, in which the hole and the electron propagators are independent of one another. In the description of absorption experiments, in which the excited electron remains in the sample, it is evident that the effects of the electron–hole interaction, i.e. the excitonic effects, cannot be neglected. The effects of the electron–hole interaction in the spectra can be included in MBPT through an effective two-body Hamiltonian, the so called excitonic Hamiltonian, which is the projection of the Bethe–Salpeter equation for the four-point modified polarizability ${}^4\overline{P}$

$$ {}^4\overline{P} = {}^4P_{IQP} + {}^4P_{IQP}K\,{}^4\overline{P} \tag{15} $$

in the transition space, i.e. into a basis made of couples of single quasiparticle states, usually labelled by band and wave vector indices. The kernel K of this integral equation contains an electron–hole exchange $\overline{v}$ and an electron–hole attraction $-W$ term. The excitonic Hamiltonian is not necessarily hermitian, however, in calculations just its hermitian part is usually taken into account, which is:

$$ H^{2p,\mathrm{exc}}_{(vck)(v'c'k')} = (E_{ck} - E_{vk'})\delta_{vv'}\delta_{cc'}\delta_{kk'} + 2v^{v'c'k'}_{vck} - W^{v'c'k'}_{vck}. \tag{16} $$

Here $E_{ck}, (E_{vk'})$ are the quasiparticle energies, calculated within the GW approximation, of the states (ck) and (vk'). In terms of the eigenvalues and eigenvectors of the excitonic Hamiltonian, namely:

$$ H^{2p,\mathrm{exc}}_{(n_1n_2)(n_3n_4)}A^{(n_3n_4)}_{\lambda} = E^{\mathrm{exc}}_{\lambda}A^{(n_1n_2)}_{\lambda} \tag{17} $$

the macroscopic dielectric function is:

$$\varepsilon_M(\omega) = 1 - \lim_{q\to 0} \nu(q) \sum_{\lambda} \frac{\left| \sum_{(n_1 n_2)} \langle n_1 | \mathrm{e}^{-\mathrm{i}qr} | n_2 \rangle A_{\lambda}^{(n_1 n_2)} \right|^2}{E_{\lambda}^{\mathrm{exc}} - \omega - \mathrm{i}\eta}, \tag{18}$$

where each label n_i represents a couple of band and wave vector indices. Comparing this formula with the RPA dielectric function Equation (14), we can see that in this case the dielectric function has poles at the eigenvalues of the excitonic Hamiltonian which are no longer differences of occupied and unoccupied quasiparticle state energies. This fact usually moves the position of the structures in the spectra to lower energies. Moreover, as we can see from Equation (17), each eigenstate of the excitonic Hamiltonian (17) is made by a sum of independent quasiparticle transitions; each transition contributes to it with a weight equal to $A_{\lambda}^{n_1 n_2}$. This mixing of independent transitions is present in the numerator of the dielectric function Equation (18) and its effect is to strongly modify the lineshape of the spectra. From Equation (18), we can see that to obtain the macroscopic dielectric function we need to diagonalize the excitonic Hamiltonian and to know the quasiparticle wave functions (in order to compute the dipole matrix elements present in the numerator). Usually in most ab-initio calculation, it is assumed that Kohn-Sham wave functions are a very good approximation to the quasiparticle ones, the calculation of W is limited to a static RPA screening, and the quasiparticle energies are computed within the GW approximation of the self energy. To summarize, in order to compute the excitonic spectra we need a well converged structure calculation, Kohn-Sham wave functions, quasiparticle energies within GW and the (statically) screened Coulomb interaction present in the excitonic Hamiltonian.

3. ZERO-DIMENSIONAL SYSTEMS

3.1. Free-standing silicon nanocrystals

In a Si zero-dimensional system the strong quantum confinement can increase the optical infrared gap of bulk Si and consequently shift the optical transition energies towards the visible range [65,66]. This is the reason for which silicon nanocrystals (Si-NCs) with a passivated surface are used as the natural trial model for theoretical simulations on Si based light emitting materials, such as porous Si or Si nanocrystals dispersed in a matrix. In this section we present a comprehensive analysis of the structural, electronic and optical properties of Si-NCs as a function of size, symmetry and surface passivation. We will also point out the main changes induced

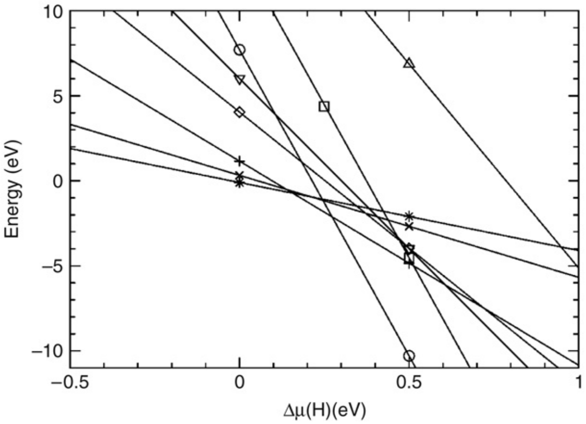

Figure 1 Calculated phase diagram of the hydrogen exposed Si_1 (stars), Si_2 (crosses $\times$), Si_5 (crosses $+$), Si_{10} (diamonds), Si_{14} (down triangles), Si_{29} ($\mathrm{Si}_{29}\mathrm{H}_{24}$ up triangles and $\mathrm{Si}_{29}\mathrm{H}_{36}$ squares) and Si_{35} (circles) clusters. The chemical potential of H, μ_{H}, is given with respect to molecular H.

by the nanocrystal excitation through a Δ-SCF (see Section 2.1.1) or a Many-Body perturbation theory approach (see Section 2.2).

3.1.1. Hydrogenated silicon nanocrystals

The starting point of our study is represented by Si-NCs whose surface is fully passivated by hydrogen atoms (H–Si-NC). The study of H–Si-NCs has been done within DFT, using a pseudopotential, plane-wave approach. All the calculations have been performed with the ABINIT code [67]. Norm-conserving, non-local Hamann-type pseudopotentials have been used. The Kohn-Sham wave functions have been expanded within a plane-wave basis set, choosing an energy cutoff of 32 Ry. The gradient-corrected Perdew–Burke–Ernzerhof (GGA-PBE) exchange–correlation functional has been used for both structural and electronic states calculations. The calculations performed are not spin-polarized. Each H–Si-NC has been embedded within a large cubic supercell, containing enough vacuum to make nanocrystal-nanocrystal interactions negligible [68]. The calculations for each cluster have been performed both in the ground and excited states as described in Section 2.1.1. The starting configuration for each cluster has been fixed with all Si atoms occupying the same position as in the bulk crystal, and passivating the surface with H atoms placed along the bulk crystal directions, at a distance determined by studying the SiH_4 molecule. It is worth pointing out that the starting H–Si-NC has T_d symmetry, which is kept during relaxation in the ground state configuration. Nevertheless for excited state configurations such symmetry is generally lost, due to the occupation of excited energy levels. We have first investigated the stability of Si nanoclusters exposed to an H atmosphere looking at their formation energies as a function of the size. The interest in this kind of calculation consists in understanding which clusters are more likely to form under different growth conditions. The stability of each cluster can be evaluated by calculating the formation enthalpy (F) through the formula:

$$F(Si_N H_M) = E_{\text{TOT}}(Si_N H_M) - N\mu_{\text{Si}} - M\mu_{\text{H}}, \tag{19}$$

where E_{TOT} is the ground-state total energy of a given $Si_N H_M$ cluster, and μ_{Si} and μ_{H} the chemical potentials for Si and H, respectively. The chemical potential for Si (μ_{Si}) is fixed at the bulk value, while the chemical potential for H changes to simulate different growth conditions. Figure 1 shows the phase diagram of the clusters with respect to different conditions in the H atmosphere. All the possible values for μ_{H} we have considered have been referred to the calculated molecular H chemical potential. Thus, $\Delta\mu_{\text{H}} = 0$ corresponds to the situation where the clusters are exposed to molecular H at $T = 0$ K, negative values of $\Delta\mu_{\text{H}}$ correspond to a H-poor atmosphere in the growth chamber, positive values of $\Delta\mu_{\text{H}}$ mean that also atomic H is available (H-rich conditions that exists when Si nanoclusters are formed by reducing $SiCl_4$ with metal hydrides [69] or by HF etching of bulk Si [70]). All the considered clusters are passivated by H atoms placed along the bulk Si crystal directions except for the $Si_{29}H_{24}$ structure, which is obtained from $Si_{29}H_{36}$ by simply removing 12 hydrogens. This induces a surface reconstruction with the formation of Si–Si dimers. As expected, the $Si_{29}H_{24}$ structure, when compared with $Si_{29}H_{36}$, is stabler in H-poor growth conditions (not visible in Figure 1), and less stable in an H-rich atmosphere. The exposure to molecular H or to an H-poor atmosphere gives higher stability to smaller clusters, while in H-rich growth conditions larger clusters are stabler. On increasing the H concentration (that is, moving from left to right in Figure 1) the stablest cluster changes from Si_1H_4 to Si_5H_{12} and, finally, to $Si_{35}H_{36}$.

After the stability analysis we have investigated the structural distortions caused by the relaxation of these structures in different electronic configurations. To qualitatively appreciate the structural changes, we have plotted in Figure 2 the relaxed structures of some of the considered clusters, both in ground- and excited-state configurations. The analysis of the structural properties reveals that the average Si–Si bond approaches the bulk bond length as the cluster dimension increases. In particular, moving from the center of the cluster toward the surface, a contraction of the outer Si shells is observed. The presence of a electron–hole pair in the clusters causes a strong deformation of the structures with respect to their ground-state configuration, and this is more evident for smaller systems and at the surface of the H–Si-NCs. This is what we expect, since for large clusters the charge density perturbation is distributed throughout the whole structure, and the effect it locally induces becomes less evident (small adjustments of

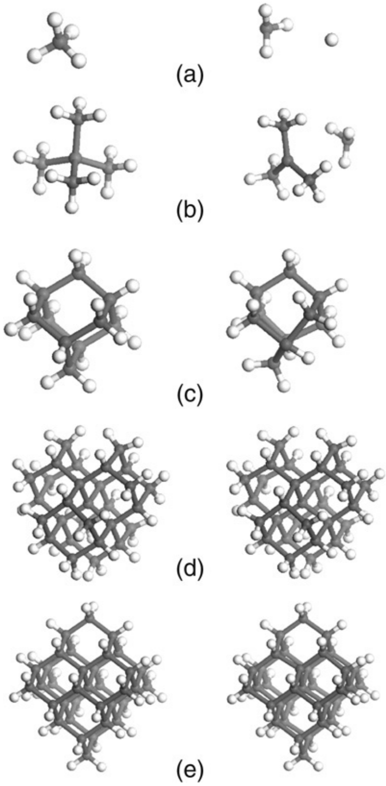

Figure 2 Structural models for the (a) Si_1H_4, (b) Si_5H_{12}, (c) $Si_{10}H_{16}$, (d) $Si_{29}H_{36}$ and (e) $Si_{35}H_{36}$ clusters at relaxed geometry in the ground- (left panels) and excited-state (right panels) configuration.

bonds and angles occur with respect to the ground state). Baierle et al. [17] and Allan et al. [29] stressed the importance of bond distortion at the Si-NC surface in the excited state in creating an intrinsic localized state responsible for the PL emission. The structural analysis is immediately reflected in the electronic structure. In Table 1 we report the calculated energy gaps for the Si_1H_4, Si_5H_{12}, $Si_{10}H_{16}$, $Si_{29}H_{36}$ and $Si_{35}H_{36}$ clusters in both the ground- and excited-state configurations.

One can note the expected decrease of the energy gap on increasing the cluster dimension and also that the excitation of the electron–hole pair causes a reduction of the energy gap, more significant as the cluster gets smaller. For small excited clusters the HOMO and LUMO become strongly localized in correspondence of the distortion, giving rise to defect-like states which reduce the gap. The distortion induced by the nanocluster excitation gives a possible explanation of the observed Stokes shift in these systems. The radiation absorption of the cluster in its ground state configuration induces a

Table 1 Calculated values for the ground (GS) and excited (EXC) state HOMO–LUMO energy gaps and for the absorption and emission energies calculated within the Δ-SCF approach for the considered H–Si-NC. All values are in eV

	Absorption	GS HOMO–LUMO gap	Emission	EXC HOMO–LUMO gap
Si_1H_4	8.76	7.93	0.38	1.84
Si_5H_{12}	6.09	5.75	0.42	0.46
$Si_{10}H_{16}$	4.81	4.71	0.41	0.55
$Si_{29}H_{36}$	3.65	3.58	2.29	2.44
$Si_{35}H_{36}$	3.56	3.50	2.64	2.74

Table 2 Stokes Shift values for hydrogenated Si clusters: present work versus theoretical data present in literature. All values are in eV

H–Si	Diameter	Theory					
Clusters	(nm)	This work	Ref. [75]		Ref. [76]	Ref. [79]	Ref. [80]
Si_1H_4	0.0	8.38					
Si_5H_{12}	0.45	5.67					
$Si_{10}H_{16}$	0.55	4.40	LDA	QMC			
$Si_{29}H_{36}$	0.9	1.35	0.69	1.0	2.92	0.22	0.70
$Si_{35}H_{36}$	1.1	0.92	0.57	0.8			1.67
$Si_{66}H_{64}$	1.3		0.50				
$Si_{87}H_{76}$	1.5		0.22		0.32		
$Si_{29}H_{24}$	0.8	0.84	0.34	0.4			1.17

transition between the HOMO and LUMO levels, which for all these clusters is optically allowed. Such a transition is followed by a cluster relaxation in the excited state configuration, giving rise to distorted geometries (as previously shown) and to new LUMO and HOMO, whose energy difference is smaller than that in the ground-state geometry. It is between these two last states that emission occurs, thus explaining the Stokes shift. It is also worth pointing out how such a shift changes as a function of the dimension. The distortion being smaller for larger clusters, it is expected that the Stokes shift decreases on increasing the dimension. This is shown in Tables 1 and 2: in the first the HOMO–LUMO gap for both the ground and excited states together with the Δ-SCF (see Section 2.1.1) absorption and emission energies are reported, while in the latter the derived Stokes shift compared with other theoretical data available in literature is shown.

A number of papers present in literature consider the HOMO–LUMO gaps of the ground and excited state as the proper absorption and emission energies; this leads to the wrong results, mostly for smaller clusters. In fact, from Table 1 it is clearly seen that the smaller the H–Si-NC, the greater is the difference between the absorption and HOMO–LUMO ground-state

(GS) gap and between emission and HOMO–LUMO excited-state (EXC) gap (Delerue et al. [71] have pointed out that for clusters with diameter larger than 1.2 nm there is a cancellation between the self-energy correction and Coulomb terms: thus the lowest excitonic energy is "correctly" predicted by the single-particle band gap. In our calculations, on going from smaller to larger clusters the difference between the HOMO–LUMO gap in the ground state and the absorption gap becomes smaller). In conclusion, trying to deduce the Stokes shift simply from the HOMO–LUMO gaps leads to errors, especially for small clusters. In particular, the GS HOMO–LUMO gap tends to be smaller than the absorption energy, while the EXC HOMO–LUMO gap tends to be larger than the emission energy.

When comparing our results for the ground state with other DFT calculations we note that there is, in general, a good agreement between them. Actually, for Si_1H_4, Grossman et al. [72] have found 7.8 eV for the HOMO–LUMO gap while Onida and Andreoni [73] have obtained 8.1 eV; these values have to be compared with our calculated 7.93 eV result. At the same time for the $Si_{29}H_{36}$ cluster, our 3.65 eV calculated absorption gap is in nice agreement with the 3.6 eV [74] obtained with the same method both by Puzder et al. [75] and Franceschetti et al. [76]. It is worth mentioning that our results for the absorption gaps of the Si_1H_4 (8.76 eV) and Si_5H_{12} (6.09 eV) clusters agree quite well with the experimental results of Itoh et al. [77]. They have found excitation energies of 8.8 eV and 6.5 eV respectively. GW calculations find an absorption gap of 9.0 eV for Si_1H_4 [78], while LDA results by Hirao et al. [79] show a HOMO–LUMO gap of 4.62 eV and 3.32 eV for $Si_{10}H_{16}$ and $Si_{29}H_{36}$, respectively. All these data are in very good agreement with ours. Regarding the Stokes shift, very little data exist in literature as Table 2 shows [75,76,79,80], and, in particular for really small H–Si-NCs (from Si_1H_4 to $Si_{10}H_{16}$), no data exists at all. The dependence of the Stokes shift on the H–Si-NC size qualitatively agrees with the calculations of Puzder et al. [75] and Franceschetti et al. [76]. Nevertheless, it is seen that the data for the $Si_{29}H_{36}$ cluster show a large spread, which can be attributed to the different approaches used. Experimentally, very few measurements exist on hydrogenated Si clusters and what emerges is a decreasing of the Stokes shift value with increasing cluster dimension [81,82]. Concerning the optical properties of the hydrogenated clusters and the comparison between different ab-initio methods, Figure 3 shows the absorption spectra of the Si_5H_{12} cluster calculated using different DFT-based methods [67]. In particular we have performed an LDA calculation (RPA-LDA, neglecting Local Fields), we have calculated the self-energy corrections within the GW method (RPA-GW), then the excitonic effects have been included, both performing a time dependent local density approximation (TDLDA) calculation and a fully excitonic calculation through the Bethe–Salpeter equation (BSE). As usual we note an underestimation of the optical gap in the RPA-LDA scheme with respect to the experimental value (6.5 eV) [77].

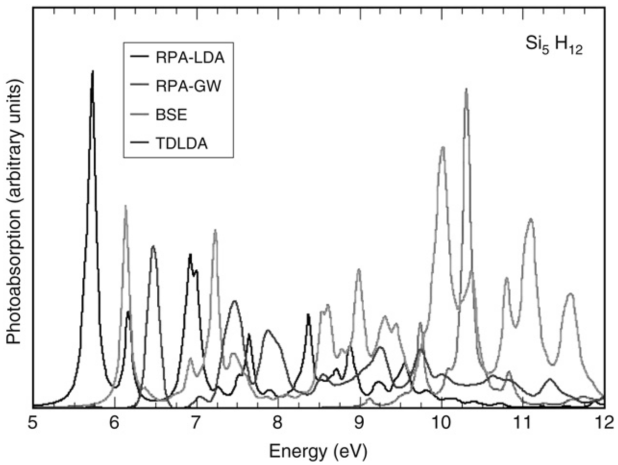

Figure 3 Absorption spectra of the Si_5H_{12} cluster calculated using different DFT based methods: LDA-RPA black (black), GW-RPA red (dark gray), BSE violet (light gray), TDLDA blue (light black).

Concerning the RPA-GW method, the main result is a huge opening of the optical gap. The effects of the electron–hole interaction on the optical properties (BSE result) is also quite large, the excitonic binding energy is of the order of 3 eV, resulting in a sort of compensation with respect to the GW opening. Interestingly the BSE and TDLDA results are similar regarding the absorption onset and in agreement with the experimental result.

3.1.2. Oxidized silicon nanocrystals

Recent experimental data have shown strong evidence that the surface changes of Si-NCs exposed to O produce a substantial impact on their optoelectronics properties, thus oxidation at the surface has to be taken into account. In this section we will analyze the structural, electronic and optical properties of oxidized Si-NCs, discussing the effects of the different Si/O bond geometries and of size, and considering the specific case of multiple O passivation with silanone-like Si=O bonds [20–22]. Different theoretical approaches have been used, each of them based on the DFT in a plane-wave pseudopotential scheme. In some cases calculations both in ground and excited state electronic and/or structural configurations have been performed, through the Δ-SCF method (see Section 2.1.1) [68,75,76, 83] or going beyond the DFT using the Many-Body perturbation theory (see Section 2.2). The first set of results concerns the ground state study of isolated oxidized nanocrystals in the DFT limit. As a first approach, two different codes have been used: FHI98MD [84] and CASTEP [85–87]. In the first case the electron–ion interaction has been described via norm-conserving pseudopotentials [88,89]; in the second case via ultrasoft

Table 3 List of the studied clusters, classified by the type of surface passivation (rows) and by the core size (columns). Full-H stands for a passivation by H atoms only; Si–O–Si by H atoms plus O in the bridge geometry; Si=O by H atoms plus O in the double-bond geometry; and Si–O–Si + Si=O by H atoms plus O both in the bridge- and double-bond geometry

Bond/size	0.5 nm	0.7 nm	1.0 nm
full-H	$Si_{10}H_{16}$	$Si_{14}H_{20}$ $Si_{12}H_{16}$	$Si_{35}H_{36}$
Si–O–Si	$Si_9H_{14}{>}O$	$Si_{14}H_{20}{>}O_2$ $Si_{13}H_{18}{>}O$ $Si_{12}H_{16}{>}O_2$	$Si_{34}H_{34}{>}O$
Si=O	$Si_{10}H_{14}{=}O$ $Si_{10}H_{12}{=}O_2$ $Si_{10}H_{10}{=}O_3$ $Si_{10}H_8{=}O_4$ $Si_{10}H_6{=}O_5$ $Si_{10}H_4{=}O_6$	$Si_{14}H_{18}{=}O$ $Si_{14}H_{16}{=}O_2$ $Si_{14}H_{14}{=}O_3$ $Si_{14}H_{12}{=}O_4$ $Si_{14}H_8{=}O_6$ $Si_{13}H_{18}{=}O$ $Si_{12}H_{16}{=}O_2$	$Si_{35}H_{34}{=}O$ $Si_{35}H_{32}{=}O_2$ $Si_{35}H_{30}{=}O_3$ $Si_{35}H_{28}{=}O_4$ $Si_{35}H_{24}{=}O_6$
Si–O–Si+Si=O		$Si_{13}H_{16}{>}O{=}O$	

pseudopotentials [90]. Different cutoffs for the wave-function kinetic energy have thus been adopted: 680 eV in FHI98MD and 380 eV in CASTEP. The structural relaxation has been achieved using either code, while the optoelectronic properties at relaxed geometry have been determined with CASTEP. Five classes of clusters have been considered: one with a mean core diameter of 1.0 nm (Si_{35}-core based), three with a mean core diameter of 0.7 nm (Si_{14}-, Si_{13}-, and Si_{12}-core based), and one with a mean core diameter of 0.5 nm (Si_{10}-core based). Two types of Si/O bond geometry have been extensively studied: the Si–O–Si bridge-bond and the silanone-like (Si=O) bond. The oxidized clusters have been built up substituting H and/or Si atoms of the initial H-capped structures (see previous subsection) with O atoms. In particular the Si=O bonds have been obtained by replacing, with one O atom, pairs of H atoms bonded to the same Si atom. At each O introduction we have studied the different possible configurations of the surface, i.e., different relative locations for the Si=O bonds, playing with the symmetry of the systems and with the possible O-double-bond sites available for each cluster. All the systems, classified by the type of Si/O bond and Si-core size, are listed in Table 3. All the clusters have been relaxed by total-energy minimization. The relaxation produces structural changes with respect to the initial geometry which strongly depend on the type of surface passivation. A full-H saturation, as expected, leaves the initial bulk-like structure of the Si core unchanged. When Si=O bonds are added at the surface, the modification of the Si core is very limited. In the relaxed geometry the Si=O bond orientation is always perpendicular to the surface,

Table 4 Energy gap values for the Si-NC with mean diameter of 0.7 nm at relaxed geometry

Si-NC structures	Energy gap (eV)
$Si_{14}H_{20}$	4.1
$Si_{14}H_{20}{>}O_2$	4.0
$Si_{14}H_{18}{=}O$	2.4
$Si_{14}H_{16}{=}O_2$	2.3
$Si_{14}H_{14}{=}O_3$	2.2
$Si_{14}H_{12}{=}O_4$	2.1
$Si_{14}H_8{=}O_6$	2.1
$Si_{13}H_{18}{>}O$	3.7
$Si_{13}H_{18}{=}O$	2.4
$Si_{13}H_{16}{>}O{=}O$	2.2
$Si_{12}H_{16}$	3.8
$Si_{12}H_{16}{>}O_2$	3.6
$Si_{12}H_{16}{=}O_2$	2.3

i.e., in the same plane of the two nearest Si–Si bonds, along the bisecting line. This final geometry, which does not depend on the number of Si=O bonds present at the surface, seems to be supported by an X-ray absorption fine-structure study on the interface between Si and SiO_2 [91], which reveals a strong Si/O bonding oriented preferentially closer to the surface normal. On the other hand, the introduction of the O atoms in the bridge configuration produces an appreciable modification of the Si core in the vicinity of the bond position, especially when the O are placed in between the first nearest-neighbor Si atoms ($Si_{14}H_{20}{>}O_2$). The angle and bond-length variations go towards a final geometry for the Si–O–Si close to the quartz one.

Considering the large number of studied cases, for more clarity, we will first focus on clusters with the same Si-core size (core diameter of 0.7 nm) and finally discuss the role played by size.

Concerning the electronic properties we see from Table 4 that the energy band gap (E_g) changes as a function of the Si/O bond type at the cluster surface. In comparison with the result for $Si_{14}H_{20}$ we see, for the Si–O–Si bridge cases, a very small reduction in $Si_{14}H_{20}{>}O_2$ and a more evident one in $Si_{12}H_{16}{>}O_2$. Only for $Si_{14}H_{16}{=}O_2$ a huge reduction of the energy gap happen. In this Si-NC, as just shown, the structural variations are very small; thus the reduction is practically due only to the presence of new Si=O-related states which strongly modify the band edges. This view is confirmed by the analysis of the distribution of HOMO and LUMO states (see Figure 4). It is clear from this figure how, only in the Si=O case, both HOMO and LUMO are localized around the O of the Si=O bonds; while, for the two Si–O–Si bridge cases, only part of the LUMO is around it, HOMO, in fact, maintains the character of the H-covered structure located along peculiar Si–Si bonds of the

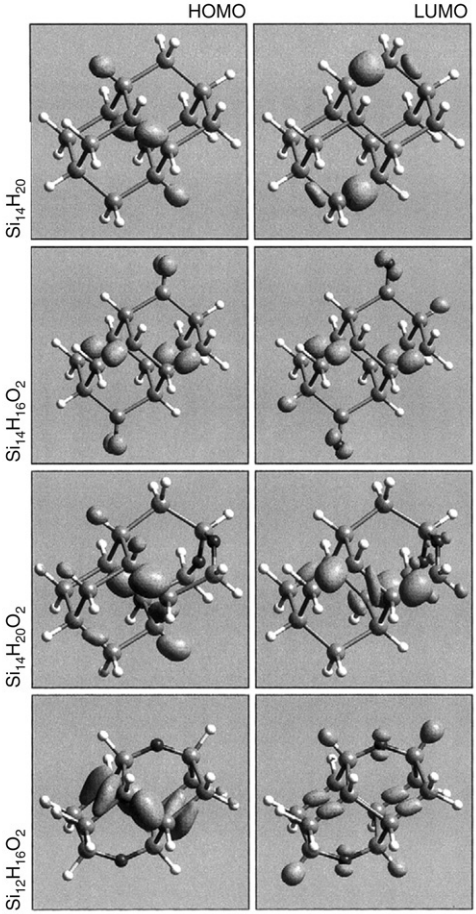

Figure 4 Isosurfaces of the square modulus of the HOMO and LUMO for $Si_{14}H_{20}$, $Si_{14}H_{16}{=}O_2$, $Si_{14}H_{20}{>}O_2$, $Si_{12}H_{16}{>}O_2$ at the optimized geometry. The isosurfaces are plotted at 50% of their maximum amplitude.

Si skeleton. The electronic properties are instead less affected by the addition of Si–O–Si bridges; this is due to the HOMO state that, as already said, maintains its hydrogenated like character. The E_g is reduced, but not as in the Si=O bond cases. Also when the addition of O atoms implies the substitution of some atoms of the Si core, miming the attack of O towards the inner structure, the reduction is still of the order of a few tenths of eV. The addition of both types of bonds on the same structure ($Si_{13}H_{16}{>}O{=}O$) produces a final E_g value strongly red-shifted, very close to the corresponding results for the double-bond case ($Si_{13}H_{18}{=}O$). This means that the electronic, and consequently the optical, behavior of the clusters is mainly characterized by the double bonded O.

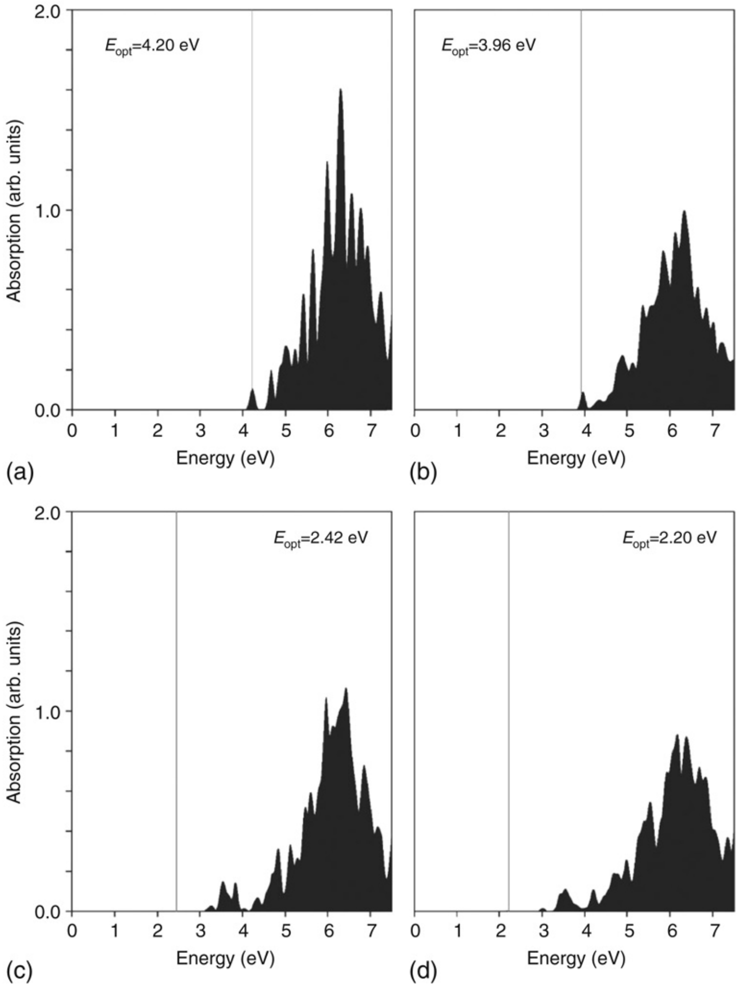

Figure 5 Calculated absorption spectra for four different Si clusters: (a) $Si_{14}H_{20}$, (b) $Si_{14}H_{20}{>}O_2$, (c) $Si_{14}H_{18}{=}O$, (d)$Si_{13}H_{16}{>}O{=}O$ (an artificial Gaussian smearing of 0.05 eV has been applied).

The results of the optical properties reflect the electronic ones. In Figure 5 we show, as an example, the absorption spectra of some of the clusters. In the presence of the Si=O bond, the first transitions in an absorption process involve the Si–O interface states only, while for the Si–O–Si bridge bonds the first transitions are still influenced by the crystalline Si structure. This results in a strong red-shift of the absorption onset when the double bonded O is present (compare Figures 5(a) and 5(c), whereas O in the bridge geometry slightly modifies the absorption behavior (Figure 5(b)). With the simultaneous presence of O in the double and bridge bond configuration

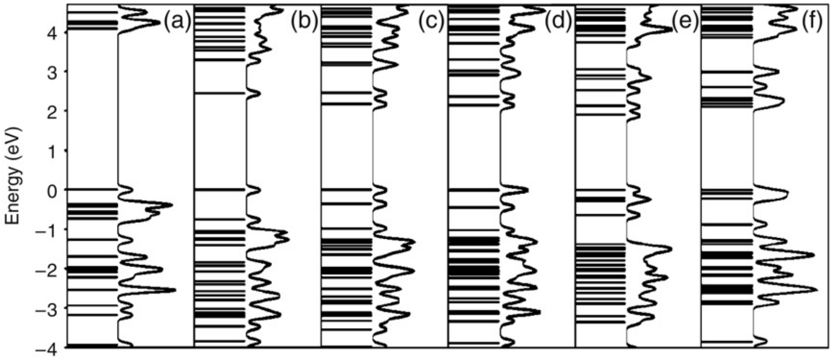

Figure 6 Energy levels at Γ and TDOS for $\mathrm{Si_{14}H}_n$-O_m clusters. (a) $m = 0$, (b) $m = 1$, (c) $m = 2$, (d) $m = 3$, (e) $m = 4$, and (f) $m = 6$.

(Figure 5(d)) the absorption onset is set exactly at the energy of the transition between HOMO and LUMO (which are Si=O related states), showing that the first optical transitions in this case are mainly due to the Si=O presence. In general it emerges that for all the oxidized clusters the absorption onsets correspond exactly to the HOMO–LUMO allowed transition.

In order to ideally simulate the air exposure of the crystallites, as for example in porous Si samples, the number of O atoms in the Si=O geometry has been progressively increased at the cluster surface. There is no linear E_g dependence on Si=O numbers; the more Si=O bonds are drawn at the surface the more new O-related states approach the band edges and accumulate there. The E_g arrives at a sort of saturation limit; only one Si=O bond is enough to abruptly reduce the E_g (in the $\mathrm{Si_{14}}$-core-based case the E_g is reduced by 1.5 eV with the introduction of the first O) and this reduction necessarily has a chemical character. This red-shift weakly increases, increasing the number of Si=O bonds at the surface. This behavior is clearly shown in Figure 6, where, as an example, the energy levels and total density of states (TDOS) for the $\mathrm{Si_{14}H}_n$=O_m clusters are reported. For one Si=O bond we see one new localized state at the top of the valence band and one at the bottom of the conduction band, within the gap relative to the fully hydrogenated case. For two Si=O bonds we clearly distinguish two states at both band edges; for three, four, and six they become three, four, and six. Thus, increasing the number of Si=O bonds at the surface causes a directly proportional number of localized states, which pile up at the band edges. When the Si=O bonds are placed in equivalent relative positions a level degeneracy is induced on the states within the gap.

Another way of seeing the E_g behavior as a function of the Si=O bond number is to plot the relative red-shift with respect to the full-H E_g, as done in Figure 7. The zeros corresponds to the full-H case. A saturation tendency is clearly displayed in all the three cases; this model with multiple Si=O

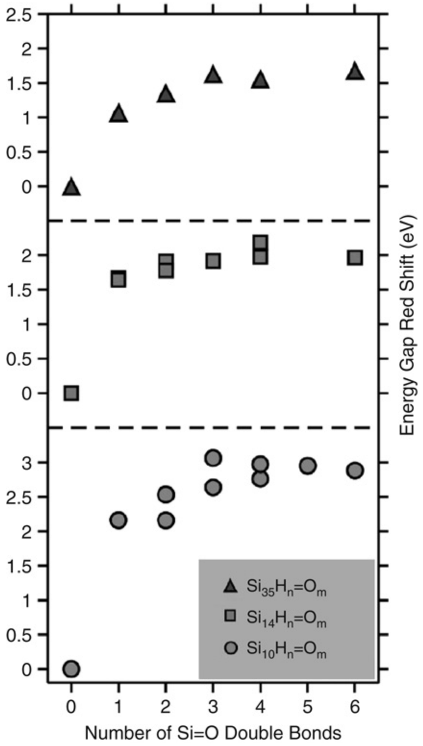

Figure 7 Energy-gap red-shift for three different classes of clusters as a function of the number of Si=O bonds at the surface. Circles: $Si_{10}H_n$-O_m; squares: $Si_{14}H_n$-O_m and triangles: $Si_{35}H_n$-O_m. The red-shift is calculated as the difference between a specific surface configuration and the corresponding fully hydrogenated one (thus the zero in the plot for each class stands for the nonoxidized case $m = 0$).

bonds at the surface reproduces, amazingly well, the experimental outcomes on the optical behavior of intentionally oxidized crystallites in porous Si samples [18]. Actually, in their experiment, Wolkin et al. [18] measure the PL behavior of freshly etched porous Si samples made of crystallites of various sizes. These spectra show a large PL red-shift when the samples are exposed to open air. A great amount of the reduction is achieved in the few first seconds of exposure [18] when the oxidation has just begun and it is supposed that only a few O atoms have attacked the surface. This means that our hydrogenated clusters with some Si–H bonds replaced by Si/O bonds can be a reasonable model for this type of samples at the beginning of the exposure [22].

Now, to go beyond the ground state properties of our oxidized Si-NC we focus on a smaller group of structures. In the Δ-SCF scheme, two classes of systems have been studied, based on the Si_{10} and the Si_{29} core based nanoclusters [92]. Through a formation energy calculation, the bridge

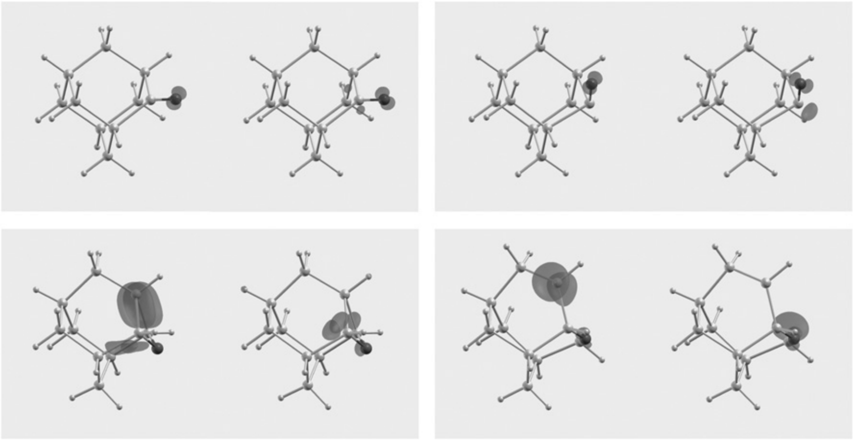

Figure 8 Calculated HOMO (first and third column) and LUMO (second and fourth column) charge density for $Si_{10}H_{14}O$-double (top panel), $Si_{10}H_{14}O$-bridge (bottom panel) for the ground (first and second column) and excited (third and fourth column) states; the structures shown are the relaxed ones.

bonded configuration has been demonstrated to lead to the stablest isomer configuration by Gatti and Onida [93,94]. The geometries for the $Si_{10}H_{14}{>}O$ (bridge bond) and the $Si_{10}H_{14}{=}O$ (double bond) are shown in Figure 8, both for the ground and excited state electronic configuration. Full relaxation with respect to the atomic positions is performed within the DFT limit for all systems, both in the ground and excited configurations, using a norm conserving LDA pseudopotential with an energy cutoff of 60 Ry [95]. The ionic relaxation has produced structural changes with respect to the initial geometry which strongly depend on the type of surface termination. In the case of $Si_{10}H_{14}{=}O$, the changes are mainly localized near the O atom, in particular the angle between the double bonded O and its linked Si atom is modified (see Figure 8). In the bridge structure, instead, the deformation is localized around the Si–O–Si bond producing a considerable strain in the Si–Si dimer distances [94]. Similar results are obtained for the larger Si_{29} based clusters. The only difference is that now the distortion induced by the promotion of an electron is smaller, as expected, since for larger clusters the charge density perturbation is distributed throughout the structure, and the locally induced effect becomes less evident. These structural changes are reflected in the electronic and optical properties.

In Figure 8 we also show the HOMO and LUMO charge density for the systems studied. It is evident that in all cases these states are mainly localized in the distorted region of the cluster.

In Table 5 absorption and emission gaps are reported: the red-shift of the emission gap with respect to the absorption is less evident for the case of the cluster with the double-bonded O (see the Stokes shift values); the same

Table 5 Stokes shift, i.e. difference between absorption and emission energy gaps calculated as total energy differences within the Δ-SCF approach. All values are in eV

	Stokes shift	Absorption	Emission
$Si_{10}H_{14}{=}O$	1.70	2.79	1.09
$Si_{10}H_{14}{>}O$	3.90	4.03	0.13
$Si_{29}H_{34}{=}O$	1.65	2.82	1.17
$Si_{29}H_{34}{>}O$	0.28	3.29	3.01

Table 6 Absorption and emission gaps calculated as HOMO–LUMO differences within DFT–LDA and GW approaches and as the lowest excitation energy when excitonic and local field effects (BS-LF) are included. In the last column the Stokes shift calculated in the BS-LF approximation is reported. In parenthesis the lowest dark transitions (when present) are also given. All values are in eV

	Absorption			Emission			Stokes Shift
	LDA	GW	BS-LF	LDA	GW	BS-LF	
$Si_{10}H_{14}{=}O$	3.3 (2.5)	7.3 (6.5)	3.7 (2.7)	0.8	4.6	1.0	2.7
$Si_{10}H_{14}{>}O$	3.4	7.6	4.0	0.1	3.5	1.5	2.5
$Si_{29}H_{34}{=}O$	2.5	6.0	3.7 (3.1)	0.9	4.1	1.2	2.5
$Si_{29}H_{34}{>}O$	2.3	4.8	2.3	0.4	3.0	2.2 (0.3)	0.1

can be observed for the double-bonded $Si_{29}H_{34}O$. The O double-bonded case hence seems almost size independent: actually, the presence of this kind of bond creates localized states within the gap that are not affected by quantum confinement as previously predicted by Luppi and Ossicini [22].

Our aim is to allow a direct comparison between experimental data and theoretical results, thus we have calculated not only the transition energies within the Δ-SCF approach but also, directly, the absorption and emission optical spectra. Actually, for both the calculated GS and EXC optimized geometry, we have evaluated the optical response $\mathrm{Im}(\varepsilon_{nc}(\omega))$ (the imaginary part of the nanocrystal dielectric function) through first-principles calculations also beyond the one-particle approach. We have considered the self-energy corrections by means of the GW method and the excitonic effects through the solution of the Bethe–Salpeter (BS) equation. The effect of the local fields (LF) is also included, to take into account the inhomogeneity of the systems. In Table 6, the calculated gaps (as energy differences between LUMO and HOMO) at different levels of approximation are reported for both the Si_{10} and Si_{29} based nanocrystals. The main result, common to absorption and emission, is the opening of the LDA band-gap with the GW corrections by amounts weakly dependent on the surface termination, but much larger than the corresponding 0.6 eV of the Si bulk case. Looking at the BS-LF calculations, we note a sort of compensation (more evident in the GS than in the EXC) of the self-energy and excitonic contributions:

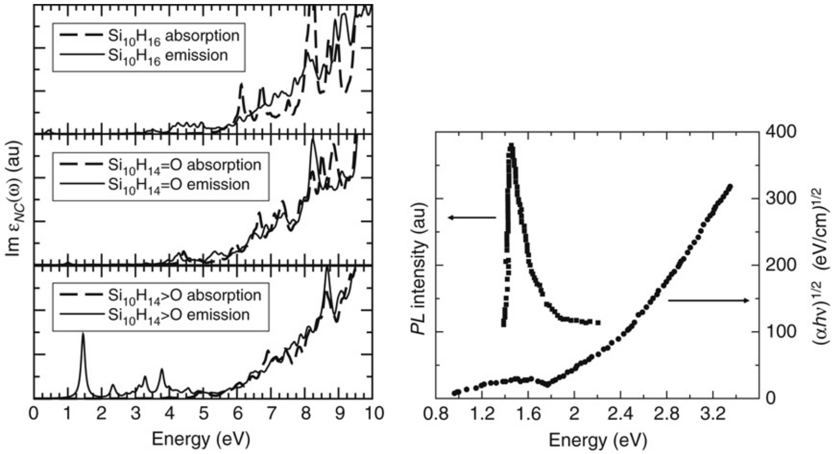

Figure 9 Emission (solid line) and absorption (dashed line) spectra: imaginary part of the dielectric function for the three considered Si-NCs. On the left: $Si_{10}H_{16}$ (top panel), $Si_{10}H_{14}{=}O$ (central panel) and $Si_{10}H_{14}{>}O$ (bottom panel). On the right: experimental results for emission (curve on the left) and absorption (on the right) by [96].

the BS-LF values remain similar to the LDA ones. The only exception are the BS-LF calculations for the excited state geometries of the clusters with Si–O–Si bridge bonds at the surface. Concerning the differences between the values of the Stokes shifts calculated through the Δ-SCF approach in Table 5 or through the MBPT in Table 6; these are essentially due to the ability or not of the two methods to distinguish dark transitions. In the MBPT the oscillator strengths of each transition are known, while the Δ-SCF approach only gives the possibility of finding the energy of the first excitation: if this transition is dark (and the Δ-SCF approach does not give this information) the associated energy is not the real optical gap. A clearer insight on the MBPT results is offered by Figure 9 (left panel), where the calculated absorption and emission spectra for all the oxidized Si_{10} based clusters are depicted and compared with the fully hydrogenated cluster. Self-energy, local-field and excitonic effects (BS-LF) are fully taken into account.

Concerning the absorption spectra (Figure 9, dashed lines), all three cases show a similar smooth increase in the absorption features. The situation is different for the emission related spectra (Figure 9, solid lines). Here, whereas the situation remain similar for the fully hydrogenated $Si_{10}H_{16}$ (top panel) cluster and for the $Si_{10}H_{14}{=}O$ (central panel) cluster, in the case of a Si–O–Si bridge bond (Figure 9 (bottom panel)) an important excitonic peak, separated from the rest of the spectrum, is evident at 1.5 eV. Actually bound excitons are also present in the fully hydrogenated (at 0.4 eV) and in the $Si_{10}H_{14}{=}O$ (at 1.0 eV) clusters, nevertheless, the related transitions are almost dark and the emission intensity is very low. Only in the case of

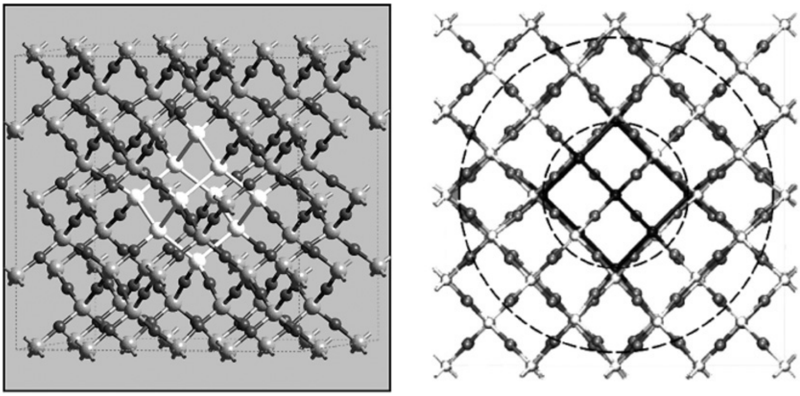

Figure 10 Stick and ball pictures of the final optimized structure of Si_{10} in SiO_2. The dark gray spheres represent O atoms, light gray Si atoms and white the Si atoms of the nanocrystal.

the Si–O–Si bridge bond does a clear PL peak appear thanks to the strong oscillator strength of the related transition. The right panel of Figure 9 shows the experimental absorption and emission spectra measured by Ma et al. [96] for Si-nanodots embedded in a SiO_2 matrix. A strong PL peak appears around 1.5 eV. Comparison of the experimental spectra with our results suggest that the presence of a Si–O–Si bridge bond at the surface of Si-NCs and the relative deformation localized around the Si–O–Si bond can explain the nature of luminescence in Si nanocrystallites: only in this case the presence of an excitonic peak in the emission related spectra, red-shifted with respect to the absorption onset, provides an explanation for both the observed Stokes shift and the visible PL in Si-NCs. Similar results have been obtained in the case of Si_{29}-based clusters. Only in the case of O in the bridge position there is a cage distortion at the interface that allows the presence of significant emission features in the optical region.

3.2. Silicon nanocrystals embedded in a SiO_2 matrix

In this section our goal is to build a simple model to study the properties of Si nanocrystals embedded in a SiO_2 matrix from a theoretical point of view [20]. We wanted, at the same time, two fundamental qualities: a Si skeleton with a crystalline behavior for simulating the Si-NC and the simplest Si–SiO_2 interface, with the minimum number of dangling bonds or defects. For these reasons we have started with a cubic cell ($l = 1.432$ nm) of SiO_2 beta-cristobalite (BC), which is well known as having one of the simplest Si/SiO_2 interfaces because of its diamond-like structure [97]. We get, repeating twice along each cartesian axis, the unit cell of SiO_2 BC. Then we obtained a small cluster by simply deleting some O atoms of the SiO_2 matrix and linking together the Si atoms left with dangling bonds, as shown in Figure 10.

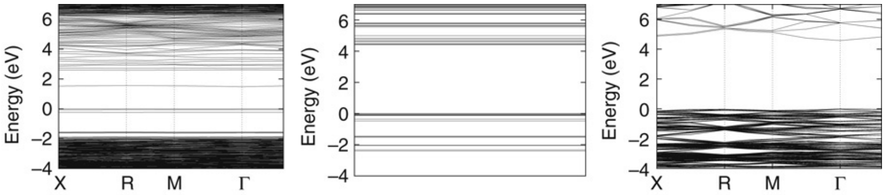

Figure 11 Band structure along high symmetry points of the BZ for the Si_{10} cluster in SiO_2 (left panel) compared with the band structure of beta-cristobalite bulk (right panel) and the energy levels at the Γ point for the isolated $\mathrm{Si}_{10}\mathrm{H}_{16}$ cluster (central panel).

In this way we have built an initial supercell of 64 Si and 116 O atoms with 10 Si bonded together to form a small crystalline skeleton (T_d interstitial symmetry) with a very highly strained bond length with respect to the bulk case: 3.1 Å. We have performed a molecular dynamics simulation through a Car-Parrinello approach to fully relax the system. Electronic and optical calculations have been performed with a 30 Ry energy cutoff. Figure 10 shows the final relaxed supercell structure after the geometry optimization for the Si-NC (Si_{10}) in SiO_2. Looking at the cluster behavior we find that the skeleton is still crystalline-like (diamond) with a Si–Si bond length of 2.67 Å; this means a strain of 14% with respect to the bulk case. This rearrangement causes a complex deformation of the SiO_2 matrix around the cluster, both in bond lengths and angles. Nevertheless the deformation does not affect the whole SiO_2 matrix. Actually it is still possible to find a good BC crystalline structure, in terms of angles and bond length, at a distance from the cluster atoms of 0.8–0.9 nm. This means that the cluster is surrounded by a cap-shell of stressed SiO_2 BC, with a thickness of about 1 nm, which progressively goes towards a pure crystalline BC. We have in summary a three-region picture: (i) a strained Si-NC, (ii) a cap shell, with a thickness of 0.8–0.9 nm, of distorted SiO_2, and (iii) an unstressed crystalline SiO_2. These three regions are highlighted in Figure 10 (right panel). Despite the simplicity of the model this picture is in close agreement with what has emerged from energy-filtered transmission electron microscopy (EFTMEM) and x-ray measurements on Si nanocrystals in SiO_2 samples produced by PECVD [98,99], and fairly well with recent theoretical results [100,101].

This view is also supported by the analysis of the electronic properties reported in Figure 11. The calculated E_g for the cluster in the matrix is 1.48 eV, which must be compared with the value of 4.58 eV for the E_g of BC SiO_2 (bulk) [102].

The strong reduction is caused by the presence, at the valence and conduction band edges, of confined, flat, states completely related to the Si_{10}–SiO_2 interface. Actually neither the isolated, H-passivated cluster (see Figure 11, central panel), nor the pure SiO_2 matrix (see Figure 11, right panel) show these states, whereas deep inside the valence and conduction

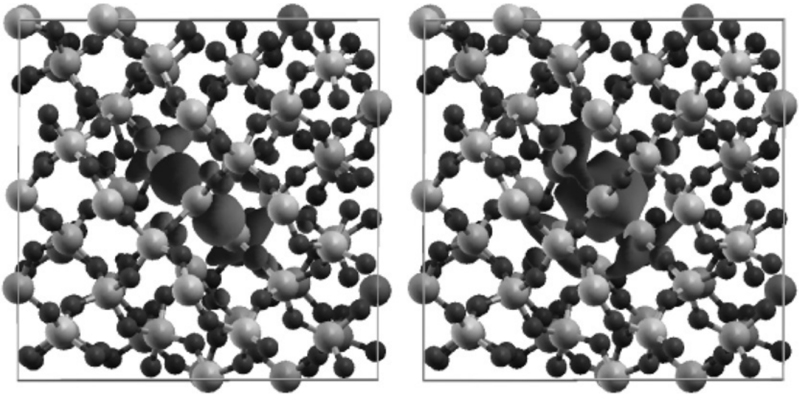

Figure 12 Isosurfaces at fixed value (10% of max. amplitude) of the square modulus of the highest occupied (HOMO) and lowest unoccupied (LUMO) Kohn-Sham orbitals for the Si_{10} cluster in the SiO_2 matrix.

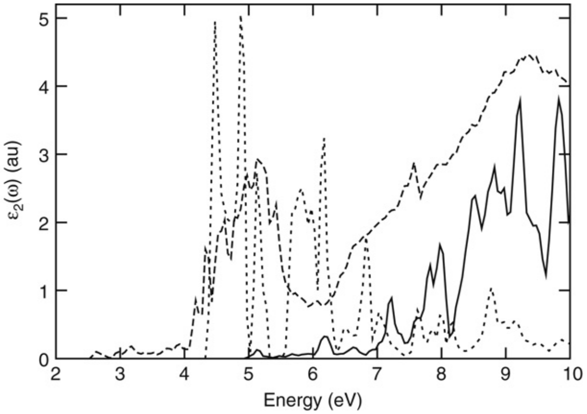

Figure 13 Imaginary part of the dielectric function for the Si_{10} cluster in BC matrix (dashed line) compared with that of an isolated, hydrogenated Si_{10} cluster (dotted line) and of the beta-cristobalite bulk (solid line).

bands the more k-dispersed states related to the SiO_2 matrix are still present. In Figure 12 the HOMO and LUMO isosurfaces at the fixed value of 10% are reported; we clearly see that the distribution is totally confined in the Si-NC region with some weight on the interface O atoms. These cluster-related states cause strong absorption features in the optical region, as witnessed from Figure 13 where absorption spectra of the isolated Si_{10} cluster, of the pure matrix and of the composed system are reported. These features are entirely new, they do not exist for the isolated cluster or for the pure matrix, and so have to be due to the nature of the interface region. The origin of the

PL observed in the red optical region for Si-NC immersed in a SiO_2 matrix can then be found in the properties of this interface. Our result, concerning the role of both Si-NC and the interface Si–O region with respect to the absorption process, is in close agreement with X-ray absorption fine structure measurements [98] that indicate the presence of an intermediate region between the Si-NC and the SiO_2 matrix, about 1 nm thick, that participates in the light emission process.

3.3. Doped silicon nanocrystals

In recent years we have performed several theoretical studies that also consider the single and simultaneous doping of Si-NCs with n- and p-type impurities [103–111].

Here we resume our results for single doping, and we report on a comprehensive investigation of the structural, electronic and optical properties of B and P simultaneously doped Si-nanocrystals using ab-initio Density Functional Theory. Our results are obtained in a plane-wave pseudopotential DFT scheme, using the ESPRESSO package [95]. Full relaxation with respect to the atomic positions is performed for all systems. All the DFT calculations are performed within the generalized gradient approximation using Vanderbilt ultrasoft pseudopotentials [112] for both the determination of the structural and electronic properties, and a norm conserving pseudopotential within the LDA at the relaxed geometry to evaluate the optical properties. All the considered Si nanostructures are embedded in large supercells in order to prevent interactions between the periodic replicas. A careful analysis has been performed in order to test the convergence of the structural and electronic properties with respect to both the supercell side and plane-wave basis set cut-off.

3.3.1. Single-doped silicon nanocrystals

Here we consider the effects of the size and shape of Si-NCs on the incorporation of group-III (B and Al), group-IV (C and Ge), and group-V (N and P) impurities. Single-doping has been investigated both in spherical-like and faceted-like Si-NCs [103,113]. The spherical-like Si-NCs are built taking all the bulk Si atoms contained within a sphere of a given radius and terminating the surface dangling bonds with H; whereas faceted Si-NCs result from a shell-by-shell construction procedure which starts from a central atom and adds shells of atoms successively. The spherical-like Si NCs are the $Si_{29}H_{36}$, $Si_{87}H_{76}$, $Si_{147}H_{100}$, and $Si_{293}H_{172}$ clusters and the faceted Si NCs are the Si_5H_{12}, $Si_{17}H_{36}$, $Si_{41}H_{60}$, and $Si_{147}H_{148}$ clusters. The average diameter of doped and undoped Si NCs after relaxation is about 2.3 nm for the largest crystal considered. The substitutional impurity site is one of the Si atoms at the center of the Si-NCs. As for impurities in bulk Si, Jahn–Teller distortions occur in the neighborhood of the impurity sites and the bond lengths show a dependence with respect to the size and shape of the Si-NCs.

After ionic relaxation the Si-X bond lengths (X = B, Al, C, Ge, N, and P) tend to be longer for faceted than for spherical-like Si-NCs. A small variation of the impurity levels with respect to the shape of the Si NCs is observed. Boron and aluminum give rise to shallow acceptor levels, whereas phosphorus gives rise to a shallow donor level and nitrogen to a deep donor level. The energetic positions of the impurity levels become deeper as the size of the Si-NC decreases and tend towards the position of the corresponding impurity levels of Si bulk as the size of the Si-NCs increases. For all the impurities considered the lowest-energy transitions occur at lower energies than the ones in the corresponding undoped Si NCs.

Starting from the Si_nH_m nanocluster [68], the formation energy (FE) for the neutral X impurity can be defined as the energy needed to insert the X atom, with chemical potential μ_X, into the cluster after removing a Si atom (transferred to the chemical reservoir, assumed to be bulk Si)

$$E_f = E(\mathrm{Si}_{n-1}X\mathrm{H}_m) - E(\mathrm{Si}_n\mathrm{H}_m) + \mu_{\mathrm{Si}} - \mu_X, \qquad (20)$$

where E is the total energy of the system, μ_{Si} the total energy per atom of bulk Si, and μ_X the total energy per atom of the impurity. The results show that for smaller Si-NCs a larger energy is needed for the formation of the impurity. There is a slight tendency in formation energy that suggests that the incorporation of the impurities is more favored in spherical than in faceted Si NCs. This tendency is not valid for the neutral Ge and P impurities, which present a formation energy nearly independent of the shape, or by the Al impurity, for which the incorporation is slightly favored for faceted Si NCs. We have also calculated how the FE changes as a function of the impurity position within the Si-NC [103] (see Figure 14). For the B neutral impurity in the large $Si_{146}BH_{100}$ cluster we have moved the impurity from the cluster center toward the surface along different paths still considering substitutional sites. It results that, as far as the internal core is concerned, variations no higher than 0.06 eV are found. On the contrary, an energy drop between 0.25 and 0.35 eV is found as the B impurity is moved to the Si layer just below the surface. This is explained by considering that such positions are the only ones which allow a significant atomic relaxation around the impurity, because in the other cases the surrounding Si cage is quite stable. Thus, as the B atom is moved toward the surface the FE decreases, making the subsurface positions more stable. The situation is different for the P atom.

3.3.2. Co-doped silicon nanocrystals

As already said in the introduction, simultaneous doping with n- and p-type impurities represents a way to overcome the low radiative recombination efficiency in our systems, so, starting from the already described hydrogenated Si-NCs, and following the work of Fujii et al. [32–34], we have

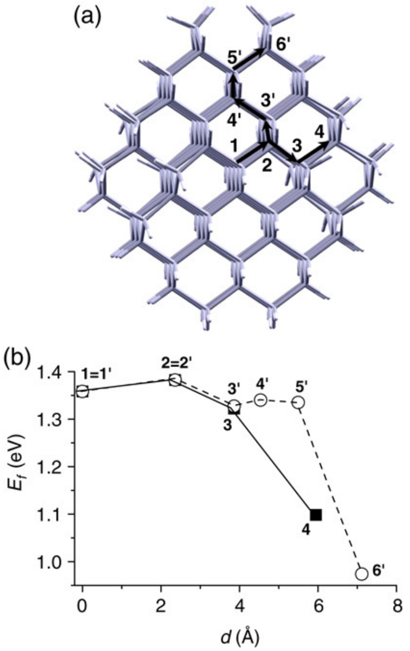

Figure 14 Formation energies for neutral impurities as a function of the impurity position within the cluster (b). The impurity is moved along two different paths toward the surface, as shown in (a). The lines are a guide for the eyes.

doped the Si clusters by locating the B and P impurities in substitutional positions just below the nanocrystal surface. It is worth mentioning that this arrangement represents the most stable configuration, as confirmed in the previous section and by theoretical and experimental works [103,114,115]. Full relaxation with respect to the atomic positions has been allowed and electronic properties have been computed through DFT calculations.

Here we will present, as an example, all the results relative to the $Si_{33}BPH_{36}$ nanocrystal, whose relaxed structure is presented in Figure 15. The choice of the small $Si_{33}BPH_{36}$ cluster (diameter around 1 nm) is due to the fact that the GW-BSE calculation [116], necessary to obtain the many-body optical spectra, is very computationally demanding.

First of all, it is interesting to look at the changes in the structural properties induced by the presence of the impurities, comparing the B and P co-doped cases with the single-doped ones.

Table 7 gives the optimized bond lengths around the impurities for the $Si_{35}H_{36}$ nanocrystal. Comparing these bond lengths with those of the corresponding Si atoms in the pure Si-NC it is clear that some significant relaxation occurs around the impurities. The amount of the relaxation around the impurity is directly related to the impurity valence, actually a

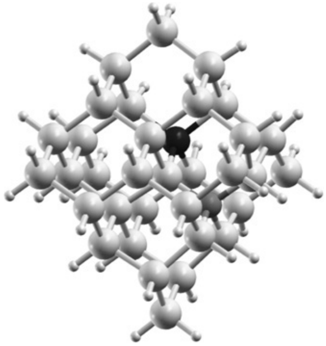

Figure 15 Relaxed structure of the $Si_{33}BPH_{36}$ co-doped nanocrystal (diameter = 1.10 nm). Gray balls represent Si atoms, while the light gray balls are the H used to saturate the dangling bonds. B (dark gray) and P (black) impurities have been located at subsurface positions in substitutional sites on opposite sides of the nanocrystals. The relaxed impurity distance is DBP = 3.64 Å.

Table 7 Bond lengths around the impurity site for the un-doped $Si_{35}H_{36}$ cluster and the single- and co-doped ones. P and B impurities have been substitutionally located at sub-surface positions (see Figure 15). Si_s and Si_i refer to surface and inner Si atoms around this site respectively

Bond	$Si_{35}H_{36}$ (Å)	Bond	$Si_{34}PH_{36}$ (Å)	$Si_{34}BH_{36}$ (Å)	$Si_{33}BPH_{36}$ (Å)
$Si–Si_s$	2.300	$P–Si_s$	2.366		2.035
$Si–Si_s$	2.300	$P–Si_s$	2.365		2.026
$Si–Si_s$	2.300	$P–Si_s$	2.364		2.026
$Si–Si_i$	2.361	$P–Si_i$	2.310		2.007
$Si–Si_s$	2.300	$B–Si_s$		2.093	2.303
$Si–Si_s$	2.300	$B–Si_s$		2.022	2.302
$Si–Si_s$	2.300	$B–Si_s$		2.022	2.297
$Si–Si_i$	2.361	$B–Si_i$		2.008	2.334

more significant distortion is found for the trivalent atom (B) than for the pentavalent one (P). In addition, it is interesting to note that in the co-doped case the differences among the four impurity-Si bond lengths are always smaller with respect to the single-doped case. Thus, if carriers in the Si-NCs are perfectly compensated by simultaneous *n*- and *p*-type impurity doping, an almost T_d configuration is recovered in which the four impurity-Si bonds are practically the same.

This tendency towards a T_d configuration in the comparison between single- and co-doped Si-NCs is found for all the considered nanocrystals, showing that these outcomes are independent of the size of the Si-NCs.

The structural deformation occurring in the single and co-doped nanocrystals has a profound influence on the stability of the systems studied.

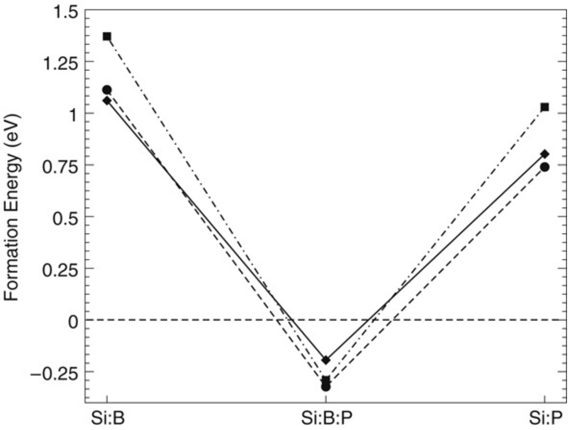

Figure 16 Formation energy for single-doped and co-doped Si-NCs. In the co-doped nanocrystals, the impurities are placed as second neighbors in the first subsurface shell. Squares are related to $Si_{35}H_{36}$, diamonds to $Si_{87}H_{76}$, and circles to $Si_{147}H_{100}$ based nanocrystals. The lines are a guide for the eyes.

Here we investigate the stability of the nanocrystals through the calculation of the formation energy. As stated in the previous section, starting from the Si_nH_m-NCs [68], the formation energy of the neutral B or/and P impurities can be defined as the energy needed to insert one B and/or one P atom within the cluster after removing one/two Si atoms (transferred to the chemical reservoir, assumed to be bulk Si). Thus generalizing the equation of the previous section we have:

$$E_f = E(\mathrm{Si}_{n-l-k}\mathrm{B}_k\mathrm{P}_l\mathrm{H}_m) - E(\mathrm{Si}_n\mathrm{H}_m) + (k+l)\mu_{\mathrm{Si}} - k\mu_{\mathrm{B}} - l\mu_{\mathrm{P}}, \qquad (21)$$

where E is the total energy of the system, μ_{Si} the total energy per atom of bulk Si and $\mu_{\mathrm{B(P)}}$ the total energy per atom of the impurity. k and l can be 0 or 1, thus one has un-doped, single B- or P-doped Si-NCs or B and P co-doped Si-NCs.

In Figure 16 we report the calculated formation energies related to $Si_{35}H_{36}$ (diameter $d = 1.10$ nm), $Si_{87}H_{76}$ ($d = 1.50$ nm) and $Si_{147}H_{100}$ ($d = 1.79$ nm) nanocrystals. In the figure, we compare the formation energy required to have B or P single-doped nanocrystals with that calculated for the case of B and P co-doped nanocrystals. In particular, in this figure, we study the case in which the B and P impurities have been placed as second neighbors in the nanocrystals (considering only sub-surface positions, this case corresponds to the nearest possible distance between the two impurities). After geometry optimization the distances between B and P impurities are $D_{\mathrm{BP}} = 3.56$ Å, $D_{\mathrm{BP}} = 3.64$ Å and $D_{\mathrm{BP}} = 3.68$ Å for the $Si_{35}H_{36}$, $Si_{87}H_{76}$ and $Si_{147}H_{100}$ nanocrystals, respectively.

From Figure 16 it is clear that simultaneous B and P doping strongly reduces (by about 1 eV) the formation energy with respect to both B or P single-doped cases and that this reduction is similar for Si-NCs of different size. While B or P single doping is very costly (in particular, the formation energy increases with decreasing nanocrystal size, in agreement with previous calculations [103,117]) B and P co-doping is much easier and there is almost no dependence on the nanocrystal size. The important point here is that Si-NCs can be more easily simultaneously doped than single-doped; this is due to both the charge compensation and the minor structural deformation.

Concerning the electronic properties, in the single-doped cases we have already shown that the presence of donor or acceptor states can considerably lower the energy gap E_G of the un-doped Si-NCs [103,104]. Actually, for single-doped Si-NCs, the HOMO level now contains only one electron and is strongly localized either on the B or P impurity. For example, in the case of the $Si_{86}BH_{76}$ single-doped nanocrystal the defect level is located just 0.28 eV above the valence band, thus the energy gap is reduced from 2.59 eV (the value for the un-doped nc) to 2.31 eV, whereas for the $Si_{86}PH_{76}$ single-doped nanocrystal the defect level is located just 0.28 eV below the conduction band, and the energy gap is thus now only 0.28 eV [104]. It is interesting to note that the experimental substitutional donor binding energy for P in Si bulk is about 33 meV, while the experimental acceptor energy for B in Si is 45 meV [118], showing how, in the case of nanocrystals, the quantum confinement effect tends to "transform" shallow impurities into "deep" centers.

Now, what is important is that the electronic properties of B- and P- co-doped Si-NCs are qualitatively and quantitatively different from those of either B- or P- single-doped Si-NCs. The presence of both a n and a p impurity leads to a HOMO level that contains two electrons and to a HOMO–LUMO gap that is strongly lowered with respect to that of the corresponding un-doped nanocrystals.

The calculated energy levels for the $Si_{35}H_{36}$ related systems at the Γ point, calculated at the optimized geometries, are shown in Figure 17, where only the levels corresponding to the HOMO, LUMO, HOMO-1 and LUMO+1 states are depicted. Calculated square modulus contour plots related to HOMO and LUMO states show their localization within the Si-NC, in particular the HOMO state is localized on the B impurity while the LUMO is localized on the P one. The presence of these donor and acceptor states lowers the energy gap from 3.51 eV, for the pure cluster, to 2.86 eV, for the doped one. In principle, starting with a bigger cluster, for which the energy gap is smaller than in this case, it is possible through co-doping also to tune the gap below the bulk Si value, as experimentally observed by Fuji and coworkers [33]. In order to give a complete description, within the many-body framework, of the co-doped Si-NC response to an optical excitation, we consider both the self-energy corrections, by means of the GW method to obtain the quasiparticle energies, and the excitonic effects, through the

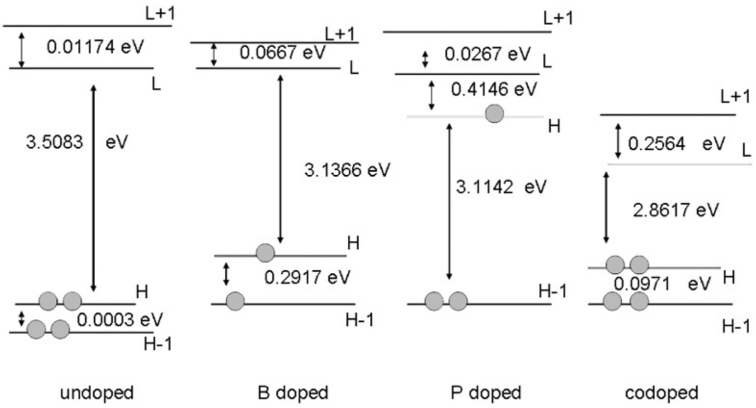

Figure 17 Calculated energy levels at the Γ point for the $Si_{35}H_{36}$-nc family. From left to right: un-doped $Si_{35}H_{36}$-nc, single-doped $Si_{34}BH_{36}$-nc, single-doped $Si_{34}PH_{36}$-nc, co-doped $Si_{33}BPH_{36}$-nc. Alignment has been performed by locating, at the same energy, the fully occupied levels with the same type of localization.

solution of the Bethe–Salpeter equation. The effect of local fields is also included, to take into account the inhomogeneity of the systems.

To carry out emission spectra calculations, we have used the excited state geometry and the ground state electronic configuration, as already described in Section 2.1.1. Thus, here, the electron–hole interaction is also considered in the emission geometry. Figure 18 (right panel) shows the calculated absorption and emission spectra fully including the many-body effects. The electron–hole interaction yields significant variations with respect to the single-particle spectra (shown in the left panel), with an important transfer of the oscillator strength to the low energy side. Moreover, in the emission spectrum, the rich structure of states characterized, in the low energy side, by the presence of excitons with largely different oscillator strengths, determines excitonic gaps well below the onset of optical absorption. Thus the calculated emission spectrum results are red-shifted to lower energy with respect to the absorption ones. This energy difference between emission and absorption, the Stokes shift, can be traced back to the relaxation of the Si-NCs after the excitation process. The new and important features that appear in the emission many-body spectra are related to the presence of both B and P impurities, as shown by Figure 19, which gives the real-space probability distribution $|\psi_{\text{exc}}(r_e, r_h)|^2$ for the bound exciton as a function of the electron position r_e when the hole is fixed in a given r_h position. In this case the hole is fixed on the boron atom and we see that the bound exciton is mainly localized around the phosphorus atom. From Table 8, it can be seen that the single-particle DFT results strongly underestimate the absorption and emission edge with respect to the GW+BSE calculation, in which the excitonic effect are taken exactly into account. This means that, in this case, the cancellation between

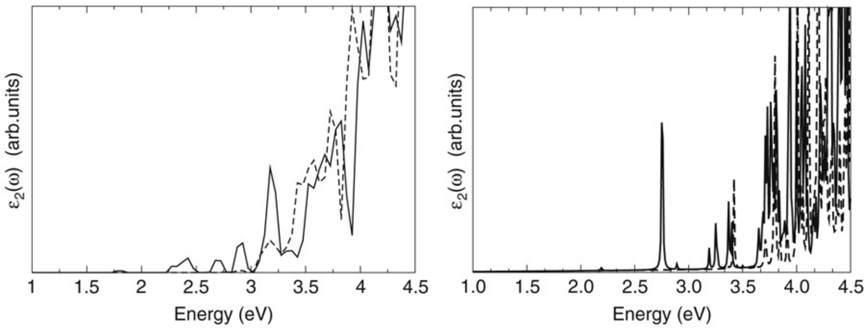

Figure 18 Left panel: Single-particle imaginary part of the dielectric function for the co-doped $Si_{33}BPH_{36}$ nanocrystal in the ground (dashed line) and excited (solid line) geometries. Right panel: absorption (dashed line) and emission (solid line) many-body spectra of $Si_{33}BPH_{36}$.

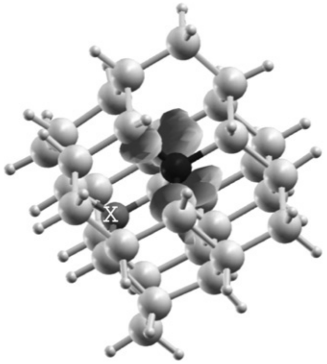

Figure 19 Excitonic wave function of $Si_{33}BPH_{36}$ (atom colors as in Figure 15). The gray isosurface represents the probability distribution of the electron, with the hole fixed (cross) on the B impurity.

GW gap opening (which gives the electronic gap) and BSE gap shrinking (which gives the excitonic gap) is only partial. The difference between the GW electronic gap and the GW+BSE optical excitonic gap gives the exciton binding energy E_b. We note the presence of exciton binding energies of 2.2 eV, which are very large if compared with bulk Si (~15 meV) or with carbon nanotubes [119,120] where $E_b \sim 1$ eV, but similar to those calculated for undoped Si-NC [92] of similar size and for Si and Ge small nanowires [121,122].

It is interesting to note that the HOMO–LUMO transition in the emission spectrum at 2.20 eV is almost dark while an important excitonic peak is evident at about 2.75 eV (see Figure 18), red-shifted with respect to the first absorption peak.

Table 8 Absorption and Emission gaps calculated as the HOMO–LUMO difference through a DFT and a GW-BSE approach

$Si_{33}BPH_{36}$	DFT	GW	GW + BSE
Abs. (eV)	2.80	5.52	3.35
Ems. (eV)	1.71	4.37	2.20

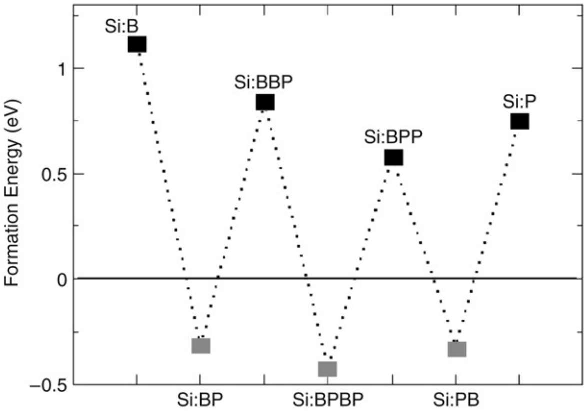

Figure 20 Formation energies for single, co-doped and multi-doped $Si_{147}H_{100}$ based nanocrystals. The lines are a guide for the eyes.

3.3.3. Multi-doped silicon nanocrystals

Here we present how the formation energy and the electronic properties of the Si-NCs are influenced by the insertion of a large number of impurities. We call this insertion of several impurities multi-doping. In Figure 20 we show how the FE of a large $Si_{147}H_{100}$-NC varies as a function of the number of impurities. We note that the presence of an odd number of dopants (1 or 3) already brings the FE to higher values. In contrast, the presence of an even, compensated number of B and P impurities strongly lowers the FE, which drop down to a negative value, indicating that as in the case of simple co-doping, multi-doping is much easier to realize when one has the same number of donor and acceptor dopant atoms. In fact the $Si_{145}BPH_{100}$-NC, $Si_{143}BBPPH_{100}$-NC and $Si_{141}BBBPPPH_{100}$-NC (not shown in the figure) show an FE of −0.32 eV, −0.42 eV and −0.97 eV respectively.

Next we investigate how the electronic levels are influenced by adding one or two more impurities to the already co-doped $Si_{145}BPH_{100}$-NC. We consider the $Si_{145}BPH_{100}$-NC, where the starting B and P pair is located in a particular site, which is the more stable configuration. Therefore we first add one single impurity in order to obtain either the $Si_{144}BBPH_{100}$-NC (with an excess of B: 2 B atoms and 1 P) or the $Si_{144}BPPH_{100}$-NC (with an excess of

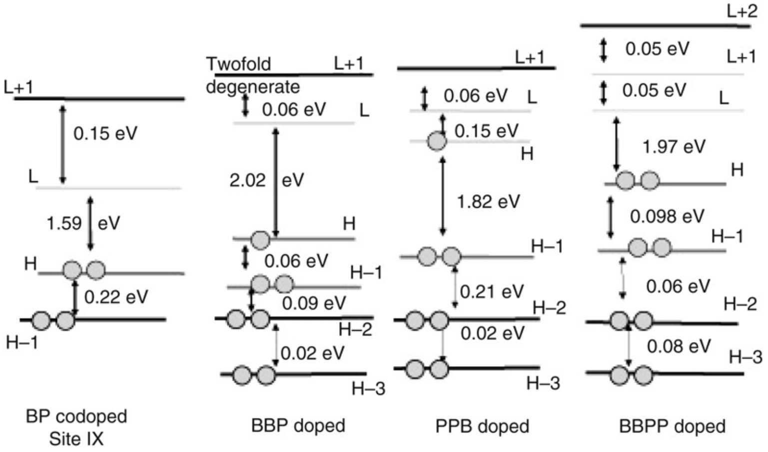

Figure 21 Calculated energy levels at the Γ point for the $Si_{145}BPH_{100}$-NC, the $Si_{144}BBP_{100}$-NC, the $Si_{144}BPPH_{100}$-NC and the $Si_{143}BBPPH_{100}$-NC. Alignment has been performed by locating, at the same energy, the fully occupied levels with the same type of localization.

P: 1 B and 2 P) and finally, adding simultaneously two B and two P atoms, we obtain the $Si_{143}BBPPH_{100}$-NC.

Looking at the electronic structure in Figure 21, the two Si-NCs with 3 impurities, presents a similar behavior to those corresponding to B or P single-doped Si-NC ($Si_{146}BH_{100}$ or $Si_{146}PH_{100}$). Every new dopant inserted gives rise to a new impurity level, which is half occupied. Looking at the figure we see that the HOMO–LUMO energy differences for the nanoclusters with an odd number of impurity atoms are very similar: 2.02 eV for the $Si_{144}BBPH_{100}$-NC with respect to 2.08 eV for the B single doped case ($Si_{146}BH_{100}$), and 0.15 eV for the $Si_{144}BPPH_{100}$-NC with respect to 0.13 eV for the P single doped case ($Si_{146}PH_{100}$) respectively. In addition, when the impurities are compensated, as in the case of $Si_{143}BBPPH_{100}$-NC, the system becomes a semiconductor, in which the HOMO again contains two electrons, and the value of the energy gap (1.97 eV) is intermediate with respect to the two corresponding extrema E_G of the co-doped $Si_{145}BPH_{100}$ with impurities located at different distances (2.03 eV for impurities closer to each other and 1.59 eV for impurities at the opposite side of the Si-NC).

The single-particle absorption spectra reflects the results for the electronic properties. As far as all the compensated co-doped Si-NCs are concerned we observe a shift of the absorption onset toward lower energy on increasing the distance between the impurities. It is worth pointing out that when impurities are at large distance the transition intensities near the band edges become weaker due to small oscillator strengths. On the other hand when the impurities are close to each other, the transitions near the band edge are more intense, due to the strong localization of HOMO and LUMO on the impurity sites.

3.3.4. Screening in silicon nanostructures

The presence in the cluster of a positively charged impurity has also been considered, analyzing, by first principles, the screening due to the Si-NCs [123,124]. A reduction of screening in Si nanostructures with respect to bulk Si has been already observed [52] and predicted [125]. This reduction is a fundamental process at the basis of the enhancement of both the electron–hole interaction and the impurity activation energies in nanosized objects, and is due to the fact that close to the surface there is a dielectric dead layer, with a finite-range reduction of the dielectric constant due to the dielectric mismatch at the nanocrystal-environment interface.

Starting from the optimized configuration of hydrogenated nanocrystals (described in Section 3.1.1), the self-consistent electronic response to an impurity atom has been studied. The screening has been studied introducing a substitutional phosphorous ion (P^+) at the nanocrystal center. The electron density induced by the impurity, into a nanocrystal with n Si and m H atoms, is calculated as [123,124]

$$n_{\text{ind}} = n[Si_{n-1}PH_m^+] - n[Si_nH_m], \tag{22}$$

where n is the real-space ground state electron density. We have calculated the spherical average of the induced density for several nanocrystals, as a function of size, and present our results in Figure 22(a). We have also calculated their integrals, namely the integrated induced densities, reported in Figure 22(b). Arrows indicate the nanocrystal radii. A close examination of Figure 22 shows an electron density depletion (i.e., a positive charge accumulation) localized at the nanocrystal surface, in such a way as to fully compensate the electron density accumulation (negative charge) around the impurity. The surface charge accumulation is exactly centered around the nanocrystal radii, as we could have supposed at the beginning. However, an interesting fact is that, as revealed in the figure, the charge is much spread around the radii, and we estimate 0.2–0.3 nm of a surface polarization layer. This depletion region is at the origin of the dielectric constant reduction with respect to the bulk system, recently reported in literature [125]. Figure 22(a) and (b) show that the real space electron response rapidly reaches the bulk limit and the curves for different sizes match each other a few Å apart from the surface. We thus argue, that far from the surface we have a bulk-like response driven by the Si static dielectric constant, while at the surface there is a dielectric dead layer, with the dielectric constant smoothly reducing to the external value of one. Moreover the surface polarization layer width is almost size-independent; the behavior around the surface of the different curves in Figure 22(b), with the reduction of the integrated electron density,

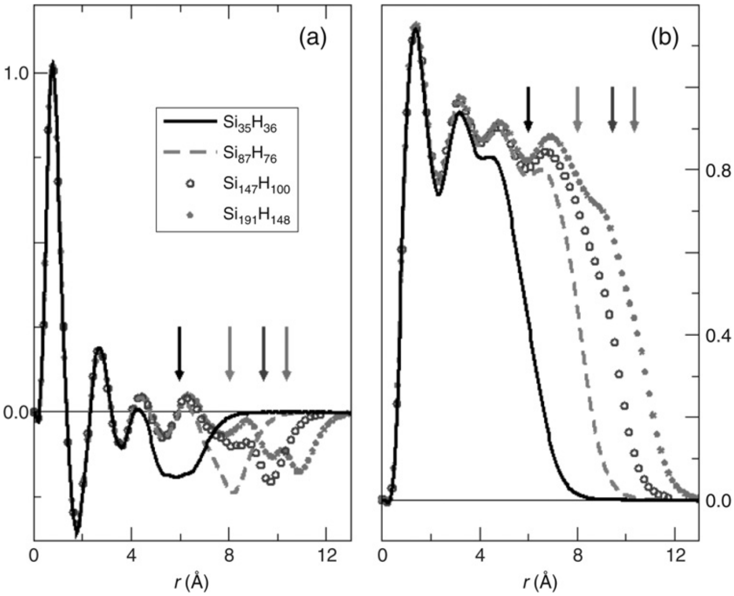

Figure 22 Spherical averaged induced density (panel (a)) and integrated induced density (panel (b)) calculated for P^+ impurities in Si nanocrystals with increasing size. The arrows point to the nanocrystal radii.

is almost the same for all the nanocrystals. The oscillating behavior in the intermediate region between the impurity location and the surface is a consequence of the polarization of the Si–Si bonds within the nanocrystal. This is a local field effect also visible in bulk Si, but it gives a minor contribution to the static dielectric constant.

As it is known from the literature, the integrated induced density of the local field oscillating behavior, tends to a constant value Q resulting from the incomplete screening of Si [126]. Q is calculated from the static dielectric constant ϵ_s:

$$Q = 1 - \frac{1}{\epsilon_s}. \tag{23}$$

It is almost impossible to derive the exact value of Q from Figure 22(b), because of the large oscillations discussed above. However, since the induced charge rapidly converges in the region far from the surface, we can reasonably assume that the reduction of Q (and thus of the screening) is limited to the region of space around the surface.

From this analysis, it is worth underlining that the surface plays the leading role in the screening. It is meaningless to neglect the surface in a calculation involving either an impurity or an excitonic screening. In spherical nanocrystals all the details of the electronic response, both due to the bulk-like local field contributions and a non negligible dielectric dead layer width, are fully covered by the macroscopic, primary surface polarization charge contribution. For such a reason, we have applied the Thomas–Fermi model for semiconductors proposed by Resta [126] in 1977 to the screening in nanocrystals (the substantial difference between a bulk structure and a nanocrystal consists in the nanocrystal surface). The Thomas–Fermi model, actually, only considers the charge accumulation around the impurity and at the surface, and then gives an excellent agreement with very accurate first-principles calculations. Details of the model are the following; let us consider a positive point charge $+1$ (atomic units are used) located at the center of a spherical nanocrystal. Because of the incomplete screening, the total induced charge near the impurity amounts to $-Q$. This charge is fully compensated by an amount of charge $+Q$ located at the nanocrystal surface. Thus, outside the screening sphere, the potential is that of a point charge $(1-Q)$ located at the nanocrystal center plus the contribution from the surface charge. From simple electrostatics it can be shown that the potential energy for an electron is

$$V_c(r) = \begin{cases} -\left(\dfrac{1-Q}{r}\right) - \left(\dfrac{Q}{R}\right) & R_s < r \leq R \\ -\dfrac{1}{r} & r \geq R. \end{cases} \tag{24}$$

where R is the nanocrystal radius. The screened potential inside R_s can be computed within the Thomas–Fermi theory. According to this [126], the potential energy $V(r)$ solves, for $r < R_s$, the linearized equation

$$\nabla^2 V(r) = q^2[V(r) - \mu]. \tag{25}$$

Here, q is the inverse of a screening length related to the valence electron density which contributes to the screening and μ is a Lagrange multiplier controlling the total number of particles. The boundary conditions to be used with Equation (23) are that $V(r)$ must match $V_c(r)$ at R_s and that $rV(r) \to -1$ as $r \to 0$. Once we have solved the Thomas–Fermi equation, we have calculated the screened function, defined as the bare impurity potential divided to the screened one, namely V_b/V.

We report here the final expression for the screening function:

$$\bar{\epsilon}(r) = \begin{cases} \left\{ \dfrac{1-Q}{qR_s}[\sinh[q(R_s - r)] + qr] + \dfrac{Qr}{R} \right\}^{-1} & 0 \leq r \leq R_s \\ \left[1 - Q + \dfrac{Qr}{R}\right]^{-1} & R_s \leq r \leq R \\ 1 & r \geq R. \end{cases} \tag{26}$$

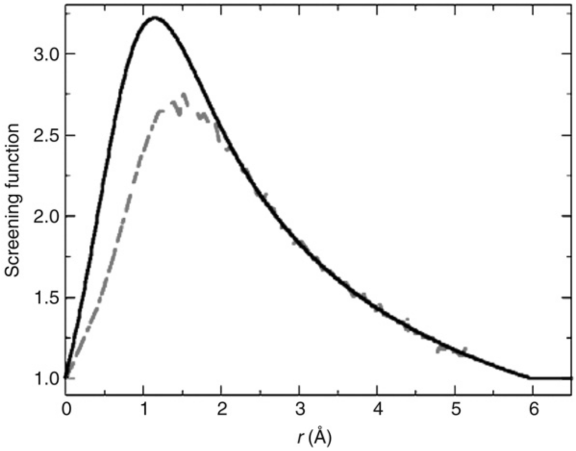

Figure 23 Screening function calculated for the $Si_{35}H_{36}$ nanocrystal, using the Thomas–Fermi model (solid line), compared to a previous first principles calculation [127] (dashed line).

The parameters here used are the ones first given by Resta; $q = 1.10$ au, $R_s = 4.28$ au, and $Q = 0.912$. It is very important to remark that the expression given here for the screening function is analytical and universal and can be applied to every spherical semiconductor nanocrystal. We show in Figure 23 the screening function calculated for $Si_{35}H_{36}$ using the present model, compared to a previous first principles calculation, based on the density functional linear response theory [127]. The novelty of the present model is that the screening function has the correct limit of one, both at the impurity location and at the nanocrystal surface. The agreement is very nice, especially in the region of space around the surface, where the screening is governed by the classical contribution. Once again, we underline the great importance of surface polarization charge, as that alone can give a good agreement with state-of-art calculations.

4. ONE-DIMENSIONAL SYSTEMS

4.1. Silicon and germanium nanowires

In recent years much effort has been spent on the development of experimental techniques to grow well defined nanoscale materials, due to their possible applications in nanometric electronic devices. Indeed the creation of nanowire field effect transistors [128–132], nano-sensors [133,134], atomic scale light emitting diodes and lasers [135,136], has been made possible by the development of new techniques, which allow one to control the growth processes of nanotubes, nanowires and quantum dots. Of particular importance, among the different atomic scale systems experimentally studied, are nanowires. Being quasi-one-dimensional structures, they exhibit quantum confinement effects such that carriers are free to move only along the axis of the wire. Further, the possibility to modify their optical response as a function of their size has become one of the most challenging aspect of recent semiconductor research. Because of their natural compatibility with Si based technologies, Si nanowires (Si-NWs) have been extensively studied and several experiments have already characterized some of their structural and electronic properties [38,129,133,137–139]. Recently it has been possible to fabricate, for example, single-crystal Si-NWs with diameters as small as 1 nm and lengths of a few tens of micrometers [37,133,140,141]. PL [3,142,143] data revealed a substantial blue-shift with decreasing size of nanowires. Further scanning-tunnelling spectroscopy data [37,143] also showed a significant increase in the electronic energy gap for very thin semiconductor nanowires, explicitly demonstrating quantum-size effects. Germanium nanowires (Ge-NWs), which can be synthesized using a variety of techniques [38,137,144], are particularly interesting due to their high carrier mobility: in fact, Ge-NWs based-devices such as field effect transistors [145], solar cells and nanomagnets [146], have been characterized or envisaged [147]. Recently it has also been shown that Ge-NWs could be used in optoelectronic components fabricated within Si based technology [148]. Despite such clear device potential, relatively few ab-initio calculations of optical properties beyond the one-particle approach have so far been performed [121,122,149,150] in order to clarify the experimental evidence and investigate the potential applications of such nanoscale materials. In fact the theoretical panorama is essentially based either on ab-initio calculations [151–158] which neglect the electron–hole Coulomb interaction effects (which instead is expected to play an important role due to the reduced dimensionality of such systems) or on Effective Mass Approximation (EMA) calculations [159] and semi-empirical approaches [160,161].

In this section we will describe the electronic properties of H passivated, free standing Si and Ge nanowires oriented along the [100], [111] and [110] directions, with diameters ranging from about 0.4 to 1.2 nm. The effective width is defined as the wire cross-section linear parameter, following the definition of Ref. [154]. Nevertheless it must be underlined that this definition of the wire size is somewhat ambiguous, indeed in literature larger diameters are reported for wires with the same number of atoms in the unit cell than the ones studied here. This is due to the fact that different definitions of the wire radius exist [161] and that in some cases the average distance among the external H atoms is taken into account.

In particular we will show the dependence of the electronic gap on both wire size and orientation. Further, in some of the studied wires, self-energy corrections, by means of the GW method, and also electron–hole interaction, by solving the Bethe–Salpeter equation, will be included in order to have an appropriate description of the excited states.

Table 9 DFT–LDA electronic gaps in Ge-NWs and Si-NWs are reported respectively in the third and fifth column, quasi-particle gaps are reported for Ge-NWs in the fourth column. All values are in eV

Wire size (nm)	Wire orient.	Ge E_g^{DFT}	Ge E_g^{GW}	Si E_g^{DFT}
0.4	[100]	3.9	6.1	3.8
	[111]	3.5	5.4	3.5
	[110]	2.1	4.5	2.7
0.8	[100]	2.6	4.0	2.5
	[111]	2.1		2.2
	[110]	1.3		1.2
1.2	[100]	1.9	3.3	1.8
	[111]	1.6		1.2
	[110]	0.9		1.3

Concerning the electronic minimum gap (which is direct or quasi-direct in all the studied wires, see Ref. [121,122,149,154] for details) at the DFT level (see Table 9) we find that it decreases monotonically with the wire diameter. The calculated values are larger than the electronic bulk indirect gap, thus reflecting the quantum confinement effect. This effect, which has been recently confirmed in STM experiments [37,143], is related to the fact that carriers are confined in two directions, being free to move only along the axis of the quantum wires. Clearly we expect that, increasing the diameter of the wire, such an effect becomes less relevant and the electronic gap will eventually approach the bulk value.

Another aspect that is interesting to note concerns the dependence of the DFT gap on the orientation of the wire, indeed, for each wire size the following relation holds: $E_g[100] > E_g[111] > E_g[110]$. As has been pointed out in Ref. [121], this is related to the different geometrical structure of the wires in the [100], [111] and [110] directions. Indeed the [100], [111] wires appear as a collection of small clusters connected along the axis, while the [110] wires resemble a linear chain. So we expect that quantum confinement effects are much bigger in the [100], [111] wires, due to their quasi zero-dimensionality, with respect to the [110] wires. Further, the orientation anisotropy reduces with the wire width and it is expected to disappear for very large wires, where the band gap approaches that of the bulk material.

Most of the results presented in Table 9 do not take into account self-energy corrections, which are necessary in order to describe, in a proper way, the one-particle excited states. In the fourth column of Table 9 we report the GW corrected band-gaps, for the smallest Ge-NWs in the [111],[110] directions, and for all the [100] Ge-NW. A complete discussion on this part can be found elsewhere [121]. We can see (Table 9, fifth column) that the effect of the GW correction is an opening of the DFT–LDA gap, by an amount which

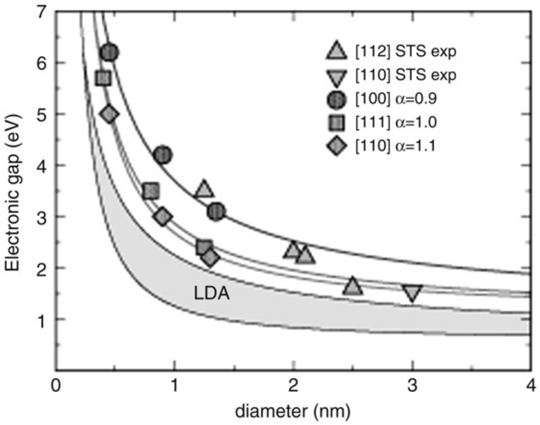

Figure 24 Scaling of the electronic gap (GW) in [100] (circles), [111] (squares) and [110] (diamonds) oriented Si-NWs as a function of wire size. The results of the STS measurements performed on Si-NWs along the [112] and [110] directions are also presented (see Ref. [37]).

is much bigger than the corresponding correction in the bulk. Furthermore it has to be noted that such corrections are also size and orientation dependent.

Concerning Si-NW, Figure 24 shows the comparison of the calculated quasi-particle electronic gaps with the experimental data obtained by Ma et al. through STM, for different Si-NWs (grown along the [112] and [110] directions), with diameters ranging from 1.3 to 7 nm [37]. We see that all the experimental gaps fall within our [100] and [110] fitting curves, which represent the two limiting cases in terms of quantum confinement effects [122], showing a good agreement with our theoretical results. This confirms that, in order to compare experimental and theoretical results for the electronic band gap, it is mandatory to include the self-energy effects in the calculations. In Figure 25, for all the different Si-NWs, we report our calculated excitonic gap (corresponding to the lowest-energy allowed transition, calculated taking into account the electron–hole interaction) together with the experimental optical data of Zhang and Bayliss [162] and Wolkin et al. [18] for Si nanostructures passivated by H. All the experimental data fall within our theoretical results, moreover we note that the data of Zhang and Bayliss [162], referring to porous Si wires prepared by electrochemical anodization of (100) Si wafers, are in very good agreement with our results relating to [100] oriented Si-NWs. This shows that for the optical spectra it is necessary to take fully into account both the self-energy correction and electron–hole interaction. To underline the importance of the many-body effects on the optical response of the studied nanowires, we report in Figure 26 the theoretical optical absorption spectra of the Ge and Si wires (grown along the [100] direction and with diameter of about 0.8 nm), for light polarized along the

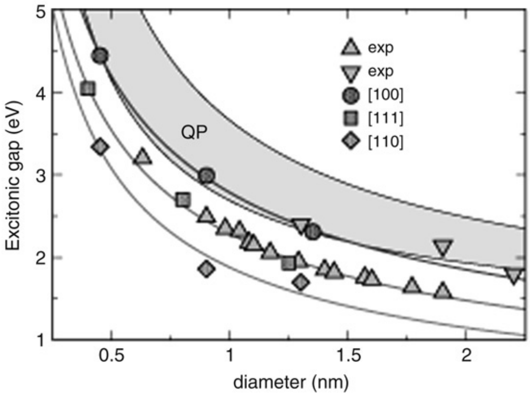

Figure 25 Calculated (full circles) lowest allowed excitonic gaps for the different Si-NWs and their comparison with the experiments. Down triangles correspond to the data of Zhang and Bayliss [162], whereas up triangles correspond to the data of Wolkin et al. [18].

wire axis. In the top panels, the spectra calculated at the RPA one-particle level, but including self-energy corrections, are shown; while, in the bottom panels, the corresponding spectra obtained including the excitonic effects, are reported. Comparing the top and bottom panels, it is clear that strongly bound excitons, of more than 1 eV, are present. Moreover we aim to underline an important difference between Si and Ge wires: in fact, already at the GW level (top panels) a large oscillator strength near the onset of optical absorption is found only in the case of Ge and not in the case of Si. With the inclusion of the excitonic effects (bottom panels), we see that an important transfer of the oscillator strength below the electronic gap appears and a strong optical peak comes out in the visible range for the 0.8nm Ge-NW, but not for the 0.8 nm Si-NW (see Figure 26). A similar finding has been obtained by comparing the optical spectra of Si and Ge nanodots [163]. This has been explained as due to the fact that in Si-NW the minimum gap remains indirect in character, as far as the optical matrix elements are considered [122,149], while in the case of Ge-NWs the first conduction band retains a clear Γ character. We underline that this excitonic peak is expected to move to lower energies with increasing wire diameter, thus fully covering the visible range.

A last important effect of quantum confinement is that related to the exciton localization in confined structures. In the case of a wire, the presence of bulges and kinks results in a stronger intensity, larger binding energy and reduced spatial size for the exciton: the size L of the electron–hole probability distribution depends on the orientation growth in the relation: $L[100] < L[111] < L[110]$ (see Figure 27). In particular, we find the strongest overlap of the electron–hole wave function (see bottom part of Figure 27) and an excitonic binding energy close to 2 eV in the [100] Ge-NW (of width 0.4 nm). This value is particularly significant when compared with typical

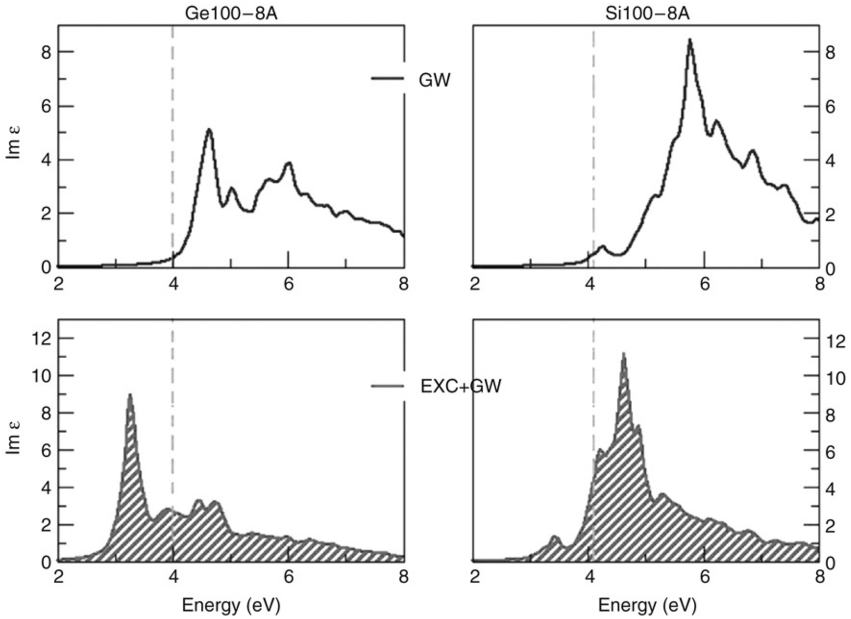

Figure 26 Imaginary part of the dielectric function of [100] oriented Ge-NWs (left panels) and Si-NWs (right panel) with diameters of 0.8 nm. The first row shows optical spectra at the GW level, the second row shows the spectra obtained including excitonic effects. The dashed line represents the GW optical gap.

binding energies of ~1 eV obtained for semiconducting carbon nanotubes of comparable effective width [119,120], where the overlap is limited to the two-dimensional nanotube wall. Furthermore, we find significant cancellation of self-energy and electron–hole interaction effects in the wires which, resembling a string of small clusters, have a quasi zero-dimensional character.

4.2. Doped silicon nanowires

Few investigations have been dedicated to the influence on the electronic and transport properties of doping [164,165]. In particular, due to their application in electronic devices, the main efforts have been devoted to the study of B and P single doped Si-NW, while only one ab-initio study has investigated B and P co-doping [165]. For this reason, we have recently performed a systematic analysis of the effect of B and P co-doping in Si-NW, focusing not only on the structural properties but also on how doping influences the electronic and optical properties. Here we aim to cover the main outcomes of this work and illustrate specific results only for one single-doped and co-doped H-passivated Si-NW (with a linear cross section of about 1 nm) grown in the [110] direction. In particular we have considered different position for the impurities in the Si-NW, moreover we have varied the unit cell in our

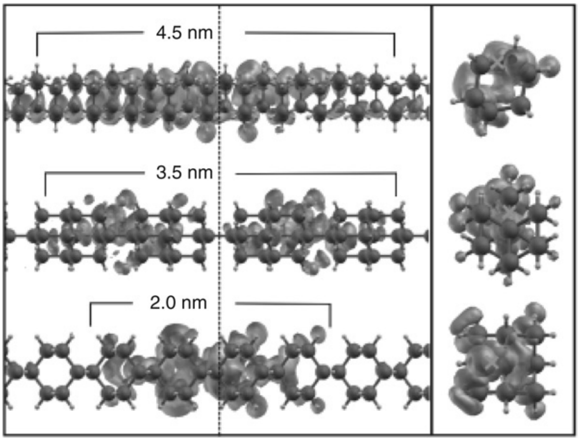

Figure 27 Geometrical structures of the 0.4 nm Ge wires in the [110] (top), [111] and [100] (bottom) directions shown from the side (left) and from the top (right). Large spheres represent Ge atoms; small spheres are H atoms used to saturate the dangling bonds. The grey isosurface gives the probability distribution $|\psi_{\text{exc}}(r_r, r_h)|^2$ of finding the electron when the hole is fixed in a given position (the e–h localization length L is reported for each wire). The hole positions lie on the dashed line in the left panel and are represented by the crosses in the right panel.

calculations. Augmenting the unit cell corresponds to an increase of the overall number of atoms within the cell and thus to a decrease in the dopant concentration. Figure 28 shows how the formation energy for the B and P co-doped Si-NW changes as a function of the position of the dopants within the nanowire. In the figure the inset shows the single Si-NC unit cell used in this case. We note that the minimum is reached when the P atom moves to a surface position. Moreover in the corresponding case (not shown in the figure) where the P impurity is located in a subsurface position and the B atom is in a surface site the FE becomes negative. Indeed it is worthwhile noting that in all cases of single-doped Si-NW the FE shows a high positive value (1.13 eV and 0.66 eV for the single B and P doped nanowire respectively), thus confirming the stabilizing role of compensated doping. Concerning the electronic properties, the band structure show a direct energy gap behavior at Γ, whose values depends on the impurity position. For the positions labelled 1, 2 and 3 in Figure 28 these values are 0.63 eV, 0.08 eV and 0.97 eV respectively.

If we concentrate on the dependence of the doped Si-NW properties on the dopant concentration, we note first that on augmenting the number of atoms in the cell (thus lowering the dopant concentration) the formation energy lowers. For the smallest unit cell (28 atoms in total) the FE shows a value of 0.41 eV, while using a two-times (56 atoms), three-times (84 atoms) and four-times (112 atoms) larger unit cell brings this value to −0.15 eV, −0.60 eV and −0.64 eV respectively. This demonstrates that a lowering of the impurity concentration results in an increase in the stability for the nanowire. The

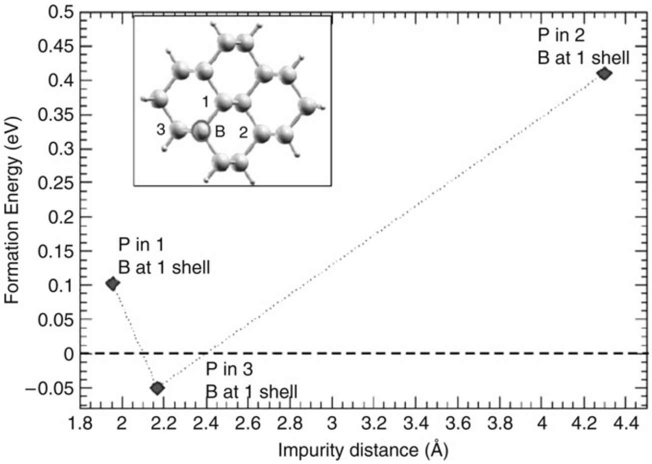

Figure 28 Formation Energy for the co-doped Si-NW (shown in the inset) as function of the related position between the two dopants. The B (impurity) is frozen in a subsurface site, while the P atom occupies different substitutional sites labelled 1, 2, and 3. The lines are guides for the eyes.

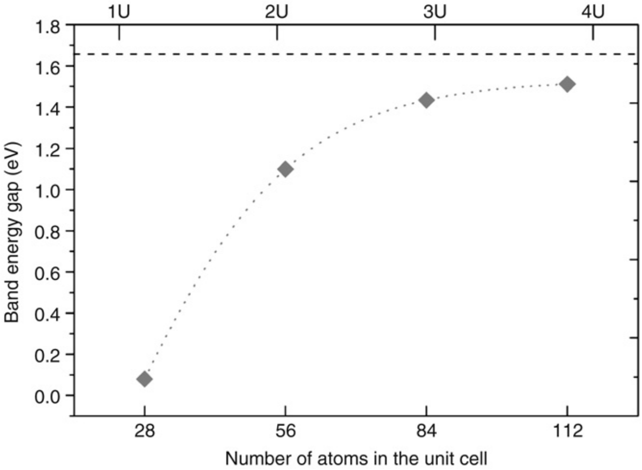

Figure 29 DFT-GGA direct band-gap calculated at the Γ point for the co-doped Si-NW with respect to the number of atoms in the unit cell. A larger number corresponds to a decrease in impurity concentration. The dotted line is a guide for the eyes. The dashed line corresponds to the band-gap for the undoped Si-NW.

impurity concentration also plays a role regarding the electronic properties. From Figure 29 we see that the direct band-gap increases as the impurity concentration lowers, asymptotically approaching the value of the band-gap of the undoped Si-NW. This is another indication of how doping can modify the electronic and optical properties of Si nanostructures.

5. TWO-DIMENSIONAL SYSTEMS

In this section we will analyze the structural, electronic and, in particular, the optical properties of Si and Ge based nanofilms [166] and of Si superlattices [167] and multiple quantum wells [168] where CaF_2 and SiO_2 are the barrier mediums. The quantum confinement effect and the role of symmetry will be considered by changing the slab thickness and orientation and also the role of interface O vacancies will be discussed.

5.1. Si and Ge nanofilms

In this section a careful comparison of the electronic and optical properties of Ge quantum films with those of Si quantum films is presented. The Si and Ge free-standing quantum films considered here are constructed keeping the same lattice periodicity and the same interatomic distance as in the bulk material. Their surfaces are oriented along the (100), (110) and (111) directions. For each orientation two effective thicknesses ($\sim$0.65 and 1.05 nm) have been chosen for the analysis. H atoms are used to terminate dangling bonds at the surface. The Si–H and Ge–H bond lengths have been taken to be 0.1481 and 0.1525 nm, respectively, corresponding to those in SiH_4 and GeH_4 molecules. The calculations of the electronic and optical properties are done within density functional theory using the linearized augmented plane wave (LAPW) method that is implemented into the WIEN97 code [169]. For details of the calculation the reader is referred to Ref. [166]. The real ϵ_1 and imaginary ϵ_2 part of the dielectric function together with the optical absorption coefficient α has then been evaluated as described in Section 2.1.1.

The band structures of Si and Ge nanosize films (1 nm thick) calculated along high-symmetry directions of the 2D Brillouin Zone (BZ) are shown in Figure 30 for all the considered orientations. First of all the valence band dispersion is found to be very similar for both Si and Ge films of the same orientation. It is also important to point out the absence of surface/interface states in the band gap energy region in all cases due to the full H passivation of surface dangling bonds. Looking at the different surface symmetry, an interesting feature for the (100)-oriented films is that the band gap appears to be direct at the Γ point, in this case, for both Si and Ge systems. A quite different character for the band gap is observed for the semiconductor (110) films. In the case of Si the gap is still direct at the BZ center, whereas for Ge the band gap is now indirect as the conduction band minimum lies on the Γ-X_1 axis. Similarities in the conduction band dispersion can be seen for the (111) slabs, even if the band gap behavior is quite different. For the Si film the folding of the bulk energy bands has resulted in the appearance of an indirect band gap along the Γ-M line. It should be noted that the Γ-M direction of the

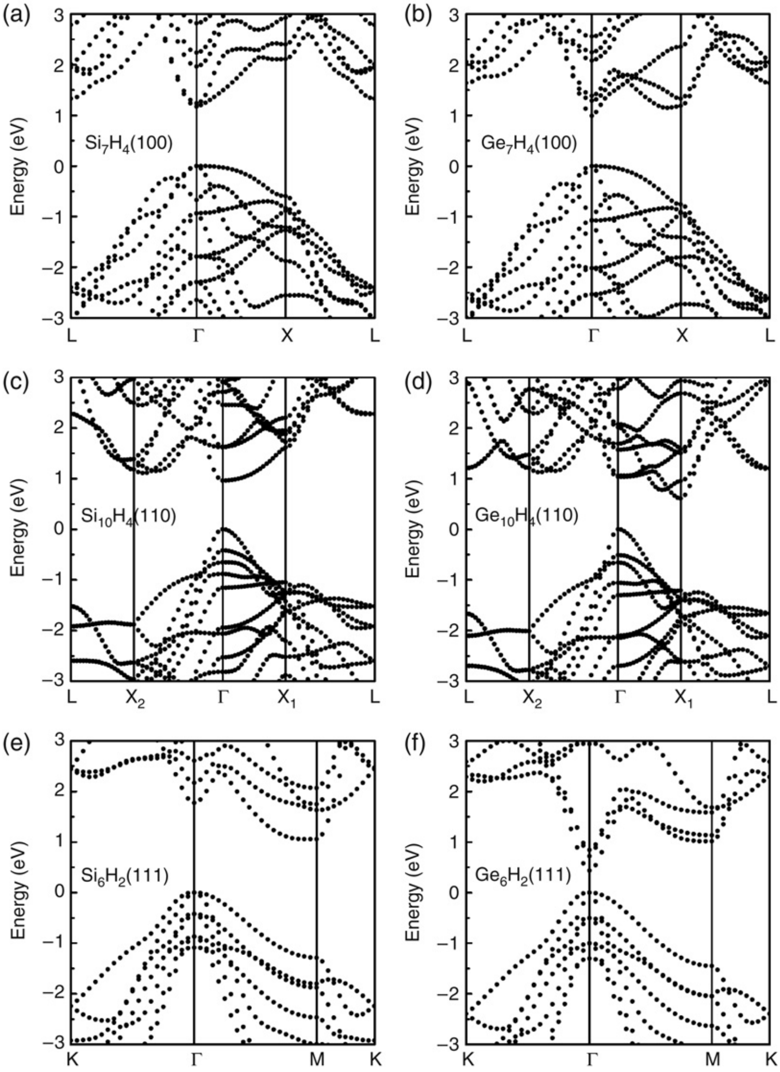

Figure 30 Electronic band structures of Si_mH_n and Ge_mH_n quantum films of about 1.0 nm thickness for different orientations (m and n refer to the number of Si(Ge) and H layers in the considered film): (a) Si_7H_4 (1 0 0); (b) Ge_7H_4 (1 0 0); (c) $Si_{10}H_4$ (1 1 0); (d) $Ge_{10}H_4$ (1 1 0); (e) Si_6H_2 (1 1 1); (f) Ge_6H_2 (1 1 1).

2D hexagonal BZ corresponds to the Γ-X direction of the three-dimensional face-centered cubic BZ where the bulk Si conduction band minimum occurs. For Ge films, instead, there is a well resolved conduction band minimum at the Γ point, thus indicating direct band gap character.

The different behavior (direct versus indirect band gap) of Si and Ge with respect to the film orientation can be explained in term of confinement effects on the conduction band minima (CBM) of the two semiconductors.Whereas the six equivalent ellipsoidal CBM of bulk Si occur in the (100) directions about 80% of the way to the zone boundary, in bulk Ge there are eight symmetry-related ellipsoids with long axes along the (111) directions centered on the midpoints of the hexagonal zone faces. Also the different confinement energy shifts with respect to the orientation of the layer can be interpreted in terms of the different highly anisotropic behavior of the effective masses for bulk Ge and Si [170,171].

Looking then at the optical properties one can see if the appearance of a direct band gap is sufficient to originate strong optical transitions at the band gap minimum. The calculated imaginary part of the dielectric function ϵ_2, as a function of photon energy, is presented in Figure 31 for all the considered Si and Ge films. In general terms, the spectral structures of ϵ_2 of both Si and Ge films has a major peak around 4 eV. This peak corresponds to the E_2 spectral feature occurring at the dielectric function of the bulk materials [172]. For both systems a reduction of the peak intensity is observed when the thickness of the film is decreased, thus reflecting a quantum confinement effect. However, for (100) and (110) surface oriented films this peak reduction is followed by its shift to higher energies, whereas for [111] films it moves to lower photon energies. An interesting comparison between optical properties of Si and Ge films can be made in the low-energy region. Taking into account the LDA underestimation of the band gap, this is the optical region of interest. Here new structures are present that are absent in the case of bulk Si and Ge. For all the structures there is a blue-shift of the ϵ_2 onset owing to the reduction in the effective-film thickness. Moreover, all the Ge films in the three directions considered have a visible shoulder at the low-energy region (about 1.01.2 eV). Since ϵ_2 is directly related to the absorption coefficient, the shoulder in the ϵ_2 curve indicates that there is a strong absorption around this characteristic energy. Moreover, since for the (100)- and (111)-oriented structures the band gap is direct, there is also the possibility of strong PL intensities in these cases. However, this intense feature does not appear for Si films though the energy band structures of (100)- and (110)-oriented structures possess a direct gap.

A deeper insight is gained by analyzing the strength of the optical transitions in the films studied. Looking at the squared optical matrix elements for significant direct transitions between the valence and conduction bands, it is found that for both (100) and (110) Ge films they are orders of magnitude higher than for analogous Si films, moreover for the Ge(100) film those related to the band gap, that is direct, are only one order of magnitude less than the corresponding in bulk GaAs. This property can be useful for optoelectronic applications of Ge quantum films. The first direct transitions in (111) Ge films is practically forbidden; only the second transitions show an appreciable weight. For all Si films the calculated squared optical matrix

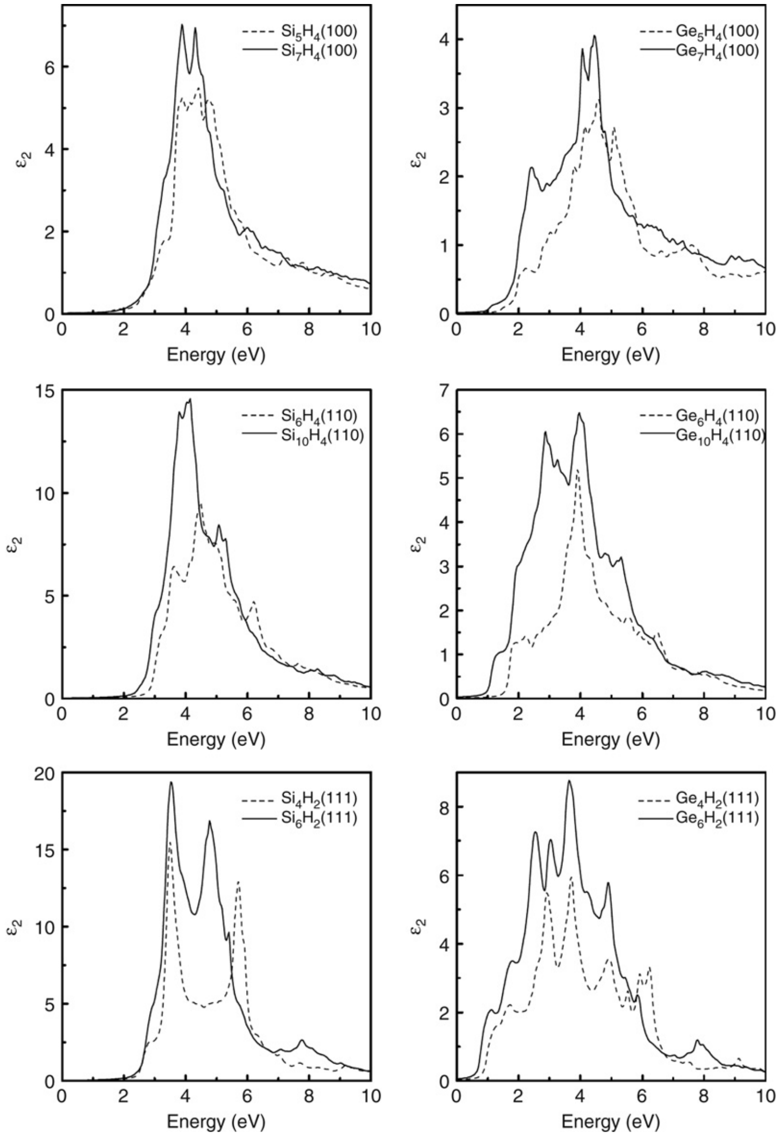

Figure 31 Calculated imaginary part of the dielectric function of Si and Ge quantum films for different orientations and thicknesses. The curves are convolved with Lorentzian broadening of 0.1 eV.

elements are small, only Si(111) films (showing an indirect gap) have an important contribution at high energies close to the direct gap of bulk Si. It is also worthwhile remarking that the squared optical matrix elements related to the second lowest conduction band for (110) and (111) Ge films have the same order of magnitude as the one for GaAs bulk.

The different behavior between the Si and Ge quantum film is related to the different character of the CBM. The CBM are obtained through the folding of the bulk energy bands on the film surface; whereas in Si the CBM mainly retain the original indirect character of the absolute conduction band minimum along the (100) direction, in the case of Ge, especially for the (100) orientation, there is an important mixing between direct and indirect character, owing to the fact that the conduction band minimum at Γ in bulk Ge is only few meV higher than the absolute conduction band minimum along the (111) direction.

The effect of quantum confinement is also pronouncedly seen in the real parts of the dielectric function. The characteristics versus photon energy behavior for all considered Si and Ge quantum films are presented in Figure 32. One can observe the reduction of the maximum value of ϵ_1 as well as its value at zero energy (static dielectric constant) when going to the thinner films. The calculated values of the static dielectric constant ($\epsilon_1(0)$) for the films considered are considerably smaller than that of bulk material. Moreover, for the same film thickness $\epsilon_1(0)$ appears to be higher for the Si structures as compared to the Ge ones, despite the fact that for bulk the Ge value is higher than the Si one. Even if, as stated above, the data shown for the dielectric functions are those relative to the supercell calculation, for films of similar width, at least, semi-quantitative comparison is possible, since the ratio between the volume occupied by the isolated layer and the supercell volume is almost constant in these cases.

5.2. Si/CaF_2 multi-quantum-wells

The lattice-matched system $CaF_2/Si/CaF_2$ is the prototype of a well-controlled and ordered Si-based system with a known microscopic structure. The self-consistent electronic structures of these systems have been calculated by means of the Linear Muffin-Tin Orbitals method in the Atomic Sphere Approximation (LMTO-ASA), which has proven to describe correctly the Si/CaF_2 interface properties [173]. Exchange and correlation effects are included within the density-functional theory in the local density approximation. These calculations for ultrathin Si(111) layers embedded in CaF_2 have shown that quantum confinement causes a band-gap opening which depends on the Si layer thickness, while Si-Ca hybridization effects at the interface lead to dipole-allowed optical transitions all over the Brillouin zone [173]. This section is devoted to the description of the first principles optical properties of Si/CaF_2 multi-quantum wells (MQWs) [167]. In order to overcome the lack of periodicity perpendicular to the interface, for MQW we use supercells formed by a variable number of Si double layers (DL's), separated by CaF_2 layers. The number of CaF_2 layers in the calculations has been chosen large enough to make the central CaF_2 layer exhibits bulk-like properties.

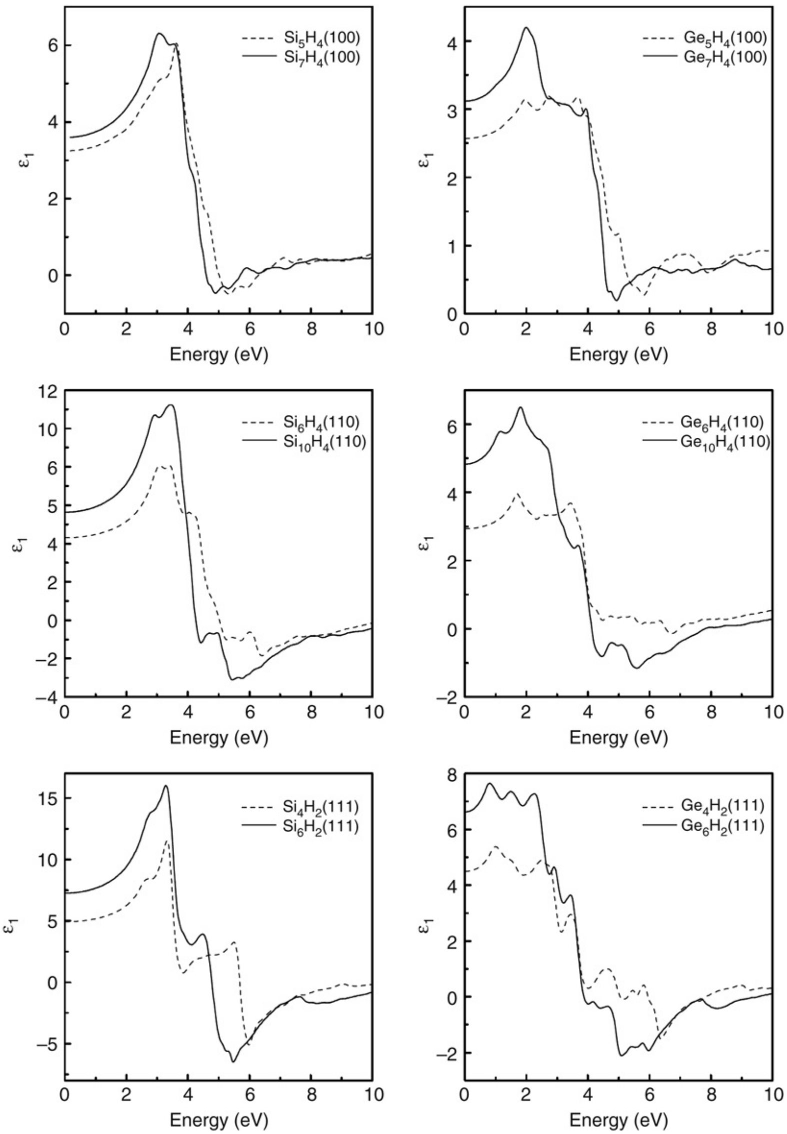

Figure 32 Calculated real part of the dielectric function of Si and Ge quantum films for different orientations and thicknesses. The curves are convolved with Lorentzian broadening of 0.1 eV.

Throughout, we have used the lattice constant of CaF_2 (only 0.6% greater than in bulk Si) except for the interfacial Si–Ca distance, which is taken to be 3.15 Å, as found [174,175] experimentally. Our structural model follows the experimental outcomes [174,175] with the first monolayer of CaF_2 losing half of its fluorine atoms leading to the Ca–Si bond at the interface. The interface Ca atoms occupy the T_4 sites; the triangular filled sites on top of the second layer Si atoms, while the F atoms are located on the H_3 sites, the triangular hollow sites on top of the fourth-layer Si atoms. For further details on the structural model used, the reader is referred to Refs. [167,173]. The thickness of the Si wells embedded in CaF_2 ranges from 0.55 to 2.44 nm. The first value corresponds to the case of a single DL of Si embedded in CaF_2, the second to seven DL's of Si. The optical properties for bulk Si and for the Si slabs embedded in a CaF_2 matrix, as a function of the Si layer thickness, have been computed by evaluating the real (ϵ_1) and imaginary (ϵ_2) part of the dielectric function, as described in Section 2.1.1. The comparison between bulk and slab results gives the possibility to explain features entirely due to the confinement effect. In Figure 33, we show the dependence of our calculated ϵ_2 on the thickness of the Si slab embedded in CaF_2. For comparison, we also report our ϵ_2 result for bulk Si (solid line). For ease of discussion, three main regions have been identified, according to the different portions of ϵ_2, and have been indicated with labels from I to III. Region III between ~10 and ~14 eV is mainly related to the CaF_2 contribution to the ϵ_2 of the MQWs. We note that the features in this region gain weight with respect to region II (between ~3 and ~6 eV) on reducing the thickness of the Si slab; clearly this is due to the increase in weight of the CaF_2 side with respect to Si in the MQWs. In fact, region II is directly related to the crystalline Si contribution to the ϵ_2 of the MQWs; this is the region to be compared directly to the Si bulk result. The main characteristic of region II is the reduction of the maximum value for ϵ_2. This reduction exactly follows the lowering in thickness of the Si slab, and it is due to the confinement effect. In particular we note that the E_1 spectral feature at ~3 eV in bulk Si is weakened and shifts to the blue as a consequence of quantum confinement effect, whereas the E_2 peak shows a red-shift. A different behavior with respect to the influence of quantum confinement of the critical points of the band structure of Si has been demonstrated in the case of extremely thin layers of porous Si [176].

More important for our discussion is the low-energy region I (between ~1 eV and ~2.5 eV). Here features appear which are completely absent in the case of bulk Si. If we take into account the ~0.5 eV LDA underestimation of the Si energy gap, this is the optical region of interest. Experiments on Si/CaF_2 MQWs [44–46] show PL and absorption gaps even in the energy region between ~1.5 and ~2.5 eV, in agreement with our results. Moreover, in Figure 34 we show a blowup of the low energy part of ϵ_2 in the 1–2 eV range. A blue-shift, consistent with quantum confinement, of the onset of ϵ_2 for decreasing Si thickness is clearly evident here and also through the energy gap values reported in Table 10. The only exception is the system with one DL of Si, for which the bonding Si–Ca interface state emerges from the valence band. Second, the features of ϵ_2 in this region are very smooth for the larger Si slab (seven DL's), while their weight increases with confinement.

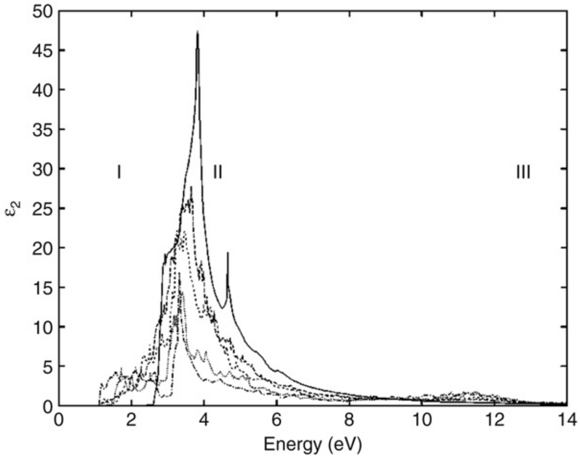

Figure 33 Calculated imaginary part of the dielectric function ϵ_2 for $\mathrm{Si/CaF_2}$ MQWs. Large dashed line: seven Si DL's; small dashed line: four Si DL's; dotted line: two Si DL's; dash-dotted line: one Si DL. The values are compared with that of bulk Si: solid line.

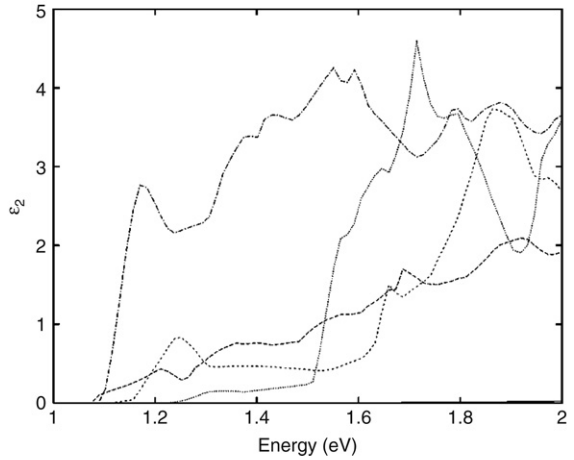

Figure 34 Same as in Figure 33, in the 1–2 eV energy range.

Table 10 Calculated energy gaps, energies and oscillator strengths for significant direct transitions at Γ for the different considered MQWs. The values are compared with that of bulk Si

Lattice	Si bulk	1 DL	2 DL	4 DL	7 DL
Size (nm)		0.55	0.87	1.49	2.44
Gap (eV)	0.56	0.76	1.24	0.63	0.56
ΔE_{cv} (eV)	2.59	2.13	1.81	1.73	1.44
f_{cv}	2.53	0.72	0.66	0.42	0.004

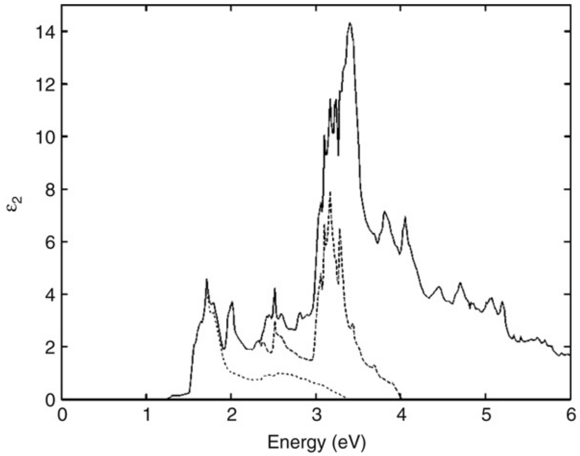

Figure 35 The most important interband contributions to the imaginary part of the dielectric function of the 2-DL $\mathrm{Si/CaF_2}$ MQWs. Solid line: total ϵ_2; short dashed line: contribution from the transition between the last occupied state and the first unoccupied one; long dashed line: the same considering the last two occupied states and the first two empty states.

In order to explain the transitions which play an important role in the low-energy region, in Figure 35 we show (again for the two-DL Si case) the total ϵ_2 (solid line), together with the contributions due to the transitions from the last valence band to the first conduction band (short dashed line), and from the last two valence bands to the first two conduction bands (long dashed line). From the figure, the predominant role played by the band edges is evident, in particular for the interface states in the optical region; we remember that for very thin Si slabs the last occupied and first unoccupied states are mostly related to interface states.
The origin of the peaks is related to the presence of significant matrix elements between particular states which are located at, or just below, the top of the valence band and at, or just above, the bottom of the conduction band. The top valence states are mainly *p* Si-derived states, whereas the bottom conduction ones are mainly *p* Si- and *s* and *d* Ca-derived states. The calculated oscillator strengths for the transitions between these states are listed and compared in Table 10. It is worthwhile noting that the oscillator strengths for the matrix elements between these states increase very rapidly as the thickness of the slabs decreases, and that, for layers with thickness less than 2 nm, they are of the same order of magnitude as the direct transition at Γ in bulk Si and only one order of magnitude smaller than those for GaAs. The reason for the rapid increase of the dipole strength with decreasing slab thickness is due to the different localization of the states involved in the transition. The intensity of the oscillator strength for a transition between two states depends not only on the localization in the reciprocal *k* space but also

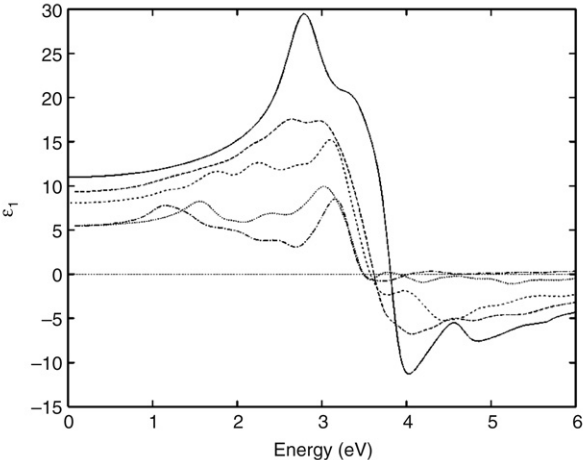

Figure 36 Real part of the dielectric function ϵ_1 for $\mathrm{Si/CaF_2}$ MQW's. Large dashed line: seven Si DL's; small dashed line: four Si DL's; dotted line: two Si DL's; dash-dotted line: one Si DL. The values are compared with that of bulk Si: solid line. Results are convolved with a Gaussian broadening of 0.1 eV.

on the localization in real space, i.e., in which layers these states are localized. For very thin slabs these states are both strongly localized at the interface, whereas for the seven-DL slab case they are spread out over the entire Si slab. Thus the optical transition matrix element which indicates the probability of the transition decrease as the number of Si layers is made larger.

The lineshape of the real part of the dielectric function for each considered MQW is shown in Figure 36 in comparison with the one of bulk Si. A strong reduction of the maximum value of ϵ_1 in going from bulk Si to quantum wells is clear; moreover, we observe that the high-energy shoulder becomes more important with respect to the main peak in the MQW case. Concerning the calculated values of the static dielectric constants $\epsilon_1(0)$, on going from bulk Si to the smaller slab these values reduces from 10.53 (bulk Si) to 9.26 (7DL), 7.98 (4DL), 5.32 (2DL), 5.32 (1DL). We see that all the values are considerably smaller in MQW's than in bulk Si, reflecting quantum confinement effects. The decrease in the static dielectric constant of Si quantum slabs is consistent with the calculated results for Si quantum dots [177] and for Si quantum wires [155]. From the experimental point of view, a similar large reduction of $\epsilon_1(0)$ (from 11.4 to $\sim$3) has been observed in porous Si [178]. Moreover it has recently been observed for Si quantum slabs embedded in $\mathrm{SiO_2}$ [52]. The importance of the reduction of the dielectric constant, in order to use Si for optoelectronic purposes, has been pointed out and discussed [179]. Another interesting implication of this reduction is that the exciton recombination energy in the ultrathin Si slabs could be significantly increased. In the case of Si quantum dots, Wang and Zunger found that for quantum dots whose radius

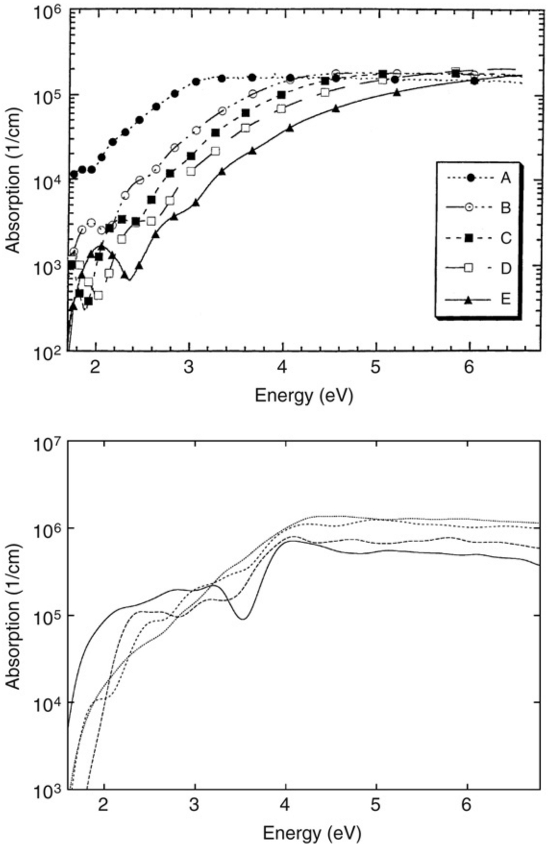

Figure 37 Log to the base ten of the absorption coefficient (cm^{-1}). Top panel: experimental results from Ref. [46]; Si thickness (A) 5.0 nm, (B) 2.0 nm, (C) 1.6 nm, (D) 1.5 nm, (E) 1.0 nm. Bottom panel: theoretical results; large dashed line: 7 Si DL's, small dashed line: 4 Si DL's, dotted line: 2 Si DL's, dash-dotted line: 1 Si DL.

is less than 2 nm the electron–hole pair is confined by the physical dimension of the dot, not by the Coulomb attraction [177].

We have also calculated the absorption coefficient α (see Figure 37 bottom panel) that can be compared with optical absorption measurements performed on Si/CaF$_2$ MQW's synthesized by molecular beam epitaxy [44,46] (see Figure 37 top panel). A striking resemblance between the two results is evident. In both results we observe a blue-shift of the onset and moreover a decrease of the optical absorption with decreasing Si layer thickness. The discrepancy in the absolute value of $\alpha(\omega)$ is a consequence of the use of the repeated slab scheme in the calculations.

5.3. Si/SiO_2 superlattices

Silicon/silicon dioxide (Si/SiO_2) interfaces today play a crucial role in semiconductor technology and could tomorrow play the same crucial role in the field of photonic applications. Through the conventional thermal oxidation process, flat Si/SiO_2 interfaces with very few interface states can easily be obtained. Why the Si/SiO_2 lattice has few interface states is an open question. Actually, the large lattice mismatch of this interface would induce defects in the structure breaking the Si–Si and Si–O–Si bonds in many places and all these defects should create a large number of interface states: this is inconsistent with the experimental evidence. For this reason some mechanisms have to act to passivate the interface states and a lot of hypotheses have been made on the passivation mechanism and on how it works. In the light of these considerations well-characterized Si/SiO_2 nanostructures with variable Si thickness are desirable in order to better understand the role played by the nature of the interface and by the dimensionality on the electronic and optical properties. In particular we are interested in the optical properties of Si/SiO_2 quantum wells and superlattices (SLs) with variable Si layer thickness that we have studied using a first principle method within the LMTO-ASA scheme [168]. We performed our theoretical investigation considering one of the most promising passivation mechanisms, the presence of an extra O atom double bonded to the Si at the interface, proposed by Kageshima and Shiraishi [180–184] and supported by other theoretical models [18,185] and experimental findings [47,186,187]. In order to overcome the lack of periodicity perpendicular to the interface, we use, for SLs calculations, supercells formed by a variable number of Si elementary cells, separated by SiO_2 layers. The elementary Si cell is constituted of five Si layers for a thickness of 0.543 nm, while the SiO_2 thickness of 0.768 nm is the same for all the considered SLs and is large enough to make the central SiO_2 layer exhibit bulk-like properties. We used a β-cristobalite structure for the SiO_2 layer, that has a diamond like symmetry as Si, and leads to a simple model for the interface. The lattice parameter for the β-cristobalite is approximately $\sqrt{2}$ times that for Si, so we obtain a perfect match using a lattice constant of $\sqrt{2} \times 0.543$ nm $=$ 0.768 nm for SiO_2, as Batra [188] and Tit and Dharma-Wardana [189] did, and applying the β-cristobalite structure along the diagonal of the (001) surface unit cell of the Si layer. Using this interface model, as many bonds as possible are formed between Si and SiO_2, but a Si atom at the interface remains unsaturated. For this reason we introduce a double bonded extra O atom (the black atoms in Figure 38) positioned at a distance of 0.1446 nm from the Si surface in accordance with the suggested passivating mechanism [180]: the model used and the atomic arrangement across the interface are shown in Figure 38. Experiments show that the interface is rather abrupt and with very few interface states (this implies a density bulge which has also been

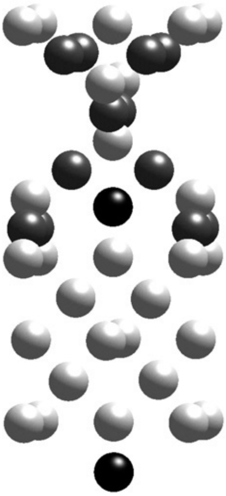

Figure 38 The Si/SiO_2 SL elementary cell with one unit of Si:Si atoms are pale grey and O atoms are dark grey. The β-cristobalite is matched to the Si by rotating the former about the [0 0 1] axis by $\pi/4$. An extra O atom (black) is added to saturate the interface bonds.

observed [190]) and it is also known that the Si/SiO_2 interface contains all the suboxide charge states Si^+, Si^{2+} and Si^{3+}. The model that we use produces a density bulge at the interface and also contains the suboxide-charge states Si^+ and Si^{2+}, but not the Si^{3+}, as is also the case for the energy optimized model due to Pasquarello et al. [191] and Kageshima and Shiraishi [180].

To analyze the role played by the dimensionality we considered three different $Si_{[n]}$-SiO_2 wells with n (the number of elementary Si cells) equal to 1, 2 and 3: the thickness of the wells, taken as the distance between the Si atoms at the two interfaces along the growth direction, is 0.543, 1.086 and 1.629 nm, respectively. To understand the role played by O related defects at the interface of the well we considered two systems, the first fully passivated through the double bonded extra O atom (the black atoms in Figure 38) added to saturate the Si dangling bonds, and the second with an O vacancy at the interface produced removing the same extra O atom.

Concerning the role of dimensionality we observed, in the three fully passivated cases, that the material is a semiconductor, as the band structure of the $Si_{[1]}$–SiO_2 SL in Figure 39(a) shows, and that there is an opening of the gap as the thickness of the Si layer decreases. The band structure shows a gap which is slightly indirect for the presence of a state at the top of the valence band (mostly related to the Si atoms in the inner Si layer), that is partially due to the interaction between the interface Si and its double-bonded O atom. If we remove this extra O, leaving the two dangling bonds of the interface Si unsaturated, we find that the material is still a semiconductor with a new

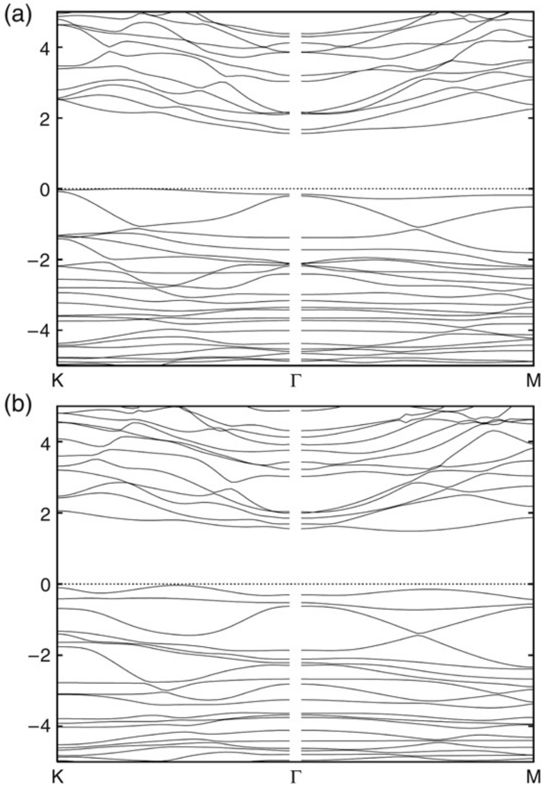

Figure 39 Band structure of the (a) fully saturated and (b) partially saturated $Si_{[1]}$-SiO_2(0 0 1) SL projected along the two symmetry directions of the 2D Brillouin zone of the (0 0 1) surface. K and M represent, respectively, the k-points in the corner and in the middle of the side of the 2D Brillouin zone. A self-energy correction of 0.8 eV has been added to the conduction states. Energies (in eV) are referred to the valence band maximum.

state, a dangling bond interface state, at the top of the valence band that reduces the band gap by 0.12 eV (Figure 39(b)). If we then consider the band structure for the $Si_{[2]}$–SiO_2 and $Si_{[3]}$–SiO_2 SLs with the O vacancy at the interface, we found that, as for the fully saturated lattices, the material is an indirect semiconductor with a progressive gap opening observed as the thickness of the Si layer is reduced and that the interface state, found for the partially passivated $Si_{[1]}$–SiO_2 SL, is now inside the valence band: the interesting fact is that the energy separation between this interface state and the bottom of the conduction band is almost unaffected by the Si layer thickness. The results obtained for the optical properties directly reflect the electronic ones. Actually, if we look at the imaginary part of the dielectric function for the fully saturated lattice with a single Si elementary cell we find new interesting optical features in the visible range completely absent in bulk Si.

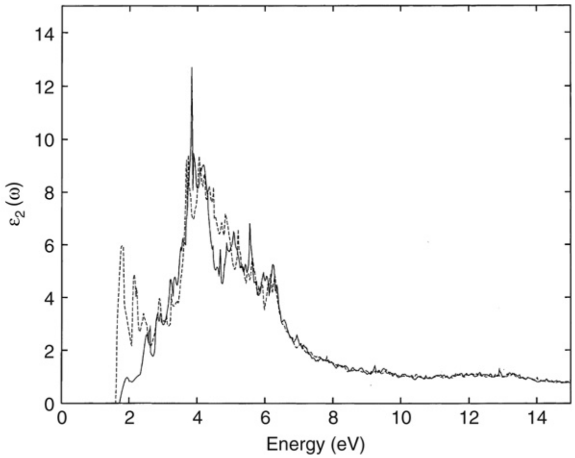

Figure 40 The imaginary part of the dielectric function, ϵ_2, for the $\mathrm{Si}_{[1]}$–SiO_2(0 0 1) fully passivated system (–) compared with the ϵ_2 of the $\mathrm{Si}_{[1]}$– SiO_2(0 0 1) system with an O vacancy at the interface (- - -). A shift of 0.8 eV higher in energy has been applied in order to overcome the LDA underestimation of the gap.

If we then introduce the interface defect (the O vacancy) in the SL, comparing the ϵ_2 for the fully saturated and partially saturated lattice (Figure 40), we observe a new intense asymmetric peak at the low energy edge. The same asymmetric peak can be observed for the $\mathrm{Si}_{[2]}$–SiO_2 and $\mathrm{Si}_{[3]}$– SiO_2 SLs with the O vacancy at the interface. In Figure 40 the imaginary part of the dielectric function is shifted higher in energy by 0.8 eV, in order to overcome the LDA underestimation of the gap, having in this way a better comparison with the experimental data. The value of this self-energy correction is appropriate for our Si confined systems as previous studies [151,192] have shown. Our results can be discussed and compared with experimental data as a function of the Si layer thickness. A lot of experimental work has been done on the optical properties of Si/SiO_2 quantum wells and SLs [15,47–50], nevertheless the situation is still not clear. Anyway, our results are in really good agreement with the experimental data of Kanemitsu and Okamoto [51]. They have studied the luminescence properties of crystalline-Si/SiO_2 single quantum wells. In thin well samples they observed efficient PL in the visible spectral region. In this asymmetric PL spectra they were able to fit two Gaussian bands: a weak band that shifts to higher energy (from ~1.5 to ~1.9 eV) with decreasing Si layer thickness (from 1.7 to 0.6 nm), and a strong band, at ~1.65 eV, almost independent of the well thickness. Kanemitsu and Okamoto [51] attributed the weak band to quantum confinement effects and the strong one to radiative recombination in the interface region; moreover, from the presence of TO phonon related structures, both in the resonant PL spectrum and in the PL polarization spectrum of the quantum confined related band, they speculated about an indirect optical-transition nature for the size quantized states of the two-dimensional (2D) Si wells.

Our task here is to clarify the experimental status for the Si/SiO_2 quantum wells and SLs through the comparison between theory and experiments. We evaluated the imaginary part of the dielectric function that is directly related to the dipole matrix elements; from these we can obtain information directly on absorption, and indirectly on the relevant radiative PL processes, considering the simplest radiative recombination mechanism in which an electron excited from the valence to the conduction band through the absorption of an energy E can directly recombine through the emission of the same energy. Actually, in our calculated ϵ_2 for the partially saturated SL (long-dashed line in Figure 40), we observed that the first asymmetric peak can be fitted by two Gaussian bands as Kanemitsu and Okamoto [51] did in their PL spectra: the first band, more intense, located at ~1.7 eV, is related to the interface state and the second one, weaker and located at ~1.9 eV, is due to the Si bulk-like states. Increasing the Si layer thickness these two Gaussian bands remain recognizable in the ϵ_2 behavior, but their position changes. Repeating the fitting of these peaks with the Gaussian bands for each lattice and plotting them together we are able to see if and how these states are affected by dimensionality.

In Figure 41 the Gaussian bands are shown labelled with a I for the interface band and with a Q for the bulk-like band for the lattices with 3 (Figure 41(a)), 2 (Figure 41(b)) and 1 (Figure 41(c)) Si cells. A shift to higher energies (from ~1.4 to ~1.9 eV) is evident for peak Q when the thickness of the Si layer decreases: this is typically a quantum confinement effect. The energy peak positions related to the quantum confinement states are also confirmed by the corresponding results for the fully saturated systems. The peak I, instead, is almost unaffected by the dimensionality of the Si slab and remain positioned at around 1.7 eV. The comparison between our outcomes in Figure 41 and Kanemitsu and Okamoto's [51] results in Figure 41 (right panel) fully confirms their interpretation on the nature of the PL in these materials. Not only the energy positions of the quantum confined and interface related peaks are in good agreement, but also the relative intensity of the two bands, with respect to each other, agrees.

6. CONCLUSIONS

In the last decade there has been considerable and reasonably satisfactory progress in the understanding of the theoretical aspects of the structural, electronic and optical properties of Si nanostructures. Here we have presented the outcomes of our theoretical study of the properties of Si nanosystems, considering Si nanodots, Si nanowires and Si nanoslabs. We have demonstrated, by first-principle calculations, also beyond the single particle approach, that the structural, electronic, and optical properties of the

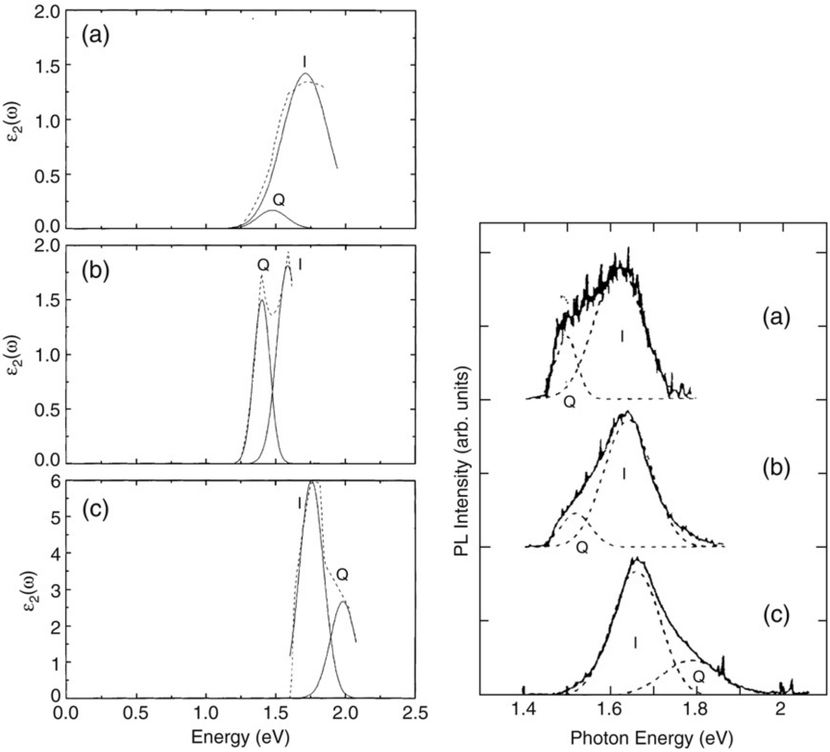

Figure 41 Left panel: calculated ϵ_2 first asymmetric peak (- - -) and its Gaussian fit (—) for the (a) $\mathrm{Si}_{[3]}$–SiO_2, (b) $\mathrm{Si}_{[2]}$–SiO_2 and (c) $\mathrm{Si}_{[1]}$–SiO_2 superlattices. The letter I indicates the interface Gaussian band while the letter Q indicates the bulk-like Gaussian band. Right panel: PL spectra of c-$\mathrm{Si}/\mathrm{SiO}_2$ single quantum wells under 488 nm laser excitation at 2 K: (a) 1.7 nm, (b) 1.3 nm and (c) 0.6 nm thickness. The asymmetric PL spectra can be fitted by two Gaussian bands, the weak Q band and the strong I band [51].

nanosystems strongly depend not only on the quantum confinement effects, but also on the different passivation regimes and on the nature of doping.

In the case of nanodots, we considered both undoped and doped Si-based nanocrystals, whose dimensions are up to the nanometer range. Particular attention has been paid to the outcomes related to the role of surface termination and to the nanocrystal's excited states. In particular we have found that the presence of an electron–hole pair in the nanocrystals causes a strong deformation of the structures with respect to their ground-state configuration, and this is more evident for smaller systems, that a significant contribution to the Stokes shift arises from relaxation after excitation of the nanocrystal, and that considering the HOMO–LUMO gaps of the ground and excited state as the proper absorption and emission energies is more in error as the cluster gets smaller. Regarding the surface termination effects, we have discussed the role of O at the interface, and we have found that the full inclusion of the excitonic effects in the calculation of the emission spectra suggest that the Si–O–Si bridge bond is responsible for the strong PL peak experimentally observed in oxidized Si nanocrystals. In relation to the doping we have demonstrated that Si nanocrystals can be more easily simultaneously doped than single-doped, and that by co-doping it is possible to engineer the PL properties of the Si nanocrystals. Moreover, the case of multiple doping has been evaluated and discussed. Concerning the Si nanocrystals embedded in a SiO_2 matrix, in comparison with experiments we have elucidated the important role played by the interface region. Indeed a model for the screening in Si nanoparticles has been presented and discussed.

For Ge and Si nanowires we showed the crucial role played by the electron–hole interaction. We highlighted the effect of the different geometrical structures of nanowires of different orientation on the optical spectra: in some cases the wire is made of connected clusters, while in other cases it resembles a nanotube. Very large excitonic effects, different in the two cases, have been calculated that clearly depend on the orientation and symmetry of the nanowires. It emerged that Ge nanowires show strong optical absorption at lower frequencies than Si nanowires, with the main peak occurring in the visible range. These outcomes, in comparison with the experimental data, helped in understanding the role of self-energy correction and electron–hole interaction on the electronic and optical properties of Si nanowires. In addition, the dependence of the optical anisotropy on the crystalline packing pointed out the structural difference between isolated nanowires and porous Si. Finally, the doping properties of Si nanowires have been calculated and the role of the impurity concentration outlined and discussed.

Concerning the Si nanoslabs, we considered Si nanofilms terminated by H and Si quantum wells covered by CaF_2 and SiO_2. For the nanofilms, zone folding due to the confinement effect has been found to result in a direct band gap for both [100] Si and Ge nanostructures. For the [110] orientation, only Si films have a direct transition at the Brillouin Zone center. In the case of [111]-oriented Si and Ge films, one may speak of indirect and direct band gap semiconductors, respectively. For the optical properties, it has been shown that for Si films a noticeable increase in ϵ_2 is observed only at high energies close to the corresponding direct band gap of bulk Si. This is due to the fact that the direct gap appearing in the Si films still retains its original indirect character. Only Ge films possess a characteristic strong shoulder on the absorption. Because of the quantum confinement effect the calculated static dielectric constants for all the considered films are considerably lower than those of bulk material. For the Si quantum wells covered by CaF_2 we have shown that the optoelectronic spectrum is affected both by confinement and by hybridization effects. The major outcome in this case is that for Si well dimensions less than 2 nm, interesting transitions appear in the optical region, with oscillator strengths which show a dramatic increase as the slab width decreases. Moreover, here the static dielectric constants for the thin slabs are also considerably smaller than that for bulk Si. In the case of Si/SiO_2 superlattices we considered both fully passivated interfaces and the presence of an O vacancy at the interface. Here our results showed the key role played both by the quantum confined states and interface states in the experimentally observed visible luminescence in Si/SiO_2 confined systems.

ACKNOWLEDGMENTS

We would like to acknowledge all the people that have been involved in our efforts, in particular C. Arcangeli, M. Amato, F. Arnaud D'Avitaya, F. Bassani, F. Bechstedt, F. Bernardini, O. Bisi, V. E. Borisenko, M. Bruno, G. Cantele, N. Daldosso, L. Dal Negro, R. Del Sole, A. Fasolino, A. Filonov, M. Gatti, R. Guerra, F. Iori, A. N. Kholod, E. Luppi, M. Luppi, R. Magri, A. Marini, I. Marri, D. Ninno, G. Onida, V. Olevano, M. Palummo, L. Pavesi, O. Pulci, L. Ramos, F. Trani and L. Vervoort. All the calculations have been performed at CINECA-Bologna (we acknowledge the "Iniziativa calcolo parallelo" of CNR-INFM) and CICAIA-Modena advanced computing facilities. Financial support through PRIN2007 and CNR Project Italia-Turchia is also acknowledged.

REFERENCES

[1] S. Ossicini, L. Pavesi, F. Priolo, Light Emitting Silicon for Microphotonics, in: Springer Tracts on Modern Physics, vol. 194, Springer-Verlag, Berlin, 2003.
[2] L. Pavesi, E. Buzaneva, Frontiers of Nano-Optoelectronics Systems, in: NATO Science Series II. Mathematics, Physics and Chemistry, vol. 6, Kluwer Academic Publishers, Dordrecht, 2000.
[3] L.T. Canham, Appl. Phys. Lett. 57 (1990) 1046.
[4] D. Bensahel, L.T. Canham, S. Ossicini (Eds.), Optical Properties of Low Dimensional Silicon Structures, Kluwer, Dordrecht, Amsterdam, 1993.
[5] B. Hamilton, Semicond. Sci. Technol. 10 (1995) 1187.
[6] Y. Kanemitsu, Phys. Rep. 263 (1995) 1.
[7] G.S. John, V.A. Singh, Phys. Rep. 263 (1995) 93–151.
[8] L.T. Canham (Ed.), Properties of Porous Silicon, INSPEC: The Institution of Electrical Engineers, London, 1997.
[9] A.G. Cullis, L.T. Canham, P.D.J. Calcott, J. Appl. Phys. 82 (1997) 909.
[10] O. Bisi, S. Ossicini, L. Pavesi, Surf. Sci. Reports 38 (2000) 5.
[11] Y. Takahashi, T. Furuta, Y. Ono, T. Tsishima, M. Tabe, Jpn. J. Appl. Phys. 34 (1995) 950.
[12] D.J. Lockwood, Z.H. Lu, J.-M. Baribeau, Phys. Rev. Lett. 76 (1996) 539.
[13] S.V. Novikov, J. Sinkkonen, O. Kilpela, S.V. Gastev, J. Vac. Sci. Technol. B 15 (1997) 1471.
[14] Y. Kanemitsu, S. Okamoto, Phys. Rev. B 56 (1997) R15561.
[15] V. Mulloni, R. Chierchia, C. Mazzoleni, G. Pucker, L. Pavesi, P. Bellutti, Phil. Mag. B 80 (2000) 705–718.
[16] B. Gelloz, A. Kojima, N. Koshida, Appl. Phys. Lett. 87 (2005) 031107.
[17] R.J. Baierle, M.J. Caldas, E. Molinari, S. Ossicini, Solid State Commun. 102 (1997) 545.
[18] M.V. Wolkin, J. Jorne, P.M. Fauchet, G. Allan, C. Delerue, Phys. Rev. Lett. 82 (1999) 197.
[19] A. Puzder, A.J. Williamson, J.C. Grossman, G. Galli, Phys. Rev. Lett. 88 (2002) 097401.
[20] M. Luppi, S. Ossicini, Phys. Rev. B 71 (2005) 035040.
[21] M. Luppi, S. Ossicini, Phys. Stat. Sol. (a) 197 (2003) 251.

[22] M. Luppi, S. Ossicini, J. Appl. Phys. 94 (2003) 2130.
[23] I. Vasiliev, J.R. Chelikowsky, R.M. Martin, Phys. Rev. B 65 (2002) 121302(R).
[24] L. Pavesi, L. Dal Negro, C. Mazzoleni, G. Franzò, F. Priolo, Nature 408 (2000) 440.
[25] L. Dal Negro, M. Cazzanelli, L. Pavesi, S. Ossicini, D. Pacifici, G. Franzò, F. Priolo, F. Iacona, Appl. Phys. Lett. 82 (2003) 4636.
[26] J. Ruan, P.M. Fauchet, L. Dal Negro, M. Cazzanelli, L. Pavesi, Appl. Phys. Lett. 83 (2003) 5479.
[27] M. Cazzanelli, D. Kovalev, L. Dal Negro, Z. Gaburro, L. Pavesi, Phys. Rev. Lett. 93 (2004) 207042.
[28] S. Ossicini, C. Arcangeli, O. Bisi, E. Degoli, M. Luppi, R. Magri, L. Dal Negro, L. Pavesi, in: L. Dal Negro, S. Gaponenko, L. Pavesi (Eds.), Towards the First Silicon Laser, in: Nato Science Series, vol. 93, Kluwer Academic Publishers, Dordrecht, 2003, p. 271.
[29] G. Allan, C. Delerue, M. Lannoo, Phys. Rev. Lett. 76 (1996) 2961.
[30] C. Delerue, G. Allan, M. Lannoo, J. Lum. 80 (1999) 65.
[31] C. Delerue, G. Allan, M. Lannoo, Phys. Rev. B 64 (2001) 193402.
[32] M. Fujii, Y. Yamaguchi, Y. Takase, K. Ninomiya, S. Hayashi, Appl. Phys. Lett. 87 (2005) 211919.
[33] M. Fujii, K. Toshikiyo, Y. Takase, Y. Yamaguchi, S. Hayashi, J. Appl. Phys. 94 (2003) 1990.
[34] M. Fujii, Y. Yamaguchi, Y. Takase, K. Ninomiya, S. Hayashi, Appl. Phys. Lett. 85 (2004) 1158.
[35] A.M. Morales, C.M. Lieber, Science 279 (1998) 208.
[36] J.D. Holmes, K.P. Johnston, R.C. Doty, B.A. Korgel, Science 287 (2000) 1471.
[37] D.D.D. Ma, C.S. Lee, F.C.K. Au, S.Y. Tong, S.T. Lee, Science 299 (2003) 1874.
[38] M. Kawamura, N. Paul, V. Cherepanov, B. Voigtländer, Phys. Rev. Lett. 91 (2003) 096102.
[39] J.C. She, S.Z. Deng, N.S. Xu, R.H. Yao, J. Chen, Appl. Phys. Lett. 88 (2006) 013112.
[40] Y. Cui, C.M. Lieber, Science 291 (2001) 851.
[41] J. Hahm, C. Lieber, Nano Lett. 4 (2004) 51.
[42] X.T. Zhou, J.Q. Hu, C.P. Li, D.D.D. Ma, C.S. Lee, S.T. Lee, Chem. Phys. Lett. 369 (2003) 220.
[43] Y. Wu, R. Fan, P. Yang, Nano Lett. 2 (2002) 83.
[44] F. Arnaud D'Avitaya, L. Vervoort, S. Ossicini, A. Fasolino, F. Bernardini, Europhys. Lett. 31 (1995) 25.
[45] F. Bassani, L. Vervoort, I. Mihalcescu, J.C. Vial, F. Arnaud D'Avitaya, J. Appl. Phys. 79 (1996) 4066.
[46] F. Bassani, I. Mihalcescu, J.C. Vial, F. Arnaud D'Avitaya, Appl. Surf. Sci. 117/118 (1997) 670.
[47] Y. Takahashi, T. Furuta, Y. Ono, T. Tsishima, M. Tabe, Jpn. J. Appl. Phys. 34 (1995) 950.
[48] D.J. Lockwood, Z.H. Lu, J.-M. Baribeau, Phys. Rev. Lett. 76 (1996) 539.
[49] S.V. Novikov, J. Sinkkonen, O. Kilpela, S.V. Gastev, J. Vac. Sci. Technol. B 15 (1997) 1471.
[50] K.S. Min, K.V. Shcheglov, C.M. Yang, H.A. Atwater, M.L. Brongersma, A. Polman, Appl. Phys. Lett. 69 (1996) 2033.
[51] Y. Kanemitsu, S. Okamoto, Phys. Rev. B 56 (1997) R15561.
[52] H.G. Yoo, P.M. Fauchet, Phys. Rev. B 77 (2008) 115355.
[53] O. Pulci, M. Marsili, E. Luppi, C. Hogan, V. Garbuio, F. Sottile, R. Magri, R. Del Sole, Phys. Stat. Sol. (b) 242 (13) (2005) 2737–2750.
[54] M. Palummo, M. Bruno, O. Pulci, E. Luppi, E. Degoli, S. Ossicini, R. Del Sole, Surf. Sci. 601 (13) (2007) 2696.
[55] P. Hohenberg, W. Kohn, Phys. Rev. B 136 (1964) 864.
[56] W. Kohn, L.J. Sham, Phys. Rev. A 140 (1965) 1113.
[57] D.M. Ceperley, B.J. Alder, Phys. Rev. Lett. 45 (1980) 566;
J.P. Perdew, A. Zunger, Phys. Rev. B 23 (1981) 5048.
[58] F. Bassani, G. Pastori Parravicini, Electronic States and Optical Transitions in Solids, Pergamon Press, New York, 1975.
[59] M. Alouani, L. Brey, N.E. Christensen, Phys. Rev. B 37 (1988) 1167.
[60] L. Fetter, J.D. Walecka, Quantum Theory of Many Body Systems, McGraw-Hill, New York, 1981.

[61] L. Hedin, Phys. Rev. A 139 (1965) 796;
R.D. Mattuck, A Guide to Feynman Diagrams in the Many Body Problem, McGraw-Hill, New York, 1976.

[62] L. Hedin, B.J. Lundquist, in: H. Ehrenreich, F. Seitz, D. Turnbull (Eds.), Solid State Phys., vol. 23, Academic Press, New York, 1969, p. 1.

[63] F. Aryasetiawan, O. Gunnarsson, Rep. Prog. Phys. 61 (1998) 237;
W.G. Aulbur Johsson, J.W. Wilkins, Solid State Phys. 54 (2000) 1–218.

[64] S.L. Adler, Phys. Rev. 126 (1962) 413;
N. Wiser, Phys. Rev. 129 (1963) 62.

[65] T. Takagahara, K. Takeda, Phys. Rev. B 46 (1992) 15578.

[66] J. Lockwood, Solid State Commun. 92 (1994) 101.

[67] First-principles computation of material properties: The ABINIT software project (URL http://www.abinit.org);
X. Gonze, J.-M. Beuken, R. Caracas, F. Detraux, M. Fuchs, G.-M. Rignanese, L. Sindic, M. Zerah, Verstraete Jollet, G. Torrent, F. Roy, M. Mikami, A. Ghosez, M. Raty, Ph. Allan, Comp. Mat. Science 25 (2002) 478.

[68] E. Degoli, G. Cantele, E. Luppi, R. Magri, D. Ninno, O. Bisi, S. Ossicini, Phys. Rev. B 69 (2004) 155411.

[69] J.P. Wicoxon, G.A. Samara, P.N. Provencio, Phys. Rev. B 60 (1999) 2704.

[70] G. Belomoin, J. Therrien, M.H. Nayfeh, Appl. Phys. Lett. 77 (2000) 779.

[71] C. Delerue, M. Lannoo, G. Allan, Phys. Rev. Lett. 84 (2000) 2457.

[72] J.C. Grossman, M. Rohlfing, L. Mitas, S.G. Louie, M.L. Cohen, Phys. Rev Lett. 86 (2001) 472.

[73] G. Onida, W. Andreoni, Chem. Phys. Lett. 243 (1995) 183.

[74] The absorption gap value for the $Si_{29}H_{36}$ cluster cited by Franceschetti is 4.3 eV but it is estimated by adding the local-spin density band-gap error of bulk Si (0.7 eV)..

[75] A. Puzder, A.J. Williamson, J.C. Grossman, G. Galli, J. Am. Chem. Soc. 125 (2003) 2786.

[76] A. Franceschetti, S.T. Pantelides, Phys. Rev. B 68 (2003) 033313.

[77] U. Itoh, Y. Toyoshima, H. Onuki, N. Washida, T. Ibuki, J. Chem. Phys. 85 (1986) 4867.

[78] M. Rohlfing, S.G. Louie, Phys. Rev. Lett. 80 (1998) 3320.

[79] M. Hirao, in: L. Brus, M. Hirose, R.W. Collins, F. Koch, C.C. Tsai (Eds.), Microcristalline and Nanocrystalline Semiconductors, in: Mater. Res. Soc. Symp. Proc., vol. 358, Material Research Society, Pittsburgh, 1995.

[80] O. Lehtonen, D. Sundholm, Phys. Rev. B 72 (2005) 085424.

[81] G. Belomoin, J. Therrien, A. Smith, S. Rao, R. Twesten, S. Chaieb, M.H. Nayfeh, L. Wagner, L. Mitas, Appl. Phys. Lett. 80 (2002) 841.

[82] Y. Kanemitsu, S. Okamoto, Phys. Rev. B 58 (1998) 9652.

[83] E. Luppi, E. Degoli, G. Cantele, S. Ossicini, R. Magri, D. Ninno, O. Bisi, O. Pulci, G. Onida, M. Gatti, A. Incze, R. Del Sole, Opt. Mater. 27 (2005) 1008.

[84] M. Bockstedte, A. Kley, J. Neugebauer, M. Scheffler, Comput. Phys. Commun. 107 (1997) 187.

[85] Cambridge Serial Total Energy Package, Version 4.2.1, 1 October 2000.

[86] V. Milman, B. Winkler, J.A. White, C.J. Pickard, M.C. Payne, E.V. Akhmatskaya, R.H. Nobes, Int. J. Quantum Chem. 77 (2000) 895.

[87] Cerius^2 Users Guide and Materials Studio 2.1.5 Users Guide for CASTEP, MSI and Accelrys Inc., 2000–2002.

[88] L. Kleinman, D.M. Bylander, Phys. Rev. Lett. 48 (1982) 1425.

[89] N. Troullier, J.L. Martins, Phys. Rev. B 43 (1991) 1993.

[90] D. Vanderbilt, Phys. Rev. B 41 (1990) R7892.

[91] R. Sammynaiken, S.J. Naftel, T.K. Shamb, K.W. Cheah, B. Averboukh, R. Huber, Y.R. Shen, G.G. Qin, Z.C. Ma, W.H. Zhong, J. Appl. Phys. 92 (2002) 3000.

[92] E. Luppi, F. Iori, R. Magri, O. Pulci, R. Del Sole, S. Ossicini, E. Degoli, V. Olevano, Phys. Rev. B 75 (2007) 033303.

[93] M. Gatti, G. Onida, Phys. Rev. B 72 (2005) 045442.

[94] The $Si_{10}H_{14}$ >O cluster we considered here corresponds to the $Si_{10}H_{14}$O-sym of [93], where O make a bridge between "second neighbors" Si atoms. We have obtained similar results have for the $Si_{10}H_{14}$O-asym case, where O is in between two "first neighbors" Si atoms..

[95] S. Baroni, A. Dal Corso, S. de Gironcoli, P. Giannozzi, C. Cavazzoni, G. Ballabio, S. Scandolo, G. Chiarotti, P. Focher, A. Pasquarello, K. Laasonen, A. Trave, R. Car, N. Marzari, A. Kokalj, The DFT calculations for oxidized clusters have been performed using the ESPRESSO package. http://www.pwscf.org/.

[96] Z. Ma, X. Liao, G. Kong, J. Chu, Appl. Phys. Lett. 75 (1999) 1857.

[97] H. Kageshima, K. Shiraishi, in: M. Scheffler, R. Zimmermann (Eds.), Proc. 23rd Int. Conf. Phys. Semicon., World Scientific, Singapore, 1996, p. 903.

[98] N. Daldosso, M. Luppi, S. Ossicini, E. Degoli, R. Magri, G. Dalba, P. Fornasini, R. Grisenti, F. Rocca, L. Pavesi, S. Boninelli, F. Priolo, C. Spinella, F. Iacona, Phys. Rev. B 68 (2003) 085327.

[99] T. Takagahara, K. Takeda, Phys. Rev. B 46 (1992) 15578.

[100] E. Lioudakis, A. Othonos, G.C. Hadjisavvas, P.C. Kelires, A.G. Nassiopoulou, Physica E 38 (2007) 128.

[101] G. Hadjisavvas, P.C. Kelires, Physica E 38 (2007) 99.

[102] The numerical values differences with respect to the previously published paper, [20] are due to the different computational code used.

[103] G. Cantele, E. Degoli, E. Luppi, R. Magri, D. Ninno, G. Iadonisi, S. Ossicini, Phys. Rev. B 72 (2005) 113303.

[104] S. Ossicini, E. Degoli, F. Iori, E. Luppi, R. Magri, G. Cantele, F. Trani, D. Ninno, Appl. Phys. Lett. 87 (2005) 173120.

[105] S. Ossicini, F. Iori, E. Degoli, E. Luppi, R. Magri, R. Poli, G. Cantele, F. Trani, D. Ninno, J. Select. Topics in Quantum Electr. 12 (2006) 1585.

[106] F. Iori, E. Degoli, E. Luppi, R. Magri, I. Marri, G. Cantele, D. Ninno, F. Trani, S. Ossicini, J. Lumin. 121 (2006) 335.

[107] F. Iori, S. Ossicini, E. Degoli, E. Luppi, R. Poli, R. Magri, G. Cantele, F. Trani, D. Ninno, Phys. Stat. Sol. (a) 204 (2007) 1312.

[108] R. Magri, E. Degoli, F. Iori, E. Luppi, O. Pulci, S. Ossicini, G. Cantele, F. Trani, D. Ninno, J. Comp. Meth. Sci. Eng. 7 (2007) 219.

[109] F. Iori, E. Degoli, R. Magri, I. Marri, G. Cantele, D. Ninno, F. Trani, O. Pulci, S. Ossicini, Phys. Rev. B 76 (2007) 085302.

[110] S. Ossicini, E. Degoli, F. Iori, O. Pulci, G. Cantele, R. Magri, O. Bisi, F. Trani, D. Ninno, Surf. Sci. 601 (2007) 2724.

[111] S. Ossicini, O. Bisi, E. Degoli, I. Marri, F. Iori, E. Luppi, R. Magri, R. Poli, G. Cantele, D. Ninno, F. Trani, M. Marsili, O. Pulci, M. Gatti, K. Gaal-Nagy, A. Incze, G. Onida, V. Olevano, J. Nanosci. Nanotechn. 8 (2008) 479.

[112] D. Vanderbilt, Phys. Rev. B 41 (1990) R7892.

[113] L.E. Ramos, E. Degoli, G. Cantele, S. Ossicini, D. Ninno, J. Furthmüller, F. Bechstedt, J. Phys.: Cond. Matt. 19 (2007) 466211.

[114] L.C. Ciacchi, M.C. Payne, Phys. Rev. Lett. 95 (2005) 196101.

[115] E. Garrone, F. Geobaldo, P. Rivolo, G. Amato, L. Boarino, M. Chiesa, E. Giamello, R. Gobetto, P. Ugliengo, A. Vitale, Adv. Mater. 17 (2005) 528.

[116] V. Olevano, Exc Code, http://www.bethe-salpeter.org.

[117] D.V. Melnikov, J.R. Chelikowsky, Phys. Rev. Lett. 92 (2004) 046802.

[118] P.Y. Yu, M. Cardona, Fundamentals of Semiconductors, Springer, Berlin, 2001.

[119] C.D. Spataru, S. Ismail-Beigi, L.X. Benedict, S.G. Louie, Phys. Rev. Lett. 92 (2004) 077402.

[120] E. Chang, G. Bussi, A. Ruini, E. Molinari, Phys. Rev. Lett. 92 (2004) 196401.

[121] M. Bruno, M. Palummo, A. Marini, R. Del Sole, V. Olevano, A.N. Kholod, S. Ossicini, Phys. Rev. B 72 (2005) 153310.

[122] M. Bruno, M. Palummo, A. Marini, R. Del Sole, S. Ossicini, Phys. Rev. Lett. 98 (2007) 036807.

[123] F. Trani, D. Ninno, G. Cantele, G. Iadonisi, K. Hameeuw, E. Degoli, S. Ossicini, Phys. Rev. B 73 (2006) 245430.

[124] D. Ninno, F. Trani, G. Cantele, G. Iadonisi, K.J. Hameeuw, E. Degoli, S. Ossicini, Europhys. Lett. 74 (2006) 519.

[125] C. Delerue, M. Lannoo, G. Allan, Phys. Rev. B 68 (2003) 115411.

[126] R. Resta, Phys. Rev. B 16 (1977) 2717.

[127] S. Öğüt, R. Burdick, Y. Saad, J.R. Chelikowsky, Phys. Rev. Lett. 90 (2003) 127401.

[128] Y. Cui, Z. Zhong, D. Wang, W.U. Wang, C.M. Lieber, Nanoletters 3 (2003) 149.

[129] Y. Cui, C.M. Lieber, Science 291 (2001) 851.

[130] Y. Huang, X. Duan, Y. Cui, C.M. Lieber, Nanoletters 2 (2001) 101.

[131] X. Duan, Y. Huang, Y. Cui, J. Wang, C.M. Lieber, Nature 409 (2001) 066.

[132] X. Duan, Y. Huang, C.M. Lieber, Nano Letters 2 (2002) 487.

[133] Y. Cui, L.J. Lauhon, M.S. Gudiksen, J. Wang, C.M. Lieber, Appl. Phys. Lett. 78 (2001) 02214.

[134] Y. Cui, Q. Wei, H. Park, C.M. Lieber, Science 293 (2001) 1289.

[135] M.H. Huang, S. Mao, H. Feick, H. Yan, Y. Wu, H. Kind, E. Weber, P. Russo, P. Yang, Science 292 (2001) 1897.

[136] X. Duan, Y. Huang, R. Agarwal, C.M. Lieber, Nano Lett. 421 (2003) 241.

[137] L.J. Lauhon, M.S. Gudiksen, D. Wang, C.M. Lieber, Nature 420 (2002) 57.

[138] Y. Wu, Y. Cui, L. Huynh, C.J. Barrelet, D.C. Bell, C.M. Lieber, Nano Lett. 4 (2004) 433.

[139] M. Menon, D. Srivastava, I. Ponomareva, L.A. Chernozatonskii, Phys. Rev. B 70 (2004) 125313.

[140] A.M. Morales, C.M. Lieber, Science 279 (1998) 208.

[141] J.D. Holmes, K.P. Johnston, R.C. Doty, B.A. Korgel, Science 287 (2000) 1471.

[142] X. Duan, J. Wang, C.M. Lieber, Appl. Phys. Lett. 76 (2000) 01116.

[143] D. Katz, T. Wizansky, O. Millo, E. Rothenberg, T. Mokari, U. Banin, Phys. Rev. Lett. 89 (2002) 86801.

[144] Y.F. Zhang, Y.H. Tang, N. Wang, C.S. Lee, I. Bello, S.T. Lee, Phys. Rev. B 61 (2000) 4518.

[145] D. Wang, Q. Wang, A. Javey, R. Tu, H. Dai, Appl. Phys. Lett. 83 (2003) 2432.

[146] A. Alguno, N. Usami, T. Ujihara, K. Fujiwara, G. Sazaki, K. Nakajima, Appl. Phys. Lett. 83 (2003) 1258.

[147] A.K. Singh, V. Kumar, Y. Kawazoe, Phys. Rev. B 69 (2004) 233406.

[148] M.P. Halsall, H. Omi, T. Ogino, Appl. Phys. Lett. 81 (2002) 2448.

[149] X. Zhao, C.M. Wei, L. Yang, M.Y. Chou, Phys. Rev. Lett. 92 (2004) 236805.

[150] M. Bruno, M. Palummo, S. Ossicini, R. Del Sole, Surf. Sci. 601 (2007) 2707.

[151] M.S. Hybertsen, M. Needels, Phys. Rev. B 48 (1993) 4608.

[152] A.J. Read, R.J. Needs, K.J. Nash, L.T. Canham, P.D.J. Calcott, A. Qteish, Phys. Rev. Lett. 69 (1992) 01232.

[153] F. Buda, J. Kohano, M. Parrinello, Phys. Rev. Lett. 69 (1992) 01272.

[154] A.N. Kholod, V.L. Shaposhnikov, N. Sobolev, V.E. Borisenko, F.A. D'Avitaya, S. Ossicini, Phys. Rev. B 70 (2004) 035317.

[155] S. Ossicini, C.M. Bertoni, M. Biagini, A. Lugli, G. Roma, O. Bisi, Thin Solid Films 297 (1997) 154.

[156] S. Ossicini, Phys. Stat. Sol. (a) 170 (1998) 377.

[157] R. Kagimura, R.W. Nunes, H. Chacham, Phys. Rev. Lett. 95 (2005) 115502.

[158] R. Rurali, N. Lorente, Phys. Rev. Lett. 94 (2005) 026805.

[159] T. Ogawa, T. Takagahara, Phys. Rev. B 44 (1991) 8138.

[160] Y. Zheng, C. Rivas, T. Lake, K. Alam, T.B. Boykin, G. Klimeck, IEEE Trans. Electr. Dev. 52 (2005) 1097.

[161] Y.M. Niquet, A. Lherbier, N.H. Quang, M.V. Fernandez-Serra, X. Blase, C. Delerue, Phys. Rev. B 73 (2006) 165319.

[162] Q. Zhang, S.C. Bayliss, J. Appl. Phys. 79 (1996) 1351.

[163] H.C. Weissker, J. Furthmuller, F. Bechstedt, Phys. Rev. B 69 (2004) 115310.

[164] M.V. Fernández-Serra, Ch. Adessi, X. Blase, Nano Lett. 6 (2006) 2674.

[165] H. Peelaers, B. Partoens, F.M. Peeters, Nano Lett. 6 (2006) 2781.

[166] A.N. Kholod, S. Ossicini, V.N. Borisenko, F. Arnaud d'Avitaya, Surf. Sci. 527 (2003) 30.

[167] E. Degoli, S. Ossicini, Phys. Rev. B 57 (1998) 14776.
[168] E. Degoli, S. Ossicini, Surf. Sci. 470 (2000) 32.
[169] P. Blaha, K. Schwarz, J. Luitz, WIEN97, Vienna University of Technology, Vienna, 1997 (improved and updated Unix version of the original copyrighted WIEN-code, which was published by P. Blaha, K. Schwarz, P. Sorantin, S.B. Trickey, in Comput. Phys. Commun. 59, 399 (1990)).
[170] A.N. Kholod, A. Saúl, J. Fuhr, V.E. Borisenko, F. Arnaud d'Avitaya, Phys. Rev. B 62 (2000) 12949.
[171] M.L. Cohen, J.R. Chelikowsky, Electronic Structure and Optical Properties of Semiconductors, Springer-Verlag, Berlin, 1989.
[172] P.N. Saeta, A.C. Gallagher, Phys. Rev. B 55 (1997) 4563.
[173] S. Ossicini, A. Fasolino, F. Bernardini, Phys. Rev. Lett. 72 (1994) 1044.
[174] R.M. Tromp, M.C. Reuter, Phys. Rev. Lett. 61 (1988) 1756.
[175] J. Zegenhagen, J.R. Patel, Phys. Rev. B 41 (1990) 5315.
[176] M. Ben-Chorin, B. Averboukh, D. Kovalev, G. Polisski, F. Koch, Phys. Rev. Lett. 77 (1996) 763.
[177] L. Wang Wang, A. Zunger, Phys. Rev. Lett. 73 (1994) 1039.
[178] N. Koshida, H. Koyama, Y. Suda, Y. Yamamoto, M. Araki, T. Saito, K. Sato, N. Sata, S. Shin, Appl. Phys. Lett. 63 (1993) 2774.
[179] L. Pavesi, R. Guardini, C. Mazzoleni, Solid State Commun. 97 (1996) 1051.
[180] H. Kageshima, K. Shiraishi, in: M. Scheffler, R. Zimmermann (Eds.), Proc. 23rd Int. Conf. Phys. Semicon., World Scientific, Singapore, 1996, p. 903.
[181] H. Kageshima, K. Shiraishi, Surf. Sci. 380 (1997) 61–65.
[182] H. Kageshima, K. Shiraishi, Surf. Sci. 407 (1998) 133–139.
[183] H. Kageshima, K. Shiraishi, Phys. Rev. Lett. 81 (1998) 5936.
[184] H. Kageshima, K. Shiraishi, Surf. Sci. 438 (1999) 102–106.
[185] T. Uchiyama, M. Tsukada, Phys. Rev. B 53 (1996) 7917.
[186] Y. Kanemitsu, T. Ogawa, K. Shiraishi, K. Takeda, Phys. Rev. B 48 (1993) 4883.
[187] Y. Kanemitsu, Phys. Rep. 263 (1995) 1.
[188] I. Batra, in: S.T. Pantelides (Ed.), The Physics of SiO_2 and its Interfaces, vol. 333, Pergamon Press, NY, 1978.
[189] N. Tit, M.W.C. Dharma-Wardana, Sol. State Comm. 106 (1998) 121.
[190] S.D. Kosowsky, P.S. Pershan, K.S. Kirsch, J. Bevk, M.L. Green, D. Brasen, L.C. Feldman, P.K. Roy, Appl. Phys. Lett. 70 (1997) 3119.
[191] A. Pasquarello, M.S. Hybertsen, R. Car, Appl. Phys. Lett. 68 (1996) 625.
[192] C.G. Van de Walle, J.E. Northrup, Phys. Rev. Lett. 70 (1993) 1156.

SUBJECT INDEX